MAGNETO-DIELECTRIC PROPERTIES OF BISMUTH SUBSTITUTED BARIUM HEXAFERRITE

Leah Margaret Ridgway, MEng.

Thesis submitted to The University of Nottingham

for the degree of Doctor of Philosophy

February 2011

The University of Nottingham

UNITED KINGDOM • CHINA • MALAYSIA

Abstract

The work contained within this thesis seeks to address the dielectric and magnetic properties of bismuth substituted barium hexaferrite (composition $BaBi_xFe_{12-x}O_{19}$ where $x = 0.0, 0.2, 0.5, 0.8, 1.0$ and 1.5) across a broad frequency spectrum. This material is potentially of interest in antenna applications (specifically a dielectric resonator antenna) where high permittivity and permeability materials can be exploited to physically minimize the size of antenna devices.

At low frequencies (20Hz – 3MHz) LCR meter based analysis was used to investigate the capacitance and inductance of the materials. The highest measured permittivity at 1MHz was $\varepsilon_r = 86.18 - 9.910j$, $tan\delta = 0.11$. High frequency (45MHz – 20GHz) permittivity was investigated using a vector network analyser (VNA) and coaxial probe. The highest recorded permittivity at 2.45GHz was $\varepsilon_r = 14.69 - 1.664j$, $tan\delta = 0.08$. A link between substitution level and permittivity and substitution level and inductance was made at either 1MHz or 2.45GHz. The homogeneity of the samples was explored using a near-field permittivity sensor. This showed small localized variations of permittivity across the surface but not significant enough to adversely effect bulk measurements. A dielectric resonator antenna was fabricated using a bismuth substituted barium hexaferrite sample. Resonant frequencies were identified at 6.6, 9.55 and 13.6GHz and radiation patterns for the system showed agreement with published theoretical results. This confirmed the suitability of the material in this application as a high permittivity material with relatively low loss.

This thesis contributes to scientific knowledge by characterising a broad range of bismuth composition materials across a wide frequency range, investigating the link between permittivity/inductance and doping level and presenting full results. The material has also been characterised using a near-field permittivity technique and used to fabricated a dielectric resonator antenna which have not previously been undertaken.

Acknowledgements

First and foremost I would like to thank my supervisor Prof. Ian Harrison for his help and guidance throughout the course of my studies (happily his attempts to escape by moving overseas failed!). My thanks also go to Dr. Philip Shepherd, Dr. Tom Cross and Prof. Eric Larkins for their assistance both before and after Ian's departure. My kind thanks also to Belle Ooi Pei Cheng at The University of Nottingham Malaysia Campus for characterising the radiation patterns of the prototype dielectric resonator antenna.

My thanks and appreciation go to my family and friends, without their love and support I would never have got this far. My Mum and Dad, Garnet, Ann and my partner Dave (sorry the owls didn't make the final cut!) have had a lot to put up with!

A PhD is a long journey and so many people have been awesome along the way, special mentions go to; Steve who I've drunk coffee with almost every working day for the last 4 years and who I'm going to miss ever-so much; to the members of the PRFEG both past and present; to John and Adam, who were with me at the start of this and were great people to live with; to Chris (Scouse), Amy, Vicky, Mark, Simon and Colette.

Finally to my 'Uncle' John Daintith who sadly passed away during my studies, who first explained to me what a 'proper' Doctor was.

Contents

Chapter 1

Introduction

All materials can be characterised in terms of their permittivity (ε_r) and permeability (μ_r). Permittivity refers to the ability of a material to store electric energy, while the permeability of a material represents the potential magnetic energy it can hold. A material with both a permittivity and permeability greater than unity is referred to as a magneto-dielectric material. Barium hexaferrite and bismuth substituted barium hexaferrite are two examples of these.

Barium hexaferrite, the parent compound, is a material which has been investigated by other authors [1] [2] [3] [4] [5] primarily because of its enhanced magnetic properties which make it suited for use in magnetic recording media [6] [7] [8] and microwave devices [9]. The material does however have disadvantages associated with it; primarily, it requires large amounts of energy to form via the conventional solid state sintering method due to its high threshold reaction temperature of 1050°C [10]. To get around this problem some authors have developed different methods to synthesise the material while others have investigated the effects of adding a sintering aid to lower the reaction temperature

[11] [12]. This work looks at substituting bismuth into the barium hexaferrite lattice. This acts as a sintering aid in addition to altering the electro-magnetic properties of the final material.

The characterisation of permittivity and permeability of materials across the frequency spectrum is important so that devices fabricated using these perform as anticipated. Testing of materials whose properties are unknown allows the potential for discovering new, more suitable for purpose compounds and thus the development of more efficient devices.

Barium hexaferrite and bismuth substituted barium hexaferrite are of particular interest in antenna applications due to the material having both a permittivity and permeability greater than unity. This allows the potential development of a material which does not have an impedance mismatch between it and free-space (being the usual medium signals propagate through), resulting in a more efficient antenna. Theoretical work modelling potential antennas using such materials has been conducted [13] [14] however published work is limited [15] [16].

Characterisation of sample permittivity can be performed across a broad frequency spectrum by the use of different techniques. At low frequencies the most common is to introduce the test material as the dielectric filling of a capacitor [17]. At higher frequencies vector network analysis techniques are employed such as coaxial probe methods and waveguide techniques [18] [19].

The vast majority of commonly used characterisation methods can only be used to quantify the bulk properties of a sample. Techniques to investigate the dielectric properties of small areas of a sample do exist and have been developed by certain universities [20]

[21] [22] [23], but have not as yet been marketed to a wider audience. The localised characterisation of bismuth substituted barium hexaferrite is of interest to investigate the homogeneity of sample permittivity.

The permeability and wider magnetic properties of a material are more difficult to characterise. The magnetic response of a material to a slowly changing magnetic field can be presented in the form of hysteresis loop data, which indicates the resistance of the sample to magnetisation and also its ability to remain magnetised after the applied field is removed [24] [25]. At low frequencies LCR meters can be used in conjunction with inductor based set-ups to measure the inductance of the resulting system. At high frequencies vector network analysis can again be used, however because two measurements are required (normally in the form of a through measurement) the physical shapes which samples can take is further restricted thus limiting the usefulness of these methods [17] [5].

1.1 Motivation for work

The writer's starting point for this thesis came from an interest in high permittivity materials and their characterisation which began with work undertaken as an undergraduate final year project. Research by others within the group into barium hexaferrite substituted with different materials contributed to a discussion that bismuth was a likely candidate material for use as a dopant.

A review of the literature currently existing on bismuth substituted barium hexaferrite produced a handful of papers [26] [27] [28] [29] which were limited in scope to either a single 'best' case result or focused more on the material formation rather than the

resultant electro-magnetic properties. This work primarily seeks to address this gap in the literature by providing a more comprehensive study with a wider ranging remit.

The sample compositions $BaBi_xFe_{12-x}O_{19}$ where $x = 0.0, 0.2, 0.5, 0.8, 1.0$ and 1.5 were produced, making this range of bismuth substituted barium hexaferrite compounds much wider than those previously tested. The greatest range previously published consists of samples with compositions $x = 0.0, 0.2, 0.3, 0.4$ and 0.8 but dielectric properties are only presented for one $x = 0.2$ composition [28].

The permittivity of these samples was characterised over a much wider frequency range. Previous frequency ranges investigated were 100Hz – 10MHz [26] and 200Hz – 1MHz [28]. However results were presented for only one bismuth substituted barium hexaferrite composition in both these papers. Low frequency results presented here range from 20Hz – 3MHz with data presented for all sample compositions and sintering regimes. No literature exists on the high frequency dielectric properties of bismuth substituted barium hexaferrite. This work presents results over the frequency range 45MHz – 20GHz. The relationship between bismuth substitution levels and permittivity is investigated with results presented. Links are made between the materials properties and the dielectric properties. A prototype near-field permittivity sensor was developed and used to characterise the surface of a bismuth substituted pellet in different places. The material has not previously been characterised in this way thus a contribution will be made about the heterogeneity of the material.

No work exists on the use of bismuth substituted barium hexaferrite as a material within a dielectric resonator antenna. This thesis will address this lack of knowledge.

The small amount of work that does exist on the magnetic properties of bismuth doped

barium hexaferrite [27] [28] is limited to presenting hysteresis loops and associated data for a small range of samples. Results presented here are for a range of bismuth substitution levels allowing more detailed conclusions to be drawn. There is no currently published work on the inductance and associated low frequency magnetic properties testing of these materials.

In summary, this thesis will contribute to scientific knowledge by investigating the dielectric and magnetic properties of bismuth substituted barium hexaferrite over a wider range of concentrations and frequency ranges than previously studied. Work was also carried out on localised permittivity and the use of the material in a dielectric resonator antenna which has not been studied previously.

1.2 Structure of thesis

The work presented within this thesis has been split into subject specific chapters each containing a short literature review relevant to its contents. After this any experimental procedures are explained, followed by results and specific observations and conclusions. Each chapter is finished with a summary of conclusions for the work conducted within it and a list of references.

Chapter 2 introduces barium hexaferrite and bismuth substituted barium hexaferrite, detailing the formation process. Results for materials characterisation including X-Ray Diffraction analysis, Scanning Electron Microscopy images, density and surface roughness measurements are presented.

Chapter 3 is concerned with low frequency permittivity characterisation. Within it the parallel plate capacitor method for quantifying the permittivity of a material at low

frequencies is detailed. Results are presented for a range of bismuth substituted barium hexaferrite compounds produced with different bismuth concentrations and subjected to different sintering regimes. Simulation results investigating non-ideal sample structures are also shown and the potential effects on characterisation considered.

Chapter 4 presents permittivity characterisation methods and results over a higher frequency range performed via a coaxial probe technique. Results for the range of sample compositions and sintering regimes are compared. Simulations investigate the theoretical results from different sample properties and comparisons with actual results are made.

Chapter 5 presents work related to the design, manufacture and testing of a near-field permittivity sensor to investigate the permittivity of small areas of a sample rather than bulk characterisation.

Chapter 6 covers the use of bismuth substituted barium hexaferrite as the dielectric material within a dielectric resonator antenna. Simulation work conducted to design an appropriate device was used to produce a prototype device which was then tested at microwave frequencies to ascertain its suitability for mobile phone and wireless network applications.

Chapter 7 is dedicated to the magnetic properties of bismuth substituted barium hexaferrite. The first part of this chapter details inductance measurements of materials taken using a LCR meter and inductor set-up. The latter part presents information and results in the form of magnetic hysteresis loops for a selection of samples.

Chapter 8 contains a summary of the main conclusions from each of the previous chapters.

1.3 References

[1] T. Ogasawara and M.A.S. Oliveira. Microstructure and hysteresis curves of the barium hexaferrite from co-precipitation by organic agent. *Journal of Magnetism and Magnetic Materials*, 217:147–154, 2000.

[2] J. Matutes Aquino, S. Diaz Castanon, M. Mirabal Garcia, and S. A. Palomares Sanchez. Synthesis by coprecipitation and study of barium hexaferrite powders. *Scripta Materialia*, 42(3):295–299, 2000.

[3] G. Benito, M. P. Morales, J. Requena, V. Raposo, M. Vzquez, and J. S. Moya. Barium hexaferrite monodispersed nanoparticles prepared by the ceramic method. *Journal of Magnetism and Magnetic Materials*, 234(1):65–72, 2001.

[4] M. Radwan, M.M. Rashad, and M.M. Hessien. Synthesis and characterization of barium hexaferrite nanoparticles. *Journal of Materials Processing Technology*, 181:106–109, 2007.

[5] P Shepherd, K. Mallick, and R. Green. Magnetic and structural properties of M-type barium hexaferrite prepared by co-precipitation. *Journal of Magnetism and Magnetic Materials*, 311(2):683–692, 2007.

[6] K Haneda, C. Miyakawa, and H. Kojima. Preparation of high-coercivity $BaFe_{12}O_{19}$. *Journal of the American Ceramic Society*, 57(8):354–357, 1974.

[7] C. Surig, K. A. Hempel, and D. Bonnenberg. Hexaferrite particles prepared by solgel technique. *IEEE Transactions on Magnetics*, 30(6):4092–4094, 1994.

[8] V.K. Sankaranarayanan, R.P. Pant, and A.C. Rastogi. Spray pyrolytic deposition of barium hexaferrite thin films for magnetic recording applications. *Journal of Magnetism and Magnetic Materials*, 220:72–78, 2000.

[9] P. Shi, S. D. Yoon, X. Zuo, I Kozulin, S. A. Oliver, and C. Vittoria. Microwave properties of pulsed laser deposited Sc-doped barium hexaferrite films. *Journal of Applied Physics*, 87(9):4981, 2000.

[10] K. Mallick, P Shepherd, and R. Green. Dielectric properties of M-type barium hexferrite prepared by co-precipitation. *Journal of the European Ceramic Society*, 27:2045–2052, 2007.

[11] S.S. Vidyawathi, R. Amaresh, and L.N. Satapathy. Effect of boric acid sintering aid on densification of barium ferrite. *Bulletin of Materials Science*, 25(6):569–572, 2002.

[12] E. Lucchini and O. Sbaizero. Mechanical properties of barium hexaferrite sintered in the presence of a low-melting glass. *Journal of Materials Science Letters*, 6(9):1098–1100, 1987.

[13] C. Fumeaux, D. Baumann, and R. Vahldieck. Advanced FVTD simulation of dielectric resonator antennas and feed structures. *Applied Computational Electromagnetics Society Journal*, 19(3):155–164, 2004.

[14] Z. Peng, H. Wang, and X. Yao. Dielectric resonator antennas using high permittivity ceramics. *Ceramics International*, 30:1211–1214, 2004.

[15] C.J. Panagamuwa, M.I. Kitra, P. McEvoy, J.C. Vardaxoglou, and J.R. James. Multiband material loaded low-SAR antenna for mobile handsets. In *Wideband and Multiband Antennas and Arrays*, 2005.

[16] M. Kitra, P. McEvoy, J.C. Vardaxoglou, and J.R. James. A Theoretical and Experimental Study of Dielectrically Loaded Antennas and their Contribution Towards Low-SAR. In *IEEE Antennas and Propagation Society International Symposium*, volume 4, pages 3593 – 3596, 2004.

[17] Agilent Technologies. Solutions for measuring permittivity and permeability with LCR meters and impedance analyzers, 2008.

[18] Agilent Technologies. Basics of measuring the dielectric properties of materials. http://cp.literature.agilent.com/litweb/pdf/5989-2589EN.pdf, 2005.

[19] Agilent Technologies. In-fixture measurements using vector network analyzers, 2006.

[20] T. Wei, X. D. Xiang, W. G. Wallace Freedman, and P. G. Schultz. Scanning tip microwave near-field microscope. *Applied Physics Letters*, 68(24), 1996.

[21] C. Gao and X. D. Xiang. Quantitative microwave near-field microscopy of dielectric properties. *Review of Scientific Instruments*, 69(11), 1998.

[22] S. M. Anlage, D. E. Steinhauer, B. J. Feenstra, C. P. Vlahacos, and F. C. Wellstood. Near-field microwave microscopy of materials properties. *Microwave Superconductivity*, pages 239–269, 2001.

[23] A. Tselev, S. M. Anlage, H. M. Christen, R. L. Moreland, V. V. Talanov, and A. R. Schwartz. Near-field microwave microscope with improved sensitivity and spatial resolution. *Review of Scientific Instruments*, 74(6), 2003.

[24] J.C. Anderson, K.D. Leaver, P. Leevers, and R.D. Rawlings. *Materials Science for Engineers*. Nelson Thornes Ltd., fifth edition, 2003.

[25] W. H. Hayt. *Engineering Electromagnetics*. McGraw-Hill, 4th edition, 1981.

[26] S. Ram. Observation of enhanced dielectric permittivity in Bi^{3+} doped $BaFe_{12}O_{19}$ ferrite. *Journal of Magnetism and Magnetic Materials*, 80:241–245, 1989.

[27] S. Ram, H. Krishnan, K.N. Rai, and K.A. Narayan. Magnetic and electrical properties of Bi_2O_3 modified $BaFe_{12}O_{19}$ hexagonal ferrite. *Japanese Journal of Applied Physics*, 28(4):604–608, 1989.

[28] M. Pal, P. Brahma, D. Chakravorty, and D.C. Agrawal. Magnetic properties of Ba hexaferrites doped with bismuth oxide. *Journal of Magnetism and Magnetic Materials*, 147:208–212, 1995.

[29] P. Winotai, S. Thongmee, and I.M. Tang. Cation distribution in bismuth-doped M-type barium hexaferrite. *Materials Research Bulletin*, 35:1747–1753, 2000.

Chapter 2

Barium hexaferrite

Barium hexaferrite is, as the name suggests, a hexagonal ferrite, the structure of which is illustrated in Figure 2.1. A ferrite is the term given to a compound which is formed from iron oxide and the oxide of one or more other metals [1]. These compounds have many different forms and applications, each with their own electric and magnetic properties.

Hexagonal ferrites occur in a variety of phases, tabulated in Table 2.1. M-type barium hexaferrite is most commonly used and will be the phase referred to when barium hexaferrite and bismuth substituted barium hexaferrite is used, unless otherwise specified. M-type barium hexaferrite, chemical formula $BaFe_{12}O_{19}$ was first developed in 1952 by Philips Industries with a trade name of 'ferroxdure' [3].

Phase	Parent compound formula
M-type	$AFe_{12}O_{19}$
W-type	$AFe_{18}O_{27}$
X-type	$A_2Fe_{30}O_{46}$

Table 2.1: Phases of hexagonal ferrites. A represents an alkali earth metal; barium is used within this thesis [2]

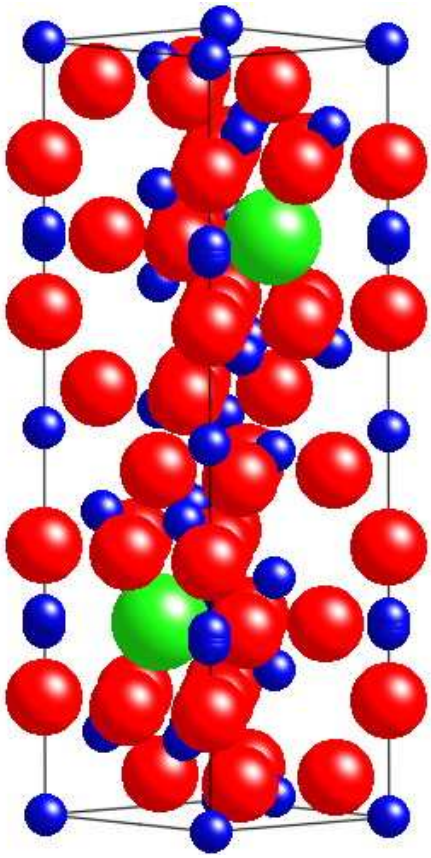

Figure 2.1: Crystal structure of $BaFe_{12}O_{19}$ where Ba ions are represented in green, Fe in blue and O in red [4]

The uses of ferrites are dependent upon the relative difficulty of demagnetising the compound (termed coercivity, measured in Oersteds, Oe). High coercivity materials are those which are hard to demagnetise and so are called "hard ferrites". Hard ferrites are used as permanent magnets; barium hexaferrite is used as a magnetic recording medium [5], while other ferrites are used in components such as electric motors. Conversely, soft ferrites are those materials which are relatively easy to demagnetise and are used in transformers and in the case of barium hexaferrite, microwave devices [6]. Barium hexaferrite exists as either a hard or a soft ferrite dependant on the formation technique which is selected dependent upon the properties required. It can also be made in bulk (as in this thesis), or as a thin film.

2.1 Formation

There are several different documented techniques available to form barium hexaferrite. The method chosen is dependent upon the final application; which will set the total sample mass, particle size and magneto-dielectric properties required. Other considerations are availability of equipment, lab facilities and the expense of chemical precursors and apparatus needed for synthesis. Listed below are the main processes, then follows a brief overview of each:

- Solid state synthesis;
- Chemical co-precipitation;
- Sol-gel;
- Hydrothermal;

- Spray pyrolysis;
- Glass crystallization.

These methods are used to produce bulk material with the exception of the final two processes listed, which are suitable for producing thin films of barium hexaferrite.

2.1.1 Solid state synthesis

Solid state synthesis is the traditional method of forming barium hexaferrite. In this method oxides and carbonates of precursor materials are mixed together and then heated to form the final compound. This method benefits from the simplicity in forming relatively large quantities of material and does not require expensive laboratory equipment. This process is used for the formation of material within this thesis and will be covered in more detail in Section 2.3.

2.1.2 Chemical co-precipitation

In chemical co-precipitation of barium hexaferrite, separate solutions containing barium and ferrite ions are precipitated from the solution (usually a nitrate or citrate) and the solid then dried out. This forms a fine powder which is then mixed and heated to react together in a similar way to the solid state synthesis method [7] [8] [9]. This method has been driven by the need for ever smaller particle sizes within the final barium hexaferrite compound. This results in a more effective material for perpendicular recording media because higher storage densities can be achieved [10]. Variations of the method produce a range of grain sizes in the final product from 0.1μm [11] to 0.5μm [12]. These procedures have been further refined such that material produced currently has grain sizes of 80-

120nm [13] [14]. Another benefit of co-precipitation is the reduction in intermediate phases present in the final product [15].

2.1.3 Sol-gel

A sol is a substance where fine particles (less than 0.1μm) are dispersed in a liquid. The sol then has either an initiator introduced, or is partially evaporated resulting in a gel of well mixed reactants being formed. This mixture can then be heated to form barium hexaferrite [16]. The chemistry of the sol-gel method results in final products which are homogeneous and form barium hexaferrite at a lower temperature [17] (as much as 500°K lower [18]) than the solid state method.

2.1.4 Hydrothermal

Hydrothermal experiments are performed within an autoclave, where reactants can be subjected to temperatures and pressures higher than normal conditions [7]. Barium hexaferrite is formed by reacting aqueous solutions of ferric nitrate and barium nitrate at different temperatures for different lengths of time [19] [20]. At a temperature of 300°C, particles of less than 0.1μm can be formed [21]. Starting solutions using chlorides instead of nitrates have also been used, resulting in nano-sized particles of barium hexaferrite (average size 12nm) at lower temperatures of 140-180°C [22]. In recent years this method has been advanced by the use of supercritical water within the autoclave to achieve greater control over particle size and thus electro-magnetic properties of the resulting compound [23] [24].

2.1.5 Spray pyrolysis

In spray pyrolysis, a thin film is formed by spraying a solution onto a heated surface. The reaction to form the compound occurs on the surface where a suitable temperature is chosen [25]. This process is used in conjunction with other methods such as citrate precursors allowing greater control over particle size from 100nm [26] to 50-80nm [27], or focusing on forming barium hexaferrite at lower temperatures (700°C) while still producing grain sizes in the nm range [28]. When used in conjunction with co-precipitation, barium hexaferrite powder with particle size of 30-60nm can be formed at a temperature of 550°C [29].

2.1.6 Glass crystallization

This method was developed with magnetic recording applications in mind; the size, shape and magnetic properties of the barium hexaferrite particles must have fine tolerance limits. In this scheme, reactant oxides are melted with a glass forming component, quenched, crystallized and then followed by chemical separation of the barium hexaferrite from the unwanted materials [30]. Early work resulted in particles of 80nm [31], later work studied controlling experimental temperatures from 200-780°C to form crystals ranging from 50-330nm as selected by the user [30].

2.2 Substituting bismuth ions into the barium hexaferrite crystal

In this work, iron oxide was reacted with barium carbonate to form barium hexaferrite. Bismuth substituted barium hexaferrite was formed by reacting iron oxide, barium carbonate and bismuth oxide. The compound formed has a chemical formula $BaBi_xFe_{12-x}O_{19}$ where $x = 0.0$, 0.1, 0.2, 0.5, 0.8, 1.0 and 1.5. It should be noted that this x-value is the starting value used in the 'green' mixture and so that there are likely to be variations in the x-value of the final material. For simplicity this thesis refers to the starting value whenever x-value is used.

The motivation of this thesis was to investigate the effect of varying levels of bismuth substitution on the magneto-dielectric ceramic. Other work on bismuth doped barium hexaferrite has established that the permittivity of the material is enhanced by the addition [32]. This study looks at a greater range of doping levels and the relationship between these levels and the dielectric properties of the compound over a wider frequency range, including much lower frequencies (20Hz – 3MHz).

Other work in the area of bismuth doped barium hexaferrite is limited; Ram et al. [33] conducted initial investigations in the topic comparing undoped barium hexaferrite samples to a single doping level with chemical formula $BaBi_{0.32}Fe_{11.68}O_{19}$, which was sintered with temperature ranges of 1100°C, 1200°C or 1300°C for either 4, 8 or 12 hours. The authors concluded that the presence of bismuth oxide reduces the reaction temperature. The electrical and magnetic properties were also enhanced. The authors reasoned that Bi^{3+} ions were substituting into the octahedral Fe^{3+} sites. From this, the argument was put that the larger size of the Bi^{3+} cation compared to the original Fe^{3+} cations distorts

the structure of the lattice causing the changes in the material properties. Bi^{3+} cations have radii of 0.96Å whilst Fe^{3+} cations have radii of 0.65Å in octahedral sites and 0.49Å in tetrahedral sites [34]. Ram et al. reported a maximum doping level of $x = 0.32$ found experimentally. This was later questioned by other writers [35].

Ion	Atomic radius (Å)
Fe^{2+}	0.77
Fe^{3+}	0.65
Bi^{3+}	0.96
Bi^{5+}	0.74

Table 2.2: Table of ionic radii for iron and bismuth ions within the barium hexaferrite lattice [34][36]

That study was supplemented by a later paper which focussed on the permittivity of the same range of samples [32]. The real part of permittivity and the loss tangent were measured using an impedance bridge system over the frequency range 100Hz – 13MHz. The permittivities of the samples were found to dramatically increase; some samples showed an increase to a maximum value of ε_r'=264,800, from an undoped value of ε_r'=5 at 100Hz.

Further work on bismuth doped barium hexaferrite was conducted by Pal et al.[35]. This considered a wider range of doping levels with chemical formula $BaBi_xFe_{12-x}O_{19}$ where $0 \leq x \leq 0.8$, using a different formation method (a variation of the solid-state method where precursors are ground under acetone before calcining and then sintering). A similar order of magnitude was found for high values of permittivity for the bismuth substituted barium hexaferrite, as observed as in the previous work by Ram et al. over the frequency range of 1kHz – 1MHz. The authors here differ in their conclusions about the positions of the bismuth cations within the crystal lattice; they argue that the X-ray diffraction (XRD) results show that the substitution in the lattice takes place where Bi^{5+} cations replace some of the Fe^{3+} cations. Considering the atomic radii of the ions involved, the

theory holds weight; Bi^{5+} has a radius of 0.74Å while Bi^{3+} as mentioned previously, has a radius of 0.96Å. These cations have the potential to substitute into the sites occupied by Fe^{3+} cations, which have a radius of 0.65Å. Therefore the Bi^{5+} cations, with their smaller radii are more likely to substitute into the Fe^{3+} sites.

These two conflicting conclusions were resolved by Winotai et al. [37], who utilized Mössbauer spectroscopy to study bismuth doped barium hexaferrite with formula $BaBi_xFe_{12-x}O_{19}$ where $x = 0.0, 0.1, 0.2, 0.3, 0.4$ and 0.6. They summarized that bismuth ions initially substitute into $4f_2$ sites and then as higher doping levels are reached, substitute into the 2b sites (Figure 2.2). They state that this is in-line with the experimentally observed initial increase in saturation magnetization and then decrease at higher bismuth concentrations. However, the authors did not conclude at which substitution level this change takes place. Work presented within this thesis will address this point. Work has also been undertaken to investigate the link between doping level and permittivity, which has not been included in past research.

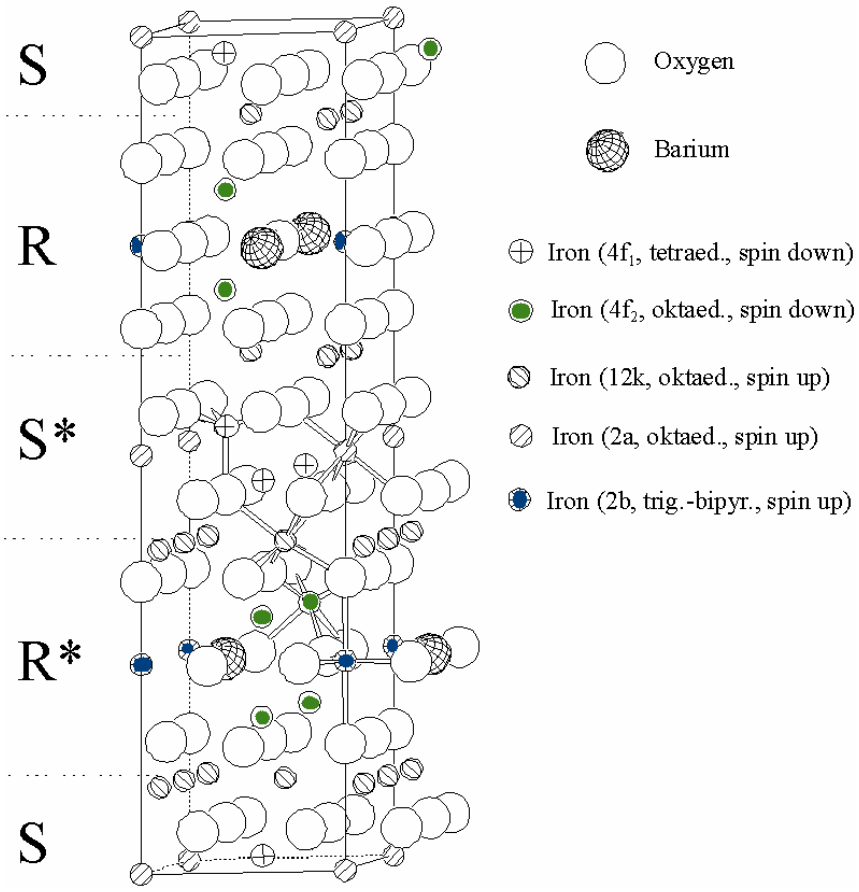

Figure 2.2: Crystal structure of two unit cells of $BaFe_{12}O_{19}$. Bismuth first substitutes into the $4f_2$ sites (marked in green) and then the 2b sites (marked in blue). Adapted from [38]

2.3 Material synthesis

Barium hexaferrite and bismuth substituted barium hexaferrite compounds were produced by the traditional solid state synthesis method where oxides and carbonates are mixed and combusted together. The reactants used were:

- $BaCO_3$ (99.98% purity, Aldrich);
- Fe_2O_3 (99.98% purity, Aldrich);
- Bi_2O_3 (99.95% purity, Aldrich).

The powder reactants were weighed out for each member of the series according to the molecular masses of each doping level as detailed below.

2.3.1 Molecular mass calculations

The mass of each compound required is dependent upon the atomic mass of the elements involved and the molecular formula of the final desired material. The atomic masses of the materials used are set out in Table 2.3.

Element	Symbol	Atomic mass
Barium	Ba	137.327
Iron	Fe	55.847
Oxygen	O	15.9994
Bismuth	Bi	208.98037
Carbon	C	12.011

Table 2.3: Table of atomic masses of elements used for materials synthesis [39]

The calculation of the masses of reactants required to form the final material is performed by first stating the composition of the bismuth substituted barium hexaferrite needed. The formula presented in Equation 2.1 is generic where the element symbols are then

replaced with their atomic masses.

$$\text{Compound mass} = \text{Ba} + (\text{Bi} \times x) + (\text{Fe} \times (12 - x)) + (\text{O} \times 19) \tag{2.1}$$

So the compound mass of $BaBi_{0.5}Fe_{11.5}O_{19}$ would be:

$$\begin{aligned} \text{Compound mass} &= \text{Ba} + (\text{Bi} \times 0.5) + (\text{Fe} \times (12 - 0.5)) + (\text{O} \times 19) \\ &= 137.327 + (208.98037 \times 0.5) \\ &\quad + (55.847 \times 11.5) + (15.9994 \times 19) \\ &= 1188.046285 \end{aligned} \tag{2.2}$$

The compound mass is then divided by the mass in grams of the material required. This result, the scaled mass, is used as a dividing factor when calculating the amount of each reactant required. Equation 2.3 shows the calculation using $BaBi_{0.5}Fe_{11.5}O_{19}$.

$$\begin{aligned} \text{Scaled mass} &= \text{Compound mass}/18 \\ &= \text{Ba} + (\text{Bi} \times 0.5) + (\text{Fe} \times (12 - 0.5)) + (\text{O} \times 19)/18 \\ &= 1188.046285/18 \\ &= 66.00257 \end{aligned} \tag{2.3}$$

The final step of the calculation is to take the molecular mass of each reactant and divide it by the scaled mass, calculated above. The molecular masses of the reactants are presented in Equations 2.4, 2.5 and 2.6. This final weighted calculation must take into account that in both Fe_2O_3 and Bi_2O_3 there are two atoms of metal present in each molecule. For example, 18g of $BaBi_{0.5}Fe_{11.5}O_{19}$ is used in Equation 2.3 to give final

masses of reactants needed in Equations 2.7, 2.8 and 2.9.

$$\begin{aligned} \mathrm{BaCO_3} &= \mathrm{Ba} + \mathrm{C} + 3 \times \mathrm{O} \\ &= 137.327 + 12.011 + 3 \times (15.9994) \\ &= 197.3362 \end{aligned} \tag{2.4}$$

$$\begin{aligned} \mathrm{Fe_2O_3} &= 2 \times \mathrm{Fe} + 3 \times \mathrm{O} \\ &= 2 \times (55.847) + 3 \times (15.9994) \\ &= 159.6922 \end{aligned} \tag{2.5}$$

$$\begin{aligned} \mathrm{Bi_2O_3} &= 2 \times \mathrm{Bi} + 3 \times \mathrm{O} \\ &= 2 \times (208.98037) + 3 \times (15.9994) \\ &= 465.95894 \end{aligned} \tag{2.6}$$

$$\begin{aligned} \text{Mass of } \mathrm{BaCO_3} &= \mathrm{BaCO_3}/\text{Scaled mass} \\ &= 197.3362/66.00257 \\ &= 2.9898\mathrm{g} \end{aligned} \tag{2.7}$$

$$\begin{aligned}\text{Mass of } Fe_2O_3 &= ((Fe_2O_3 \times (12 - x))/2)/\text{Scaled mass} \\ &= ((159.6922 \times 11.5)/2)/66.00257 \\ &= 918.23015/66.00257 \\ &= 13.9120\text{g}\end{aligned} \tag{2.8}$$

$$\begin{aligned}\text{Mass of } Bi_2O_3 &= ((Bi \times x)/2)/\text{Scaled mass} \\ &= ((465.95894 \times 1)/2)/66.00257 \\ &= 232.97947/66.00257 \\ &= 3.5298\text{g}\end{aligned} \tag{2.9}$$

2.3.2 Material processing

The "green" mixture for each sample was mixed and ground using an agate mortar and pestle, transferred into an alumina crucible and heated at 750°C for three hours. After cooling to room temperature the powder mixtures were again mixed and ground before being returned to the furnace for another two hours at 750°C. The grinding and mixing process was repeated and then a final one hour heating at 750°C was performed. This process was completed to allow mixing between the materials and aid thermal transportation mechanisms within the mixture.

The processed "green" mixtures were pressed into 20mm diameter pellets using a Specac 15011 uni-axial press to 221.9MPa. Pellets were visually inspected for cracks and other

defects; if these were present the pellet was crushed and reground and the pelletizing process repeated until the disk was of an acceptable quality.

Pellets were placed within alumina crucibles and returned to the furnace to be fired at 1100°C or 1200°C for a time ranging from 1 – 3 hours. During this period the formation of barium hexaferrite occurs as a two stage reaction as shown in Equations 2.10 and 2.11 [40].

$$\mathrm{BaCO_3 + Fe_2O_3 \rightleftharpoons BaFe_2O_4 + CO_2 \uparrow} \tag{2.10}$$

$$\mathrm{BaFe_2O_4 + 5\gamma - Fe_2O_3 \rightleftharpoons BaFe_{12}O_{19}} \tag{2.11}$$

The bismuth oxide contained within the mixture acts as a sintering aid by reducing the required threshold temperature for the reaction. The melting point of bismuth oxide is approximately 817°C [41] during the heating process; this melting enables greater mixing and reaction between components. The bismuth ions ($Bi^{3+/5+}$) also substitute into some of the iron ($Fe^{2+/3+}$) sites within the lattice (confirmed with XRD analysis, Section 2.7). This substitution leads to the formation of the bismuth doped barium hexaferrite compound denoted as $BaBi_xFe_{12-x}O_{19}$, where x is the proportion of bismuth added to the compound.

2.4 Samples after sintering

After sintering the pellets change in colour from red (due to the high iron oxide content) to grey as barium hexaferrite forms. Figure 2.3 shows a starting mixture and a formed pellet and Figure 2.4 shows a closer view of a sintered pellet surface.

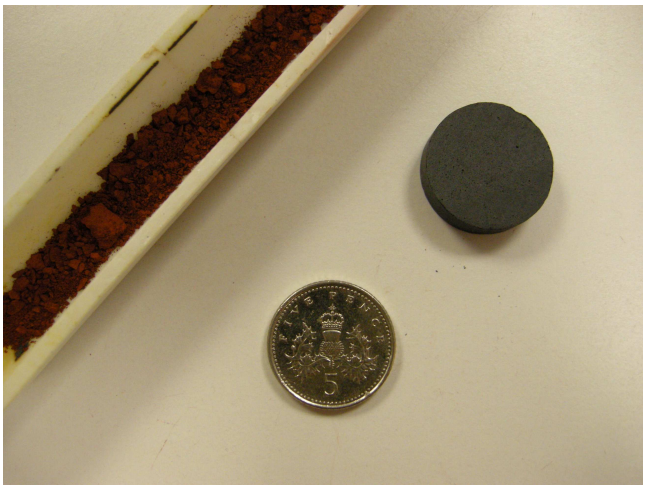

Figure 2.3: Image showing the red reactant materials in the vessel (left) and a grey sintered pellet (right). A five pence piece is shown to provide a reference scale

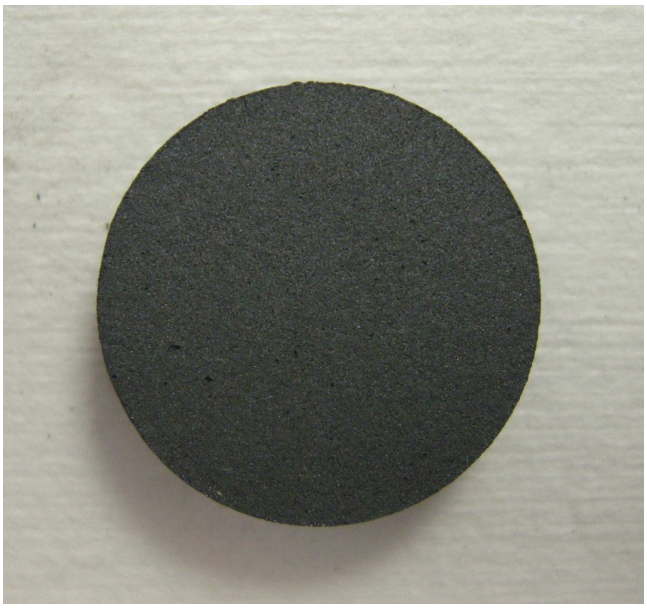

Figure 2.4: Series A pellet with composition $BaBi_{1.5}Fe_{10.5}O_{19}$ after sintering for 1 hour at 1100° and then for a further hour at 1200°C. The grey pellet surface shows some variation in depth and a roughness around the edges

2.5 Surface roughness measurements - Talystep method

Surface roughness measurements were taken using a Talystep. This profiles the smoothness of a material by dragging a stylus across the surface and outputting its vertical position on a print out. A Rank Taylor Hobson Talystep 1 machine was used with speed set to 200, which produced graphs with a good resolution where the scale was set to 0.4μm per smallest division.

Four pellets were selected for measurement which provided a range of permittivity results. The largest surface roughness variation was recorded as 11.6μm. This data provides an approximation for the order of magnitude of surface roughness, however it is limited because the nature of Talystep characterisation provides a profile across a cross section of the sample.

Samples selected for testing were series C, $x = 0.0a$ and $x = 0.2a, b$ and c. These were chosen because the $x = 0.2$ samples show the largest variation in permittivity between each side of the sample and the $x = 0.0a$ is a sample which has little variation. The speed of the Talystep was set to 200, which produced graphs with a good resolution where the scale was set to 0.4μm per smallest division. The Talystep graphs are shown in Figures 2.5, 2.6, 2.7 and 2.8 and key points from the graphs are presented in Table 2.4.

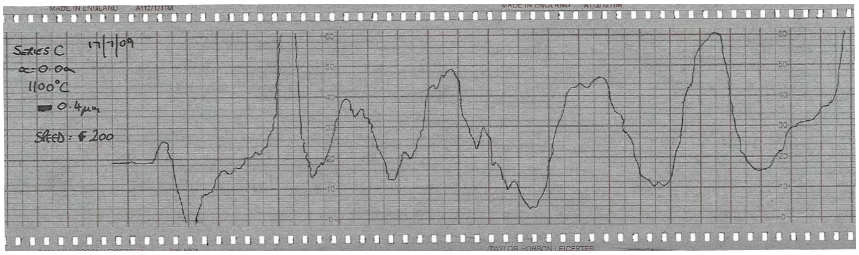

Figure 2.5: Talystep data for a cross section of pellet $x = 0.0a$ from series C.

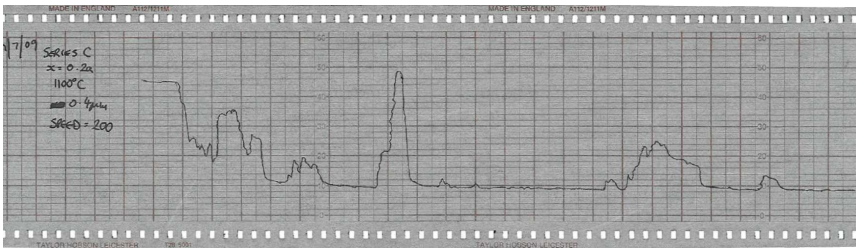

Figure 2.6: Talystep data for a cross section of pellet $x = 0.2a$ from series C.

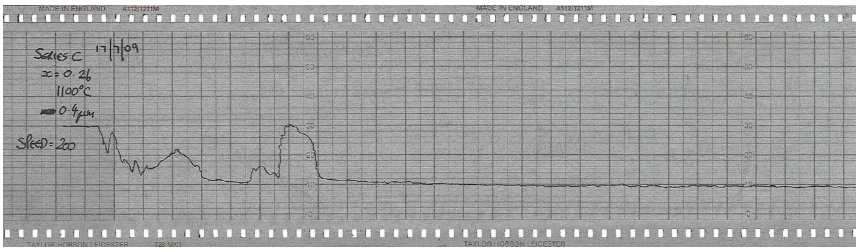

Figure 2.7: Talystep data for a cross section of pellet $x = 0.2b$ from series C.

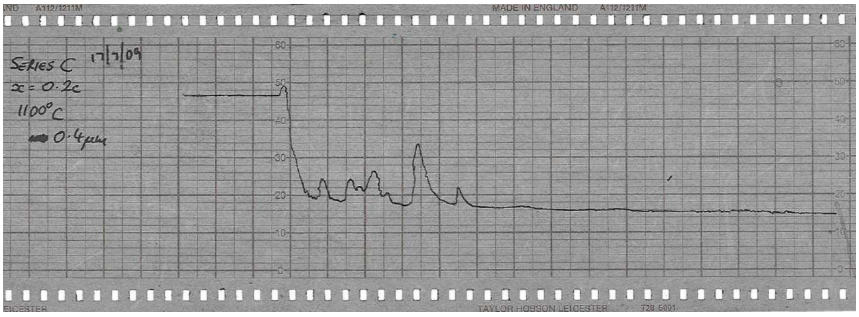

Figure 2.8: Talystep data for a cross section of pellet $x = 0.2c$ from series C.

Sample $BaBi_xFe_{12-x}O_{19}$	Range of measurements (μm)	Comments
$x = 0.0a$	11.6	Series of troughs and peaks, this trace has the most variation out of all samples studied
$x = 0.2a$	7.6	Peaks and troughs present, but less extreme than $x = 0.0a$ sample
$x = 0.2b$	4.0	Smoothest trace, large part of graph is flat
$x = 0.2c$	6.4	Some rough areas but also flat areas

Table 2.4: Table detailing measurements taken of a selection of bismuth doped barium hexaferrite pellets by Talystep profiling

From these results it can be seen that the $x = 0.0a$ pellet has the largest variation (11.6μm) in surface smoothness from all the samples tested. The $x = 0.2$ composition pellets all have more similar surface roughness measurements ranging from 4.0 – 7.6μm suggesting that the addition of bismuth improves the smoothness of the surface. With its relatively low melting temperature the bismuth could be melting and thus fitting into small gaps between platelets on a microscopic level which is smoothing the overall surface compared to the undoped barium hexaferrite. There are however, limitations in the Talystep profiling used, which have to be taken into account. The measurement taken is only a cross-section of the surface over which the stylus is drawn, thus providing a limited picture of surface roughness. For a more conclusive analysis a method which takes into account the entire surface of the pellet is required.

2.6 Density

The densities of pellets were characterised in the form of ideal pellets; assuming 100% density. Measurements of the thickness and diameter of pellets were taken using vernier callipers and the mass was recorded using Sartorius Research scales accurate to five dec-

imal places for masses below 42g. The dimension measurements were used to calculate the volume of each pellet and then this value was used to divide the mass by to find an ideal density value as given in Equation 2.12. Density is quoted in gcm^{-3} as standard, so units of mass required are g and volume is cm^{-3}.

$$\text{density} = \frac{\text{mass}}{\text{volume}} \tag{2.12}$$

2.6.1 Density of samples sintered at 1100°C

Densities of pellets sintered at 1100°C are presented in Figure 2.9 with some statistical analysis in Table 2.5. Pellets from series B and C have been sintered for one hour and pellets in series D and F have been sintered for three hours. Series F is a special case because it contains six pellets which all have the same composition of $x = 0.1$ ($BaBi_{0.1}Fe_{11.9}O_{19}$), other series contain a variety of samples with compositions ranging from $x = 0.0$ to 1.5.

The densities for the undoped ($x = 0.0$) pellets sintered for one hour show a much smaller range of densities which are some of the highest recorded. The density ranges are similar for series C and D which are sintered for one hour and three hours respectively, while series B shows more variation. Making comparisons across the different sample compositions is not simple because the optimum density is affected by the chemical make-up of the material as well as the formation process.

To investigate the range of densities for one sample composition, series F was characterised. Each pellet in this series was made from the same "green" mixture with composition $x = 0.1$ ($BaBi_{0.1}Fe_{11.9}O_{19}$). The mean average density of series F was

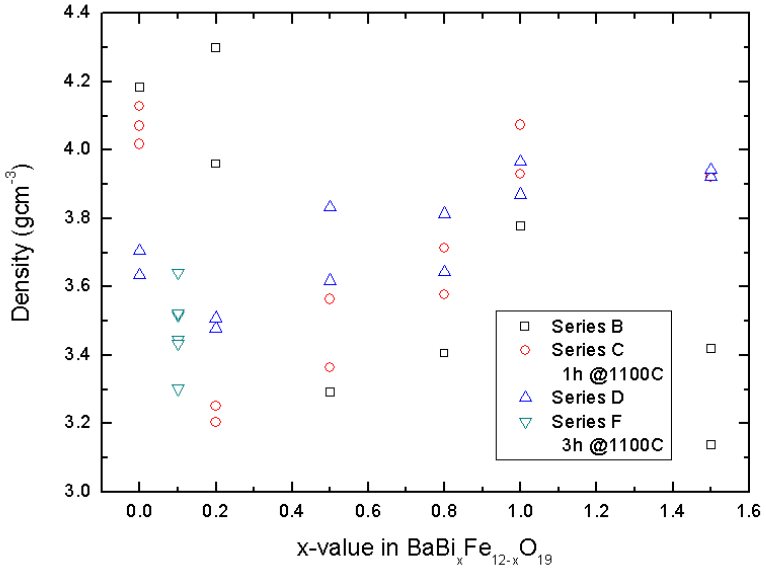

Figure 2.9: Ideal cylinder densities for series B, C, D and F: sintered for one hour or three hours at 1100°C

3.477gcm^{-3} and a standard deviation of 0.114gcm^{-3}. The densities for this series have the range compared to other series containing different composition pellets (as indicated by the relatively small standard deviation value and can also be seen in the graph shown in Figure 2.9). This result is as expected; pellets with the same composition have more similar densities than those which have a different chemical composition.

	Series B	Series C	Series D	Series F
With $x = 0.0$ sample				
Mean (gcm^{-3}):	3.683	3.750	3.745	3.477
Standard deviation (gcm^{-3}):	0.433	0.326	0.169	0.114
Without $x = 0.0$ sample				
Mean (gcm^{-3}):	3.613	3.653	3.759	3.477
Standard deviation (gcm^{-3}):	0.414	0.310	0.182	0.114

Table 2.5: Table of density data for pellets sintered at 1100°C

The average densities of the different sample series range from 3.477 – 3.750gcm^{-3} (a variation of 0.273gcm^{-3}). Other authors [33] reported a link between a longer sintering duration and higher densities for samples. This would be expected as the longer sintering

time allows the chemical reaction longer so a more complete reaction takes place. Results presented within this thesis do not display this relationship. However it was noted that the range of densities recorded (indicated by the standard deviation values) were smaller for samples which have been sintered for a longer duration; as shown by results for series D and F in Table 2.5. This implies that as the sintering duration is increased the density of the pellets becomes more uniform.

As mentioned before, the undoped barium hexaferrite has a markedly higher density than the bismuth substituted material when sintered for one hour. To quantify this effect and to investigate possible trends in the bismuth containing material, Table 2.5 also includes data on the averages and standard deviation of the pellets when the undoped material is removed from the dataset. As expected, the average density for series B and C drop, but also become more similar (3.613 and 3.653gcm^{-3} respectively). At the same time the standard deviation also falls showing that the densities are more repeatable for the bismuth substituted materials than at first observation including the $x = 0.0$ samples. It was also concluded that the range of densities is much closer for all compositions when the material is sintered for three hours rather than one. Series D has a standard deviation of 0.169gcm^{-3} and series F 0.114gcm^{-3}, compared to values in the range of 0.4 and 0.3gcm^{-3} for series B and C respectively.

2.6.2 Density of samples sintered at 1200°C

Figure 2.10 shows the densities of pellets from series A and E. Series A were sintered initially at 1100°C for one hour and then for a further hour at 1200°C, this data is presented within this set because 1200°C is the highest temperature the material has

been subjected to. Series E contains pellets which have been sintered for three hours at 1200°C.

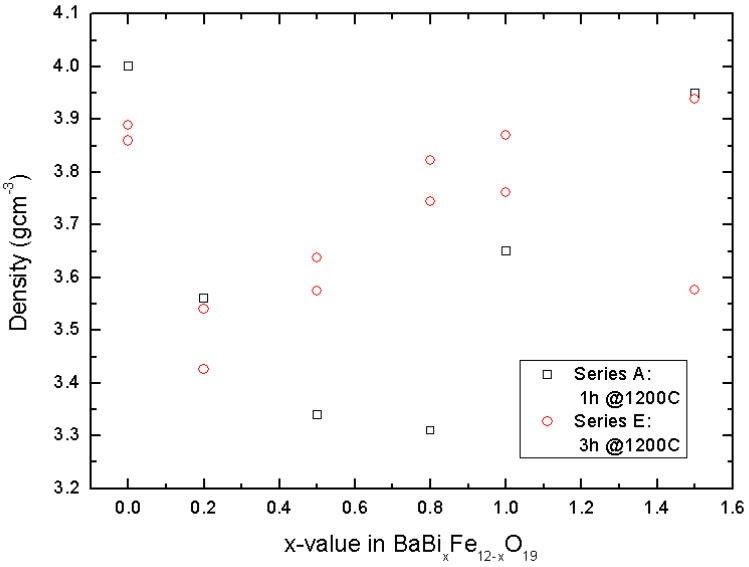

Figure 2.10: Ideal cylinder densities for series A and E: sintered for one hour or three hours at 1200°C

Due to the small number of samples in series A (one per composition) it is more difficult to draw conclusions on trends observed. The mean average and standard deviation information is presented in Table 2.6.

	Series A	Series E
With $x = 0.0$ sample		
Mean (gcm^{-3}):	3.635	3.720
Standard deviation (gcm^{-3}):	0.295	0.165
Without $x = 0.0$ sample		
Mean (gcm^{-3}):	3.562	3.689
Standard deviation (gcm^{-3}):	0.263	0.164

Table 2.6: Table of density data for pellets sintered at 1200°C

The mean average density for pellets from series E is greater than those of series A both with and without the undoped $x = 0.0$ sample included. The standard deviation which indicates the range of densities recorded across the series is smaller for series E. These results support the trends observed for the lower sintering temperature of 1100°C in the

previous section; a longer sintering duration results in a smaller range of pellet densities. However due to the small size of the data set for series A this cannot be strongly relied upon and is only an indicative result. When densities of individual pellets are plotted (Figure 2.10) it can be clearly seen that although the average density of samples from series E is higher, in half of the compositions the density of the samples from series A are in fact larger (compositions $x = 0.0, 0.2$ and 1.5).

2.6.3 Conclusions

The mean averages across all compositions are similar for both sintering durations of one hour at 1100°C (series B and C) and 1200°C (series A). A similar result is observed for the pellets sintered for three hours at both temperatures (series D and E). The standard deviations observed are slightly smaller for the pellets which have been sintered at the higher temperature of 1200°C compared to their 1100°C sintered counterparts with the same sintering duration. Bismuth containing samples (results excluding sample composition $x = 0.0$) have more similar densities when sintered for longer periods of time, shown by a lower standard deviation for both series D and E compared to their counterparts at the same temperatures.

The theoretical density of unsubstituted barium hexaferrite is 5.293 gcm^{-3} [42] while other authors have reported densities of bismuth substituted barium hexaferrite in the region of 4.8 – 4.9 gcm^{-3} [33]. The values presented here are lower than these values, however when the simple nature of the density characterisation method employed is considered this is an expected result. The results of the sample densities are still valid for comparison, however this data would benefit from a more rigorous measurement regime

which takes the porosity of samples into account.

2.7 X-ray diffraction analysis

X-ray diffraction (XRD) analysis has been used widely in the characterisation of materials since its discovery in 1912 [43]. XRD analysis is commonly used to identify unknown, or confirm the composition of chemical compounds.

X-rays used in XRD analysis are of a comparable wavelength to the size of atoms. This means that when X-rays are transmitted towards the surface of a sample some of the X-rays will pass directly through the material and some will be deflected by the atoms. The scattering pattern provides information about the distribution of the atoms within the material.

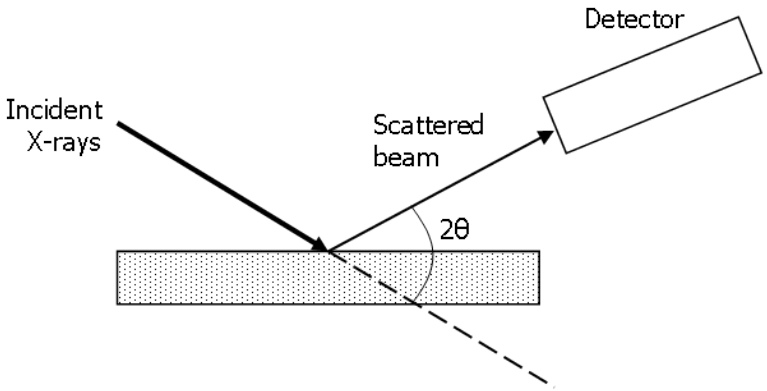

Figure 2.11: Schematic showing the experimental set-up of a XRD emitter and detector with the sample shown by the shaded block (adapted from [44]).

Different atoms interact with the incident X-rays in different ways, this can cause both constructive and destructive interference which is received at the detector resulting in maxima of varying intensities. This data is collected and compared to standard reference files to identify the material. The peak with the greatest magnitude is designated the

100% peak and the magnitude of all other peaks is defined as a percentage of the 100% peak.

XRD measurements were used to confirm the formation of barium hexaferrite and bismuth doped barium hexaferrite.

2.7.1 Bragg's Law

Bragg's Law is the theoretical basis for XRD analysis. It states that "when a beam of X-rays of wavelength λ, strikes a crystal surface in which the layers of atoms or ions are separated by a distance d, the maximum intensity of the reflected ray occurs when:

$$sin\theta = \frac{n\lambda}{2d} \tag{2.13}$$

where θ is the complement of the angle of incidence and n is an integer." [45].

The diagram in Figure 2.12 shows how X-rays interact with the atoms within the sample in accordance with Bragg's Law.

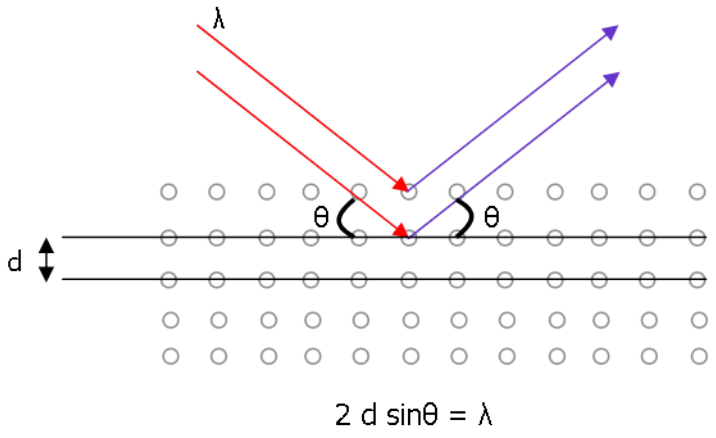

Figure 2.12: Interaction between atoms (marked as grey circles) and incident X-rays. Atoms within the material cause the X-ray photons to be deflected when they collide with electrons in the material (adapted from [44]).

2.7.2 System in use at The University of Nottingham

XRD measurements were taken of barium hexaferrite and bismuth substituted barium hexaferrite sample pellets for the samples sintered for one hour at 1100°C and also after a further hour at 1200°C. A Siemens Kristalloflex 810 using CuK_α radiation performed the required measurements. The analysis was conducted over a 2θ range of 10 – 90° with a step size of 0.05° at a rate of 2 seconds per step.

With this technique more accurate results are obtained by placing the smoothest side of the pellet upwards in the machine; this ensures that X-rays are defracted by the crystal lattice of the material and not surface imperfections of the pellet. A visual inspection was performed to decide which side was the smoothest.

Analysis of the raw data was performed using the EVA 2 software package. Data was processed first of all by stripping the $K_{\alpha 2}$ component of the signal, then removing the background noise by using a curvature of 0.5. Figure 2.13 shows the effect of post-processing on the measurement data. The trace obtained was compared to the standard database files to find a match for the material.

After processing the data was exported in .RAW format and converted into .UXD format using a file exchange program so that further analysis could be performed using the Origin Pro. 75 software suite.

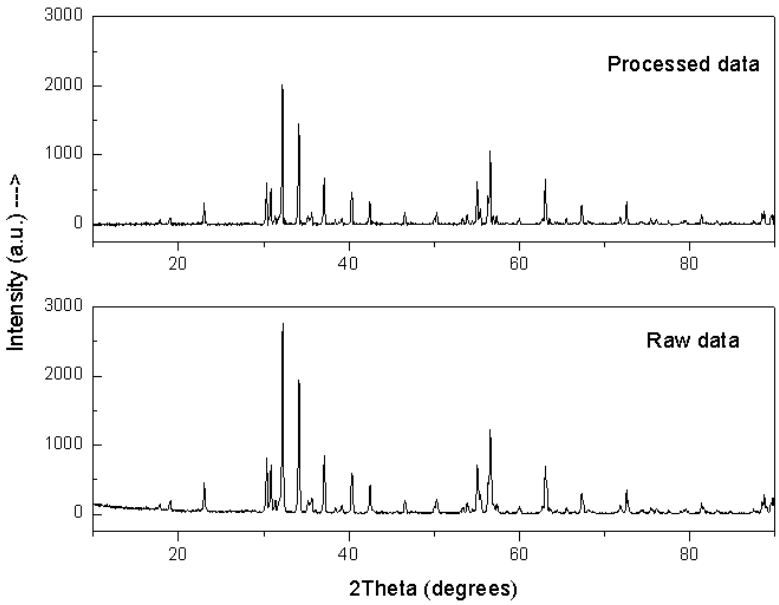

Figure 2.13: Graph showing the effect of removing $K_{\alpha 2}$ interference and background noise from the signal. The post-processing improves the quality of the signal without altering the information contained in the peaks

2.7.3 Results after sintering at 1100°C

Undoped sample

After sintering for one hour at 1100°C XRD analysis showed that the top match for the material was barium hexaferrite ($BaFe_{12}O_{19}$, JCPDS 39-1433). Other authors [42] have used standard JCPDS 27-1029 as the reference for barium hexaferrite. Although the two standards have very similar peak positions and intensities, JCPDS 39-1433 is used within this research because it is characterised over a greater 2θ range allowing more comprehensive comparisons. Figure 2.14 also shows the presence of intermediate product $BaFe_2O_4$ (JCPDS 46-0113) and also unreacted Fe_2O_3 (JCPDS 33-0664). This lead to the conclusion that the undoped barium hexaferrite compound had not yet fully formed. This result can be explained by considering the time delay in the furnace reaching the sintering temperature and the interior of the pellet reaching the target temperature;

thus not all of the sample body reached the required 1050°C threshold [42] for sintering temperature and time to form.

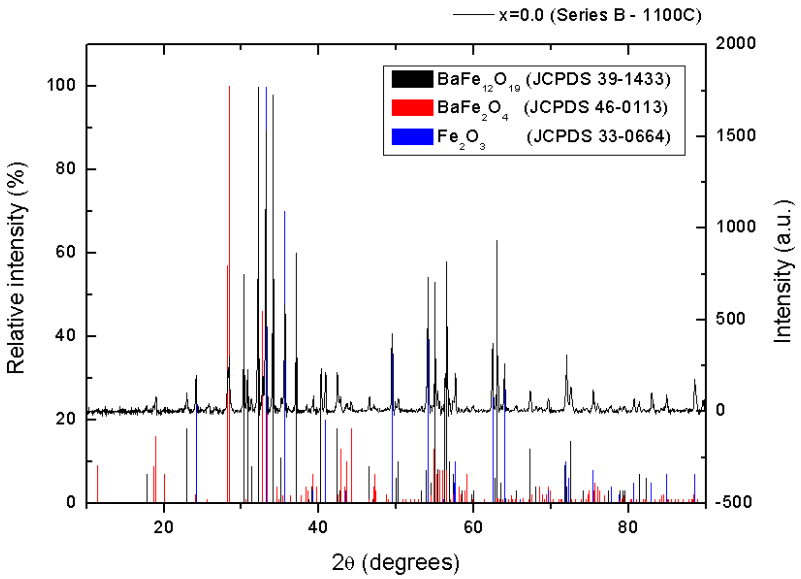

Figure 2.14: XRD analysis for undoped barium hexaferrite after sintering for one hour at 1100°C

Doped samples

Figure 2.15 shows the XRD analysis results for pellets with x-values $x = 0.0, 0.2$ and 1.5. from series B which have been sintered for one hour at 1100°C. The top match for all samples is the barium hexaferrite standard. The $x = 0.0$ sample shows a lower correlation to the standard than the other graphs in the figure, indicated by the presence of precursor materials which are not seen in the $x = 0.2$ and 1.5 pellets which contain bismuth.

The XRD data for the samples containing bismuth show some interesting differences. The first noticeable feature is the peak at 23° which is observed as a single peak for the $x = 0.2$ sample and becomes split into a double peak for the $x = 1.5$ sample. The same effect is observed for the 100% peak at 32°. This is most probably due to the presence of

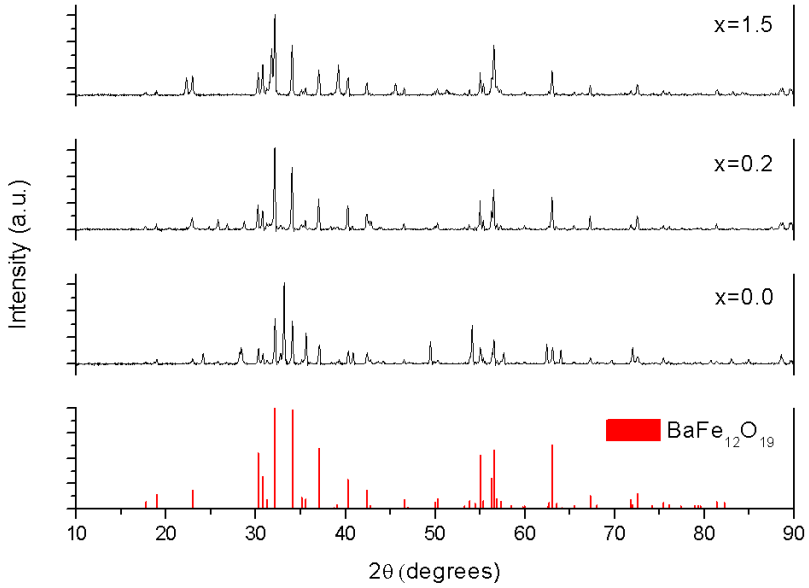

Figure 2.15: XRD analysis for $x = 0.0, 0.2$ and 1.5 samples from series B after sintering for one hour at 1100°C

the bismuth within the sample distorting the structure of the barium hexaferrite.

2.7.4 Results after sintering at 1200°C

Undoped sample

The XRD analysis for the undoped sample showed that barium hexaferrite was only partially formed. The peaks in the XRD trace showed that there was also some intermediate stage $BaFe_2O_4$ product in the pellet and also some unreacted Fe_2O_3 present. As the sintering temperature is increased this in turn increases the chemical reaction rate to form more material. Thus the presence of unreacted product was unexpected because it implies that either not all of the sample was reaching the 1050°C temperature required for the formation of barium hexaferrite [42] which is more than 100°C cooler than the current sintering temperature, or that the reactants did not reach this temperature for long enough to facilitate the reaction.

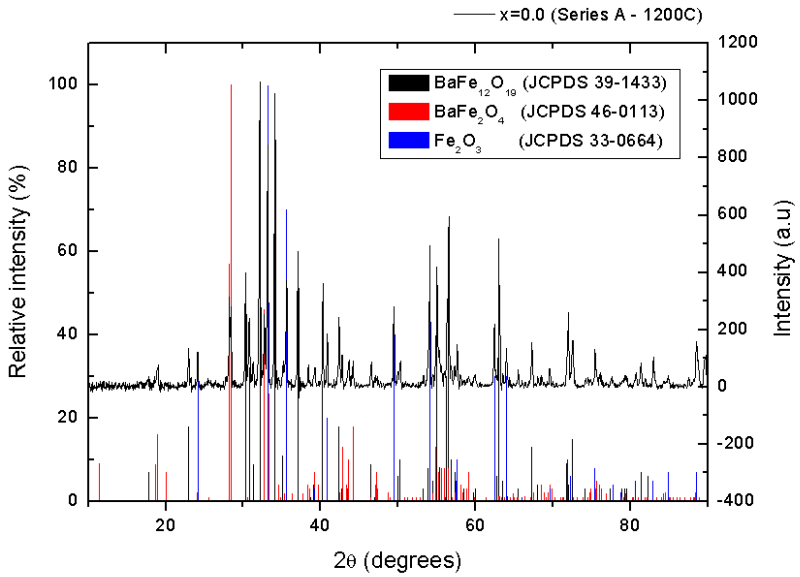

Figure 2.16: XRD analysis for undoped barium hexaferrite after sintering for one hour at 1100°C, followed by a further hour at 1200°C

Doped samples

XRD analysis indicated that the samples which include bismuth in their composition are formed by 1200°C. All bismuth substituted samples show a strong correlation to the $BaFe_{12}O_{19}$ standard file however the patterns do show variation with doping concentration. The greater the level of doping the more altered the traces become. This is a gradual process which can be seen in Figure 2.17.

The peak at 23° can be seen as a single peak in the $x = 0.2$ graph. It then becomes a double peak as the doping level increases until at $x = 1.5$ the second peak is of a comparable height to the original peak. A similar peak splitting effect is seen at the strongest peak at the 32° position where the effect increases with increased bismuth concentration.

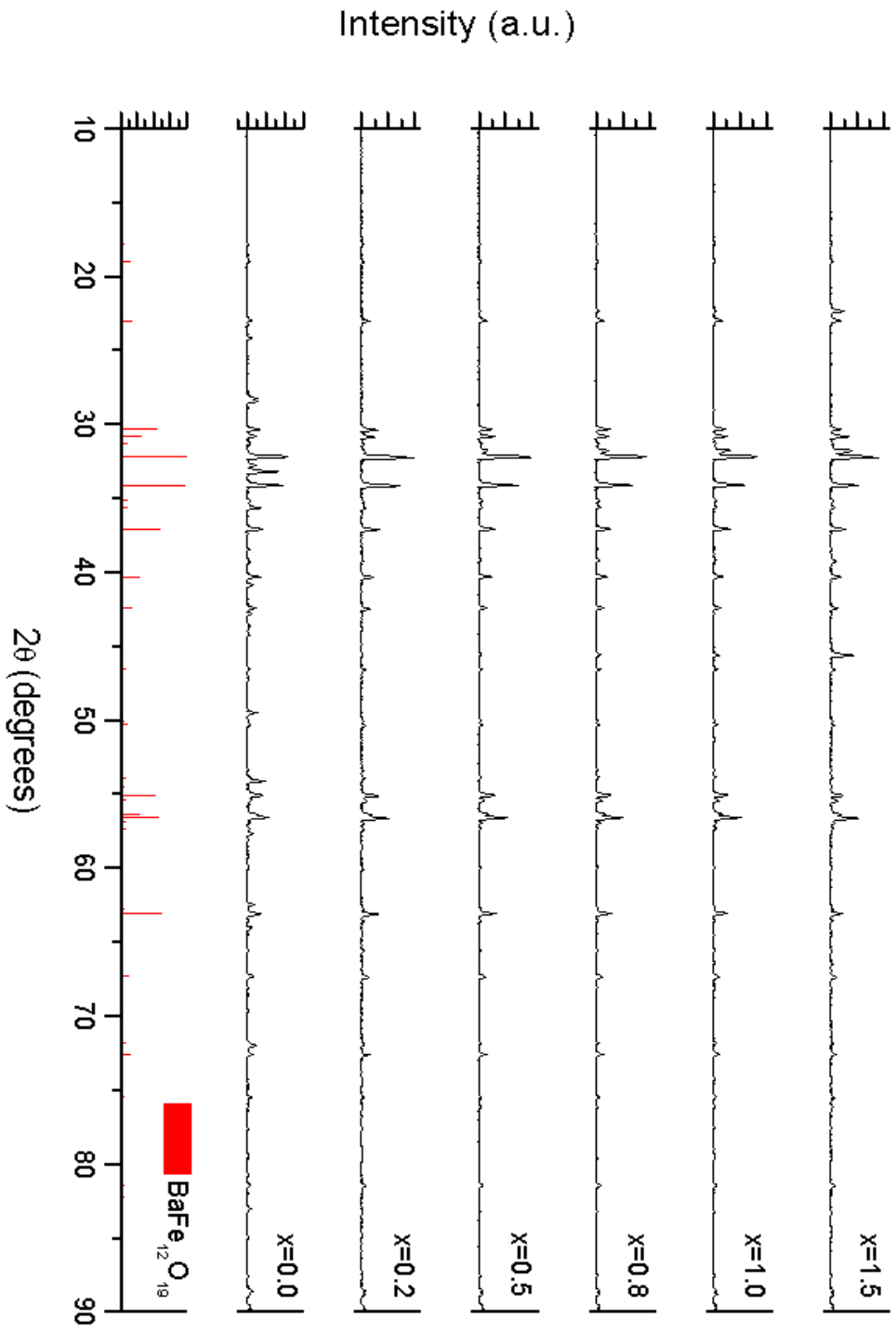

Figure 2.17: XRD analysis for barium hexaferrite doped with varying levels of bismuth after sintering for one hour at 1100°C followed by sintering at 1200° for a further hour compared to the $BaFe_{12}O_{19}$ standard file

Possible change to W-type barium hexaferrite

Shepherd et al. [46] investigated the properties of barium hexaferrite substituted with cobalt. They found that for high levels of cobalt doping the material changed phase to become a W-type ferrite ($BaFe_{16}Co_2O_{27}$). Thus the possibility that the material was changing to W-type bismuth barium hexaferrite was considered.

W-type ferrites have the general form $AMe_2Fe_{18}O_{27}$ where A is an alkali earth metal; barium in this case; and Me is a transition metal such as cobalt, zinc or nickel [47] or for this research, bismuth. Applying this, W-type barium hexaferrite has the chemical formula $BaBi_2Fe_{16}O_{27}$.

Figure 2.18 shows the XRD analysis for the sample with the maximum level of bismuth substitution ($x = 1.5$). Analysis of this compound using the EVA 2 software package shows the top match is still JCPDS 39-1433, M-type barium hexaferrite. However there are peaks present which do not match to this standard. When the standard JCPDS 19-0098, W-type hexaferrite, is added for comparison it is shown that the peak positions do not align to the position of the peaks in the sample, and thus is concluded that the material is not changing phase to a W-type ferrite. The deviation from the M-type standard is due to a cause other than a shift to W-type barium hexaferrite.

2.7.5 Conclusions

The conclusion from these observations is that barium hexaferrite is not formed after one hour at either 1100°C or 1200°C, which was not expected but it has been considered that this is due to the interior surfaces of the material not reaching the threshold temperature of 1050°C required for reaction [42]. The addition of bismuth to barium hexaferrite lowers

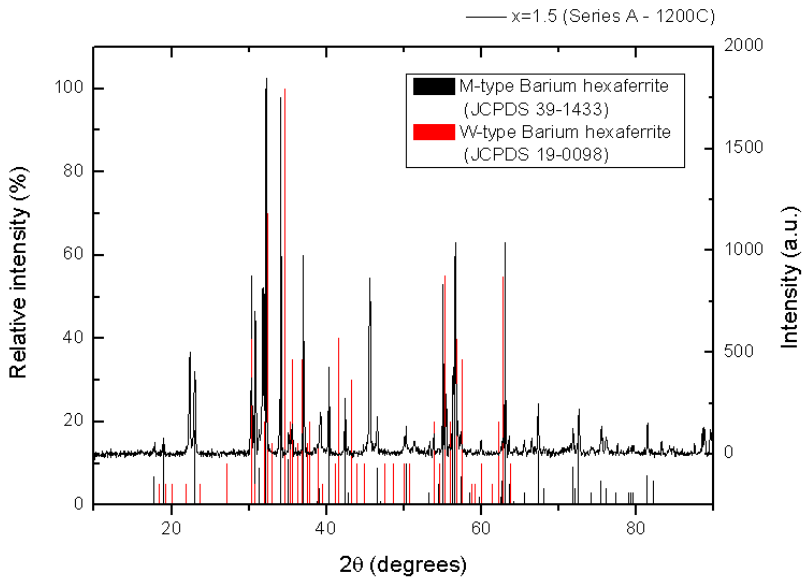

Figure 2.18: XRD analysis for maximum levels of bismuth substitution for barium hexaferrite ($x = 1.5$) after sintering for one hour at 1100°C followed by sintering at 1200° for a further hour compared to both M-type and W-type barium hexaferrite standards

the formation temperature required as bismuth containing samples are formed by both 1100°C and 1200°C, but not the undoped samples. As more bismuth is added to the compound the XRD data deviates more from the standard files as the crystal structure is distorted, seen by the increase in the presence of split peaks with increasing bismuth addition. This also suggests that there is no clear saturation point for the levels of bismuth substitution used within this work because the XRD traces continue to change, rather than remaining constant above a certain x-value. This fits with the argument put forward by Winotai et al. [37] that bismuth continues to substitute into the lattice, rather than that of Ram et al. [33] who theorised that there is a maximum x-value of $x = 0.32$. The bismuth substituted barium hexaferrite was confirmed to be M-type as this is the closest match. The potential phase shift to W-type material was considered and rejected after comparisons with W-type XRD standard data.

2.8 Scanning Electron Microscopy and Energy Dispersive X-ray analysis

Scanning electron microscopy (SEM) is a useful tool in examining the micro-structure of materials while Energy Dispersive X-ray (EDX) analysis identifies the chemical composition of a sample. SEMs provide greater magnification factors and depth of field compared to optical microscopes.

The microscope operates by emitting electrons from the gun which travel along the microscope column being focussed by condenser and objective lenses until the final spot size is a few nanometres in diameter. This focussed beam interacts with the sample causing excitation of electrons in the surface layers. Secondary and backscattered electrons are detected and used to form the image of the area under investigation [48] [49]. Figure 2.19 shows a schematic diagram of a SEM.

2.8.1 System in use at The University of Nottingham

SEM and EDX analysis was performed using a JSM 6400 scanning microscope. Images were stored on an attached PC and then exported to a local PC for analysis.

2.8.2 SEM analysis of sample micro-structure

Initially two samples were selected for the investigation of sample micro-structure. These were sample series F composition $x = 0.1$ (chemical formula $BaBi_{0.1}Fe_{11.9}O_{19}$) which have been sintered for three hours at 1100°C. Figures 2.20 and 2.21 show the grains which form the pellets. In the first image hexagonal grains which are seen in unsubstituted

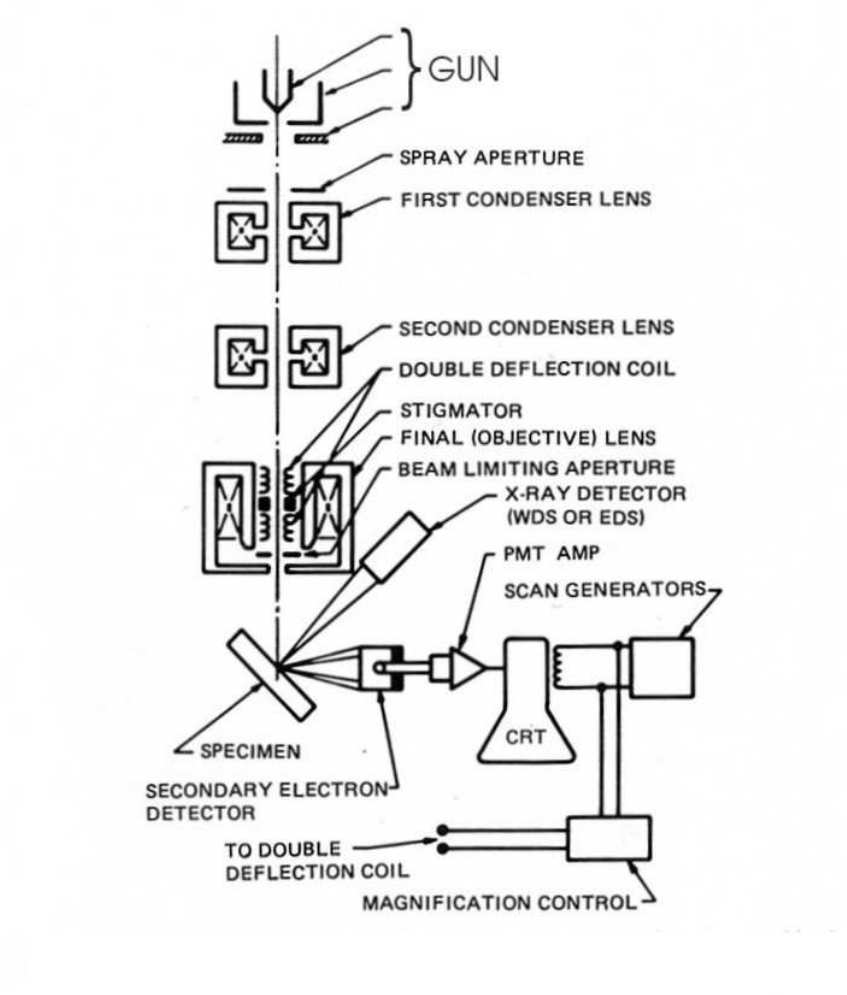

Figure 2.19: Schematic diagram of a scanning electron microscope [50]

barium hexaferrite are present and large variation in both grain size and orientation is observed. Figure 2.21 shows a smaller variation in grain size which is more common throughout the sample. Both faces of the sample pellet displayed similar grain sizes (maximum of 10μm) and random orientation observed in the SEM images.

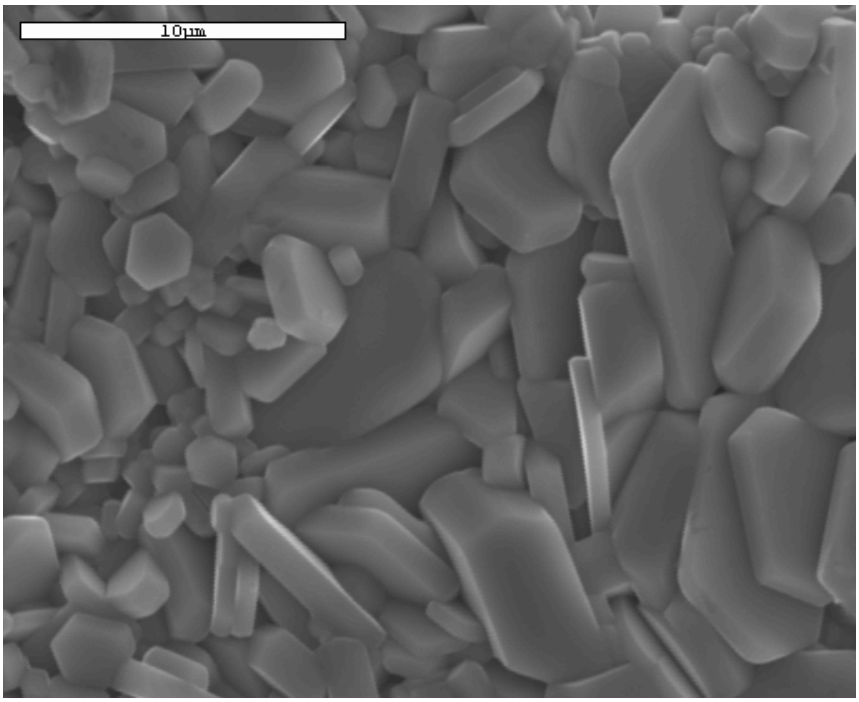

Figure 2.20: SEM image showing micro-structure for sample $x = 0.1c$ side 1

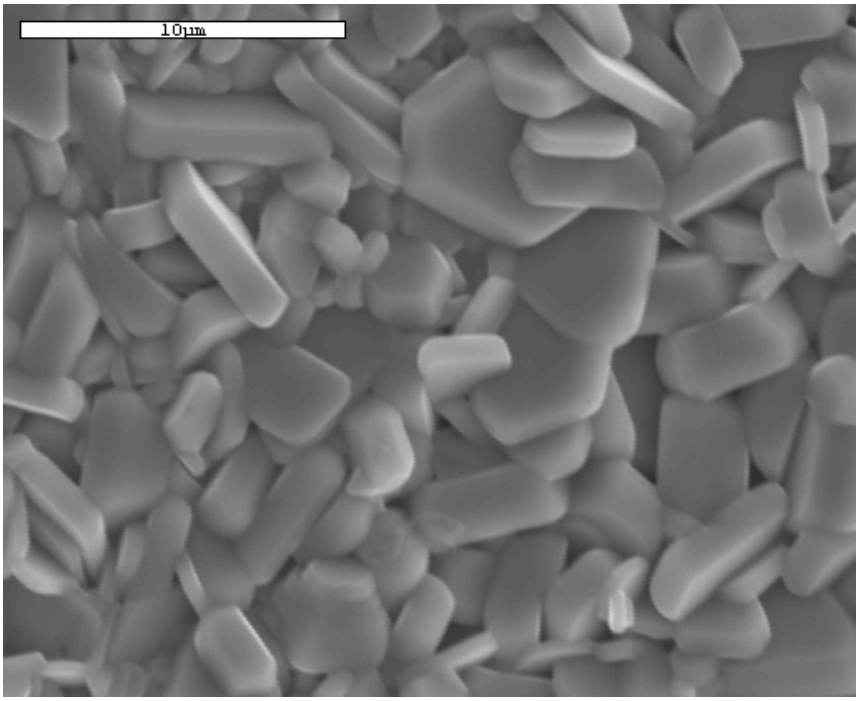

Figure 2.21: SEM image showing micro-structure for sample $x = 0.1c$ side 2

2.8.3 SEM analysis of sample surface smoothness

SEM was used to capture images of the surface of a sample in addition to its microstructure. This method does not provide a quantitative analysis of the surface roughness, however it does show imperfections on the surface. Figures 2.22 and 2.23 show the surface of the same pellet (series F, $x = 0.1c$) for both sides.

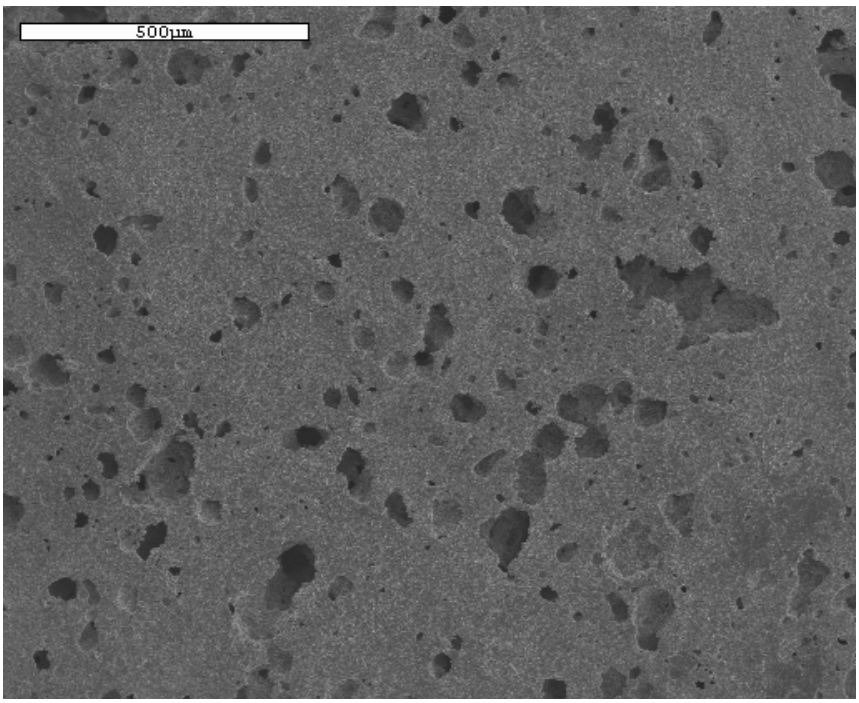

Figure 2.22: SEM image showing surface porosity for sample $x = 0.1c$ side 1

The images show that there is no significant difference in the surface roughness between the different sides of the pellet. Both figures display areas where the surface appears flat and areas where the porosity of the material is observed. The characterisation of sample permittivity is most accurate when the contact surfaces of the material under test are smooth. One technique used to improve measurement accuracy is to polish a sample to smooth the surface. However if the grain size is larger than a few microns, additional grains will be removed and the overall effect is that the material is no smoother.

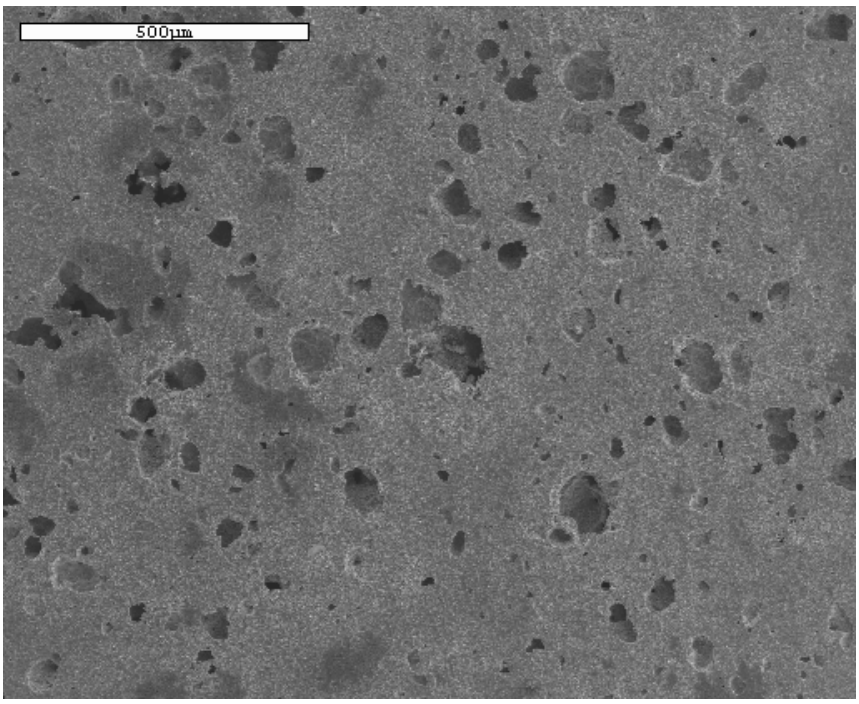

Figure 2.23: SEM image showing surface porosity for sample $x = 0.1c$ side 2

Thus with grain sizes up to 10μm, polishing the sample surface will not improve the situation.

Figure 2.24 shows the micro-structure of the material around a hole on the pellet surface. The size of the grains around the hole in the sample surface show the same variation of sizes and orientation as those on the flat areas of the pellet. Individual grains of a similar size and orientation are also observed within the hole in the surface. Thus the conclusion drawn was that the micro-structure of the material is not distorted by the presence of the holes; the grains around and inside the hole display similar properties.

SEM analysis performed on samples $x = 0.0$ and $0.2a$ from series D and $x = 0.2a$ from series E displayed similar results for grain sizes, grain orientation and porosity. Pellets were also tested using the backscattering mode of the instrument; Figure 2.25 and 2.26 show the same area of the series E $x = 0.2a$ sample in both normal and backscattering modes of operation.

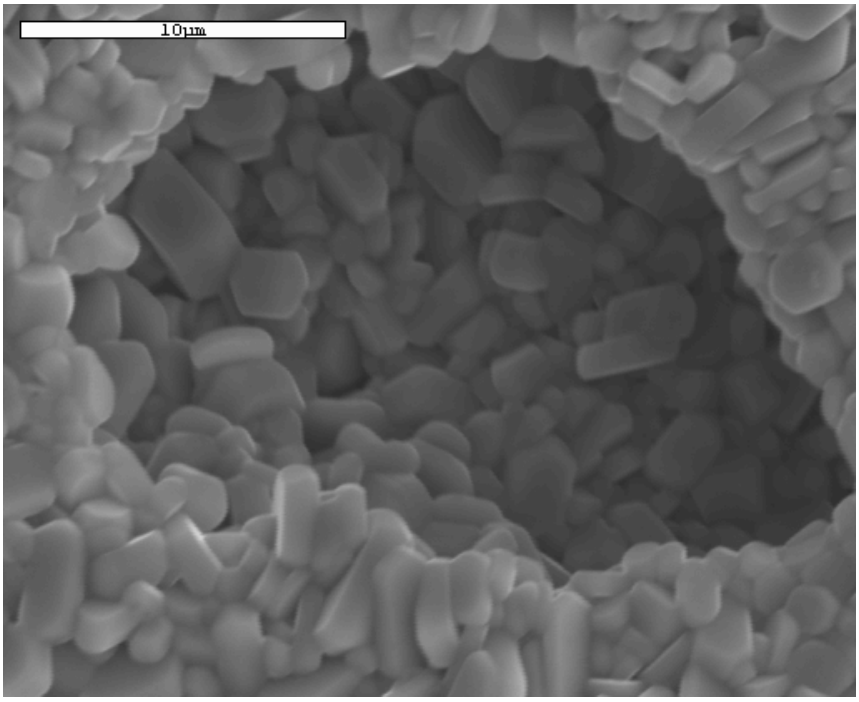

Figure 2.24: SEM image showing the micro-structure of an area around a hole on the pellet surface for sample $x = 0.1c$ side 2

The key observation in the differences between the images is that some irregularly shaped areas of the backscattered image are highlighted in white. This material is still present in the normal mode image, however it is not clearly distinguishable from the hexagonal grains. EDX analysis was used to investigate the nature of this material.

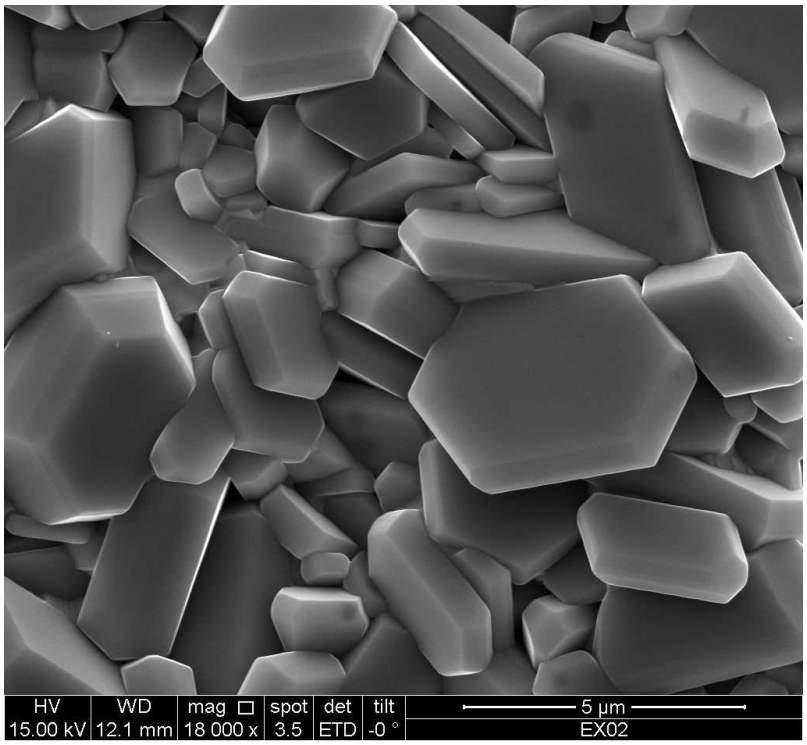

Figure 2.25: SEM image showing the micro-structure of an area on the surface of the series E $x = 0.2a$ pellet

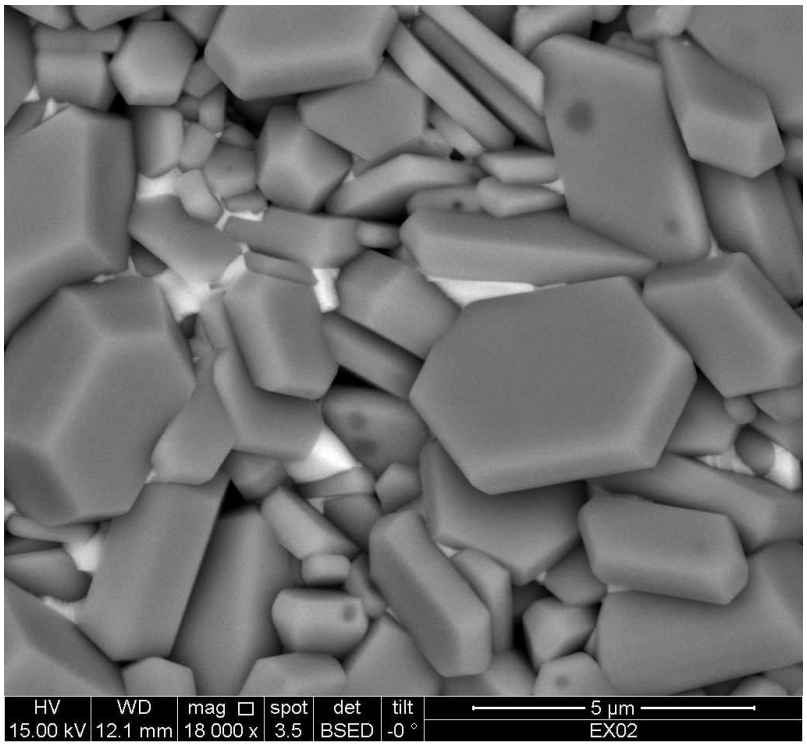

Figure 2.26: SEM image showing the micro-structure of an area on the surface of the series E $x = 0.2a$ pellet in backscattering mode

2.8.4 EDX analysis of sample composition

EDX analysis of sample composition was first conducted over a 50μm^2 area. This region covers a significant range of grain sizes and orientations and includes the filler material which was highlighted in backscattering mode. Figure 2.27 shows the SEM image with the area for EDX analysis selected and the graph at the bottom of the figure displays the composition results.

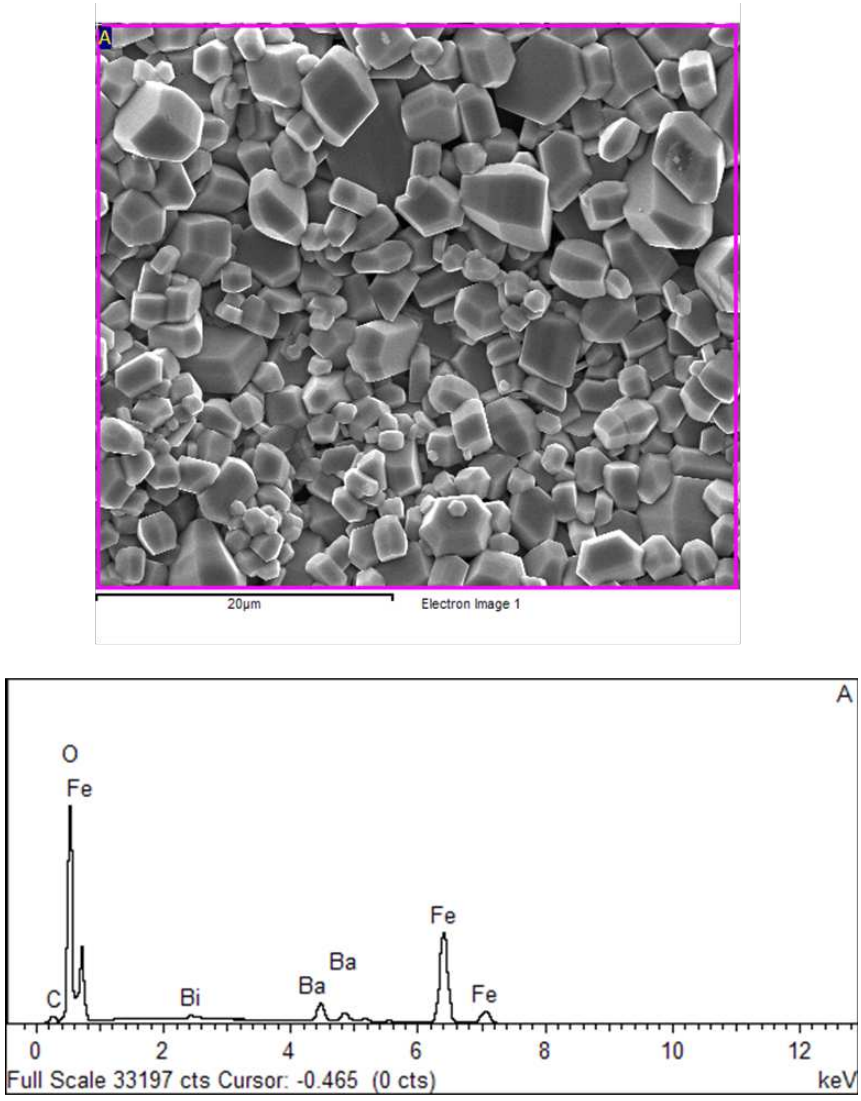

Figure 2.27: SEM image showing the micro-structure and corresponding EDX analysis for the area indicated for sample $x = 0.2a$ from series E which has been sintered for three hours at 1200°C

The data confirms the presence of the expected elements in expected proportions for the $BaBi_{0.2}Fe_{11.8}O_{19}$ sample. Within the test area iron is the element with the greatest weight, then oxygen, then barium, then bismuth (Table 2.7). There is some carbon present due to the nature of the characterisation method which can be ignored.

Element	Weight (%)	Atomic (%)
Carbon	2.19	6.00
Oxygen	28.13	57.84
Iron	56.00	32.98
Barium	12.39	2.97
Bismuth	1.28	0.20

Table 2.7: EDX results for proportions of elements present over a $50\mu m^2$ area for sample $x = 0.2a$ from series E

Further EDX analysis was performed to investigate the composition of the areas which were highlighted by the backscattered SEM image. The box labelled 'B' on Figure 2.28 was tested and both the SEM image and EDX composition data are shown.

In this region of the material the composition results are very different from those of the overall sample; significantly the proportion of bismuth has increased from 1.28% to 30.64% and as a result the ratios of the other elements decrease. Table 2.8 presents full details of the relative composition of elements.

Element	Weight (%)	Atomic (%)
Carbon	2.47	9.98
Oxygen	16.68	50.56
Iron	28.34	24.61
Barium	21.88	7.73
Bismuth	30.64	7.11

Table 2.8: EDX results for proportions of elements present over a irregular shaped region of sample $x = 0.2a$ from series E

Additional SEM/EDX analysis confirmed that the platelets in the samples are composed from barium, iron and oxygen. As a result the conclusion was drawn that when the material is formed it is composed of grains of barium hexaferrite with the added bismuth

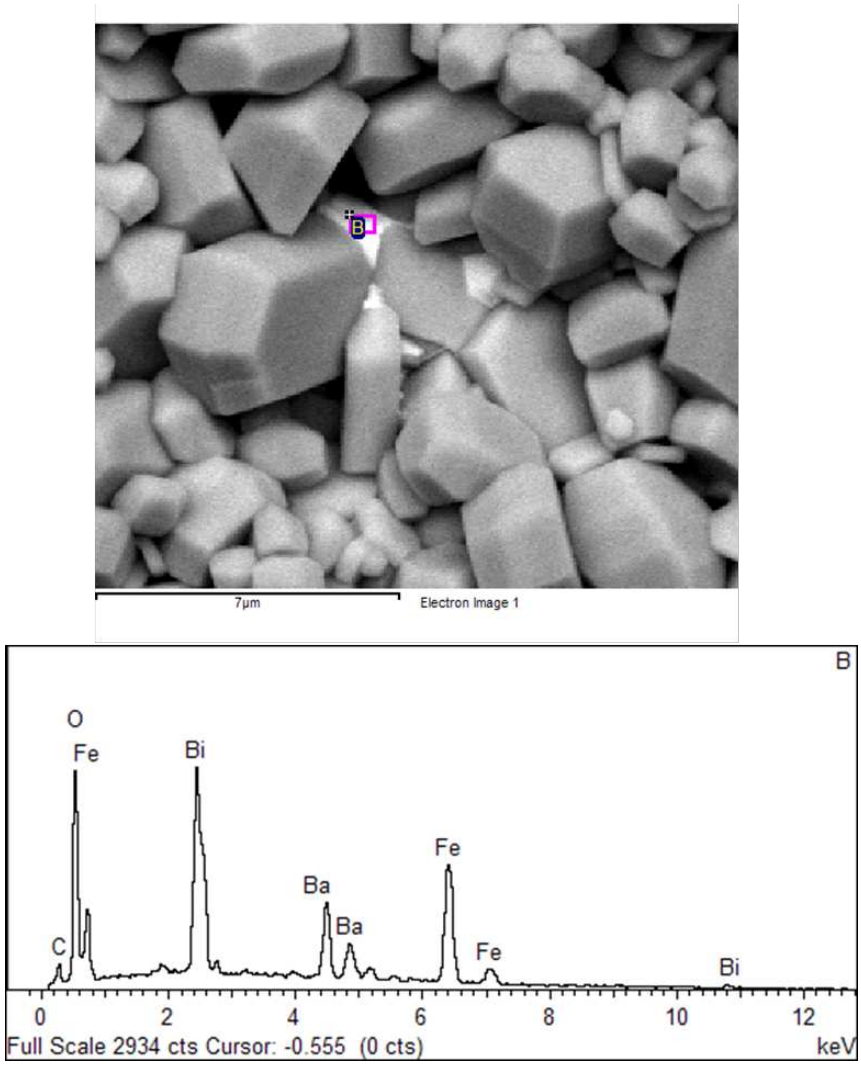

Figure 2.28: SEM image showing the micro-structure and corresponding EDX analysis for the area indicated for sample $x = 0.2a$ from series E which has been sintered for three hours at 1200°C

filling gaps between these platelets.

2.8.5 Conclusions

Based upon the SEM images of samples, the conclusion was drawn that the microstructure of the samples displayed hexagonal grains, up to 10μm in diameter (although most are smaller), which are randomly orientated. The surfaces of the pellets are not uniformly smooth; the porosity of the material results in visible gaps on the surface. The effects observed by SEM microscopy affect both sides of the sample pellet to the same degree.

EDX analysis in conjunction with SEM images provided evidence that the bismuth substituted barium hexaferrite forms as hexagonal grains of barium hexaferrite with irregularly shaped areas of high bismuth concentration fitted in gaps between these grains. When EDX data is taken over a larger area to average many grains and filled gaps the composition of the pellet shows good agreement with the chemical formula of the sample. From this the conclusion is drawn that for bulk characterisation methods it is reasonable to assume that the sample composition is homogeneous.

2.9 Microwave sintering of barium hexaferrite

Microwave sintering of barium hexaferrite has the potential advantages of rapid and uniform heating and lower required sintering temperatures [51]. Initial work in this field was conducted by Krage [52] who proposed that due to the nature of dielectric mechanisms within barium hexaferrite microwave sintering of the material would be viable and attractive to industry. The advantages over conventional heating are clear; microwave

furnaces can be physically smaller than conventional furnaces, the sintering process is rapid and efficient allowing products to be produced faster and more energy efficiently, reducing costs.

No work currently exists on the microwave sintering of bismuth substituted barium hexaferrite.

2.9.1 Initial processing

Pellets were processed up to the microwave sintering stage by the previously outlined procedure (Section 2.3). Reactants were measured out by stoichiometric ratios; mixed and ground in an agate mortar and pestle; heated in a conventional furnace at 750°C for three hours; mixed and ground again; heated for a further two hours at the same temperature; mixed and ground; heated for one hour; mixed and ground again; and finally pelletized using the uniaxial press. An undoped barium hexaferrite pellet in this form was placed within the microwave system for the final sintering step.

2.9.2 System in use at The University of Nottingham

The system used to sinter the material is based around a 3kW microwave source connected via waveguide to 2.45GHz single mode cavity. The sample pellet was contained within an alumina crucible (alumina was chosen due to its low loss at microwave frequencies so that most of the energy is absorbed by the barium hexaferrite sample) and placed within the cavity. The opposite end of the system from the magnetron was composed of a movable short to adjust the position of the maxima and minima in the standing wave relative to the sample. The set-up of the system allows for line of sight contact between

the sample with a temperature sensor which was focussed to detect the temperature on the surface of the sample. The experimental rig is shown in Figure 2.29. A radiation detector was used to ensure that safe levels of microwave radiation were not exceeded unnoticed in the event of unexpected behaviour of the system. This was important because barium hexaferrite had not been processed within this system before, thus extra care was taken during processing.

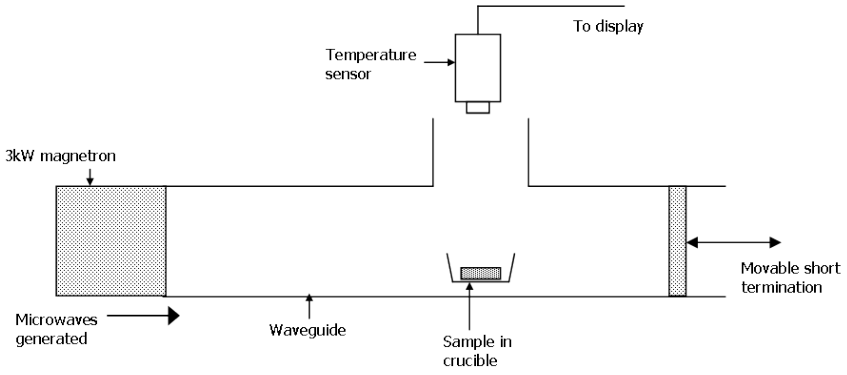

Figure 2.29: Diagram of experimental set-up for microwave sintering

During sintering the surface temperature of the pellet was monitored and the movable short position altered to the position where the maximum surface temperature was detected (indicating the maximum energy being transferred to the pellet). The surface temperature of the pellet reached a maximum of 800°C during sintering. The experiment was halted due to heterogeneous heating effects observed on the surface of the sample.

2.9.3 Results

The images in Figures 2.30 and 2.31 show the sample after microwave sintering. The material has not reacted uniformly; some areas are red where the reagent iron oxide remains unreacted, while adjacent areas are grey indicating that the reaction has taken

place. The area where the barium hexaferrite has formed shows some pitting and cracks (Figure 2.30) which does not make it an ideal sample for dielectric characterisation where a smooth sample is desirable.

Figure 2.30: Image showing the result of attempted microwave sintering of barium hexaferrite. The red areas remain unreacted while other areas (grey) in close proximity are formed. In addition the pitted surface of the reacted material can be seen

Figure 2.31 shows another interesting effect where the edge of the pellet appears shiny and molten. This is due to the microwave heating causing large variations in temperature across the pellet surface; the areas where the material has become shiny indicates where the temperature became much higher causing the melting effect. The inverse effect where the temperature does not get hot enough to enable the formation of the material is seen where the sample is still red. The heat detector recorded a maximum temperature of 800°C, however this is a measurement averaged across the whole surface of the pellet so is not accurate enough for this application as seen by the heterogeneous reaction of the pellet.

In addition to the non uniform reaction of the material, the pellet geometry was distorted

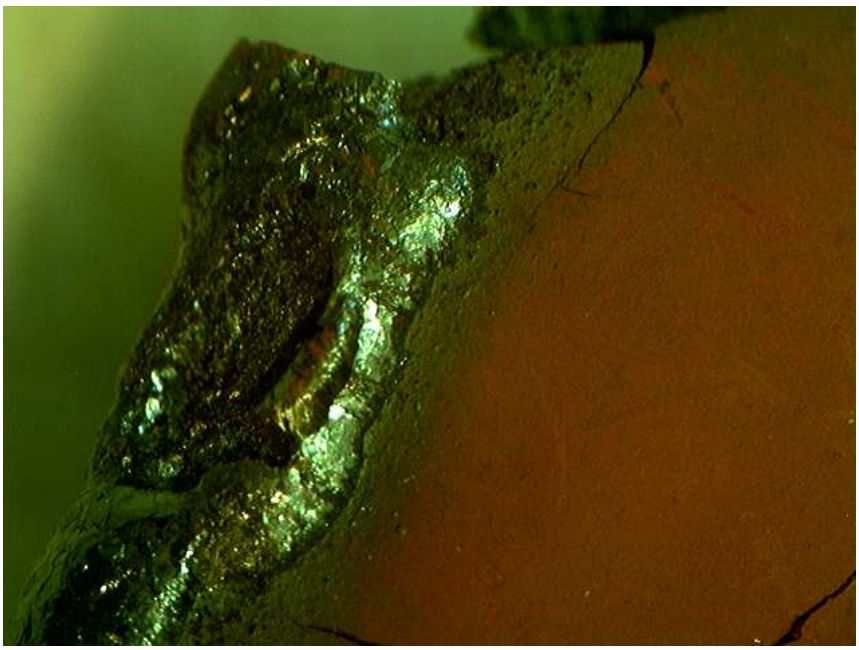

Figure 2.31: Image showing the result of attempted microwave sintering of barium hexaferrite. The red areas remain unreacted while other areas (grey) in close proximity are formed

by the heating process so that it was no longer suitable for dielectric characterisation which requires a disk with smooth contact surfaces. The sample has cracks across its surface and split into two parts.

2.9.4 Conclusions

Microwave sintering of barium hexaferrite was found to be sufficient to react some areas of the pellet to form the final compound. However the method requires further work and refinement to solve problems with the quality of the resulting sample. The degree of variation in the formation of the compound is too large to form repeatable samples of barium hexaferrite and bismuth substituted barium hexaferrite for further characterisation. The variation in temperature across the surface of the sample results in some red coloured unreacted areas, some grey reacted areas and some molten areas. The physical distortion of the pellet also needs to be addressed before this method could be used to

produce material in a usable form.

2.10 Chapter conclusions and future work

2.10.1 Conclusions

Barium hexaferrite ($BaFe_{12}O_{19}$) and bismuth substituted barium hexaferrite ($BaBi_xFe_{12-x}O_{19}$ for $x = 0.1$, 0.2, 0.5, 0.8, 1.0 and 1.5) was formed via the solid state synthesis method. Sintering regimes of either one or three hours at 1100°C or 1200°C were employed. The samples formed were dark grey pellets, 20mm in diameter and 3 – 6mm thick.

Work undertaken on bismuth substituted barium hexaferrite by other authors was summarised including the position which added bismuth takes in barium hexaferrite of which there are several conflicting opinions. The key differences between this work and that of others were highlighted. This includes a much wider range of sample compositions with the dielectric and magnetic properties characterised over a much wider frequency range incorporating much higher frequencies.

Surface roughness was characterised using the Talystep method for a selection of samples. The maximum surface roughness or the pellets ranged from 4.0 – 11.6μm.

The densities of the samples were measured in terms of the perfect cylindrical density. The mean average of pellet densities was similar for samples sintered at 1100°C and 1200°C, however bismuth containing pellets have more similar densities (shown by lower standard deviation) when sintered for a longer period of time.

X-ray diffraction (XRD) analysis was used to investigate the structure of the material. Undoped barium hexaferrite was not formed after sintering for one hour at either 1100°C

or after a subsequent further hour at 1200°C however the bismuth containing material was formed under the same sintering regime, confirming bismuth acts as a sintering aid by lowering the required temperature for reaction. As greater amounts of bismuth were added to the material the XRD graphs deviate more from the standard file as peaks at the 23° and 32°C positions split. The potential phase change from M-type to W-type barium hexaferrite was discussed and dismissed.

Scanning electron microscopy (SEM) confirmed barium hexaferrite was composed of hexagonal grains up to 10μm across which were randomly orientated. Energy dispersive X-ray (EDX) analysis in conjunction with the SEM images showed that the bismuth added to the barium hexaferrite fills in gaps between the hexagonal grains. Over a larger area the distribution of bismuth in the material is homogeneous, confirming that bulk characterisation methods are appropriate.

Microwave sintering of barium hexaferrite was attempted, however the formation was not uniform across the body of the sample. This method requires more work to be a suitable formation process.

2.10.2 Future work

Work could be extended by including an even greater range of sample compositions and sintering regimes. Surface roughness measurements taken with a Talystep could be improved upon by a method which takes into account the whole surface of the sample (rather than a cross-section) such as atomic force microscopy. Density measurement accuracy could be improved by using the Archimedes method or another scheme where the porosity of the material is accounted for. Microwave sintering is a potentially at-

tractive method for the formation of barium hexaferrite and bismuth substituted barium hexaferrite however more work is needed to make the heating process uniform and repeatable.

2.11 References

[1] Merriam Webster. "Ferrite" Merriam-Webster Online Dictionary. http://www.merriam-webster.com/dictionary/ferrite, Accessed: June 2009.

[2] P. Hernndez Gmez, C. Torres, C. de Francisco, J. M. Muoz, and K. Hisatake. Analysis of magnetic aftereffects in strontium hexagonal ferrites with W-type stoichiometry. *Journal of Applied Physics*, 93(10):7480–7482, 2003.

[3] R. Valenzuela. *Magnetic Ceramics*. Cambridge University Press, 1994.

[4] M De Graef and M. McHenry. *The Structure of Materials*. Cambridge University Press, 2007.

[5] C. Surig, K. A. Hempel, and D. Bonnenberg. Hexaferrite particles prepared by solgel technique. *IEEE Transactions on Magnetics*, 30(6):4092–4094, 1994.

[6] P. Shi, S. D. Yoon, X. Zuo, I Kozulin, S. A. Oliver, and C. Vittoria. Microwave properties of pulsed laser deposited Sc-doped barium hexaferrite films. *Journal of Applied Physics*, 87(9):4981, 2000.

[7] J. Daintith, J. Clark, H.M. Clarke, R. Cutler, D. Cooper, D.E. Edwards, R. Rennie, and D.E. Ward. *Dictionary of Chemistry*. Oxford University Press, 2008.

[8] T. Ogasawara and M.A.S. Oliveira. Microstructure and hysteresis curves of the barium hexaferrite from co-precipitation by organic agent. *Journal of Magnetism and Magnetic Materials*, 217:147–154, 2000.

[9] J. Matutes Aquino, S. Diaz Castanon, M. Mirabal Garcia, and S. A. Palomares Sanchez. Synthesis by coprecipitation and study of barium hexaferrite powders. *Scripta Materialia*, 42(3):295–299, 2000.

[10] K Haneda, C. Miyakawa, and H. Kojima. Preparation of high-coercivity $BaFe_{12}O_{19}$. *Journal of the American Ceramic Society*, 57(8):354–357, 1974.

[11] C. D. Mee and J. C. Jeschke. Single-domain properties in hexagonal ferrites. *Journal of Applied Physics*, 34(4):1271–1272, 1963.

[12] S. E. Jacobo, C Domingo Pascual, R. Rodriguez Clemente, and M. A. Blesa. Synthesis of ultrafine particles of barium ferrite by chemical coprecipitation. *Journal of Materials Science*, 32:1025–1028, 1997.

[13] J. Huang, H. Zhuang, and W. Li. Synthesis and characterization of nano crystalline $BaFe_{12}O_{19}$ powders by low temperature combustion. *Materials Research Bulletin*, 38:149–159, 2003.

[14] M. Radwan, M.M. Rashad, and M.M. Hessien. Synthesis and characterization of barium hexaferrite nanoparticles. *Journal of Materials Processing Technology*, 181:106–109, 2007.

[15] W. Roos. Formation of chemically co-precipitated barium ferrites. *Journal of the American Ceramic Society*, 63(11-12):601–603, 1980.

[16] Encyclopaedia Britannica Online. Advanced Ceramics. http://www.britannica.com/EBchecked/topic/6657/advanced-ceramics, Accessed: March 2009.

[17] F. Licci and T. Besagni. Organic resin method for highly reactive and homogeneous hexaferrite powders. *IEEE Transactions on Magnetics*, MAG-20(5):1639–1641, 1984.

[18] C. Surig, K. A. Hempel, and Ch. Sauer. Influence of stoichiometry on hexaferrite structure. *Journal of Magnetism and Magnetic Materials*, 157/158:268–269, 1996.

[19] C.H. Lin, Z.W. Shih, T.S. Chin, M.L. Wang, and Y.C. Yu. Hydrothermal processings to produce magnetic particulates. *IEEE Transactions on Magnetics*, 26(1):15–17, 1990.

[20] H. Kumazawa, Y. Maeda, and E. Sada. Further consideration of hydrothermal synthesis of barium ferrite fine particles. *Journal of Materials Science Letters*, 14:68–70, 1995.

[21] E. Sada, H. Kumazawa, and H-M. Cho. Synthesis of barium ferrite ultrafine particles by a hydrothermal method. *Industrial and Engineering Chemistry Research*, 30(6):1319–1323, 1991.

[22] S. Che, J. Wang, and Q. Chen. Soft magnetic nanoparticles of $BaFe_{12}0_{19}$ fabricated under mild conditions. *Journal of Physics: Condensed Matter*, 15:L335–L339, 2003.

[23] T. Adschiri, Y. Hakuta, and K. Arai. Hydrothermal synthesis of metal oxide fine particles at supercritical conditions. *Industrial and Engineering Chemistry Research*, 39:4901–4907, 2000.

[24] S-C. Nam and G-J. Kim. Characterization of barium hexaferrite produced by varying the reaction parameters at the mixing-points in a upercritical water crystallization process. *Korean Journal of Chemical Engineering*, 21(3):582–588, 2004.

[25] J. B. Mooney and S. B. Radding. Spray pyrolysis processing. *Annual Review of Materials Science*, 12:81–101, 1982.

[26] T. Gonzalez Carreno, M. P. Morales, and C.J. Serna. Barium ferrite nanoparticles prepared directly by aerosol pyrolysis. *Materials Letters*, 43:97–101, 2000.

[27] V.K. Sankaranarayanan, R.P. Pant, and A.C. Rastogi. Spray pyrolytic deposition of barium hexaferrite thin films for magnetic recording applications. *Journal of Magnetism and Magnetic Materials*, 220:72–78, 2000.

[28] H-F. Yu and H-Y. Lin. Preparation and thermal behavior of aerosol-derived $BaFe_{12}O_{19}$ nanoparticles. *Journal of Magnetism and Magnetic Materials*, 283:190–198, 2004.

[29] V.V. Pankov. Synthesis of $BaFe_{12}O_{19}$ powder by modified co-precipitation and spray pyrolysis methods. *Inorganic Materials*, 40(9):979–984, 2004.

[30] L. Rezlescu, E. Rezlescu, P.D. Popa, and N. Rezlescu. Fine barium hexaferrite powder prepared by the crystallisation of glass. *Journal of Magnetism and Magnetic Materials*, 193:288–290, 1999.

[31] O. Kubo, T. Ido, and H. Yokoyama. Properties of Ba ferrite particles for perpendicular magnetic recording media. *IEEE Transactions on Magnetics*, 18(6):1122–1124, 1982.

[32] S. Ram. Observation of enhanced dielectric permittivity in Bi^{3+} doped $BaFe_{12}O_{19}$ ferrite. *Journal of Magnetism and Magnetic Materials*, 80:241–245, 1989.

[33] S. Ram, H. Krishnan, K.N. Rai, and K.A. Narayan. Magnetic and electrical properties of Bi_2O_3 modified $BaFe_{12}O_{19}$ hexagonal ferrite. *Japanese Journal of Applied Physics*, 28(4):604–608, 1989.

[34] A. Collomb, O. Abdelkader, P. Wolfers, J.C. Guitel, and D. Samaras. Crystal structure and magnesium location in the W-type hexagonal ferrite: [Ba]Mg2-W. *Journal of Magnetism and Magnetic Materials*, 58(3-4):247–253, 1986.

[35] M. Pal, P. Brahma, D. Chakravorty, and D.C. Agrawal. Magnetic properties of Ba hexaferrites doped with bismuth oxide. *Journal of Magnetism and Magnetic Materials*, 147:208–212, 1995.

[36] R.G. Burns. *Mineralogical Applications of Crystal Field Theory*. Number 5 in Cambridge Topics in Materials Physics and Chemistry. Cambridge University Press, 2nd edition, 1993.

[37] P. Winotai, S. Thongmee, and I.M. Tang. Cation distribution in bismuth-doped M-type barium hexaferrite. *Materials Research Bulletin*, 35:1747–1753, 2000.

[38] S. Rosler, P. Wartewig, and H. Langbein. Synthesis and characterization of hexagonal ferrites $BaFe_{12-2x}Zn_xTi_xO_{19}$ (0 ¡ = x ¡ = 2) by thermal decomposition of freeze-dried precursors. *Crystal Research Technology*, 38(11):927–934, 2003.

[39] Lenntech. Chemical elements listed by atomic mass. http://www.lenntech.com/periodic/mass/atomic-mass.htm, Accessed: September 2008.

[40] G. C. Bye and C. R. Howard. The synthesis of barium hexferrite from iron oxide and barium carbonate: 1. General features of the reaction. *Journal of Applied Chemistry and Biotechnology*, 21(11):319–323, 1971.

[41] E. A. Kuchinskaya, A. G. Titenko, V. P. Pashchenko, Z. P. Morozova, I. F. Klochai, and S. E. Shaporenko. Effect of bismuth oxide on the phase composition and magnetic properties of the $12Fe_2O_3$. 3BaO . 2CoO system. *Powder Metallurgy and Metal Ceramics*, 16(11):863–866, 1977.

[42] K. Mallick, P Shepherd, and R. Green. Dielectric properties of M-type barium hexferrite prepared by co-precipitation. *Journal of the European Ceramic Society*, 27:2045–2052, 2007.

[43] C. Hammond. *The Basics of Crystallography and Diffraction*. Oxford University Press, 3rd edition, 2009.

[44] Santa Barbara Materials Research Laboratory, University of California. Introduction to X-ray diffraction. http://www.mrl.ucsb.edu/mrl/centralfacilities/xray/xray-basics/index.html, Accessed: July 2009.

[45] J. Daintith, J. Clark, H.M. Clarke, D. Cooper, J. Cullerne, D.E. Edwards, R. Rennie, and D.E. Ward. *Dictionary of Physics*. Oxford University Press, 6th edition, 2009.

[46] P Shepherd, K. Mallick, and R. Green. Dielectric properties of cobalt substituted M-type barium hexferrite prepared by co-precipitation. *Journal of Materials Science: Materials in Electronics*, 18:527–534, 2007.

[47] L. Trif, G. Tolnai, I. Saj, and E. Klmn. Preparation and characterization of hexagonal W-type barium ferrite nanoparticles. *Progress in Colloid and Polymer Science*, 135:38–43, 2008.

[48] M. Ohring. *Engineering Materials Science*. Academic Press, 1995.

[49] S. Swapp. Scanning electron microscopy (SEM). http://serc.carleton.edu/research-education/geochemsheets/techniques/SEM.html, Accessed: April 2010.

[50] J. Goldstein, P. Echlin, D.C. Joy, E. Lifshin, C.E. Lyman, J.R. Michael, D.E. Newbury, and L.C. Sawyer. *Scanning Electron Microscopy and X-Ray Microanalysis*. Kluwer Academic/Plenum Publishers, 2003.

[51] C.C. Sorrell, O.C. Standard, N. Ehsani, K.R. Ratinac, C.M.G. Harding, and A.J. Ruys. *Ceramic Interfaces - Properties and Applications*, volume 4. Maney Publishing, 1998.

[52] M.K. Krage. Microwave sintering of ferrites. *American Ceramic Soceity Bulletin*, 60(11):1232, 1981.

Chapter 3

Low frequency dielectrics and permittivity

A dielectric material is "a non-conductor of electric charge in which an applied electric field causes a displacement of charge but not a flow of charge" [1]. When an electric field is applied across such a material it resists the flow of charge through the material, with the degree of resistance dependent upon the properties of the material, termed the 'dielectric constant' of the material. The terms dielectric constant and relative permittivity are often used interchangeably. Relative permittivity is the preferred term because the permittivity of a material is dependent upon frequency, hence the term 'dielectric constant' is slightly misleading. Relative permittivity is commonly referred to simply as 'permittivity'. This is because the permittivity used in calculations is the permittivity of the material divided by that of free space ($\varepsilon_0 = \frac{1}{36\pi} \times 10^{-9}$F m^{-1}, Equation 3.1), forming a complex value with a real and imaginary part. The real part of permittivity (ε_r') represents the electrical energy stored within the material. The imaginary part (ε_r'') represents the energy dissipated. The

loss tangent (*tan* δ) is the ratio of the imaginary part to the real part and is used as a measure of the 'lossiness' of the material. Losses in a dielectric material are due to two primary mechanisms; conduction loss which occurs in all materials through which an electric current can flow; and secondly dielectric loss which is due to the movement and rotation of atoms and molecules in the presence of an applied electric field [2]. The relationships between each value are detailed in Equations 3.1, 3.2 and 3.3.

$$\varepsilon_r = \frac{\varepsilon}{\varepsilon_0} \tag{3.1}$$

$$\varepsilon_r = \varepsilon_r' - j\varepsilon_r'' \tag{3.2}$$

$$tan\delta = \frac{\varepsilon_r''}{\varepsilon_r'} \tag{3.3}$$

For many applications which make use of dielectric materials it is desirable to have a high real part of permittivity (such as for use in capacitors or dielectric loaded antennas), however the loss must also be taken into account and sometimes a compromise must be achieved.

3.1 Frequency dependence of permittivity

When a dielectric material is exposed to a changing electric field, by means of an alternating current, at different frequencies the dominant dielectric mechanism within the material will change. This leads to the material displaying a different permittivity at

different frequencies. Dielectric mechanisms are related to the type of bonding and alignment between atoms in the material. These mechanisms exist because the charge carriers within the material are displaced when they move in an attempt to compensate for the affect of the electric field. Figure 3.1 shows the affect of different dielectric mechanisms on the real and imaginary part of permittivity with varying frequency.

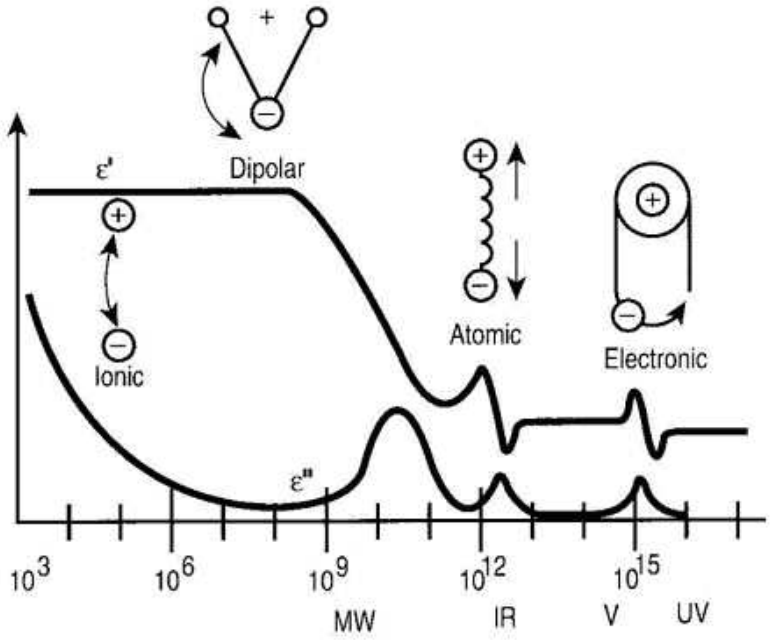

Figure 3.1: Effect of different dielectric mechanisms on the real and imaginary part of permittivity of a material with varying frequency [3].

There are four different dielectric mechanisms:

- Ionic relaxation;

  Ionic relaxation is the mechanism which dominates at low frequencies. This is where the average position of positive and negative ions in a material changes under the influence of an applied electric field. Ionic conductivity within the material usually contributes only to the imaginary part of permittivity [4] [5].

- Dipolar relaxation;

Moving into the microwave frequency range, dipolar relaxation dominates the permittivity response. The presence of an applied electric field causes the dipoles within the material to rotate in an attempt to align with the field. If sufficient time is allowed for all the dipoles to align then the maximum real permittivity is reached with minimum loss. This time provides a frequency dependent response for individual materials [6].

- Atomic polarisation;

  Atomic relaxation is the first resonant effect observed with the increase in test frequency. The electron cloud surrounding the positive nuclei is deformed by the presence of an applied electric field resulting in parts of the cloud becoming more negative and other regions more positive. [7]

- Electronic polarisation.

  This second resonant effect is caused by the applied electric field distorting the electron density of the electron cloud surrounding the nucleus of a neutral atom, resulting in the negative and positive charges no longer being centred in the same position. [8]

3.1.1 Permittivity of standard materials

The permittivity of some example materials for comparative purposes are detailed in Table 3.1.

The permittivity of materials is often quoted as a dielectric constant, however the value will depend upon the frequency of operation. As a general rule the real part of permittivity will present its greatest value at DC so this can be assumed to be the best case result.

Material	ε'_r 60Hz	$tan\delta$ 60Hz	ε'_r 1MHz	$tan\delta$ 1MHz
Air	1.000585	-	1.000585	-
Alumina	-	-	8.80	0.00033
Barium titanate	1250	0.056	1143	0.0105
Carbon tetrachloride	2.17	0.007	2.17	0.00004
Castor oil	3.7	-	3.7	-
Glass (soda-borosilicate)	-	-	4.84	0.0036
Lucite	3.3	-	3.3	-
Mylar	2.5	-	2.5	-
Nylon	3.88	0.014	3.33	0.026
Paraffin	2.25	-	2.25	-
Plexiglass	3.4	0.06	2.76	0.014
Polyethylene	2.26	0.0002	2.26	0.0002
Polypropylene	2.25	0.0005	2.25	0.0005
Polystyrene	2.56	0.00005	2.56	0.00007
PTFE	2.1	0.0005	2.1	0.0002
PVC	3.2	0.0115	2.88	0.016
Quartz	3.78	0.0009	3.78	0.0001
Vaseline	2.16	0.0004	2.16	0.0001

Table 3.1: Table detailing permittivity of a range of materials. Adapted from [2].

Often when designing a device which requires a high permittivity material component a balance will have to be struck between an acceptable value for both the real part (dielectric constant) and the loss. If a material has a high real part of permittivity but also a high loss then it may not be suitable. This is because losses reduce the performance of a device; it will be less efficient and will dissipate energy which may render the device inoperable. The ideal dielectric would have a high real part of permittivity, a low loss tangent, be low cost and be easily manufactured into devices, no such material currently exists, hence the need for compromise and research into new materials.

3.2 Low frequency permittivity measurement: parallel plate capacitor method

The parallel plate capacitor method is a simple means to find the permittivity of a sample at low frequencies. The material is placed within a specially designed sample holder which forms a capacitor with the material under test becoming the dielectric within the capacitor. The sample holder is connected to a LCR meter or impedance analyser which provides an alternating current source to excite the material. The dielectric properties of the material are calculated from the measured capacitance and dissipation factor collected via the LCR meter, combined with a knowledge of the physical dimensions of the material under test (thickness and diameter). This information is collated together and processed off-line after data collection.

This method provides flexibility in the characterisation of a number of different material properties. Both bulk solids and liquids and even mixtures of liquids or solids can be analysed by an appropriate sample holder and allowances in software for permittivity calculations [3] [9].

The parallel plate capacitor system where the material under test (MUT) forms the dielectric filling is shown in Figure 3.2 complete with the equivalent circuit for the system. The MUT is represented by the capacitance of the sample (C_p) in parallel with a conductance (G) which forms an admittance (Y). Other symbols used are the area of the electrodes (A) and sample thickness (t).

The following theory applies to both solid and liquid samples, however since the samples used within this work are solid, the assumption will be made that solid samples are

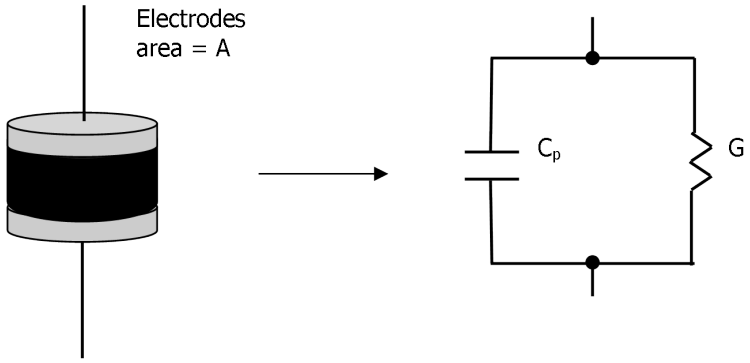

Figure 3.2: Parallel plate capacitor set-up where the material under test (either solid or liquid depending on sample holder) forms the dielectric filling with equivalent circuit. Adapted from [9].

being considered as standard. The formula for the admittance of the system in terms of conductance and capacitance is given in Equation 3.4. Symbols are defined as above and in addition C_0 is the capacitance of air.

$$\begin{aligned} Y &= G + j\omega C_p \\ &= j\omega C_0 \left(\frac{C_p}{C_0} - j\frac{G}{\omega C_0} \right) \end{aligned} \tag{3.4}$$

From this, a rearrangement incorporating the relationship between relative permittivity and free space in Equation 3.1, it is possible to express the complex permittivity of the material in terms of capacitance and conductance for the system (Equation 3.5).

$$\varepsilon_r = \frac{C_p}{C_0} - j\frac{G}{\omega C_0} \tag{3.5}$$

In practice the application of the parallel plate capacitor theory is not as simple as first appears. When the MUT is placed within the two capacitor electrodes there are stray (or fringing) capacitances formed at the extremes of the plates. This effect introduces errors into the system because the capacitance recorded by the LCR meter is the sum of

the capacitances due to the dielectric MUT and the stray capacitances.

A technique to reduce this measurement error is to use a modified electrode design which incorporates a guard ring. The purpose of this guard ring is to absorb the electric field formed at the edges of the electrodes, resulting in the measured capacitance being due to the presence of the MUT between the electrodes only. There will still be some stray capacitances present however these are vastly reduced [9].

When using the parallel plate capacitor method to characterise permittivity a major source of errors comes from air gaps between the MUT and the contact electrodes; this affects both systems which include guard electrodes and those which do not. The simplest form of this measurement method which neglects the presence of air gaps is termed the 'contacting electrode method'. An alternative form which includes an air gap has the potential to increase measurement accuracy but has the disadvantage that it is more time consuming to perform because two separate measurements are required [9]. Permittivity was calculated using the contacting electrode method. Section A.1 covers the alternative 'non-contacting electrode method' in detail.

3.2.1 System in use at The University of Nottingham

Sample dielectric properties were determined using a Wayne Kerr Precision Component Analyzer 6440B in conjunction with a Solartron 12962 sample holder. The LCR meter was connected to a PC and a Matlab script used to capture capacitance and dissipation factor data over the test frequency range. The sample is introduced as the dielectric material between the two plates of the test fixture. A diagram of the experimental set-up is shown in Figure 3.3. The synthesis method employed at The University of Nottingham produces

approximately 20mm diameter circular pellets with a thickness of between 3 and 5 mm. The thickness of the sample (t) is recorded, then the capacitance (C) and dissipation factor (D) over the desired frequency range (20Hz – 3MHz) is measured by the LCR meter and then used to calculate the complex permittivity of the sample (Equations 3.6, 3.7 and 3.8):

$$C = \varepsilon_0 \varepsilon_r' \frac{A}{t} \tag{3.6}$$

$$\varepsilon_r' = \frac{Ct}{\varepsilon_0 A} \tag{3.7}$$

$$\varepsilon_r'' = D \times \varepsilon_r' \tag{3.8}$$

Where C is the measured capacitance; ε_0 is the permittivity of free space; ε_r' is the real part of permittivity of the MUT; A is the area of the guard electrode; t is the thickness of the MUT; ε_r'' is the imaginary part of permittivity of the MUT; and D is the measured dissipation factor.

The Solartron 12962 sample holder is supplied with a selection of electrode plates which have different diameter guard rings for characterising a wide variety of sample diameters. There is also a special vessel with sides for characterising liquids. Suitable plates for forming the electrodes of the capacitor set-up were selected and screwed into place. Because the sample pellets used are 20mm in diameter, the smallest plate area was selected for the sample holder which has a diameter of 5mm in contact with the sample.

This means the guard ring on the electrode is a suitable distance from the edge of the sample to allow the reduction of stray capacitances to be effective.

Set up and calibration of system

The appropriate 5mm diameter guard ring sample holder plates were selected and attached to the screw fittings on the sample holder main unit. The terminals on the sample holder were connected to the LCR meter using the 4 terminal BNC cables. The experimental rig was switched on for a minimum of one hour before use to reduce any drift errors from the equipment. The calibration procedure was commenced by using the micrometer screw to close the two parallel plates on the sample holder into contact. The zero point was established by opening and closing the gap and resetting the zero point until three consecutive 0.000mm gaps were confirmed as the distance between the plates. The electrodes were separated and the short circuit calibration component was then placed between the plates and the micrometer screw used to bring the plates together, closing down onto the short component. The distance between the places was recorded and then opened and closed again until the gap was a constant distance for three repeat measurements. This plate separation distance was then used to calibrate the open circuit condition. Only once this was completed could the high frequency lead

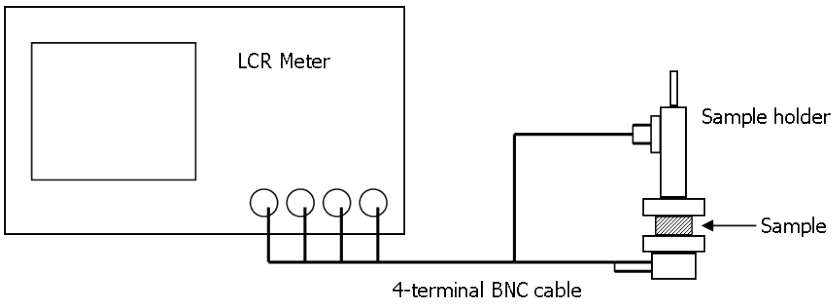

Figure 3.3: Diagram showing the experimental setup with the LCR meter connected via 4-terminal BNC cable to the sample holder. Sample is placed between the plates to measure bulk capacitance

compensation be added to the calibration. This component was supplied with the sample holder and was placed between the electrodes, which were closed and the separation distance noted. This was repeated until there were three identical separation distances, then the high frequency lead calibration was performed.

3.3 Improving accuracy of the parallel plate characterisation method

To ensure an accurate measurement of the capacitance and loss of the sample which is placed between the plates of the sample holder it should be in the same position in the centre of the electrodes completely covering the guard ring visible on the bottom plate. Initially this placement was performed by visually aligning the pellet to the correct position. It was felt that there was scope to improve the repeatability of this placement and hence increase the accuracy of the measurement.

The importance of positioning the sample in the centre of the plate completely over the guard ring was investigated by taking a sample and moving it across the bottom plate of the sample holder for a series of measurements. Table 3.2 details the position, plate separation and a brief description of the pellet corresponding with Figure 3.4.

As expected the permittivity is greatest when the sample is placed in the centre of the plate covering the guard ring and reduces as the sample covers less of the guard ring. When the sample is not over the guard ring the recorded permittivity is comparable with that of air when a sample is not present. The plate separation distance changes as the sample is moved, this is due to the dimensions of the sample holder; the area of the plate

Position	Plate separation (mm)	Description
1	4.009	Back of plate, not over guard ring
2	4.009	Slightly over guard ring
3	4.096	Quarter over guard ring
4	4.112	Half over guard ring
5	4.115	Three quarters over guard ring
6	4.109	Covering guard ring
7	4.095	Covering guard ring
8	4.143	Slightly off edge of guard ring
9	4.148	Half over guard ring
10	4.131	Quarter over guard ring
11	4.019	Off guard ring, touching edge of it
12	4.018	Front of plate, not over guard ring

Table 3.2: Table detailing position of pellet experiment notes for use with Figure 3.4

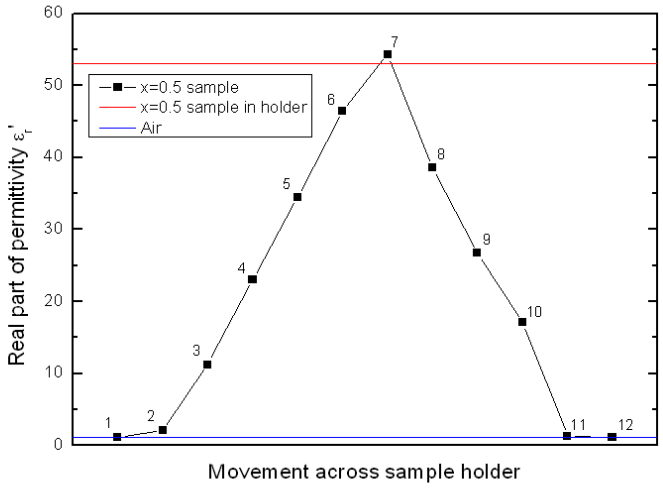

Figure 3.4: Graph showing the effect of moving a sample across the plate of the sample holder. The maximum permittivity is recorded when the sample is over the centre of the plate.

within the guard ring is raised slightly compared to the surrounding area. This combined with the slight variations in the smoothness of the pellet surface results in the deviation of the plate separation distances.

3.3.1 Sample holder for parallel plate measurement

To improve upon the accuracy of visually locating the sample pellet into position, a thin cap with a hole cut in the centre for the pellet was used to provide greater measurement repeatability.

Design

The construction material was nylon. This was selected because the physical properties allow it to be machined into the desired shape and because the permittivity is significantly lower than that of the material under test so it will not severely affect the capacitance measurements. The design of the component is shown in Figure 3.5.

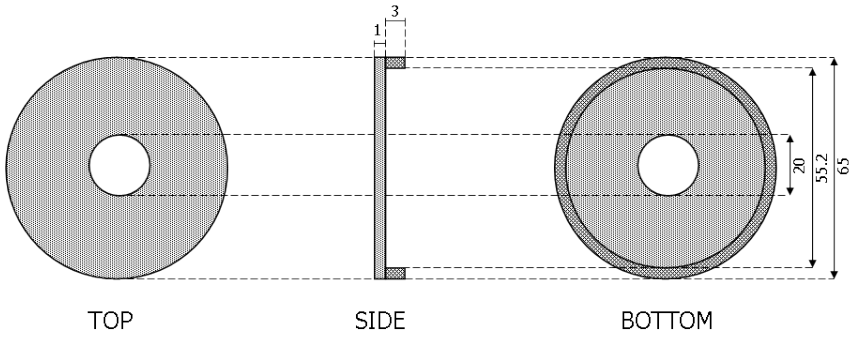

Figure 3.5: Design for nylon cap to hold sample pellet in place in the center of the plates of the sample holder. All dimensions given are in mm

The detail of the design ensures the thickness of the nylon over the plate at 1mm was much thinner than that of the pellets being tested. This reduces the negative impact

upon capacitance measurement and therefore permittivity calculations. The secondary ring around the edge of the cap clips over the edge of the bottom plate of the sample holder. This holds it in place so that when the pellet is placed in the gap in the nylon it is over the centre of the plate. This provided conditions which made capacitance measurements of samples more repeatable and more accurate.

Sample holder cap capacitance

To ensure that the sample holder cap did not have an unacceptable influence on the measured capacitance, measurements of the capacitance of the system both with and without the cap were carried out at a range of plate separation distances. The separation distances were 3.2, 4, 5 and 6mm. These were selected as being representative of the range and extremes of pellet thicknesses the equipment would be used to characterise. Figure 3.6 shows the results of the test of capacitance of the empty sample holder both with and without the sample holder cap.

The presence of the sample holder cap has no discernible affect on the measured capacitance. The traces with and without the cap are very similar and indeed overlap in places as shown in Figure 3.6. When permittivity is calculated from the results it is within the accuracy levels of the test set-up without it. The permittivity value of air obtained with the sample holder cap is $\varepsilon_r \approx 1.15 + j0.01$. This measurement is larger than the ideal value, however is within the accuracy range expected; the accuracy of the LCR meter when measuring very small capacitances (such as these) is $\pm$15% [10]. This is the "worst case" situation; when a sample is contained within the electrodes the capacitances measured are much larger (around 10pF range as opposed to 0.1pF range) and the accuracy of the LCR meter is increased to $\pm$0.5% [10].

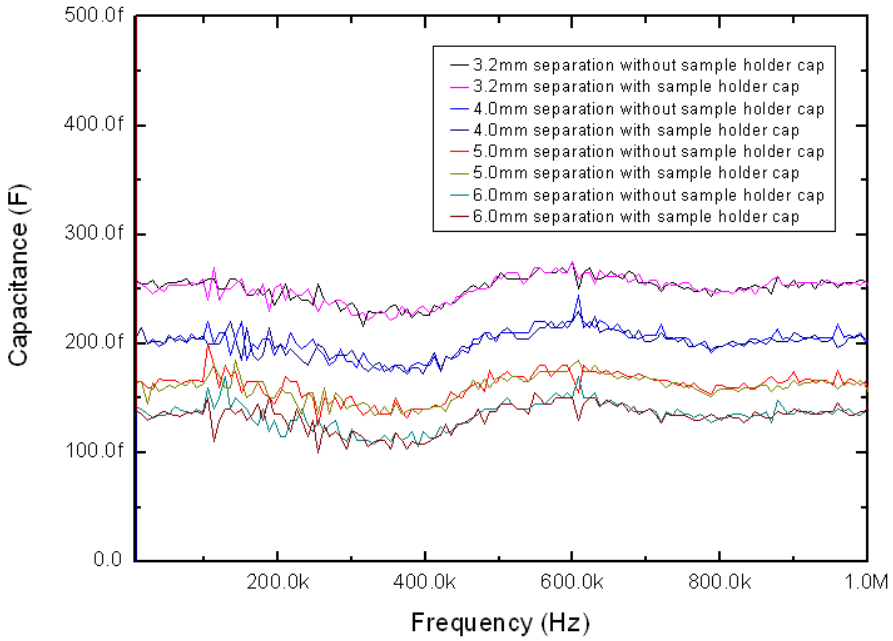

Figure 3.6: Graph showing the change in measured capacitance for different plate separation distances both with and without the sample holder cap.

3.4 Low frequency permittivity results

Data was collected for each set of sample pellets over the frequency range 20Hz – 3MHz. The dielectric properties of the samples are presented either as a function of frequency for each series set, or as a function of x-value for $BaBi_xFe_{12-x}O_{19}$ at a specific frequency point. At higher frequencies the permittivity of the samples does not alter much and so permittivity with respect to x-value is used to display more clearly the effect of bismuth doping on the parent barium hexaferrite. It should be noted that the data with respect to frequency has been altered to omit the symbols and instead replaced with line graphs with occasional symbols to improve clarity.

During the analysis of permittivity data it was found that the value was different depending on the orientation of the sample between the electrodes. The results presented

here are the higher values because this represents the value which is closest to the actual material value. The reasons for the discrepancies in measurements is explored in Section 3.5.

Doping barium hexaferrite with bismuth was found to alter the dielectric properties of the material by increasing both the real and imaginary parts of permittivity.

3.4.1 Permittivity results after sintering at 1100°C

Series F

Permittivity results for pellets from series F are presented first. Since series F contains six pellets with the same chemical composition ($x = 0.1$, $BaBi_{0.1}Fe_{11.9}O_{19}$) which have been subjected to the same sintering conditions concurrently, the data provides a measure of both the accuracy and repeatability of both the sample fabrication process and the characterisation method.

Figure 3.7 shows the real and imaginary permittivity results for series F pellets characterised using the parallel plate capacitor method. The largest values for the real part of permittivity and the corresponding imaginary parts are presented.

The real part of permittivity for all samples is constant across most of the frequency range. All samples, except $x = 0.1e$, display a slightly higher permittivity at lower frequencies before the response flattens after 500kHz. The $x = 0.1e$ pellet has a slightly lower permittivity at low frequencies in contrast to the other samples in the series, before that trace also flattens at the earlier point of 100kHz. The actual values of the sample permittivities are different; three pellets have similar values which are the lowest of the

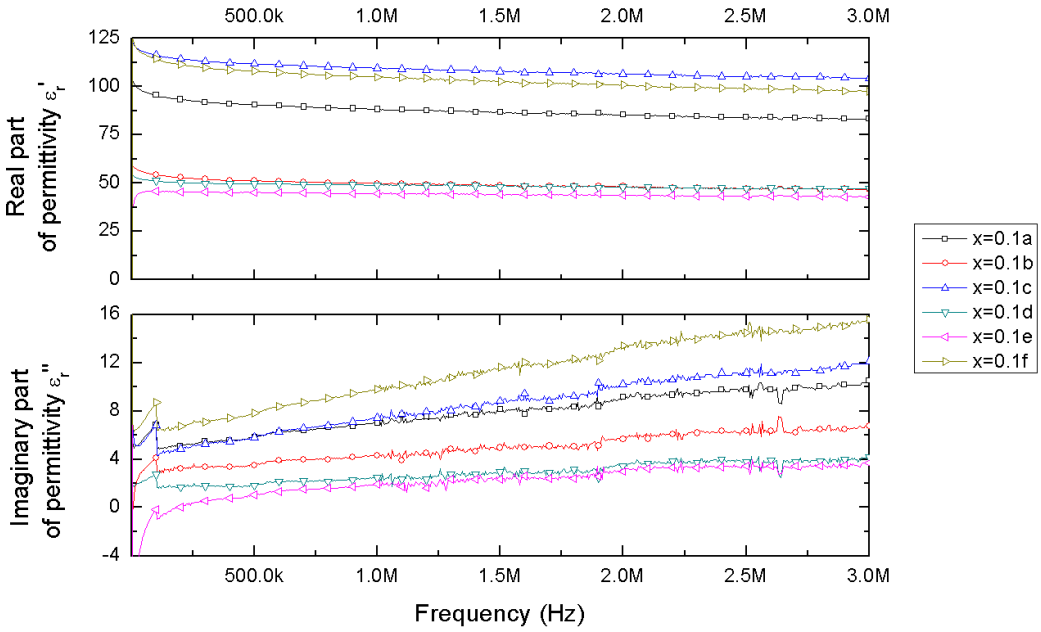

Figure 3.7: Real and imaginary part of permittivity for series F $BaBi_xFe_{12-x}O_{19}$ after sintering for three hours at 1100°C

series; then there is a gap of 38 to the $x = 0.1a$ sample; followed by a smaller gap of 15 to the second highest $x = 0.1f$ pellet; the highest permittivity sample is the $x = 0.1c$ pellet with a permittivity of $\varepsilon_r = 107.34 - 6.95j$. The values for all samples at 1MHz is given in Table 3.3.

Sample	ε'_r	ε''_r	$tan\delta$
$x = 0.1a$	87.93	6.96	0.0791
$x = 0.1b$	49.46	4.09	0.0827
$x = 0.1c$	107.34	6.95	0.0647
$x = 0.1d$	49.09	2.52	0.0513
$x = 0.1e$	44.59	1.95	0.0437
$x = 0.1f$	103.55	9.28	0.0896

Table 3.3: Table of permittivity values and loss tangents for series F pellets at 1MHz

The wide range of values for the real part of permittivity was unexpected. Some variation is expected within experimental work taking into account both the inaccuracies of the permittivity characterisation and the fabrication process, however the differences are greater than anticipated. The scale of the differences implies that although surface

roughness and other physical effects will have some influence, there may be some material properties influencing the results. Interestingly the loss tangents for all samples in series F are low and and do not follow the trends of the imaginary part as strongly. This means that although a sample with a higher real part of permittivity is more likely to have a larger loss tangent, the hierarchy of the real and imaginary parts of permittivity are not directly followed.

The imaginary part of permittivity for series F pellets (bottom graph of Figure 3.7 shows broadly similar trends in terms of how the pellets rank in order of permittivity as the real part. Some degree of correlation between the real and imaginary parts of permittivity is expected due to the the relationship between these values set out in Equation 3.8. All samples show an increase up to 100kHz before dropping off and then increasing again with increasing frequency up to the maximum test frequency of 3MHz. The measured quantities of capacitance (C) and the dissipation factor (D) used to calculate the permittivity do not suffer a loss of resolution on the LCR meter at the 100kHz boundary. Further investigation found that the calibration procedure of the LCR meter is performed in internal stages and there is a change of scale at 100kHz [10], thus it is theorised that this is causing the step within the graph, rather than any dielectric properties. It is also unlikely that any resonant effect would be observed in a dielectric at such a low frequency. Losses in the system cause the imaginary part of permittivity to increase with frequency for all samples and there is an increase in variation of the data at frequencies above 1MHz, which will be discussed further in the next section.

3.4.2 Accuracy of the LCR meter

The data for all series shows a significant change in the variation of the traces for the imaginary part of permittivity at frequencies higher than 1MHz. The Wayne Kerr 6440B LCR meter used to record capacitance and loss from which permittivity is calculated has limits to the resolution which can be achieved. At frequencies below 1MHz the dissipation factor (D) is measured to four decimal places, whereas over 1MHz a change of scale on the LCR meter results in this now only being measured to three decimal places [10]. The loss of resolution above 1MHz means that measurements are coerced to the nearest value, which is more of a step change than recorded at lower frequencies; causing greater variation in the graph for the imaginary part of permittivity. The capacitance measurements recorded by the LCR meter are also subject to accuracy limitations, but this does not effect the permittivity results as significantly. The accuracy limits for capacitance are presented in Table 3.4. Accuracy above 1MHz is lower than measurements below that frequency threshold, however the change of resolution usually falls from four decimal places to three, so does not significantly impact upon the dielectric data extracted. The change of scale with respect to capacitance measurements is more significant for thicker sample pellets because a greater electrode separation results in a smaller recorded capacitance, hence lower accuracy as values are coerced to their nearest values on a coarser scale.

Series A

When measurements for these samples were made the orientation of the pellet in the sample holder was not recorded. At this stage is was not realised that the permittivity

	Measured capacitance (F)	Resolution (decimal places)
Frequencies below 1MHz:	$\times 10^{-11}$	4
	$\times 10^{-12}$	3
	$\times 10^{-13}$	2
Frequencies 1MHz and above:	$\times 10^{-11}$	3
	$\times 10^{-12}$	2
	$\times 10^{-13}$	1

Table 3.4: Resolution of capacitance measurement using Wayne Kerr 6440B LCR meter across operating frequency range

of the sample is different depending upon the placement of the sample in the holder. As a result only one measure of permittivity was taken, so results presented here cannot be compared directly to other series.

The real part of permittivity is approximately constant across the frequency range. A small increase in the imaginary part is seen with increasing frequency as the dissipation factor increases. The sample with the highest real part of permittivity is the $x = 0.2$ sample with a value of $\varepsilon_r' = 66.63$ at 1MHz, then there is a large gap before the next highest sample ($x = 0.5$). Other than the $x = 0.2$ pellet, all bismuth containing samples fall within the range $\varepsilon_r' = 27.31 - 43.73$ at 1MHz. The unsubstituted barium hexaferrite pellet has the lowest permittivity of all samples with a value of $\varepsilon_r = 12.36 - 0.88j$ at 1MHz. The imaginary part of permittivity displays a similar permittivity ranking for the samples as the real part, with the $x = 0.2$ sample having the largest imaginary part and the $x = 0.0$ pellet the lowest. It is interesting to note that the discontinuity in the traces at 100kHz is also present for the $x = 0.0$ sample, but the overall trend is for the imaginary part of permittivity to initially reduce with increasing frequency and then remain approximately constant after 1MHz.

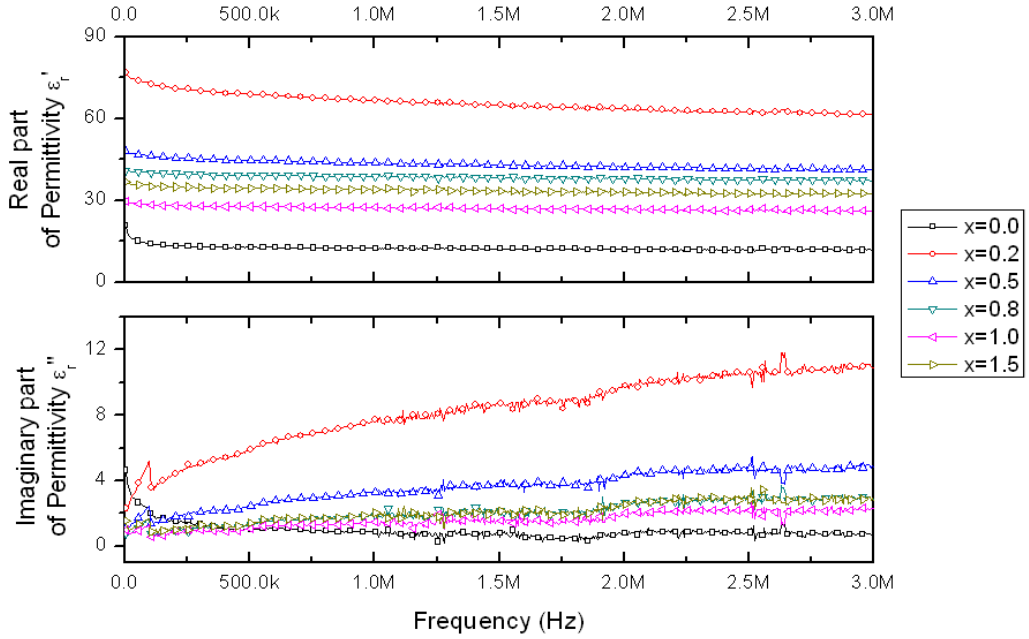

Figure 3.8: Real and imaginary part of permittivity for series A $BaBi_xFe_{12-x}O_{19}$ after sintering for one hour at 1100°C

Series B

Series B is composed of pellets with a variety of bismuth substitution levels. After sintering for one hour at 1100°C the real part of permittivity was increased from an undoped permittivity of $\varepsilon_r = 17.3 - 1.8j$ to a maximum value of $\varepsilon_r = 72.3 - 4.8j$ for the sample of $x = 1.0$ at 1MHz. The real part of permittivity is approximately constant across the frequency range although slightly greater at low frequencies. There is an increase in the imaginary part of permittivity with frequency as losses increase, this is greater for samples with a higher real part of permittivity. Figure 3.9 shows the data for the highest permittivity recorded for each sample, because these values are closest to the true material value.

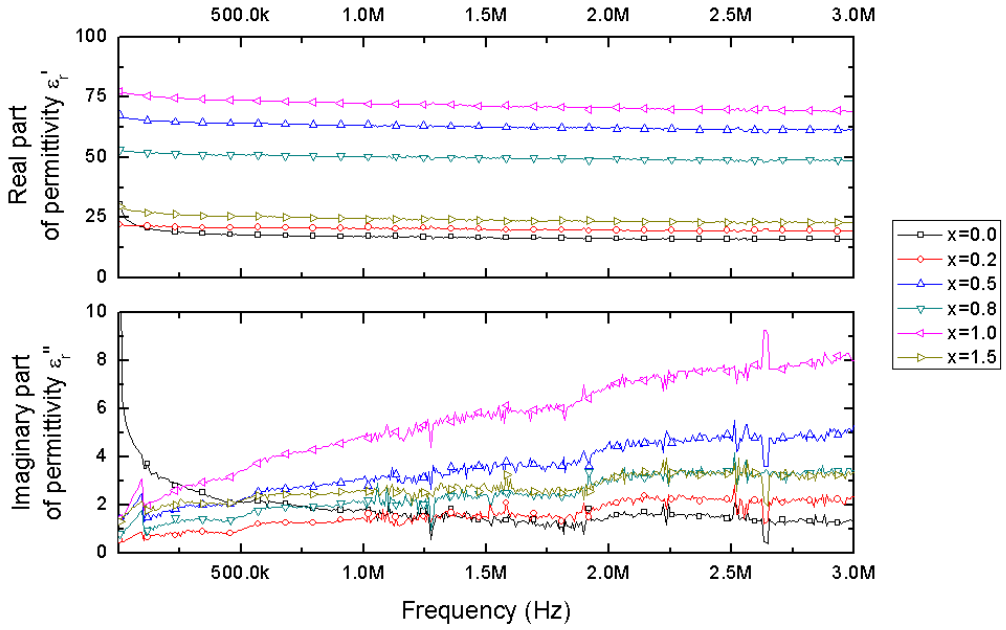

Figure 3.9: Real and imaginary part of permittivity for series B $BaBi_xFe_{12-x}O_{19}$ after sintering for one hour at 1100°C

Series C

Series C contains pellets which, like series B, have been sintered for one hour at 1100°C. Within this set, there were three pellets for the $x = 0.0, 0.2$ and 1.5 compositions and two for the $x = 0.5, 0.8$ and 1.0 samples.

The sample with composition $BaBiFe_{11}O_{19}$ has the highest permittivity ($\varepsilon_r = 93.2 - 7.1j$ at 1MHz, compared to an undoped value of $\varepsilon_r = 17.6 - 1.5j$ at the same frequency). This sample has the same composition of that which has the highest permittivity for series B, however the exact values vary by a real part of 20.9, which is a significant difference. In Chapter 2 Section 2.5 the surface roughness of samples were investigated, it was found that three pellets of the same composition ($x = 0.2$ in this case) had a surface roughness variation ranging from 4.0 – 7.6μm. The inference drawn is that variations in the permittivity measured for the samples could be due to the pellets having different

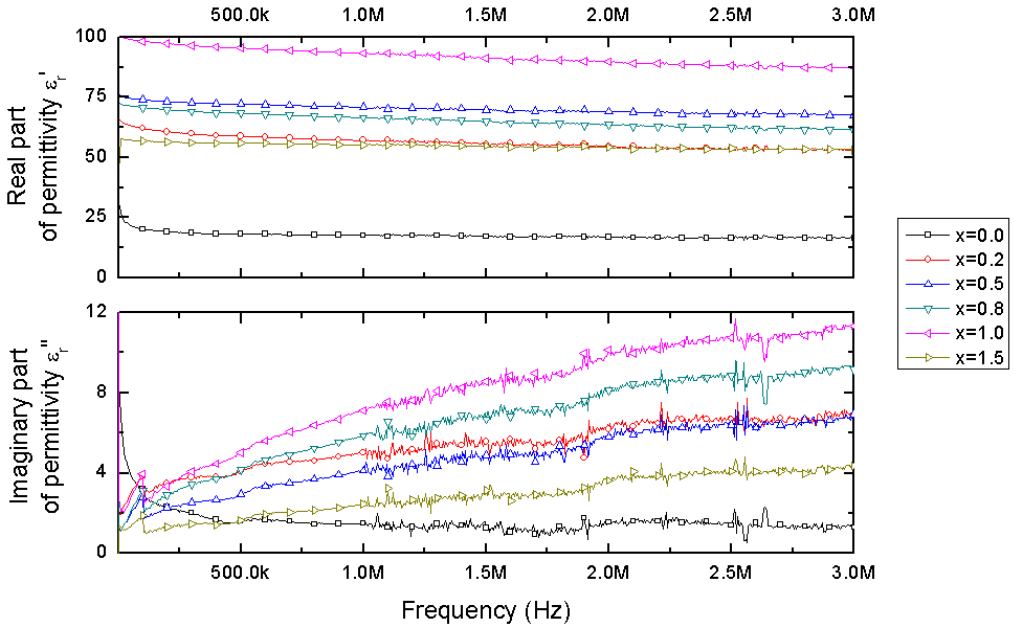

Figure 3.10: Real and imaginary part of permittivity for series C $BaBi_xFe_{12-x}O_{19}$ after sintering for one hour at 1100°C

degrees of surface roughness;l a rougher surface would cause a reduction in measured capacitance and hence a lower calculated permittivity. The undoped samples have very similar values; $\varepsilon_r = 17.3 - 1.8j$ and $\varepsilon_r = 17.6 - 1.5j$ for series B and C respectively even though the observation from results in Section 2.5 was that the undoped material was actually rougher than the bismuth containing samples. Thus although surface roughness is likely to cause errors in permittivity measurements it is most noticeable for higher permittivity materials where an air gap caused by surface roughness is more significant (this argument will be presented in more detail in Sections 3.6.3 and 3.7. However the trends and the similar values observed for some sample pellets provide evidence that the method is repeatable for different pellets.

The overall trends for the compositions are similar for the series; $x = 1.0$ is the highest permittivity sample in each case then $x = 0.5$ and 0.8. In series B, the $x = 1.5$ sample has the next highest permittivity followed closely by $x = 0.2$. In series C, this observation is

reversed, however the permittivities are very similar. For both series the undoped sample has the lowest permittivity. Although the exact values vary, the trends observed are consistent.

Series D

Pellets in series D were processed in the same way as the previous series before being sintered at 1100°C for three hours, rather than the previous one hour. Figure 3.11 shows both the real and imaginary part of permittivity over the 20Hz – 3MHz frequency range.

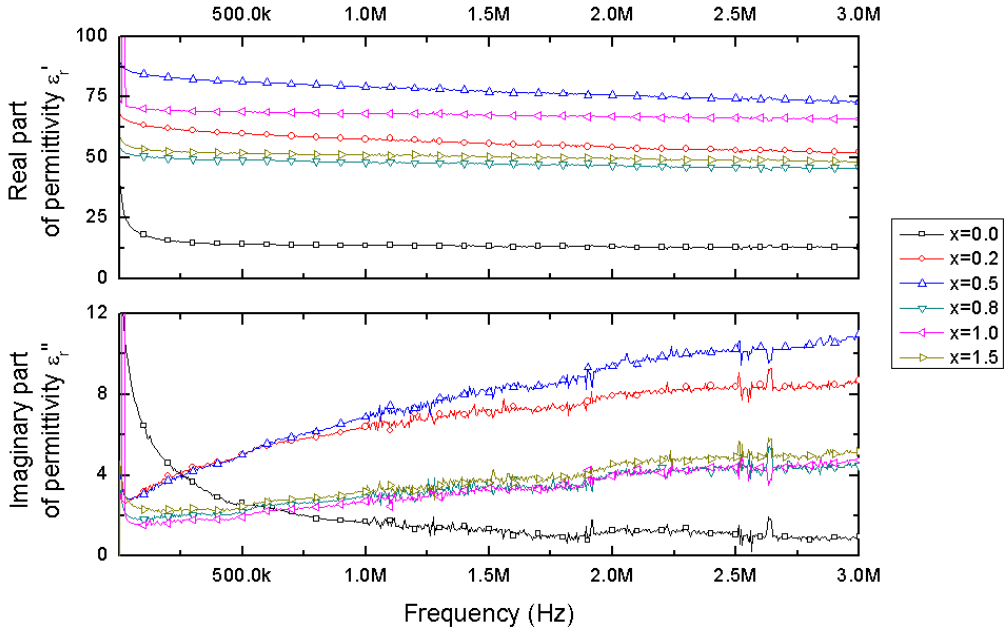

Figure 3.11: Real and imaginary part of permittivity for series D $BaBi_xFe_{12-x}O_{19}$ after sintering for three hours at 1100°C

Interestingly, this series shows different trends for the permittivities of the samples. The highest permittivity sample is the $x = 0.5$ composition where $\varepsilon_r = 79.2 - 6.9j$ and the lowest remains the undoped sample with $\varepsilon_r = 13.7 - 1.7j$. These values are lower than expected, especially the simple barium hexaferrite sample which has showed more con-

sistent permittivity values than the other materials. All compounds containing bismuth have a real part of permittivity of over 50.

It was expected that the longer sintering time would allow the material to form more completely resulting in a higher permittivity for the undoped sample (as predicted in the literature). However, XRD results (Section 2.7) discussed previously found that this material was not fully formed at the 1100°C temperature, hence the lack of increase in permittivity. For the samples which contain bismuth, Ram et al.[11] found that permittivity dramatically increased compared to the parent barium hexaferrite compound. This effect has been repeatedly observed in these experimental results, however not of the same order of magnitude of other authors. The results presented here are approximately constant across the frequency range for the real part and the imaginary part increases with frequency, which is as expected. This provides confidence in the measurement procedure.

3.4.3 Permittivity results at 1100°C as a function of substitution level

To aid clarity in the presentation of results to enable the drawing of conclusions upon the effect of varying doping levels of bismuth within the material upon the permittivity, results are given here at a fixed frequency of 1MHz. Results presented up to this point have shown that the real part of permittivity remains approximately constant across the 20Hz – 3MHz range. The imaginary part increases slightly, but results remain the same relative to each other, thus making this a valid means of presenting data.

Figure 3.12 shows repeatable trends in both the real and imaginary part of permittivity after sintering at 1100°C. The largest variation of results can be seen for the lowest

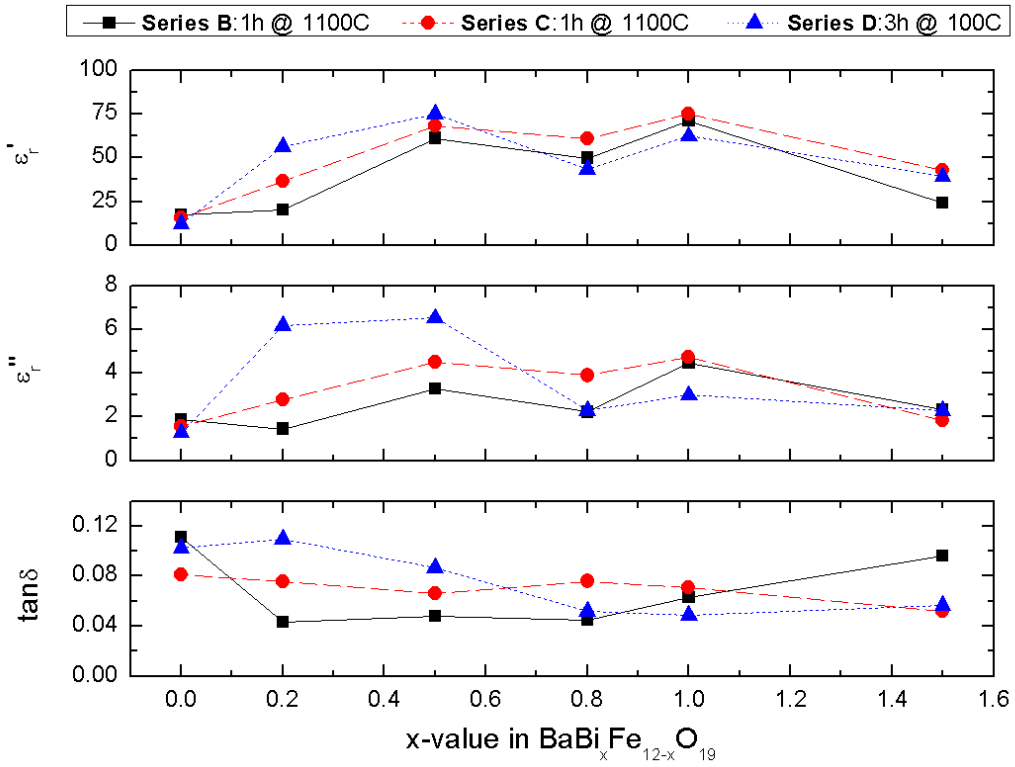

Figure 3.12: Real and imaginary part of permittivity and loss tangent for pellets sintered at 1100°C for one or three hours plotted against x-value in $BaBi_xFe_{12-x}O_{19}$

substitution level ($BaBi_{0.2}Fe_{11.8}O_{19}$). This result can be attributed to the small amount of bismuth present, combined with the low sintering temperature. Work by Ram et al. [11] concluded that the maximum bismuth substitution which can be achieved was an x-value of 0.32, after this the surplus bismuth does not contribute to enhance the permittivity, while Winotai et al. [12] suggested this was where bismuth first substitutes into the $4f_2$ sites. The theory put forward here to explain this result is that the $x = 0.2$ value is a critical point for the formation of the material. There is no excess bismuth in the mixture, hence the lower sintering temperature is more critical in the formation of the compound; resulting in the wide range in the absolute value of permittivity which is found experimentally as bismuth substitutes into the first $4f_2$ sites in varying degrees but not to saturation. This assumption is supported as the highest value within this sample composition is the pellet from series D ($\varepsilon_r = 57 - 6j$) which has been sintered for three hours, rather than one. The longer sintering time would lead to a greater level of formation than the shorter duration. Data presented here shows that the $x = 0.5$ and $x = 1.0$ samples have the largest real parts of permittivity with a slight drop in between at $x = 0.8$. The reasons for this are unclear. Possibly the $x = 0.5$ value is the critical maximum doping level for the first substitution position in the lattice rather than the $x = 0.32$ value suggested by Ram or that the excess bismuth for this level combined with a lower sintering temperature mean this higher permittivity is consistently achieved. Interestingly the $x = 0.8$ where the permittivity drops was shown by XRD to be the composition where the peak splitting at 23° is first visible (Figure 2.17, Section 2.7). This peak splitting could be related to the drop in permittivity.

The results for the loss tangents of the samples in Figure 3.12 show consistently larger values for the undoped barium hexaferrite sample than for bismuth containing pellets. It

is mostly likely that this is due to the incomplete formation of the unsubsituted material shown by XRD analysis (Section 2.7). For the samples with bismuth content the trends observed were that the loss tangent follows the trend shown for both parts of permittivity; thus a material with a high permittivity is likely to have a higher value of tanδ, however there are some small variations present.

Bismuth substituted barium hexaferrite compares favourably to the permittivity and loss values of other materials quoted in the literature. Most substances display a permittivity of between 2 and 5 with a loss between 0.00001 and 0.001 (see Table 3.1). It has a significantly higher permittivity and compounds present losses in the range 0.04 – 0.12 which although is increased, is not a significant gain given the much enhanced permittivity.

3.4.4 Permittivity results at 1200°C

Series A

Pellets from series A were sintered for one hour at 1100°C followed by a further hour at 1200°C. The permittivities of the pellets were characterised and the results for the highest permittivity sides are shown in Figure 3.13.

The real part of permittivity is approximately constant across the frequency range with the exception of the $x = 0.2$ pellet which shows a marked drop in the real part from a high value of $\varepsilon_r' = 99.8$ at 20Hz to a low value of $\varepsilon_r' = 77.8$ at 3MHz. This composition is the highest real part of permittivity of all the samples, the next highest is the $x = 0.5$ sample, then $x = 1.0, 1.5, 0.8$ and finally $x = 0.0$ with the lowest permittivity of $\varepsilon_r = 9.4 - 0.4j$ at 1MHz.

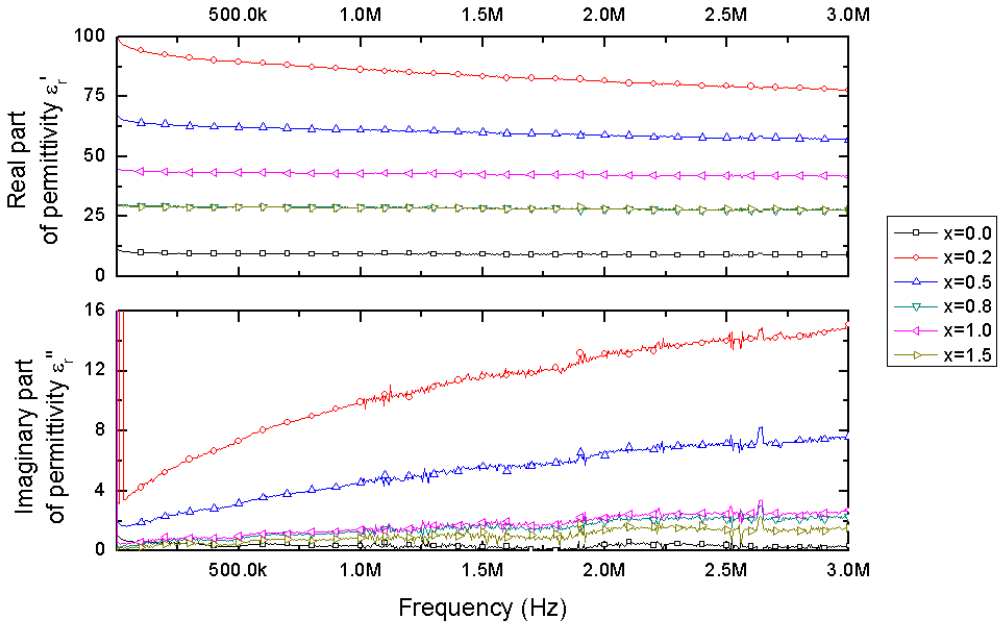

Figure 3.13: Real and imaginary part of permittivity for series A $BaBi_xFe_{12-x}O_{19}$ after sintering for one hour at 1200°C

Concerning the imaginary part of permittivity, by far the largest is the $x = 0.2$ pellet as expected due to the relationship between the real and imaginary parts of permittivity. The $x = 0.5$ sample also displays a considerable loss through the imaginary part. The remaining samples have a much smaller loss (all under $\varepsilon_r'' = 2.5$).

Series PS

Series PS contained pellets which had been processed by Philip Shepherd up to the sintering stage. They were sintered using the same equipment as the other series. The dimensions of these sample disks vary from the others in that they are 16mm in diameter and up to 7mm thick. Due to the thickness of the samples the accuracy of the permittivity results is lower than that of thinner samples because a smaller capacitance is recorded and with it a loss of measurement resolution. Additionally the smaller diameter meant that samples were visually aligned into the correct position covering the guard ring on

the electrode. Only samples of composition $x = 0.5$, 0.8 and 1.5 were of an acceptable physical quality for characterisation however they do provide a useful number of samples to compare and contrast to other results.

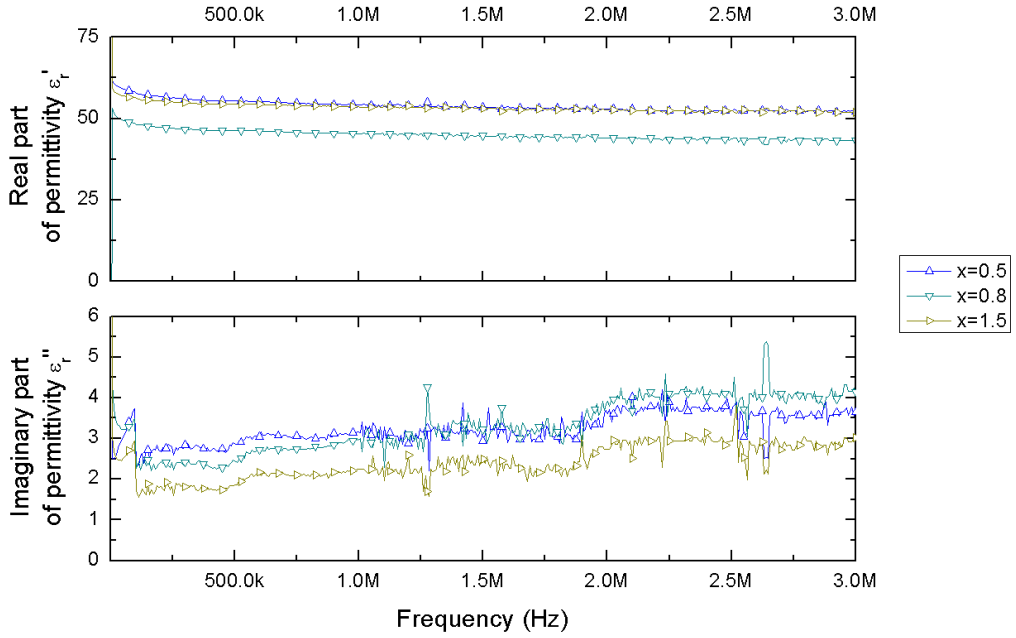

Figure 3.14: Real and imaginary part of permittivity for series PS $BaBi_xFe_{12-x}O_{19}$ after sintering for one hour at 1100°C followed by a further hour at 1200°C

Figure 3.14 shows the permittivity values for the suitable series PS pellets over the 20Hz – 3MHz range. The highest permittivity sample is $x = 0.5$ where $\varepsilon_r = 54.18 - 3.142j$ at 1MHz, closely followed by the $x = 1.5$ material, with the $x = 0.8$ pellet having the lowest permittivity of $\varepsilon_r = 45.30 - 2.990j$ at the same frequency.

Series E

Pellets in series E were processed in the same way as the previous series before being sintered at 1200°C for three hours, rather than the previous one hour. The permittivity measurements are shown in Figure 3.15.

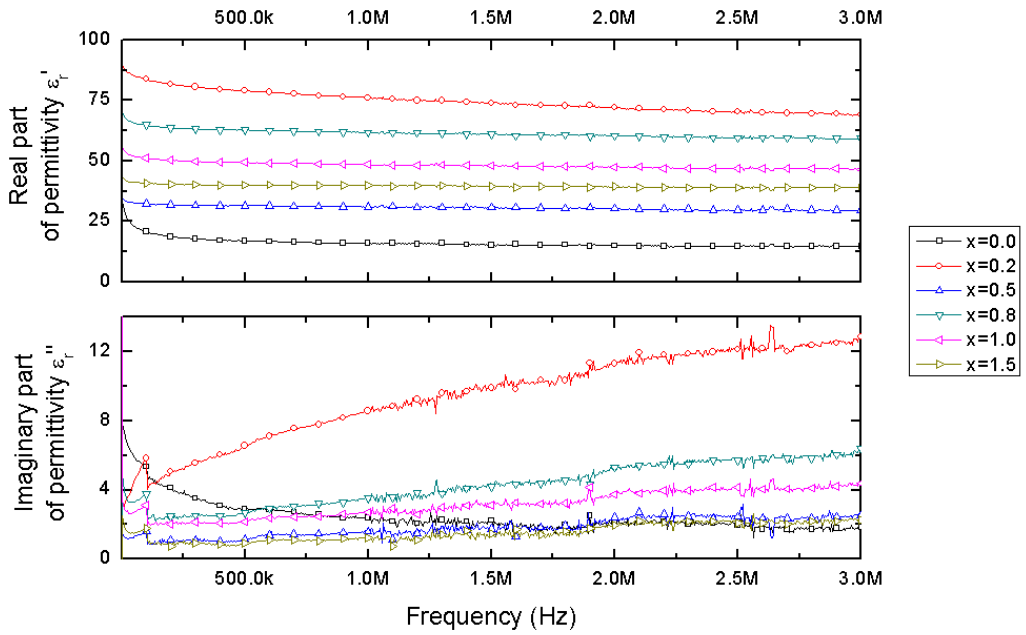

Figure 3.15: Real and imaginary part of permittivity for series E $BaBi_xFe_{12-x}O_{19}$ after sintering for three hours at 1200°C

The highest permittivity is the $x = 0.2$ pellet, with $\varepsilon_r' = 76.1 - 8.6j$ at 1MHz, then pellets with composition $x = 0.8, 1.0, 1.5, 0.5$ and finally $x = 0.0$ with $\varepsilon_r = 16.0 - 2.4j$ at 1MHz. The imaginary part of permittivity follows the same trends for the pellet compositions as the real part. The largest imaginary part of permittivity is the $x = 0.2$ pellet where $\varepsilon_r'' = 12.8$ at its maximum at 3MHz.

3.4.5 Permittivity results at 1200°C as a function of substitution level

This analysis is provided to aid clarity in comparing the pellets from each series to one another at a constant frequency of 1MHz. This is a valid presentation because the permittivity trends remain approximately constant across the remaining frequency range up to 3MHz. Figure 3.16 shows the highest permittivity pellets from series A, PS and E which have been sintered at 1200°C.

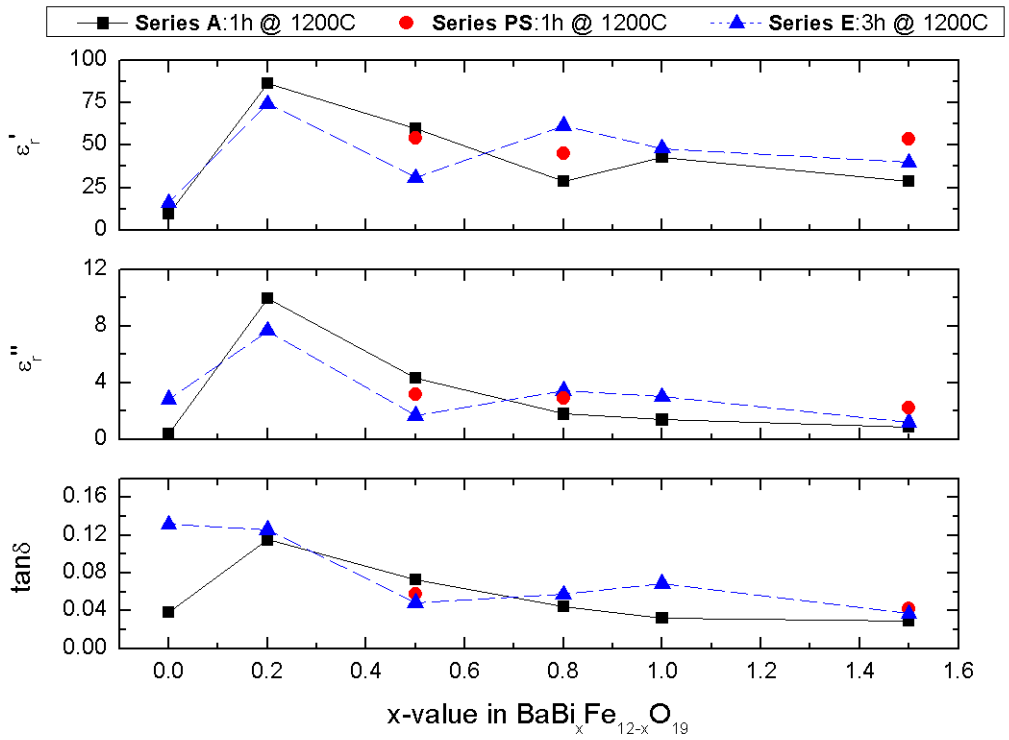

Figure 3.16: Real and imaginary part of permittivity and loss tangent for pellets sintered at 1200°C for one or three hours plotted against x-value in $BaBi_xFe_{12-x}O_{19}$

The real and imaginary parts of permittivity follow the same trends, as was expected given the relationship between the two values. Across all series the undoped barium hexaferrite compound has the lowest real and imaginary part of permittivity. The highest permittivity is now the $x = 0.2$ material, from this composition with increasing x-values the general trend is for the permittivity to reduce relative to this maximum point. The data for the loss tangent ($\tan\delta$) follows similar trends to the permittivity results with the exception of the undoped barium hexaferrite material which shows a much higher loss for the series E $x = 0.0$ pellet which has been sintered for three hours at 1200°C.

An explanation for the high $x = 0.2$ sample result is found by again considering the effect of the bismuth substitution at the $x = 0.2$ level. Here the bismuth content of the material is closest to the maximum bismuth substitution level quoted by Ram et al.

as $x = 0.32$ [11]. Therefore these results are in agreement and the highest permittivity values are observed. Any additional bismuth present in higher concentrations (sample compositions $x = 0.5, 0.8, 1.0$ and 1.5) still contributes to the permittivity of the material in comparison to the undoped material by possibly substituting into other iron sites in the lattice as theorised by Winotai et al. [12].

The permittivity of the material is enhanced by the addition of bismuth; all bismuth containing compounds display a higher real part of permittivity than the unsubstituted barium hexaferrite.

The losses of the bismuth substituted barium hexaferrite compound are within the same range as those observed at the lower sintering temperature of 1100°C, which as was observed is a larger value than other materials values, however there are also significant gains in the real part of permittivity to offset these losses.

An unexpected feature in Figure 3.16 is that the pellets sintered for three hours do not have a repeatedly higher permittivity than those sintered for one hour, as observed for the 1100°C sintering regime. Also the absolute values for the real part of permittivity are no higher than those of the lower temperature sintered samples. Two potential explanations for this have been identified; the first being the potential loss of bismuth from the material as it is heated and the second being complete formation of the material resulting in little change in permittivity values between the materials.

Bismuth oxide has a relatively low melting point of 817°C and a boiling point of 1890°C [13]. As higher sintering temperatures are reached the melting point of bismuth oxide is exceeded, contributing towards the lower formation temperature of the bismuth substituted barium hexaferrite compounds compared to the parent material. However this

lower melting point can potentially lead to the evaporation of bismuth oxide which reduces the overall bismuth content of the sample. This effect would be more pronounced at the higher sintering temperature of 1200°C.

The second point concerns the formation of bismuth substituted barium hexaferrite; results presented from XRD analysis (Section 2.7) showed that the compound was formed after sintering for one hour at 1200°C. Thus the permittivity for samples sintered for one or three hours at this temperature will all be fully formed and thus the permittivity between these series will not be dissimilar.

It was concluded that although some bismuth may have evaporated into the atmosphere during the longer sintering process, it it more likely (as supported by XRD results) that the material is fully formed and variations in permittivity results are more likely due to physical imperfections on the pellets.

3.4.6 Permittivity of samples over the range 20Hz – 10kHz

Graphs presented in the previous section showed that at the lower end of the test frequency range more variation and changes were observed. To investigate this effect further, characterisation was repeated across the lower frequency range of 20Hz – 10kHz.

Samples after sintering at 1100°C

The graphs below in Figure 3.17, 3.18 and 3.19 show the low frequency permittivities up to 10kHz for samples from series B, C and D respectively.

From these graphs it was observed that as expected, the permittivity trends are the same

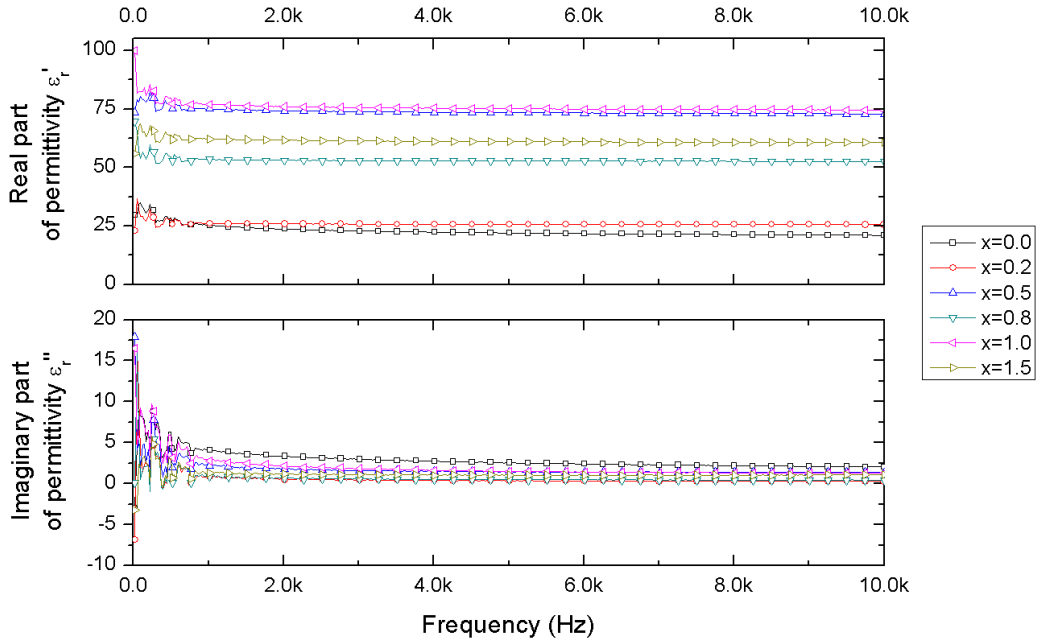

Figure 3.17: Real and imaginary part of permittivity for series B $BaBi_xFe_{12-x}O_{19}$ after sintering for one hour at 1100°C

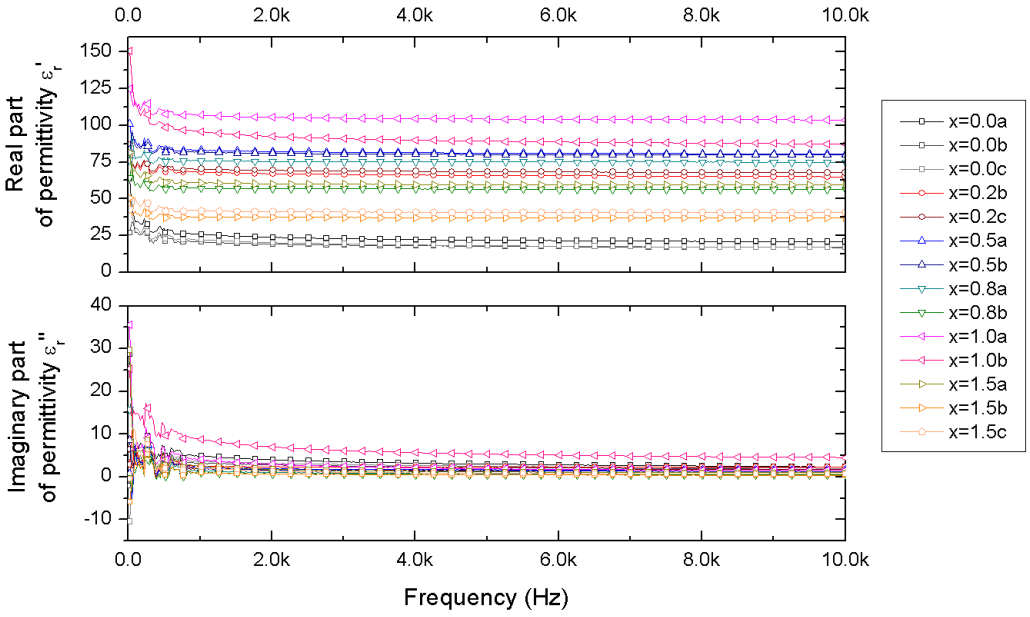

Figure 3.18: Real and imaginary part of permittivity for series C $BaBi_xFe_{12-x}O_{19}$ after sintering for one hour at 1100°C

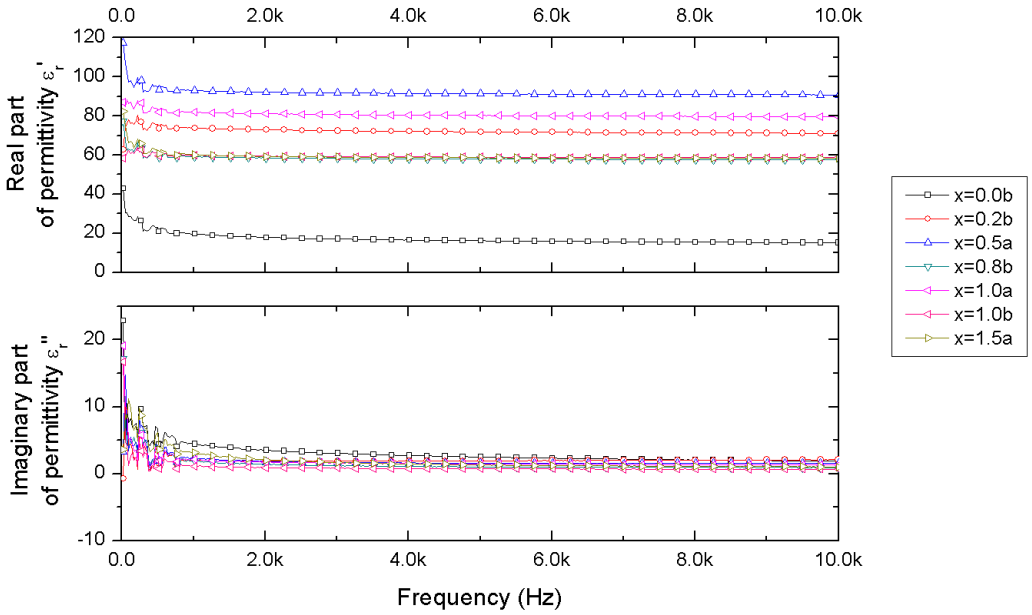

Figure 3.19: Real and imaginary part of permittivity for series D $BaBi_xFe_{12-x}O_{19}$ after sintering for three hours at 1100°C

as those across the higher frequency range 20Hz – 3MHz. The real parts of permittivity show a smaller decrease due to the larger scale however there there is now a degree of variation in the measurements seen at the lowest frequency range up to 1kHz. This is also observed for the imaginary part of permittivity.

Samples after sintering at 1200°C

Samples from series A and E which have been subjected to a maximum sintering temperature of 1200°C were recharacterised over the frequency range 20Hz – 10kHz. Permittivity results for series A are presented in Figure 3.20 and for series E in Figure 3.21.

The trends seen in the graphs show that the permittivity hierarchy is the same as those in the higher frequency range (20Hz – 3MHz) for both the real and imaginary part of permittivity. The real part displays a higher permittivity at the lowest reaches of the test frequency range with some variation in the overall trends at frequencies up to 500Hz. The

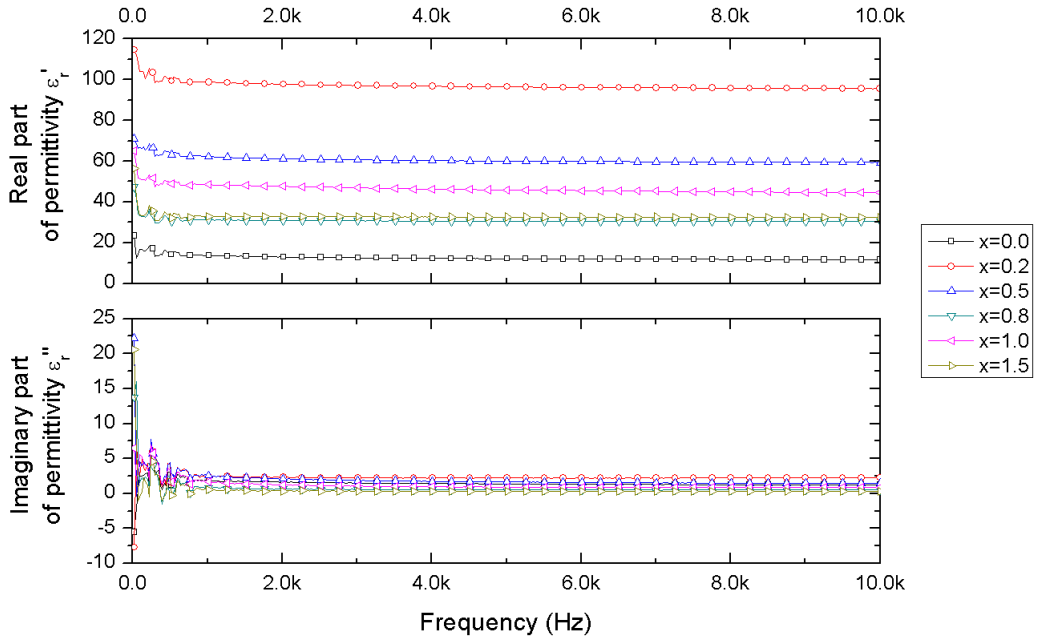

Figure 3.20: Real and imaginary part of permittivity for series A $BaBi_xFe_{12-x}O_{19}$ which have been sintered for one hour at 1100°C followed by a further hour at 1200°C

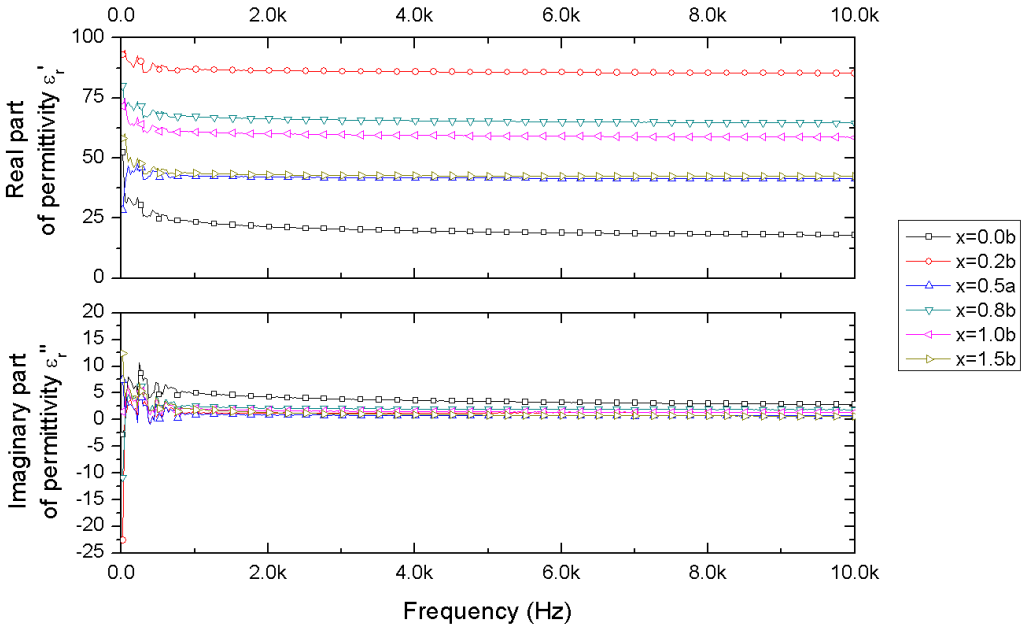

Figure 3.21: Real and imaginary part of permittivity for series E $BaBi_xFe_{12-x}O_{19}$ which have been sintered for three hours at 1200°C

largest variations in the imaginary part of permittivity are also seen over this frequency range.

It was hypothesised that the variation in the permittivity results at very low frequency is caused by the comparatively large measurement step size (quantisation) in comparison to the test frequency. This results in a much coarser measurement resolution at low frequency which is displayed as the variation visible in Figures 3.20 and 3.21. However to further investigate this effect, further testing was carried out within even lower test frequency ranges.

3.4.7 Permittivity of samples at very low test frequencies

Samples from series A which have been sintered for one hour at 1100°C followed by a further hour at 1200°C with a range of bismuth concentrations were tested first over the frequency range of 20Hz – 1kHz (shown in Figure 3.22) and then repeated over the range 20Hz – 100Hz (Figure 3.23).

The trends for the real part of permittivity are the same for both test frequency ranges and these in turn agree with the results at higher frequencies up to 3MHz. The absolute values of permittivity are higher at lower frequencies which was expected because the high frequency results did show higher permittivity values at the start of the measurement sweep at the lower frequency range and this is the area which is now the focus of the graphs.

The data taken up to 1kHz shown in Figure 3.22 shows some variation in the real part of permittivity, with the greatest magnitude of this variation at the lower end of the test frequency range. The variation is not large enough to obscure the overall trends in

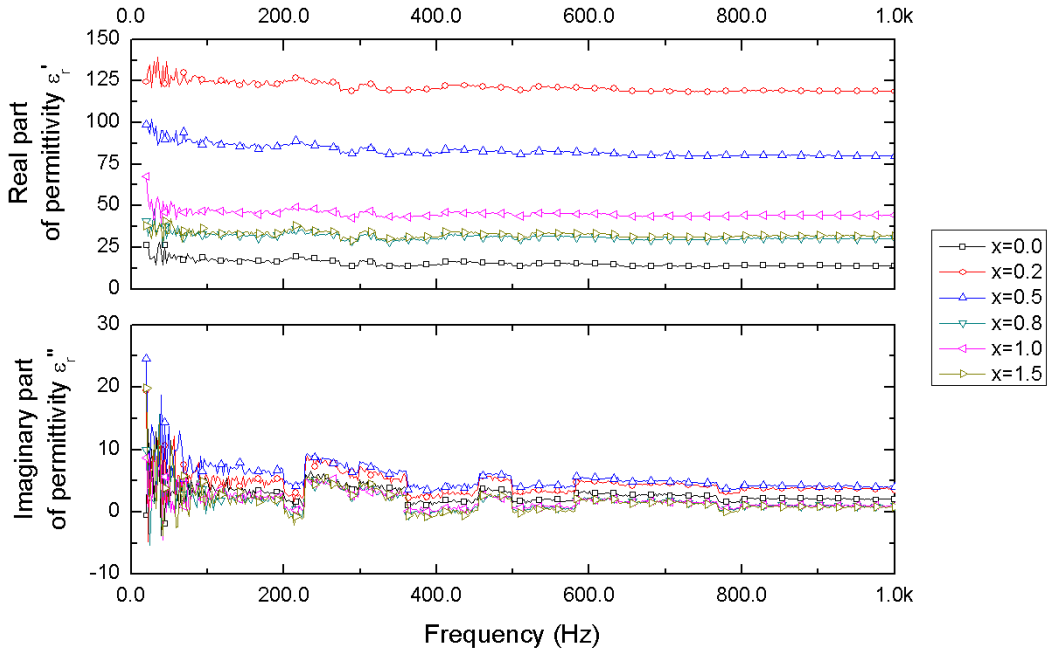

Figure 3.22: Real and imaginary part of permittivity for series A $BaBi_xFe_{12-x}O_{19}$ which have been sintered for one hour at 1100°C followed by a further hour at 1200°C over the test frequency range of 20Hz – 1kHz

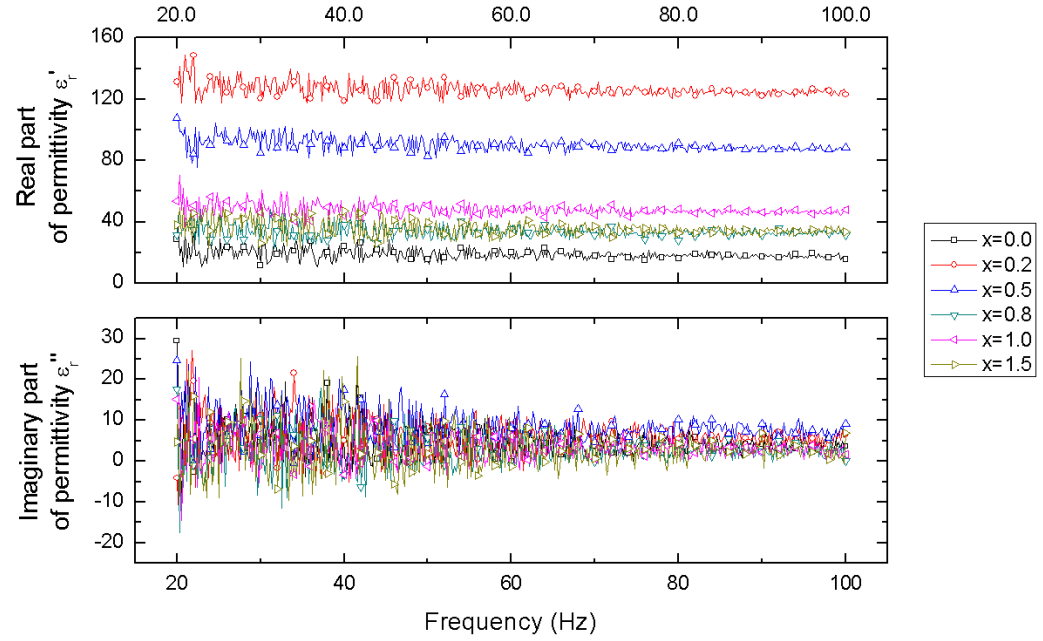

Figure 3.23: Real and imaginary part of permittivity for series A $BaBi_xFe_{12-x}O_{19}$ which have been sintered for one hour at 1100°C followed by a further hour at 1200°C over the test frequency range of 20Hz – 100Hz

permittivity values. The imaginary part of permittivity also shows more variation at the lowest reaches of the test frequencies, however in this situation the permittivity trends are not still visible and do not appear until after 150Hz. The imaginary part of permittivity shows more change than the real part however trends are clearly visible in both.

The permittivity results over 20Hz – 100Hz presented in Figure 3.23 again show the same trends for the real part however there is much more variation in the data for the imaginary part, to the degree that it is no longer possible to distinguish between the samples. Again the greatest variation is at the lower range of the test frequency spectrum which smooths out as the frequency increases.

From these results it was concluded that the results for the real part of permittivity are accurate at frequencies higher than 50Hz and for the imaginary part at frequencies higher than 150Hz. These values were taken from observations of the graphs of permittivity in Figures 3.22 and 3.23.

3.4.8 Conclusions

The addition of bismuth to barium hexaferrite enhances the low frequency permittivity of the material. All bismuth containing materials have a greater real part of permittivity than their unsubsituted relatives in each series. The samples display the largest ε'_r values at the lowest test frequencies which then reduce slightly to form a constant value for much of the frequency range (this effect is most exaggerated by the highest permittivity materials). The imaginary part of permittivity is also increased with bismuth content and is greatest for the samples which display large real parts of permittivity (as expected due to the relationship between the quantities). The losses do increase slightly with

frequency for bismuth samples, but not pure barium hexaferrite.

At 1MHz the highest overall permittivity was displayed by the $x = 0.2$ pellet from series A where $\varepsilon_r = 86.177 - 9.910j$. The lowest permittivity was exhibited by the $x = 0.0$ sample also from series A where $\varepsilon_r = 9.381 - 0.395j$.

When pellets are sintered at 1100°C the greatest permittivity is achieved at the $x = 0.5$ doping level. This was credited to an excess of bismuth for substitution into the $4f_2$ sites combined with a lower sintering temperature. At low substitution levels and low temperatures higher permittivity can be achieved by sintering for a longer period of time.

At the higher sintering temperature of 1200°C the greatest permittivity is displayed by the $x = 0.2$ value samples in each series. It is concluded that at this higher temperature it is possible for a greater number of $4f_2$ sites to be filled with bismuth than at the lower 1100°C temperature.

The formation of high permittivity samples at relatively low temperatures with short sintering durations was confirmed.

3.5 Different permittivity of different sides

When the permittivity of bismuth doped barium hexaferrite samples was calculated a discrepancy in the results was discovered. After further investigation the cause was found to be that one side of the pellet possesses a higher permittivity compared to the other. The difference in permittivity between the two faces of the pellets was greater for samples which possessed a larger overall permittivity.

This difference was observed for all pellets in the bismuth doped series after sintering at both 1100°C and 1200°C, suggesting this was not an anomalous result. The fabrication process was considered in an attempt to locate the source of the discrepancy. Possible causes of this difference between the permittivities of the sample faces can be split into physical and chemical properties;

- Physical properties and effects:
  - The positioning of the sample in the alumina boat during sintering, causing a groove where the face of the pellet is in contact with the edge of the vessel.
  - The placement of the pellet in the vessel resulting in one face of the sample being more exposed to the heater elements in the furnace.
  - Small variations in surface roughness of the sample pellets causing large variations in the measured permittivity on each face.
- Chemical properties and effects:
  - Heterogeneous composition and distribution of bismuth throughout the sample.
  - Incomplete chemical reaction resulting in a partially formed material and so non-repeatable results.

3.6 Physical properties and effects

The alumina boats used to contain the samples in the furnace were used for both the sample powder during the heating and grinding stages, then cleaned before holding the pelletized samples for sintering. When the pellet is placed in this vessel, it lies at an acute

angle with one face in contact with the edge of the alumina boat as shown in on the left of Figure 3.24. The contact between the two surfaces causes a groove to form on the sample. This was observed very clearly on some samples but was barely distinguishable on others. An example of a clear groove or line, is seen in the Figure 3.25 which shows the series A $BaBi_{1.5}Fe_{10.5}O_{19}$ pellet. Conversely, this groove can hardly be seen on the pellet $BaBi_{0.5}Fe_{11.5}O_{19}$ the same series (Figure 3.26). Both of these samples have been subjected to the same synthesis and sintering regime.

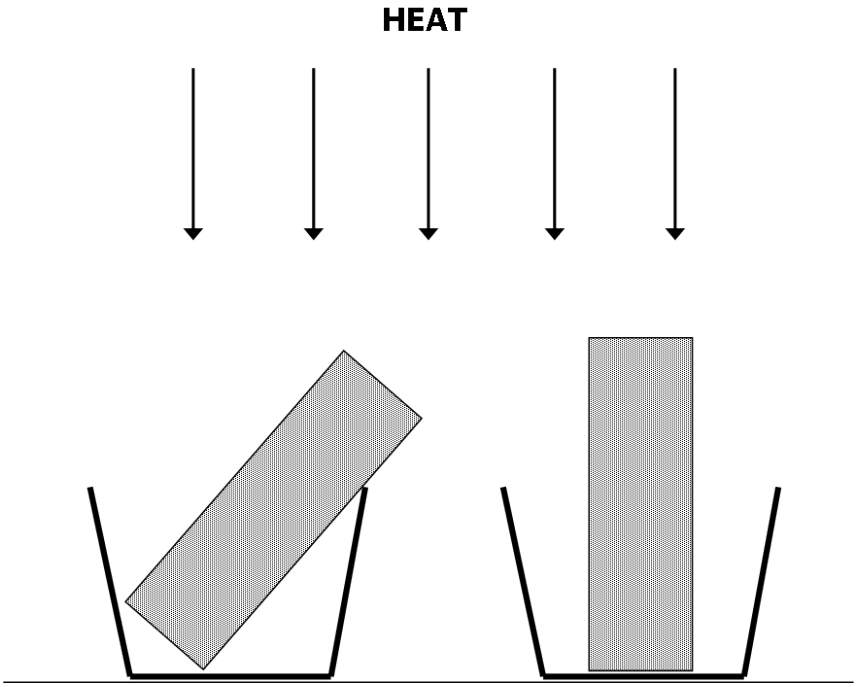

Figure 3.24: Cross section diagram showing orientation of sample pellets in alumina boats placed in the furnace and the direction of radiative heat. The sample on the left has been rested on the side of the vessel and that on the right has been balanced on an edge.

The characterization of low frequency permittivity was adversely affected by this groove. The parallel plate method to measure the capacitance of a sample requires a flat, smooth surface to provide accurate data. Any air gap present will reduce the value of the permittivity of the material. This is because the lower permittivity of the air gap will be included within the properties of the material under test because this is a bulk characterization

Figure 3.25: A clear groove can be seen between the points marked on pellet series A $BaBi_{1.5}Fe_{10.5}O_{19}$ after sintering at 1200°C

Figure 3.26: Groove can not be seen clearly on pellet series A $BaBi_{0.5}Fe_{11.5}O_{19}$ after sintering at 1200°C, markers present for clarity

method.

The second reason considered for the discrepancy in permittivity was also related to the placement of the sample pellet in the alumina boat, but this time due to the differing exposure to the heating elements in the furnace. The Vecstar furnace used in conjunction with Eurotherm 2132 and 2416 controllers has radiative heater elements in the top of the furnace cavity. This means that as heat is generated it first of all radiates downwards, before secondary conventional heating begins. The surface of the pellet which is facing downwards into the boat (see left side of Figure 3.24) is shielded from the radiative heat. The presence of the alumina boat will also reduce the bottom surface exposure to reflected and conventional heat. The result is this surface will be sintered at a lower temperature to the upper surface. This could in turn have an effect on the formation of the bismuth doped barium hexaferrite.

XRD analysis (Chapter 2, Section 2.7) confirms the formation of the bismuth doped barium hexaferrite samples, but also confirms that the undoped $BaFe_{12}O_{19}$ is not formed after sintering at 1200°C for one hour. The formation temperature of $BaFe_{12}O_{19}$ is reported in the literature to be 1050°C [14], so the failure of the compound to form was unexpected. Therefore it was concluded that at least part of the sample was not reaching this threshold temperature or for long enough duration to react completely. The lack of exposure of part of the sample to the radiative heat of the furnace is an explanation for this result. The bismuth containing samples are less affected by this issue due to the lower temperature required for reaction, as reflected in the XRD results.

3.6.1 Using a different vessel for sintering

A different vessel was used to contain a sample for sintering in an attempt to provide uniform heating on one face of the pellet. A 30mm internal diameter round alumina crucible was used to contain a 20mm diameter undoped barium hexaferrite sample for sintering. The pellet was placed flat in the bottom of the vessel and then placed in the furnace and sintered for one hour at 1100°C then left to cool to room temperature overnight. When removed it was found that the pellet had become attached to the base of the crucible and shattered when an attempt was made to remove it. It was concluded that due to the destruction of the sample, this method was not a suitable solution.

The use of alumina boats for containing the sample pellets provide the best means for sintering; despite the disadvantages detailed above they are more suitable than the alternative alumina crucible.

3.6.2 Altering the positioning of the pellet in the vessel

Another method to eliminate the line from the sample which was considered was to place the pellet in the alumina boat on its edge so that it was balanced upright (right side of Figure 3.24). This did indeed remove the line from the sample, confirming the assumption that contact with the edge of the vessel had been the cause. However the effect of the new positioning was that the pellet was deformed in a different manner; pellets were no longer circular, showing a flat edge from the contact surface with the vessel. This form is more acceptable than the grove on the face of the pellet because it is less detrimental to experimental accuracy for characterisation methods used within this work.

3.6.3 Surface roughness effects - Talystep method

An investigation was conducted to establish if there was a relationship between the surface roughness of pellets and the variation of permittivity. Air gaps have the potential to reduce the measured capacitance of the system, leading to a misleadingly low permittivity value. The concept here was to compare the results of surface roughness measurements to the permittivity results of a sample. Table 3.5 summarises the results of the Talystep surface roughness measurements along with the permittivities of the samples. (Further information and Talystep results are located in Chapter 2 Section 2.5).

Sample $BaBi_xFe_{12-x}O_{19}$	Surface roughness (μm)	ε_r'
$x = 0.0a$	11.6	15.622
$x = 0.0b$	–	14.367
$x = 0.0c$	–	14.274
$x = 0.2a$	7.6	43.805
$x = 0.2b$	4.0	12.750
$x = 0.2c$	6.4	53.725

Table 3.5: Table presenting summary of surface roughness performed by Talystep method with highest permittivity values for each sample at 1MHz

Pellets from series C with compositions $x = 0.0a$ and $x = 0.2a, b$ and c were examined. The $x = 0.0a$ pellet shows the largest variation in surface roughness, however this sample displays the most similar permittivity to other samples of the same composition in the series. The $x = 0.2a, b$ and c samples have a wide variation in measured permittivity while being smoother than the $x = 0.0a$ pellet. The variation in permittivity values for the $x = 0.2$ samples show no correlation between sample roughness and permittivity. Therefore while it is likely that the surface roughness of the pellets will have a negative impact on the measured permittivity of a material, it is unlikely that this is the only cause for the large variations recorded in the $x = 0.2$ samples and ergo other sample pellets.

3.6.4 Relationship between density and permittivity

This section investigates the relationship between the perfect cylinder density of a pellet and its permittivity. Previous work with barium hexaferrite and other dopants indicated that an increase in density corresponds to an increase in permittivity [11] [15]. Figure 3.27 shows the density of each pellet plotted against the highest measured real part of permittivity.

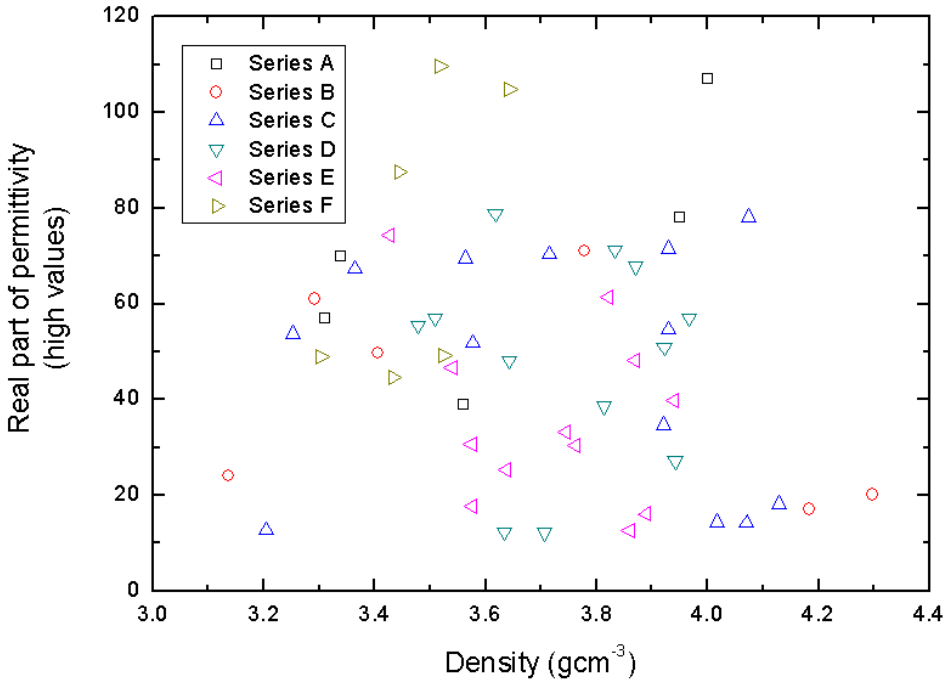

Figure 3.27: Density vs. highest measured permittivity for series A, B, C, D, E and F

The graph shows a wide scattering of results with no clear pattern; if there was a relationship between density and permittivity there would be a trend line visible. Most of the pellets have a density between 3.5 – 4.0 gcm^{-3} and a permittivity of less than $\varepsilon_r' = 80$. Samples from series F which have the same composition vary from 3.30 – 3.64 gcm^{-3} however a high or low permittivity does not correspond to a higher or lower

density measurement.

3.6.5 Density and the difference in permittivity between different sides of a sample

To investigate a potential link between density and the different values of permittivity measured for each side, Figure 3.28 was generated. This shows the density plotted against the absolute difference between the different permittivities for each side.

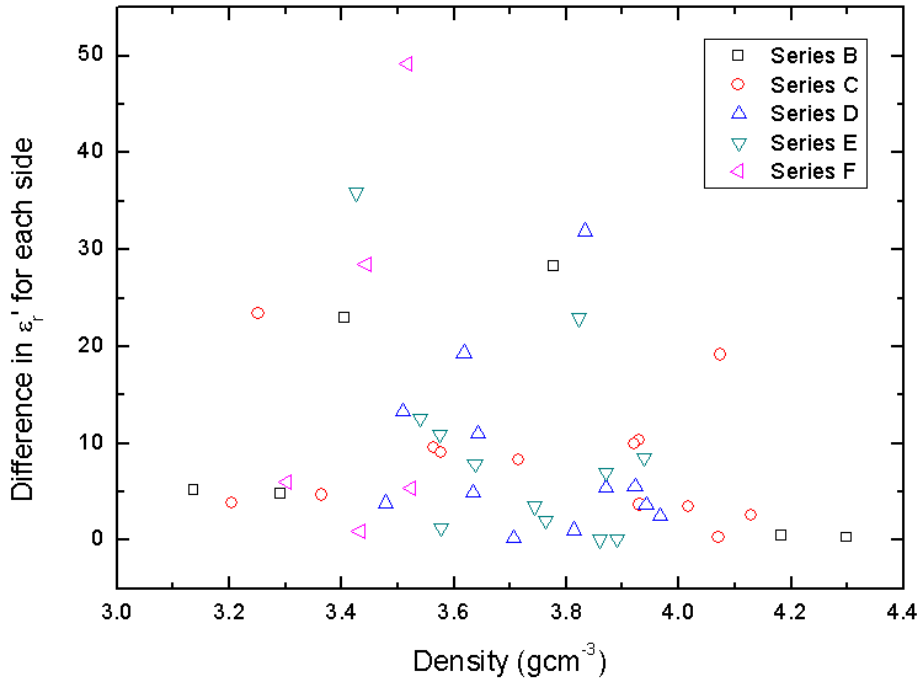

Figure 3.28: Density vs. difference in permittivity between pellet sides for series A, B, C, D, E and F

This graph shows a clearer trend where most samples fall between a difference in real part of permittivity between sides of 0 – 10 and clustered within a density range of 3.4 – 4.0 gcm^{-3}. However there is no link between density and difference in permittivity of different sides, which would be seen by a diagonal line trend in Figure 3.28. From this it was concluded that there is no connection between the density of the pellet and the

permittivity difference between sides of the pellet.

3.6.6 Conclusions

Data presented here shows that there is no clear link between density and permittivity, or between density and the difference of permittivity between pellet sides. Further work is required to confirm this due to the simple nature of the density characterisation employed.

3.7 Modelling in Comsol Multiphysics to investigate the impact of air gaps and surface roughness on characterisation

Comsol Multiphysics 3.3a is a finite-difference time-domain (FDTD) based software package which allows the development of problem geometries which are solved using finite element analysis of physics problems. Using the AC/DC module: electrostatics mode, a model of the parallel plate capacitor system was developed to examine the relationship between the sample, air gaps, surface roughness and the resulting capacitance measured.

It was decided that this investigation was necessary because although it is widely known and accepted that surface roughness and air gaps reduce measurement accuracy, little information upon the quantitative effect this has is available. The purpose of this section is to provide a measure of to what degree undesirable physical effects impede measurement accuracy.

A model of the situation was initially developed in three-dimensions. This provided results as expected for a perfect sample, however when more complex sample geometries were modelled the mesh became too fine resulting in the solver running out of memory, so the decision was taken to model in two-dimensions. The information and results for three-dimensional modelling of the parallel plate capacitor system in Comsol can be found in Appendix A.2

It should be noted that the Comsol interface does not provide a facility for modelling the losses of a dielectric material, so the data which follows is intended for comparison of different sample properties rather than a series of absolute values.

3.7.1 Two-dimensional modelling - perfect sample

Comsol Multiphysics was used to establish a simple two-dimensional model of a perfect sample. Although this geometry could be represented using 2D axial symmetry to solve the problem more rapidly this was decided against so that direct comparisons could be made with more complex models which are not possible to design using the axial mode (sample roughness was represented as a random variation which would not be possible in axial 2D).

The first model was of a perfect sample (dimensions; 20mm diameter, 4mm thick) where there is no air gap between the sample and the plates of the sample holder. The 10mm diameter guard ring is shown on the bottom plate of the model as shown in the geometry in Figure 3.29.

The boundary settings were established so that the top plate of the capacitor behaves as a port (input port, energy method), the bottom plate as a ground and the external

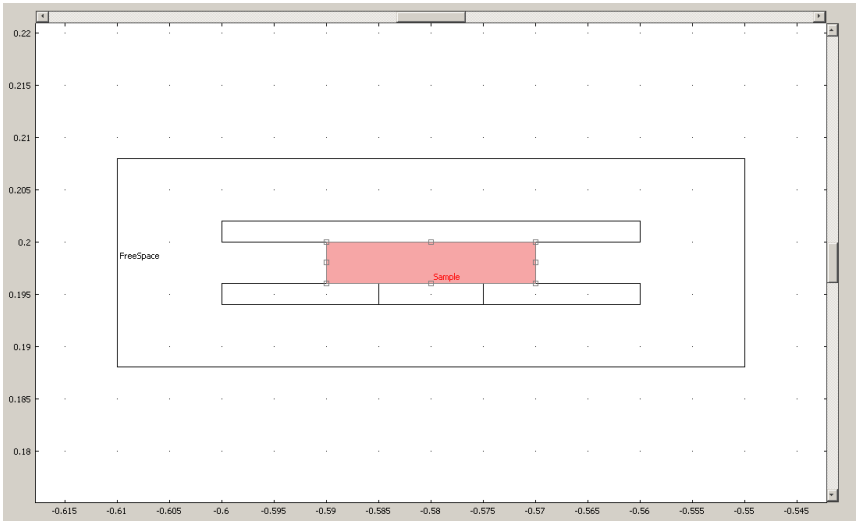

Figure 3.29: Two-dimensional geometry of a perfect sample highlighted in the image. Axis units are in metres.

boundaries of the model as zero charge/symmetries.

For each scenario modelled three different sample permittivities were tested; $\varepsilon_r = 15 - 0j$, $35 - 0j$ and $75 - 0j$. These values were chosen to represent a wide range of sample permittivities.

Figure 3.30 shows the electric potential and field of an ideal sample enclosed between parallel plates. It can be seen that the electric potential is uniform across the sample from a maximum at the top plate down to ground at the bottom plate and the electric field (white arrows) is uniform across the radius of the sample. The fringing fields can be seen at the edges of the plates and are far enough away from the guard ring not to adversely affect the capacitance measurement. The calculated capacitance of the system was 720pF. This is much larger than the value found from the 3D model, however this can be accounted for by considering the geometry of the model. In a 3D (or indeed, an axial 2D) model, the simulation area is explicitly defined in three-dimensions, whereas in the 2D model, it is only defined in two. This means that the third dimension is a large undefined region extending backwards, resulting in a larger simulated capacitance value.

Although the 2D version is not as representative of the physical system, it still provides a useful comparison for changing conditions.

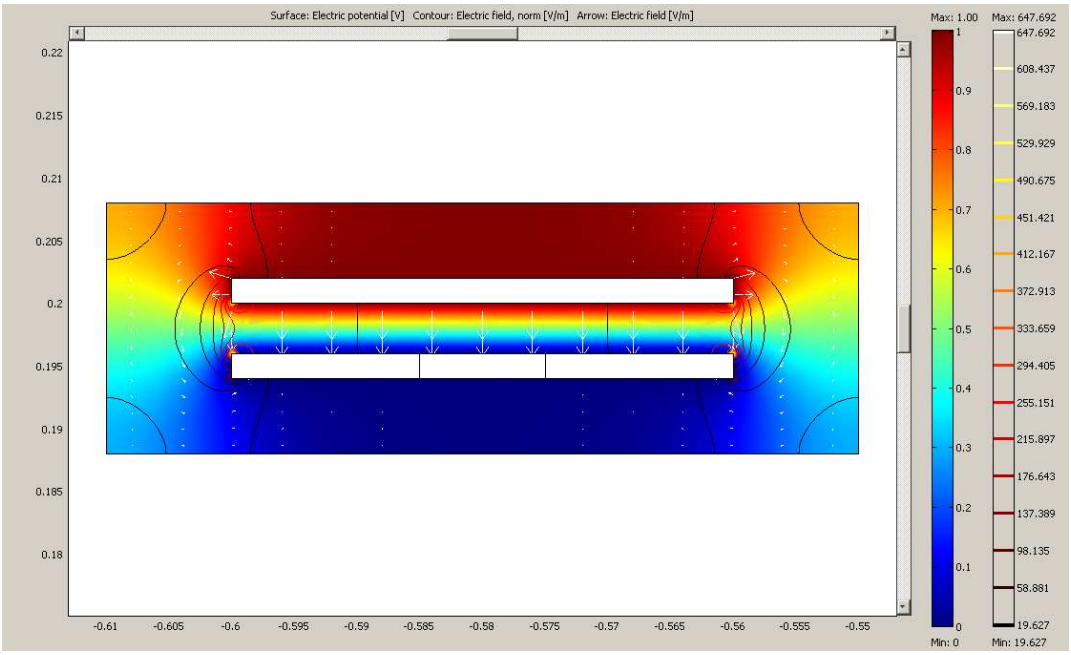

Figure 3.30: Sample permittivity $\varepsilon_r = 15 - 0j$. Colour gradient shows electric potential, contour shows normalised electric field, arrow plot shows direction of electric field where the size of the arrows is proportional to the electric field strength.

The simulation was repeated with different sample permittivities. There was some change to the result; lower permittivity samples produce lower capacitance values, as given in Table 3.6. The fringing fields become more significant for higher permittivity samples, but are still too far from the measurement region of the guard ring in the centre of the plate to cause an adverse effect.

Sample permittivity (ε_r)	Capacitance (pF)
15 - 0j	720
35 - 0j	1605
75 - 0j	3376

Table 3.6: Simulation results for ideal samples of different permittivities with no air gap between sample holder plates.

3.7.2 Perfect sample with air gap between sample and plate

A series of simulations were performed to investigate the effect on the capacitance of the system with different permittivity samples with an air gap between the material and the top plate of the capacitor. The geometry of the sample was set up so that a pellet with 20mm diameter and 3.9mm thickness was placed between two conducting plates which were 4mm apart. The remaining 0.1mm between the plates was set as a separate area which was also 20mm wide (so in effect a second, smaller layer of the pellet) which was allocated a permittivity equal to that of air. The model was arranged so that the area representing the pellet was in contact with the bottom plate and between the pellet and the top electrode the air gap section was located.

The sub-domain settings of the model were altered so that the sample permittivity was either $\varepsilon_r = 15 - 0j$, $35 - 0j$ or $75 - 0j$ dependent on the simulation. The 0.1mm interface between the sample and the capacitor plate was set as $\varepsilon_r = 1 - 0j$ to represent a thin layer of air. The boundary conditions were unchanged from the previous model; the top plate of the capacitor was set as a port, excited by the energy method; the bottom plate was set as a ground condition; the furthest boundaries are zero charge/symmetry conditions; and the other boundaries are internal continuity conditions.

Figure 3.31 shows the result of a simulation for a sample with permittivity $\varepsilon_r = 15 - 0j$. In this image the effect of the air gap between the top capacitor plate and the sample can be clearly seen by the change in the electric potential across the simulation region represented by the sharp change in the colour gradient. This effect becomes more pronounced as the permittivity of the sample increases; Figures 3.32 and 3.33, show simulation results for samples with permittivities of $\varepsilon_r = 35 - 0j$ and $75 - 0j$ respectively.

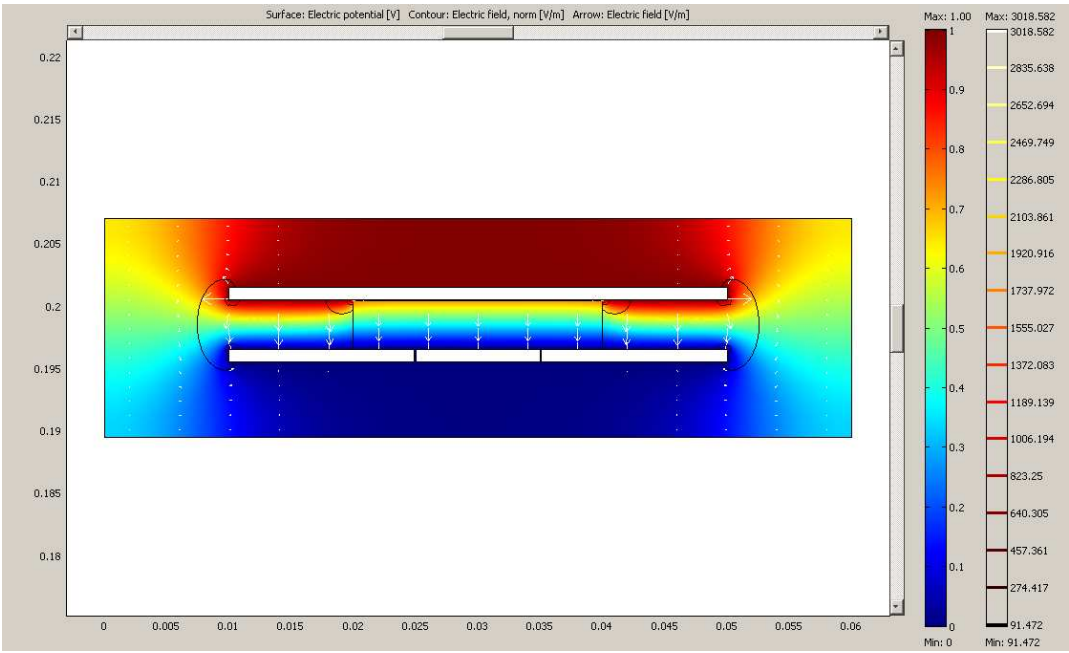

Figure 3.31: 3.9mm sample with permittivity $\varepsilon_r = 15 - 0j$ and a 0.1mm air gap between sample and top plate. Colour gradient shows electric potential, contour shows normalised electric field, arrow plot shows direction of electric field where the size of the arrows is proportional to the electric field strength.

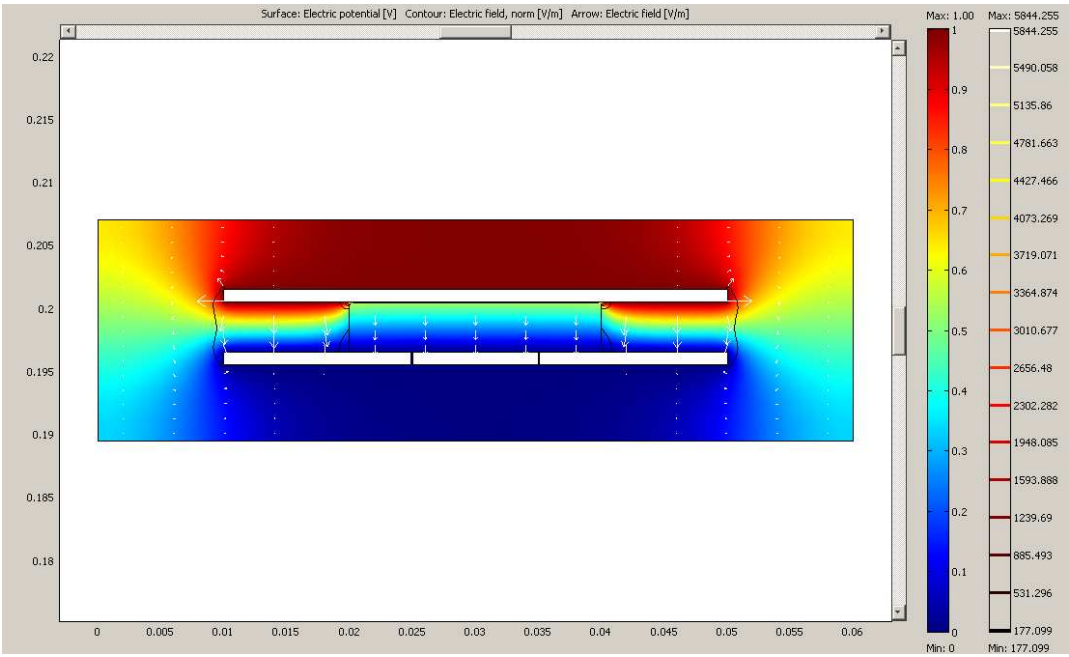

Figure 3.32: 3.9mm sample with permittivity $\varepsilon_r = 35 - 0j$ and a 0.1mm air gap between sample and top plate. Colour gradient shows electric potential, contour shows normalised electric field, arrow plot shows direction of electric field where the size of the arrows is proportional to the electric field strength.

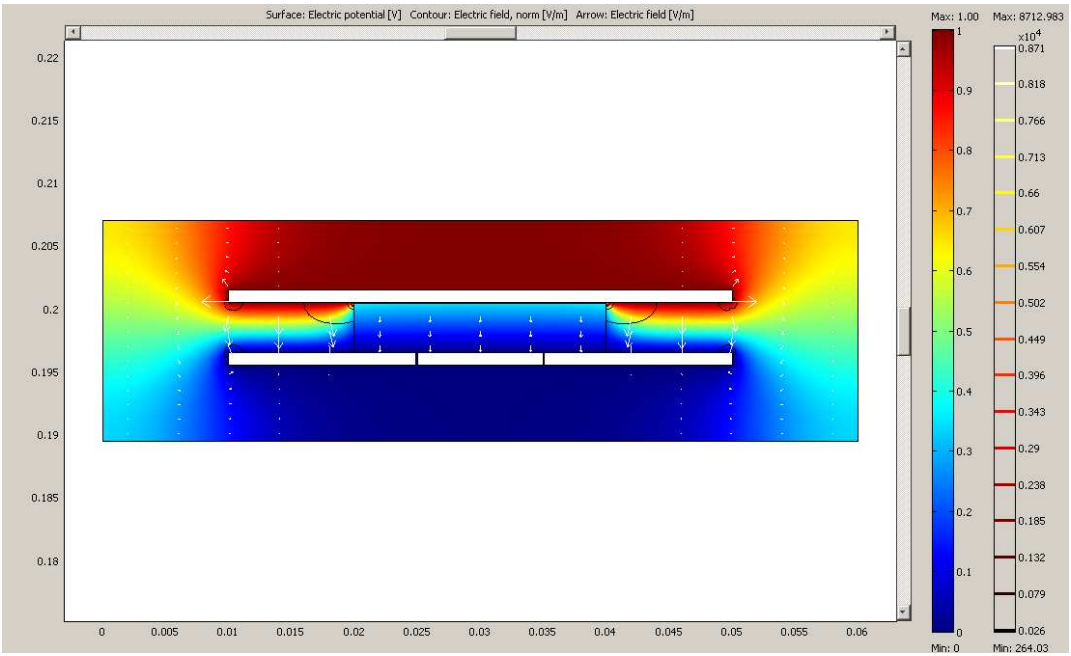

Figure 3.33: 3.9mm sample with permittivity $\varepsilon_r = 75 - 0j$ and a 0.1mm air gap between sample and top plate. Colour gradient shows electric potential, contour shows normalised electric field, arrow plot shows direction of electric field where the size of the arrows is proportional to the electric field strength.

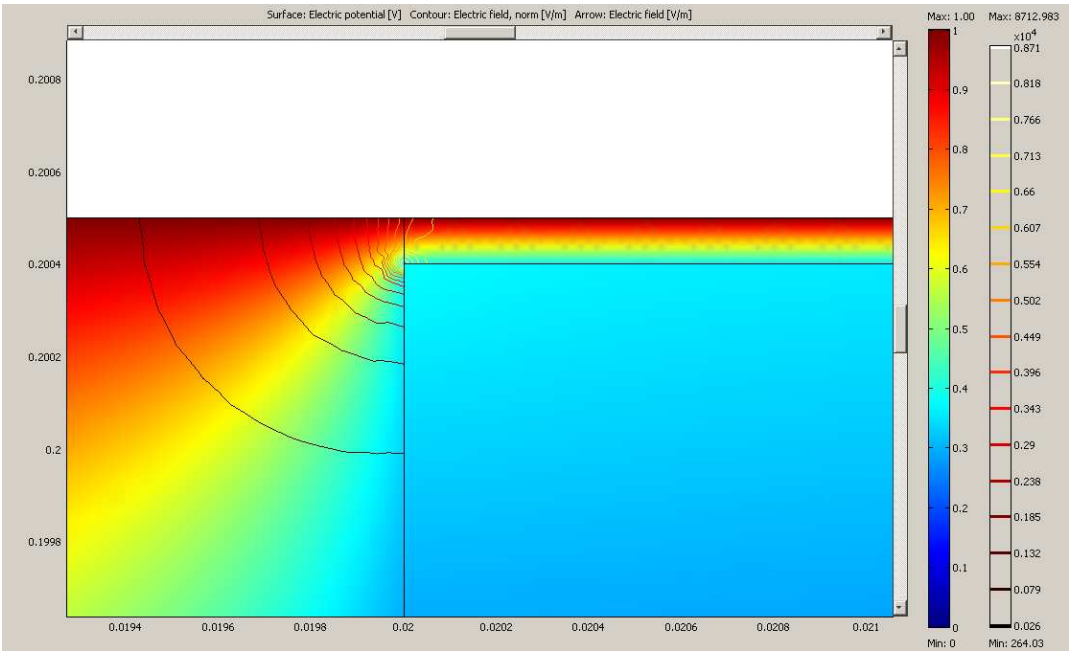

Figure 3.34: Larger scale image of the electric field around the interface between the sample, air gap and top conducting plate. Sample permittivity $\varepsilon_r = 75 - 0j$. Colour gradient shows electric potential, contour shows normalised electric field, arrow plot shows direction of electric field where the size of the arrows is proportional to the electric field strength.

Sample permittivity (ε_r)	Capacitance (pF)	% of perfect sample Capacitance
15 - 0j	550	76.4
35 - 0j	901	56.1
75 - 0j	1236	36.6

Table 3.7: Simulation results for 3.9mm thick samples of different permittivities with a 0.1mm air gap between the sample and the top plate of the capacitor. Information is also given providing the capacitance as a percentage of the simulated perfect sample capacitance.

Table 3.7 gives values for the simulated capacitance of the system and the capacitance as a percentage of the equivalent perfect sample capacitance. The modelled capacitance reduces as sample permittivity decreases as was observed for previous models. More significant is the reduction in capacitance compared to the perfect sample; this ranges from 76% to only 37% of the ideal capacitance being transmitted to the ground plate. This is a large difference compared to the simulated values for an air gap of the same size between the sample and the bottom plate (the worse case value here is 98.5% efficiency for the $\varepsilon_r = 75 - 0j$ sample).

This result can be explained by considering the system as two capacitors in series; the sample is represented by a large capacitor in series with a small capacitor which represents the air gap such that:

$$\frac{1}{C_{total}} = \frac{1}{C_{sample}} + \frac{1}{C_{airgap}} \tag{3.9}$$

where C_{total} is the overall capacitance of the material between the electrodes, C_{sample} is the capacitance due to the high permittivity sample and C_{airgap} is the capacitance due to the air gap between the plates.

When capacitors are connected in series the result is that the total capacitance is reduced compared to the individual largest capacitor which is part of the chain. The capacitance

recorded by the system is reduced, which is most noticeable for high permittivity materials because the difference in permittivities and therefore capacitance of the material is marked.

Conclusions

Simulations were performed with an ideal homogeneous perfectly smooth sample placed between the capacitor plates. A higher permittivity sample results in a higher capacitance as expected due to the higher permittivity meaning the material can store more energy with it.

When a 0.1mm air gap is introduced the capacitance output of the simulation reduces. The amount it decreases by is dependent upon the permittivity of the MUT, with lower permittivity materials being less negatively impacted by the air gap.

The implication from these simulations to the experimental set-up is that any air gaps are indeed significant in contribution to measurement errors. Fortunately the simulation situation here is an extreme case in using a 0.1mm gap. Air gaps on the actual sample will be significantly smaller. It was useful to quantify and confirm that higher permittivity samples are more susceptible to measurement errors resulting from air gaps.

3.7.3 Two-dimensional modelling - imperfect sample: one rough surface

In this model the ideal pellet was 20mm across with a thickness of 4mm. The main body of the sample in the surface roughness simulations is 3.9mm thick, with an additional slice which is 0.1mm thick. This thin region was modified so that there was a random

variation over the 0.1mm which was in contact with the electrode. The other face of the sample had a perfect connection to the capacitor plate. A representative section of the sample geometry is shown in Figure 3.35.

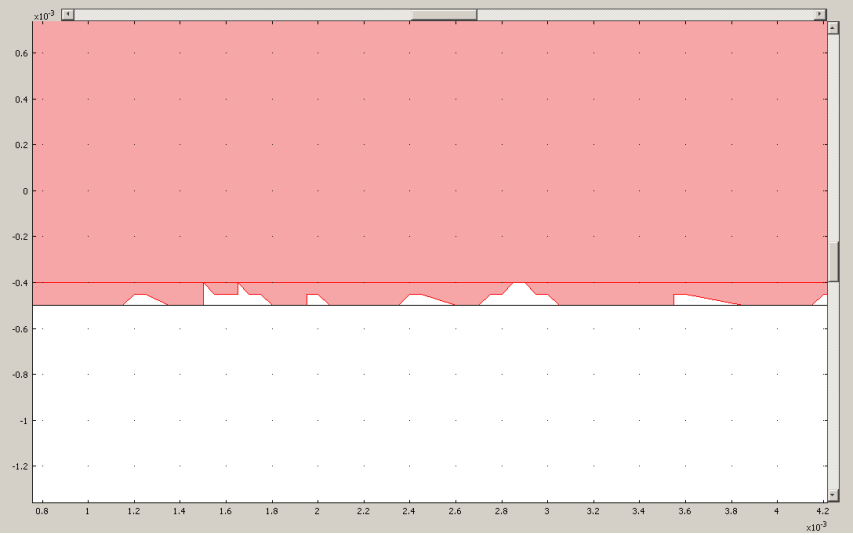

Figure 3.35: Section of model geometry for a sample with one rough surface in contact with the parallel plate capacitor. The random interface varies over 0.1mm.

The rough surface of the sample was established at the interface with the top conducting plate. The sub-domains of the sample were set for a range of permittivities dependent upon the simulation. The values of $\varepsilon_r = 15 - 0j$, $35 - 0j$ and $75 - 0j$ were used for the reasons outlined in the previous section. The area representing the air gaps between the sample and the conducting plate were set to $\varepsilon_r = 1 - 0j$ (ie. that of air). Boundary conditions were established so that the top plate of the capacitor was a port where the energy method input condition was supplied and the bottom plate was set to ground. The areas of the sample which were not in contact with the plates are internal boundaries and thus are handled as continuity conditions by Comsol. The outlying boundaries of the simulation area were set as zero charge/symmetry conditions.

Figure 3.36 shows the simulation results for a sample with permittivity $\varepsilon_r = 75 - 0j$ as it again presents the most extreme results. The fringing fields on the far edges of the

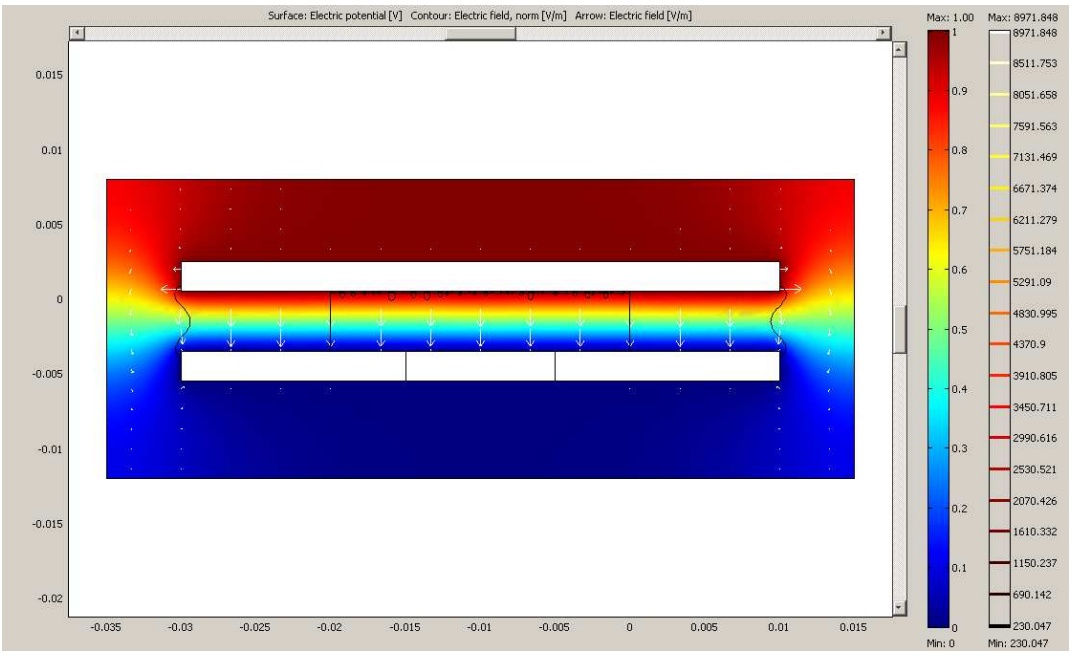

Figure 3.36: Simulation results for a 3.95mm thick sample with $\pm$0.05mm random variation at the interface with the top plate (sample permittivity $\varepsilon_r = 75 - 0j$). Colour gradient shows electric potential, contour shows normalised electric field, arrow plot shows direction of electric field where the size of the arrows is proportional to the electric field strength.

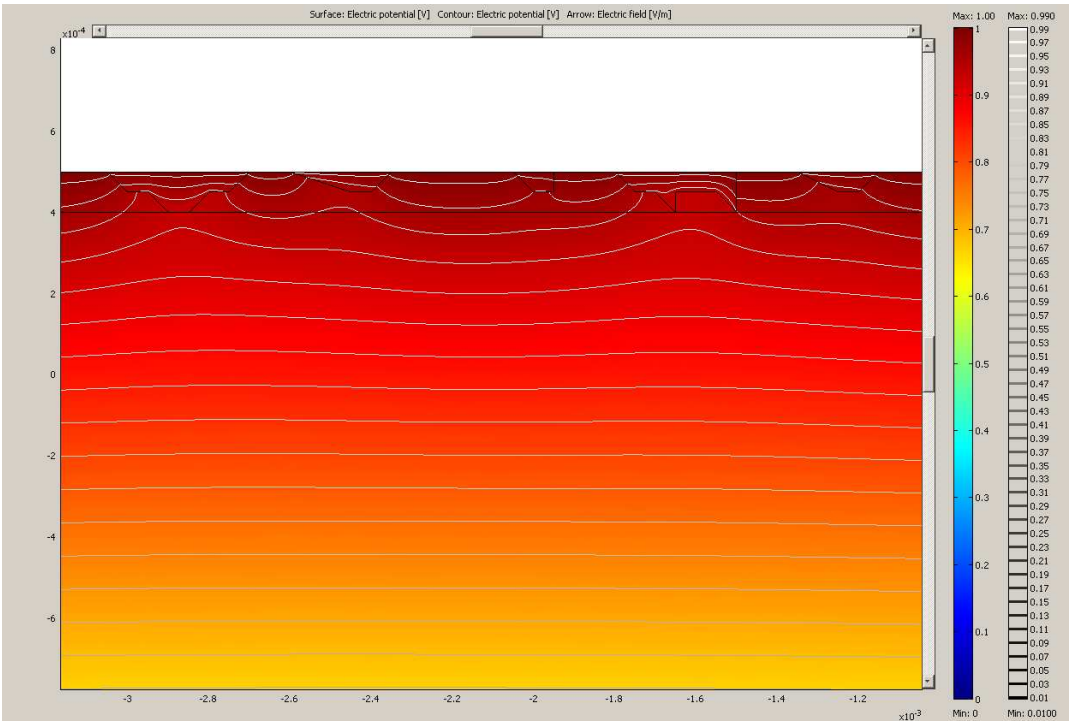

Figure 3.37: Detailed image of simulation results for a 3.95mm thick sample with $\pm$0.05mm random variation at the interface with the top plate (sample permittivity $\varepsilon_r = 75 - 0j$). Colour gradient and contour plot show electric potential, arrow plot (white arrows) shows direction of electric field where the size of the arrows is proportional to the electric field strength.

capacitor are observed and confirmed as being an acceptable distance from the guard ring on the bottom plate so as not to affect the measurement accuracy. The electric potential is mostly uniform across the sample and this is also observed for the other sample permittivity simulations. As before; the region of interest is the interface between the rough surface of the sample and the conducting plate, where the non-uniform electric field can be seen around the interface. Figure 3.37 shows a zoomed-in section of the simulation results.

The image shown in Figure 3.37 shows the changes in the electric potential value caused by the variation in the sample surface (where sample permittivity $\varepsilon_r = 75 - 0j$). In the cases where the sample permittivity is less the electric potential is distorted slightly less around the air gaps.

Table 3.8 gives the simulated capacitance values for the system where different sample permittivities are considered.

Sample permittivity (ε_r)	Capacitance (pF)	% of perfect sample Capacitance
15 - 0j	713	99.0
35 - 0j	1585	98.6
75 - 0j	3329	98.6

Table 3.8: Simulation results for samples of different permittivities with a random variation of air gaps over 0.1mm in contact with the top plate of the capacitor. The bottom interface is perfect. Information is also given providing the capacitance as a percentage of the simulated perfect sample capacitance.

The capacitance of the system is very similar to results for a perfect sample; the air gaps have a very small impact upon the simulated capacitance. This result is expected when we consider the situation for the materials between the plates is now equivalent to capacitors in parallel such that:

$$C_{total} = C_{sample} + C_{airgap} \tag{3.10}$$

where C_{total} is the overall capacitance of the material between the electrodes, C_{sample} is the capacitance due to the high permittivity sample and C_{airgap} is the capacitance due to the air gap between the plates.

The result of this being that the small air gaps have a much lesser impact upon the recorded capacitance of the system than compared to the air gap between the plates which was effectively in series. This confirms the simulation results.

3.7.4 Two-dimensional modelling - imperfect sample - heterogeneous sample

In this model a 4mm sample between two conducting plates was set-up with the modification that the sample contained several randomly placed squares of a different permittivity material, which were either 200μm or 10μm square. Figure 3.38 shows a section of the sample geometry.

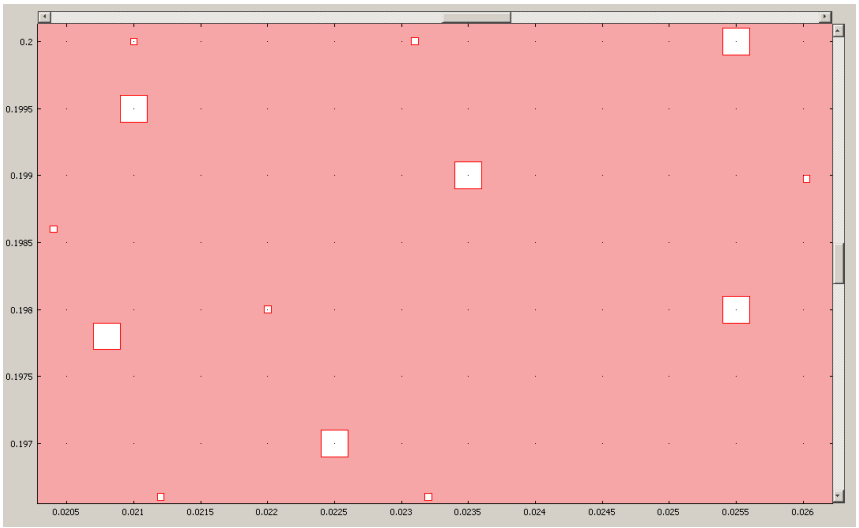

Figure 3.38: Geometry for a heterogeneous sample with air pockets 200μm or 10μm square distributed throughout the sample

The sub-domain settings were established so that the main body of the sample was either

$\varepsilon_r = 15 - 0j$, $35 - 0j$ or $75 - 0j$. The small squares representing the air pockets and the surrounding free space area were set with $\varepsilon_r = 1 - 0j$. The boundary settings were relatively simple; the top conducting plate was set as an input port and excited using the energy method; the bottom plate was set to ground. The outermost edges were set as zero charge/symmetry conditions and the remaining boundaries (including the edges of the air pockets within the sample) were internal continuity conditions.

Figure 3.39 shows the simulation outcome when the main body of the sample is $\varepsilon_r = 75 - 0j$.

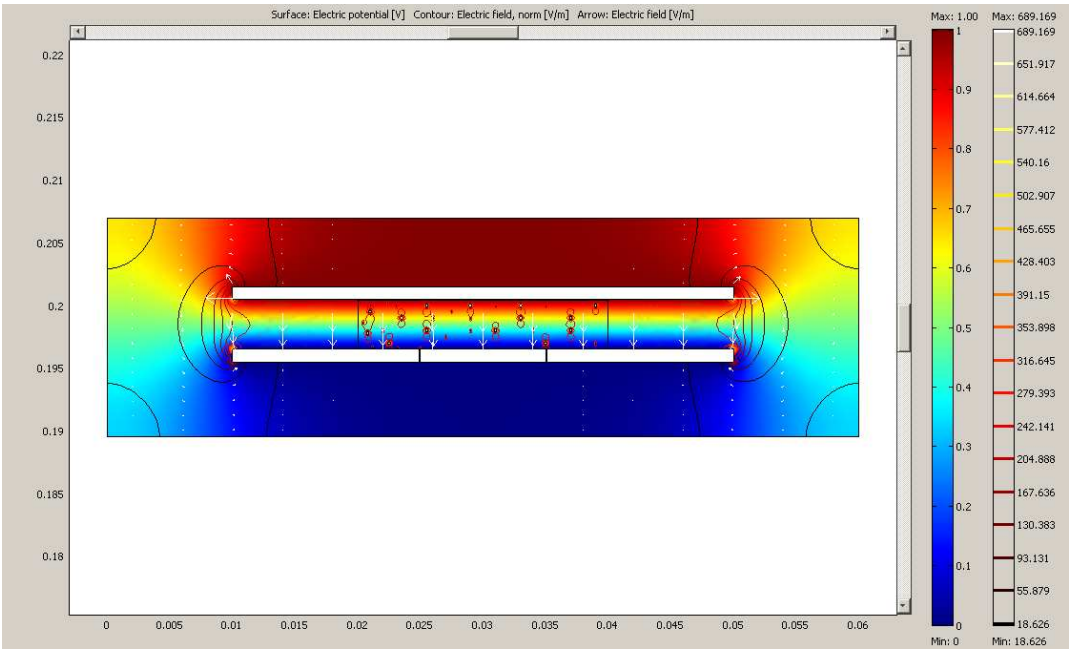

Figure 3.39: Simulation results for a 4.0mm thick sample with air pockets (sample permittivity $\varepsilon_r = 75 - 0j$). Colour gradient shows electric potential, contour shows normalised electric field, white arrow plot shows direction of electric field where the size of the arrows is proportional to the electric field strength.

The electric potential drops approximately approximately uniformly across the sample area with some small variations around the air pockets where distortion is noted. Figure 3.40 shows a closer view of an area with air pockets within the sample. This image is focused around the bottom of the sample, near to the ground plate of the capacitor

which can be seen as the white space in the image. The air pockets within the sample can be clearly seen from the variation in the electric potential shown in the contour plot.

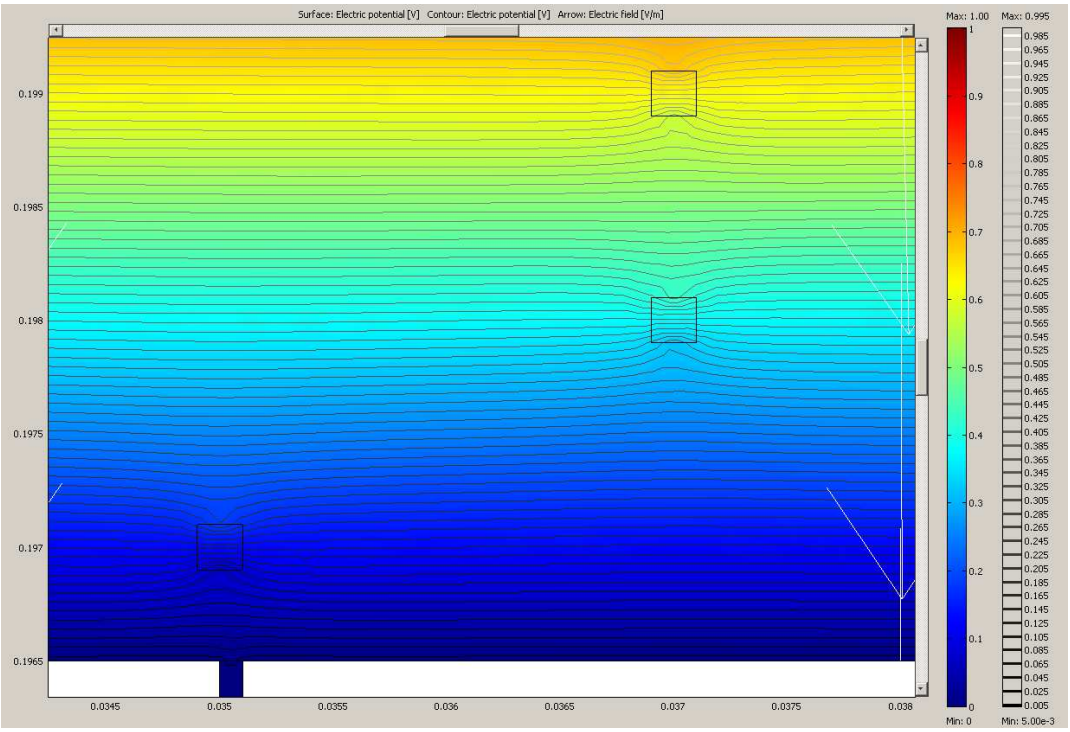

Figure 3.40: Detailed area showing simulation results for a 4.0mm thick sample with air pockets (main sample permittivity $\varepsilon_r = 75 - 0j$). Colour gradient and contour plot show electric potential, white arrow plot shows direction of electric field where the size of the arrows is proportional to the electric field strength.

Sample permittivity (ε_r)	Capacitance (pF)	% of perfect sample Capacitance
15 - 0j	711	98.8
35 - 0j	1583	98.6
75 - 0j	3326	98.5

Table 3.9: Simulation results for samples of different permittivities with small air pockets within the sample body (interfaces at the electrodes are perfect). Information is also given providing the capacitance as a percentage of the simulated perfect sample capacitance.

Table 3.9 shows the simulated capacitances for a model with the same geometry where the permittivity of the main sample body is altered. As expected, the capacitance is larger for the higher permittivity models. These values are close to the capacitances for the ideal equivalent samples, indicating that a sample containing small air gaps does not

have a dramatic effect on the capacitance of the system.

3.7.5 Conclusions

The conclusion which can be drawn from the simulations into surface roughness and air gaps is that samples with rough surfaces or an air gap between the sample and plate will have a lower measured capacitance than a smooth sample. It is further assumed that a sample with a rougher surface (thus having more air gaps between the sample and plate) will have a lower capacitance than a comparatively smoother sample. Heterogeneous or porous samples (those with small air gaps within the sample) have a lower permittivity than a perfect sample, however the capacitance measured in these simulation conditions is still 98% of the perfect material.

The worst case scenario from simulations was produced when a high permittivity sample has a 0.1mm gap between the input electrode and the sample where only 37% of the perfect sample equivalent capacitance was recorded. The significance of this upon the experimental results is that a sample which has a roughness of $\pm$0.05mm does not have a significant effect on the measured capacitance and neither does a sample with small air gaps within it. It is however, reasonable to assume that increasing surface roughness and a more porous sample will reduce the accuracy of measurements because the equations used assume that the sample is perfect.

The cause of the experimentally observed different permittivities for different sides of a sample are most likely to be caused by a combination of the factors. Potential sources of difference which cannot be simulated are:

- distribution of the added bismuth within the pellet;

a heterogeneous distribution could cause one side to have a different permittivity to the other.

- compression effects;

  the action of forming the pellet within the uniaxial press causes distortion to the pellet which means it is not a perfect uniform disk. These include edge effects where the material is more compressed at the edges of the pellet which also means that is is possible that the surface of the pellet is not flat and has a gradient associated with it. This potentially causes a hybrid of the air gap and surface roughness effects investigated by simulation.

- platelet orientation;

  SEM images confirm that the samples are made up of hexagonal platelets with a maximum size of around 10μm, the orientation of these is not controlled. If these are not entirely randomly distributed within the sample (which is a possibility when considering that pellets are subjected to a large compressive force in one direction when pressed) this could have an impact upon the measured capacitance and therefore permittivity of each side.

- location of air gaps;

  A sample may have a concentration of air gaps or be exceptionally rough near to or on the boundary of the guard ring on the bottom electrode. This would have a detrimental effect on the measured capacitance. The effect could be more exaggerated on one face leading to different permittivities.

Of the factors which can be controlled or taken into account; measurement accuracy can be improved by reducing the surface roughness of the pellets as much as possible

and ensuring that any air gaps between the sample and the conducting plates of the capacitor are minimised. Alternatively the faces of the samples could be coated by a thin conductive layer which would reduce the impact of air gaps on the characterisation scheme.

3.8 Chapter conclusions and future work

3.8.1 Conclusions

The concept of permittivity as a frequency dependent value composed of a real part representing energy stored and an imaginary part representing losses was introduced and the underlying mechanisms responsible explained.

A parallel plate capacitor method for calculating the permittivity of a material at low frequencies was presented. In this regime the sample pellet was placed between the electrodes of the capacitor, which was in turn connected to a Wayne Kerr 6440B LCR meter which recorded the capacitance and loss of the system over the test frequency range of 20Hz – 3MHz. This information used in conjunction with a knowledge of the sample thickness and electrode diameter allowed calculation of the real and imaginary parts of permittivity.

The accuracy of the system was improved by the use of a specially designed sample holder cap to locate the sample in the centre of the capacitor electrodes.

Results were presented for the low frequency permittivity of barium hexaferrite and bismuth substituted barium hexaferrite pellets containing varying levels of bismuth which have been subjected to a range of sintering temperatures and durations. The results of

series F which contains six pellets of the same $x = 0.1$, $BaBi_{0.1}Fe_{11.9}O_{19}$ composition which had been subjected to the same sintering conditions of three hours at 1100°C were presented first. This allowed for direct comparison of the permittivity results and ascertain the accuracy of the process. Results for the permittivity ranged from a minimum of $\varepsilon_r = 44.59 - 1.95j$ to a maximum of $\varepsilon_r = 107.34 - 6.95j$ at 1MHz. However this result was more likely to be due to varying levels of formation of the bismuth substituted barium hexaferrite with low bismuth doping levels rather than the fault of the measurement system. This series was also used to investigate the accuracy of the LCR meter; at frequencies above 1MHz the measured capacitance reduces by one decimal place, so a value of a few picofarads would be measured to three decimal places below 1MHz and to only two decimal places above that value.

Samples consistently display their highest real part of permittivity at low frequency, which reduces less rapidly with increasing frequency until the response becomes constant at high frequencies. The imaginary part of permittivity is smallest at low frequencies and increases with frequency, with samples with a higher real part of permittivity also having a larger imaginary part.

Permittivity results for series which contain a range of barium hexaferrite and bismuth substituted barium hexaferrite show that the addition of bismuth consistently increases the permittivity of the material. For samples sintered at 1100°C the highest permittivity sample had a composition of $x = 0.5$ which had been sintered for three hours and had a permittivity of $\varepsilon_r = 75.04 - 6.517j$ at 1MHz. The largest spread of results at this frequency were for the $x = 0.2$ composition pellets, thus the conclusion was drawn that this was due to the $x = 0.2$ being a significant value for bismuth doping as bismuth substitutes into the first $4f_2$ sites but not to saturation.

Samples which have been sintered at 1200°C display different trends for permittivity when differing compositions were compared at 1MHz. Here the highest permittivity sample ($\varepsilon_r = 86.18 - 9.910j$ for the $x = 0.2$ composition sample from series A) was sintered for one hour at 1100°C followed by a further hour at 1200°C. The increase in permittivity for this composition material was attributed to the higher sintering temperature allowing a greater level of formation as more bismuth is able to substitute into the $4f_2$ sites.

Pellets were characterised again over the frequency range 20Hz – 10kHz. These results showed that permittivity values agreed with data taken at higher frequencies but the permittivity was still larger at the lowest range of the test frequency and there was also more variation in the imaginary part.

Samples from series A were re-characterised at very low test frequencies of 20Hz – 1kHz and 20Hz – 100Hz. From this the conclusion was drawn that permittivity results for the real part are only reliable above 50Hz and for the imaginary part above 150Hz.

The permittivity of the sample pellets was found to change dependent on the orientation of the sample in the sample holder. The highest permittivity values were presented because these values were closest to the ideal ones. The potential reasons for this difference were discussed and the conclusion was drawn that it was most likely due to a combination of physical properties such as air gaps and surface roughness effects, and chemical properties such as non uniform reaction which means different areas of the pellet potentially having different degrees of formation. Attempts were made to reduce the surface roughness and allow exposure of both sides of the pellet to a uniform heat. No link was found between surface roughness and different permittivity between faces or between this quantity and density.

Comsol Multiphysics 3.3a was used to model the impact of air gaps and heterogeneous samples on the measurement accuracy of the parallel plate capacitor regime. It was found that samples with a rough surface do have a reduced permittivity however this is only a small effect. The same was found for heterogeneous samples. More significant was the presence of air gaps between the sample and electrode where in the worst case scenario only 37% of the perfect sample capacitance was recorded. The presence of air gaps and other defects have a greater negative impact upon higher permittivity samples.

3.8.2 Future work

Data for low frequency permittivity of the samples could be improved by using a different LCR meter to confirm results and ideally also expand the test frequency range.

Samples placed between the electrodes of the sample holder could be coated with a thin conductive film to reduce the effect of air gaps and surface roughness on the measurement accuracy. This work was not undertaken due to the destructive effect it has on the samples, rendering them unusable for any other purpose afterwards.

3.9 References

[1] J. Daintith, J. Clark, H.M. Clarke, D. Cooper, J. Cullerne, D.E. Edwards, R. Rennie, and D.E. Ward. *Dictionary of Physics*. Oxford University Press, 6th edition, 2009.

[2] G. Johnson. Lossy Capactiors. Online: http://www.eece.ksu.edu/ gjohnson/tcchap3.pdf, Accessed: August 2011.

[3] Agilent Technologies. Basics of measuring the dielectric properties of materials. http://cp.literature.agilent.com/litweb/pdf/5989-2589EN.pdf, 2005.

[4] L. F. Chen, C. K. Ong, C. P. Neo, V. V. Varadan, and V. K. Varadan. Microwave Electronics: Measurement and Materials Characterization. John Wiley and Sons Ltd., 2004.

[5] G. Blaise and D. Treheux. *Dielectric Materials for Electrical Engineering*. John Wiley and Sons Ltd., 2010.

[6] B. Lambert. Dielectric spectroscopy. http://www.psrc.usm.edu/mauritz/dilect.html, Accessed: August 2009.

[7] B R Mollow. Progress in Optics. In E Wolf, editor, *Theory of intensity dependent resonance light scattering and resonance fluorescence*, volume 19. North-Holland, 1981.

[8] University of Cambridge Department of Materials Science & Metallurgy. Polarisation mechanisms of dielectric materials, April 2009.

[9] Agilent Technologies. Solutions for measuring permittivity and permeability with LCR meters and impedance analyzers, 2008.

[10] WayneKerr Electronics. Precision component analyzer 6430B/6440B user manual, 2003. Issue A.

[11] S. Ram. Observation of enhanced dielectric permittivity in Bi^{3+} doped $BaFe_{12}O_{19}$ ferrite. *Journal of Magnetism and Magnetic Materials*, 80:241–245, 1989.

[12] P. Winotai, S. Thongmee, and I.M. Tang. Cation distribution in bismuth-doped M-type barium hexaferrite. *Materials Research Bulletin*, 35:1747–1753, 2000.

[13] P. Patnaik. *Handbook of Inorganic Chemical Compounds*. McGraw-Hill, 2003.

[14] K. Mallick, P Shepherd, and R. Green. Dielectric properties of M-type barium hexferrite prepared by co-precipitation. *Journal of the European Ceramic Society*, 27:2045–2052, 2007.

[15] S. Ram, H. Krishnan, K.N. Rai, and K.A. Narayan. Magnetic and electrical properties of Bi_2O_3 modified $BaFe_{12}O_{19}$ hexagonal ferrite. *Japanese Journal of Applied Physics*, 28(4):604–608, 1989.

Chapter 4

High frequency dielectrics and permittivity

With increasing frequency the permittivity of any dielectric material will change because the dielectric response is delayed by the arrangement of atoms within it (previously discussed in Chapter 3 Section 3.1). At different frequencies the dielectric mechanisms contributing to permittivity will change. An understanding of the underlying mechanisms is vital when analysing dielectric materials and for predicting their response in high frequency applications.

At higher frequencies the dielectric properties of a sample are determined using network analysis techniques. This encompasses a range of methods which can be separated into two groups; broadband and resonant methods. The choice of characterisation set-up will be dependent not only on the desired frequency range and acceptable measurement accuracy but also by the physical form of the material under test.

Resonant methods provide a high accuracy value at a single frequency point. For example

split post resonators are capable of characterising the dielectric properties of films and thin samples at a range of points over the 1 – 20GHz range [1]. Resonant cavities are also capable of characterising dielectric properties of powders or rods over a range of temperatures in conjunction with an adjacent furnace [2].

Broadband methods provide the characterisation of materials over a wide frequency range and operate using reflection and transmission measurements of a sample placed within a suitable characterisation fixture.

4.1 High frequency permittivity measurement: Coaxial probe method

The high frequency coaxial probe regime is a broadband method used to investigate the dielectric properties of a sample which can be implemented in a number of ways. Most commonly the sample under test forms the termination of the line. The specific physical properties of the probe and sample dictate the modelling method for the system. This experimental regime has several advantages [3] [4] [2];

- The non-resonant coaxial probe is a broadband experimental set-up:

  The dielectric properties of the sample under test can be characterised over a wide frequency range (several GHz).

- It is a non-destructive characterisation scheme:

  This is an attractive feature of this method which allows samples to be tested and then used again.

- Provides a suitable environment for testing materials with high loss:

Other methods to characterise the permittivity of materials such as airlines and cavity perturbation are suitable only for materials with low loss. The coaxial probe regime is able to test materials with a high loss because the input signal is effectively absorbed. This means losses are less critical to the system compared to transmission or perturbation characterisation regimes.

4.1.1 Approaches to modelling the open ended coaxial probe

There have been many models developed for simulating the behaviour of an open ended coaxial probe. The most commonly used models are:

- Capacitance model [5][3];
- Antenna model [6];
- Virtual line model [7];
- Rational function model [8];
- Full-wave simulation method [9][10].

Each model has a different basis which makes it suitable to different applications dependent on the probe design and the physical sample properties. For example the virtual line model provides accurate results for the permittivity of high loss materials (such as biological tissue) but is unsuitable for low or lossless materials [11]. The models outlined here will now be presented in turn in more detail.

Capacitance model

The open ended coaxial probe regime is a reflection method where a coaxial line is terminated by a material which must be homogeneous within a volume large enough to appear electrically infinite in size [3]. This means that ideally the thickness of the sample under test will be at least twice that of the outer radius of the probe which can be designed with or without a grounding flange [12]. For illustrative purposes the coaxial probe termination into a sample is shown in Figure 4.1 where the solid arrows represent the electric field distribution. From this representation of the system a lumped circuit model can be developed as shown in Figure 4.2.

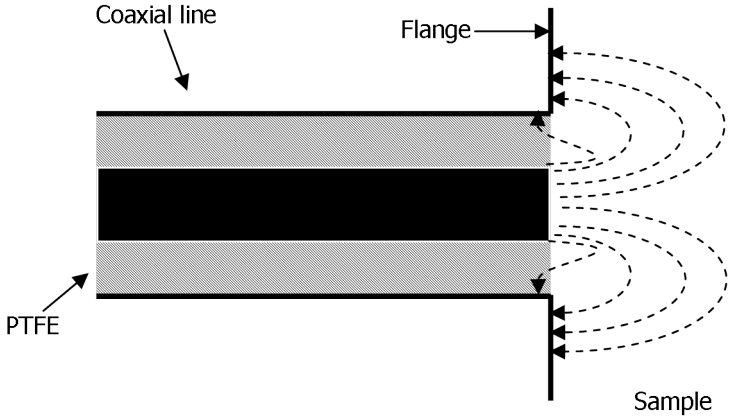

Figure 4.1: Coaxial probe with infinite flange terminated by an infinite sample. Dashed arrows represent the electric field at the termination of the line. Adapted from [13].

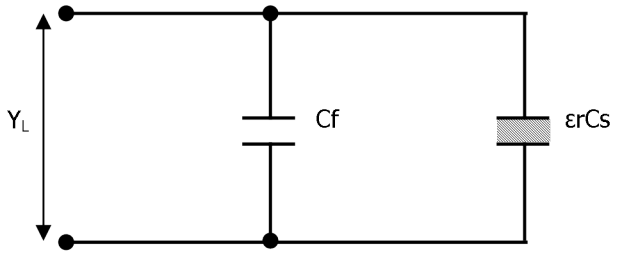

Figure 4.2: Equivalent lumped circuit model for broadband coaxial probe. Y_L is the admittance of the probe termination caused by the fringing fields in the coaxial line (Cf) and εrCs which represents the material under test.

In this representation of the probe Y_L is the lumped admittance for the probe termination.

This is caused by two elements; the capacitance caused by the fringing fields in the coaxial line (in this situation a PTFE filled line) Cf and a lossy capacitor εrCs which models the effect of the sample under investigation [3][13].

This equivalent model is not suitable at high frequencies because the physical dimensions of the coaxial probe are small compared to the wavelength of the radiation at higher frequencies [3]. It is also not suitable because the capacitance of the sample is dependent upon frequency and by assuming a uniform radiation pattern the calculated values will be only approximate. [13][14]. However this model benefits from its simplicity; it requires little computing power to solve and provides acceptable measurements for relatively low loss materials at low frequencies [11].

Initial capacitance models calculated a permittivity value assuming that the line either had an infinite grounding flange or none at all. Okoniewski et al. adapted the model for the coaxial probe using finite-difference time-domain (FDTD) methods to calculate the influence of a grounding flange with a finite radius [15].

Antenna model

This scheme is also referred to as the radiation model, where the probe is considered as a radiation source. This is based upon the assumption that an open ended line immersed in a lossy medium will radiate into that medium, allowing the probe to be treated as a functional antenna [6].

The elements in the model are C_1, $\varepsilon_r C_2$ and G. C_1 is predominantly dependent on the probe parameters and is independent of the material under test. The sample is represented by the capacitor $\varepsilon_r C_2$ in parallel with an admittance G, where G is mainly

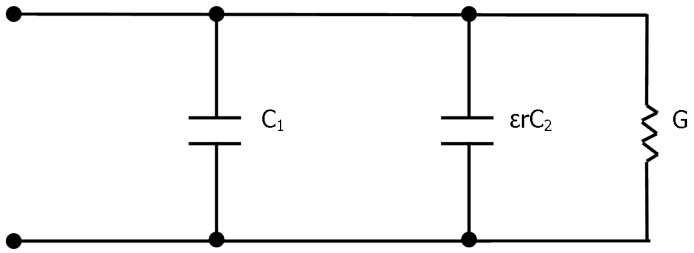

Figure 4.3: Equivalent circuit for Antenna model of open ended coaxial probe. C_1 represents the parameters of the coaxial probe, $\varepsilon_r C_2$ the sample and G relates to the radiation from the end of the probe. Adapted from [16].

related to the radiation from the end of the probe. This model requires calibration by testing the probe system with three reference materials of known dielectric constant [16].

Virtual line model

This approach by Ghannouchi and Bosisio [7] works from the assumption that when the open ended coaxial probe is terminated by a dielectric sample, the fringing field can be modelled as a segment of equivalent transmission line as shown in Figure 4.4.

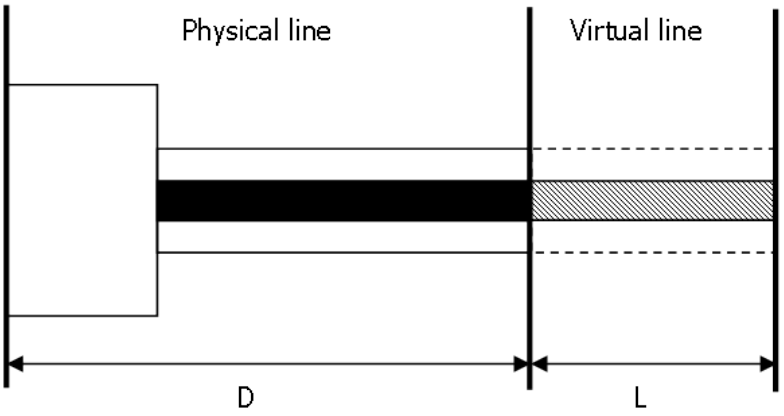

Figure 4.4: Representation of probe and sample as a physical line terminated by a virtual line respectively. Adapted from [16].

The model contains two parts, a physical line with length D and a virtual line section of length L. The complex admittance of the line is related to the characteristic impedance

of the virtual line which can then be used to calculate the dielectric properties of a sample under test when used in conjunction with knowledge of the physical dimensions of the line. This method, like others, requires a calibration through testing two standard media; the most commonly used are air and deionized water. [7][16]

Rational function model

This method is applied to model the dielectric properties of a liquid which the probe is immersed in. The moment method is used to calculate the complex admittance of the line and is most effective when the liquid under test has a real and complex part of permittivity between $1 - 80$ when tested within a frequency range of $1 - 20$ GHz [8] [16] [17].

Full-wave simulation method

In this regime the processing power of modern computers is utilised to conduct a full-wave analysis of a model of the probe. From this it is possible to evaluate the admittance of the sample and then calculate the permittivity. This has the advantage that a large number of probes with different variations can be modelled to a high degree of accuracy. [8][9][10]

4.2 System in use at The University of Nottingham

The experimental set-up in use at Nottingham utilises a HP 8510C Vector Network Analyser (VNA). The S-parameter test set used covers the frequency range 45MHz – 25GHz. Set-up, calibration and measurements are conducted via an interface to a PC.

The connected PC also calculates the real and imaginary parts of permittivity and the loss tangent from the S-parameters taken from the VNA when the calibration and probe parameters have been taken into account [18]. A diagram showing the relevant parts of the system is shown in Figure 4.5.

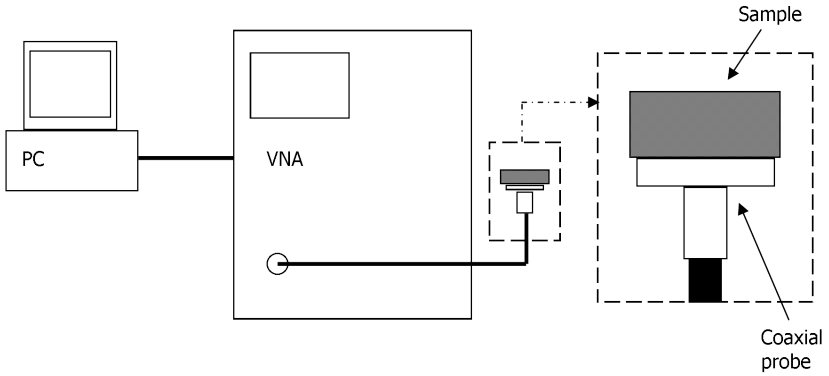

Figure 4.5: Diagram showing the set-up of the high frequency coaxial probe system. The interface between the probe and the sample is shown to a larger scale in the dashed box.

The software on the PC calculates the permittivity and loss of the material under test by utilising a point matching approach, which is a variation of the antenna model considered in Section 4.1. Developed by Grant et al. [13] it refined work undertaken by Mosig et al. [19]. The point matching approach is a numerical solution where the dielectric properties of the material at the termination of the probe are calculated from the reflection coefficient of the fundamental TEM mode and a few higher order $TM_{0,n}$ modes [18] [2]. The forward permittivity to reflection coefficient relationship is relatively straightforward to compute, leading to the derivation of reflection coefficients from a known permittivity material. However the reverse solution from reflection coefficients to permittivity values is a more challenging problem with no direct solution. As a consequence a solution is found using an iterative Newton-Raphson approach. This was tested by Grant et al. with common solvents (deionized water, methanol, ethanol and propan-1-ol) by calculating both the forwards and inverse solutions [13]. When the method was first developed

it required significant computational power compared to other methods outlined in the previous section, however significant accuracy gains were produced.

4.2.1 Measurement procedure

The VNA was powered on for a minimum of an hour before calibration. A one-port calibration was used and is appropriate because the coaxial probe characterisation method uses only S11 reflection data. The calibration procedure is automated by the PC attached to the VNA which prompts the user to attach the appropriate standard. The three standards used were:

- Short;
- Open;
- Load.

If any of the standards do not fall within the threshold standards set within the programme the user is prompted either to repeat the measurement or to accept the standard as it is. Once this process was complete, the calibration data was saved. The cable connecting the probe to the VNA was held stationary using a retort stand and clamp to improve measurement accuracy.

The coaxial probe was orientated vertically so that sample pellets could be placed onto the probe surface. This eliminated some problems associated with ensuring contact between the probe and the sample. Pellets were placed onto the probe and characterised; the real and imaginary parts of permittivity were saved. The pellet was then turned over and the process was repeated, characterising the other side of the sample.

The real and imaginary parts of permittivity and the loss tangent of the sample across the frequency range were recorded on the connected PC and then transferred to another computer for analysis.

4.3 High frequency permittivity results

The following section contains graphs and discussion of the permittivity of the barium hexaferrite and bismuth substituted barium hexaferrite samples over the 45MHz – 25GHz frequency range using the coaxial probe characterisation scheme. Permittivity of standard solvent liquids were characterised and compared to published results.

4.3.1 Permittivity of standard liquids

Before characterising the dielectric properties of the barium hexaferrite samples, the coaxial probe was used to measure the permittivity of four standard liquids; deionized water, isopropanol, acetone and methanol which were then compared to results published in literature [20]. The probe was inverted and immersed in each solvent in turn (dried and cleaned between liquids). By using a transparent beaker the surface of the probe was checked for air bubbles and if present the probe was removed from the solvent and re-immersed. This was important because the presence of air bubbles reduces measurement accuracy in the same way as air gaps with a solid sample [2]. The solvents were characterised over the frequency range 1 – 4GHz to allow comparison with published results and provide a measure of the accuracy of the system.

The results presented in Figure 4.6 show good agreement between the measured values and published data. Greatest agreement was for the real part of permittivity. The

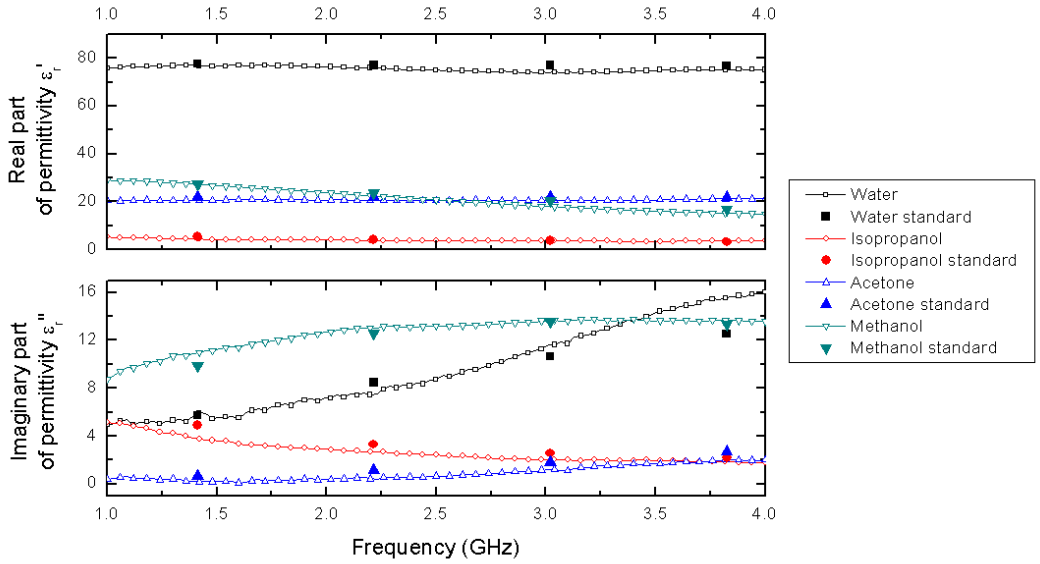

Figure 4.6: Real and imaginary part of permittivity for solvents (deionized water, isopropanol, acetone and methanol) over frequency range 1 – 4GHz. Standard values taken from [20].

imaginary part of permittivity shows more variation with particular note to the values obtained for water at high frequencies. This means that care should be taken when characterising the loss of high permittivity materials as accuracy is lowest for these types of substance.

4.3.2 Permittivity results after sintering at 1100°C

The following section presents data for barium hexaferrite and bismuth substituted barium hexaferrite samples over the frequency range 45MHz – 25GHz taken using the coaxial probe method. For each series the highest value of permittivity for each pellet is presented because this represents the value closest to the idea.

Series F

Results for pellets from series F are presented first. These samples all have the same composition of $x = 0.1$, $BaBi_{0.1}Fe_{11.9}O_{19}$ and have been subjected to the same sintering regime of three hours at 1100°C. The similarity of these pellets allows for direct comparisons to be made and the suitability of the experimental method to be commented upon.

Figure 4.7 shows the permittivity data collected for series F pellets and the results for each sample at 2.45GHz are presented in Table 4.1.

Sample	ε_r'	ε_r''	$tan\delta$
$x = 0.1a$	6.5825	0.97294	0.14781
$x = 0.1b$	8.2768	1.60725	0.19419
$x = 0.1c$	6.0417	0.81695	0.13522
$x = 0.1d$	6.9190	1.06714	0.15423
$x = 0.1e$	7.4969	1.25567	0.16749
$x = 0.1f$	13.4035	4.51339	0.33673

Table 4.1: Table of permittivity values and loss tangents for series F pellets at 2.45GHz

Both the real and imaginary parts of permittivity and also the loss tangent show very similar results for the samples $x = 0.1a, b, c, d$ and e with $x = 0.1f$ an outlying result. The relationship between the loss tangent and the imaginary part of permittivity is clearly seen; both show the same variation with frequency in the graphs. Interestingly the $x = 0.1f$ sample has a markedly higher real and imaginary part of permittivity ($\varepsilon_r = 13.40 - 4.513j$ at 2.45GHz). Normally an outlying result would be expected to have a lower permittivity caused by sample imperfections reducing the value from its ideal equivalent. The reasons for this material having a higher permittivity are unknown and unexpected due to all samples in this series undergoing the same synthesis and sintering process concurrently. At low frequencies (Chapter 3 Section 3.4.1) the results for series F

do not show pellet $x = 0.1f$ as outlying data although it is the second highest permittivity result. This sample does however display the largest imaginary part of permittivity and loss tangent, so there is some correlation between results.

When the $x = 0.1f$ pellet is discarded all other samples fall within the ranges: ε_r' : $6.04 - 8.28$ and ε_r'' : $0.817 - 1.607$. This shows a good degree of repeatability between samples. Also the trace for the permittivity of air remains constant across the frequency range with $\varepsilon_r = 0.96 - 0.016j$. From this it was concluded that measured permittivities may be slightly lower than they actually are, but overall the characterisation scheme is valid.

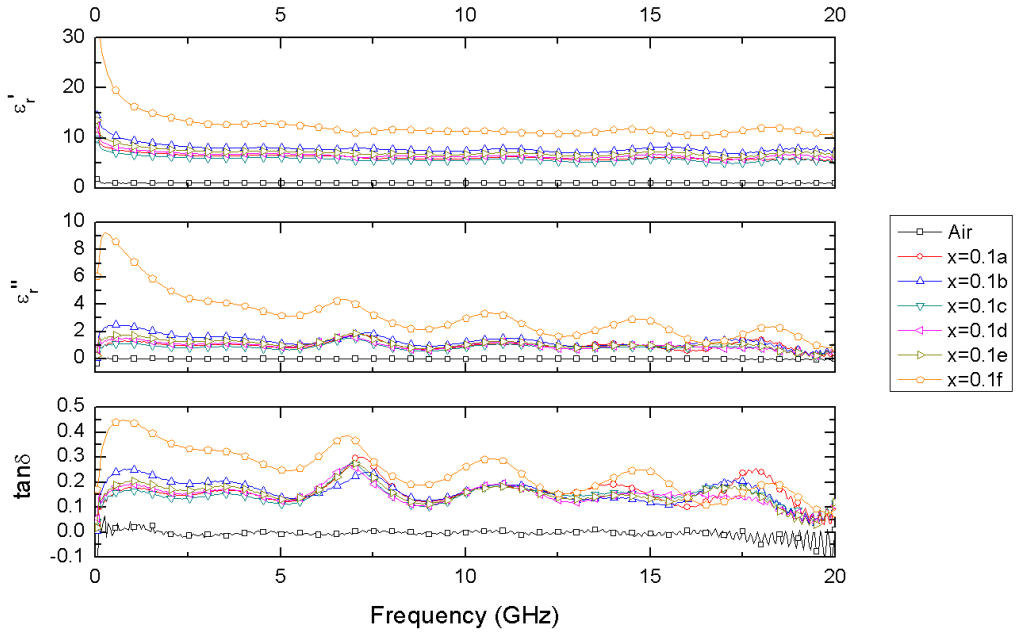

Figure 4.7: Real and imaginary parts of permittivity (ε_r', ε_r'') and loss tangent (tanδ) for series F $BaBi_{0.1}Fe_{11.9}O_{19}$ after sintering for three hours at 1100°C

Series A

There are no results for Series A at 1100°C because these samples had been further sintered at 1200°C when high frequency measurements were taken.

Series B

After sintering for one hour at 1100°C, samples in series B displayed a range of values for the real part of permittivity, between $\varepsilon_r' = 6 - 9$ at low frequencies up to 6GHz. The imaginary part of permittivity is also constant and similar over this frequency range for all samples; $\varepsilon_r'' = 0 - 2$. The highest permittivity sample is $x = 1.0$ ($BaFe_{11}BiO_{19}$) with $\varepsilon_r = 8.54 - 0.89j$ at 2.45GHz. At frequencies above 6GHz the permittivity measurements begin to oscillate due to reflections from the back surface of the pellet (detailed later in this section). The unsubstituted barium hexaferrite sample ($x = 0.0$) shows larger magnitude variations in the graphs for both the real and imaginary part of permittivity. The permittivity for air is shown for reference; the value of $\varepsilon_r = 0.934 - 0.094j$ at 2.45GHz is slightly lower than the expected value for air where $\varepsilon_r = 1 - 0j$, however the recorded value is sensible when experimental error is considered.

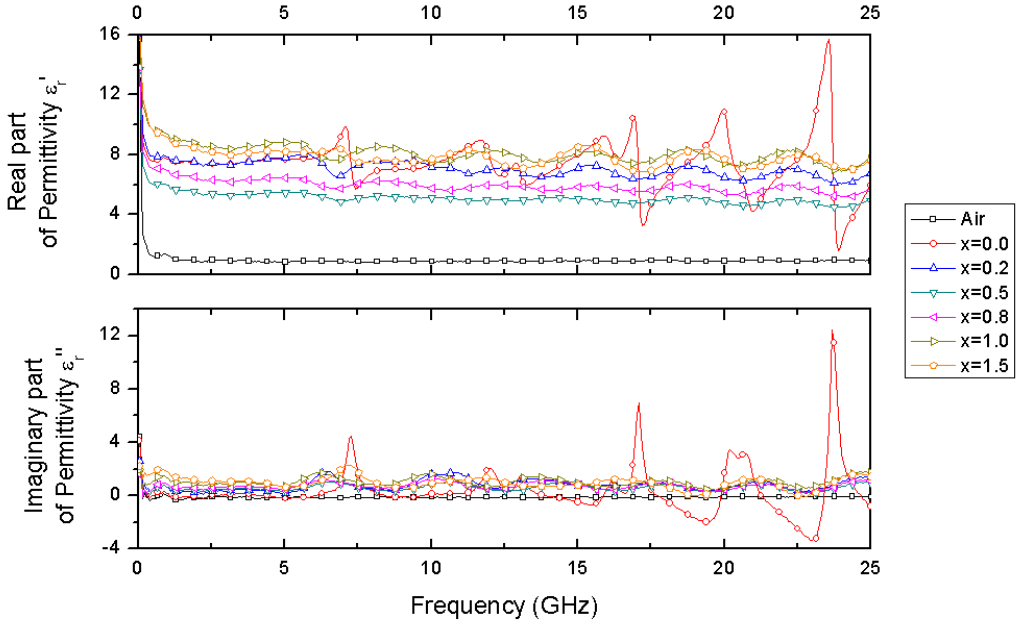

Figure 4.8: Real and imaginary part of permittivity for series B $BaBi_xFe_{12-x}O_{19}$ after sintering for one hour at 1100°C. Oscillations for sample $x = 0.0$ is caused by back reflections.

Series C

Series C contains samples which have been sintered for one hour at 1100°C. Figure 4.9 shows the highest permittivity recorded for each sample composition.

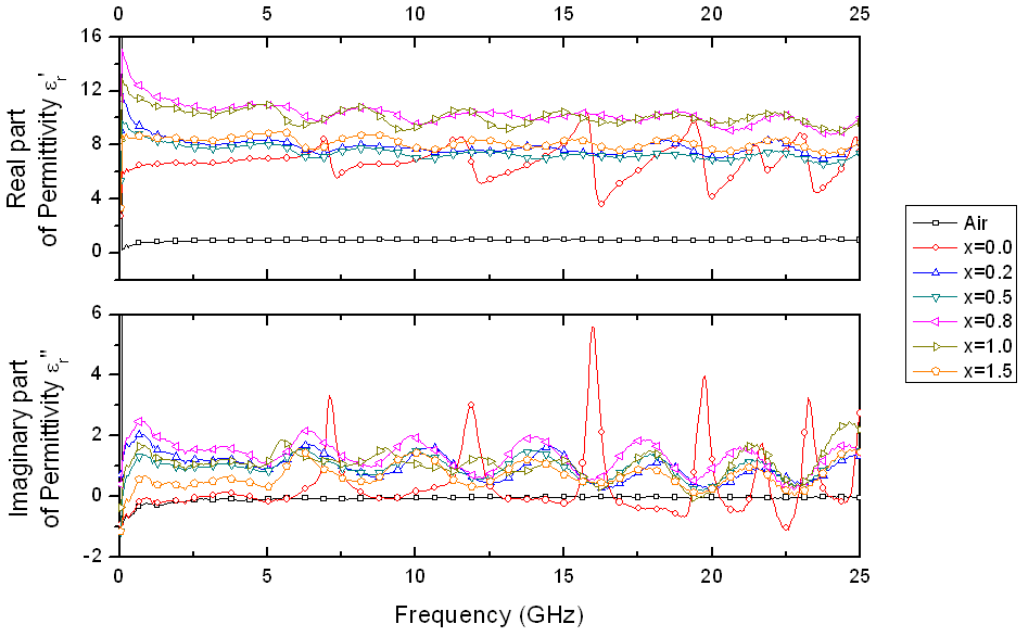

Figure 4.9: Real and imaginary part of permittivity for series C $BaBi_xFe_{12-x}O_{19}$ after sintering for one hour at 1100°C. Oscillations for sample $x = 0.0$ is caused by back reflections.

At 2.45GHz sample $x = 0.8$ ($BaBi_{0.8}Fe_{11.2}O_{19}$) has the highest permittivity of $\varepsilon_r = 10.84 - 1.55j$, closely followed by sample $x = 1.0$ where $\varepsilon_r = 10.45 - 1.05j$. The lowest permittivity sample is the undoped barium hexaferrite sample with $\varepsilon_r = 6.63 - 0.06j$. The permittivity values are all slightly higher than those recorded for series B pellets, which have been subject to the same sintering regime. The variation in the permittivity graphs is larger than that seen for series B, however the $x = 0.0$ sample still shows the greatest change of all the samples.

Series D

Series D permittivity results are show in Figure 4.10. The values for the real part of permittivity are centred about a higher value than the previous series (centred at $\varepsilon_r' = 10$ rather than 8). The compositions $x = 0.2$, 0.5 and 1.5 all have a higher permittivity than those compositions sintered for a shorter duration. The permittivity of the $x = 1.5$ sample is especially high with $\varepsilon_r = 14.69 - 1.66j$ at 2.45GHz, compared to the lowest permittivity of the unsubstituted barium hexaferrite where $\varepsilon_r = 7.10 - 0.06j$ at the same frequency. Another interesting feature of this result set is the resonances caused by the reflections from the back surface of the pellet are not as large at the lower frequency ranges than other series.

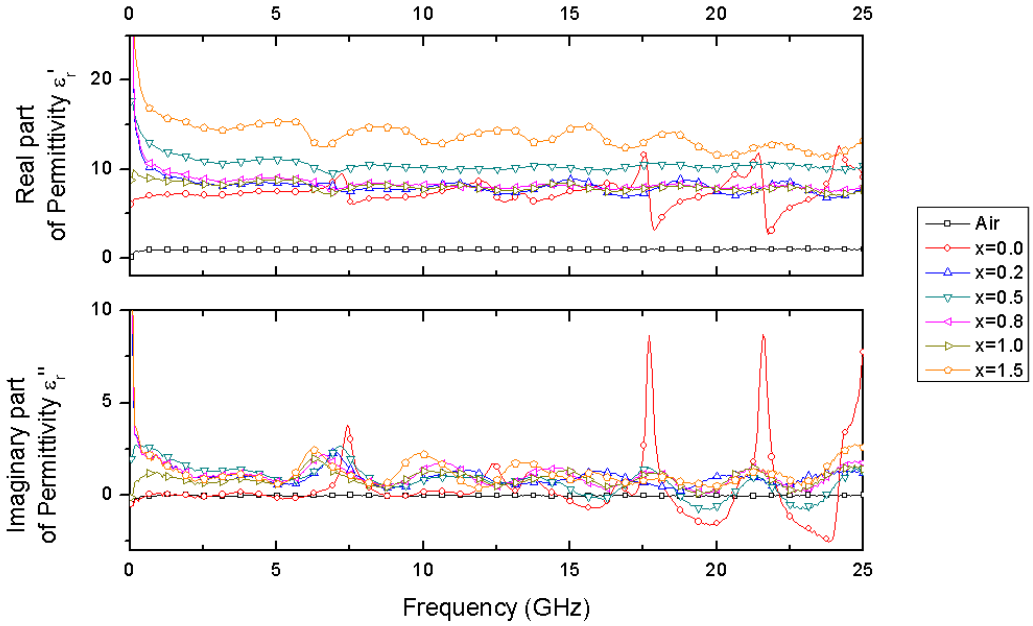

Figure 4.10: Real and imaginary part of permittivity for Series D $BaBi_xFe_{12-x}O_{19}$ after sintering for three hours at 1100°C. Oscillations for sample $x = 0.0$ is caused by back reflections.

4.3.3 Permittivity results at 1100°C as a function of substitution level

This section presents the real and imaginary parts of permittivity and the loss tangent for series B, C and D which have been sintered for either one or three hours at 1100°C at a constant frequency of 2.45GHz. This allows the permittivities of different compositions and sintering regimes to be directly compared. The frequency of 2.45GHz was selected for a number of reasons; this frequency is within the stable region for permittivity results, allowing more accurate comparisons; 2.45GHz is also an important frequency for the potential antenna applications of the material. This is the operating frequency of wi-fi and Bluetooth making characterisation of the permittivity at this frequency vital so device properties and behaviour can be predicted.

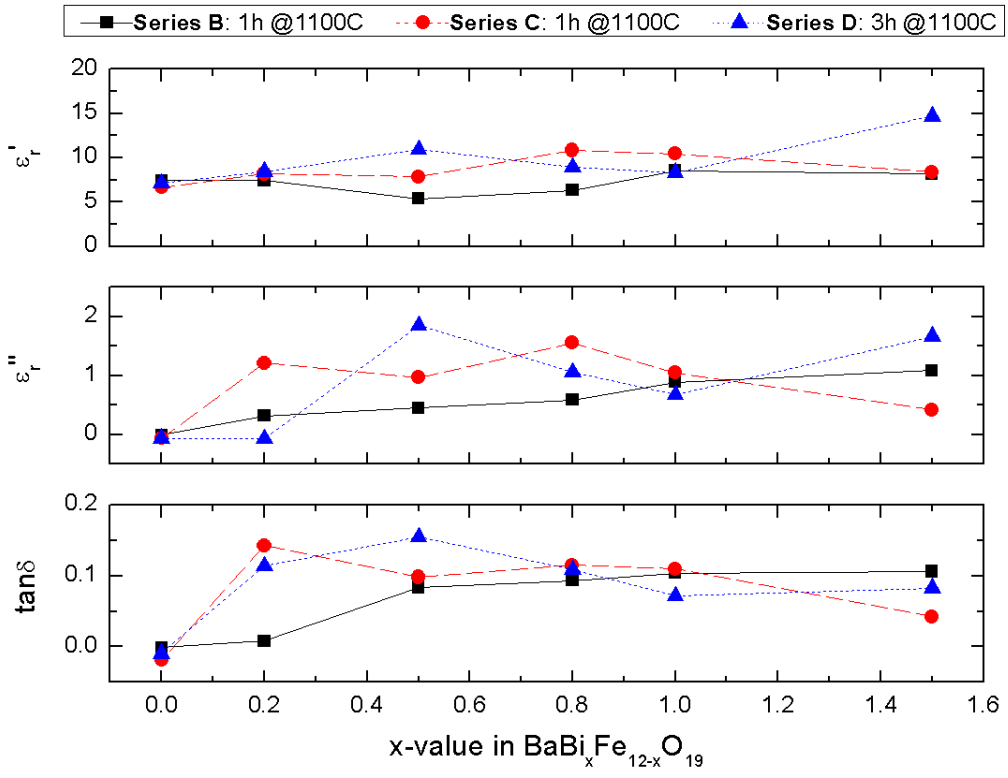

Figure 4.11: Real and imaginary part of permittivity (ε_r', ε_r'') and loss tangent (tanδ) for series B, C and D $BaBi_xFe_{12-x}O_{19}$ after sintering for one or three hours at 1100°C at 2.45GHz.

Figure 4.11 shows the comparison of the samples from the three sintering regimes where

the sample composition is plotted against permittivity at 2.45GHz. All sintering regimes show similar values for the undoped barium hexaferrite samples where permittivity varies from ε_r' : $6.63 - 7.39$ and ε_r'' : -0.059 to -0.008. The loss of a dielectric material should not be negative (this indicates gain) so the conclusion was drawn that this is most likely due to a calibration error when small values of loss are recorded. When bismuth is added the permittivity values diverge and different trends appear. For the lowest level of added bismuth at $x = 0.2$ the real and imaginary parts of permittivity remain similar with the series D pellet having interestingly the highest real part of permittivity and the lowest imaginary part where $\varepsilon_r = 8.46 + 0.065j$. The loss is so small that it becomes positive due to lack of measurement resolution close to zero values. This means that the material has a relatively large real part of permittivity with negligible loss.

When the bismuth content is increased to $x = 0.5$ the permittivity of samples diverge with the lowest value from series B ($\varepsilon_r = 5.39 - 0.451j$) and the highest is series D ($\varepsilon_r = 10.95 - 1.852j$). The series C sample value falls in the centre of these two values. After this the series B and C samples display more similar results at first, both increasing at the $x = 0.8$ point. At the $x = 1.0$ sample value the real part of permittivity begins to converge before finally at $x = 1.5$ the values for ε_r' are 8.17 and 8.37 for series B and C respectively. The imaginary part of permittivity follows the trends of the real part with the exception of the final $x = 1.5$ point where despite very similar real parts the imaginary parts vary significantly more with ε_r'' values of 1.080 and 0.417 for series B and C in turn. This indicates that the series C pellet has a much lower loss.

The trends for series D where pellets have been sintered for three hours rather than one vary from the other sets. The real part of permittivity first increases as bismuth content increases up to $x = 0.5$. After this the permittivity decreases (but remains higher than

the unsubstituted barium hexaferrite sample) before a sharp increase to the maximum permittivity of $\varepsilon_r = 14.69 - 1.664j$ for the $x = 1.5$ sample.

At the high test frequencies observed here there are few reported results with which to compare the bismuth substituted barium hexaferrite compound. However for use within a dielectric resonator antenna a real part of permittivity of between 6 – 100 is acceptable with ideally as low loss as possible [21]. The synthesised material reaches these requirements with a real part of permittivity within this range and losses of a maximum of 0.15.

The observed values for both the real and imaginary parts of permittivity are a lot lower at higher frequencies. This is expected, when moving into the microwave frequency range ionic relaxation no longer dominates the dielectric response resulting in lower permittivity values (see Chapter 3 Section 3.1 for more information on the frequency dependence of permittivity).

The overall permittivity trends for the series vary from the low frequency data presented in Chapter 3 Section 3.4.3. Both data sets present the most similar values between series for the undoped barium hexaferrite samples. The trends for the $x = 0.2$ and 0.5 samples also agree with the low frequency measurements. After this point the trends diverge. The reasons for this are unclear, the combination of higher bismuth concentration and high test frequency creates the highest permittivity of $\varepsilon_r = 14.69 - 1.664j$ at 2.45GHz for the series D $x = 1.5$ sample which has been sintered for three hours at 1100°C. One possible reason for the divergence in measurements compared to low frequency results which was considered is related to the measurement regime at high frequencies. The coaxial probe is by nature, a reflection technique thus the surface in contact with the

probe is of great importance. The measurement will be dominated by the material at the contact surface of the pellet and less influenced by the bulk of the sample. This could potentially lead to differing results in comparison to the low frequency measurements however it is difficult to ascertain how likely this is.

4.3.4 Permittivity results after sintering at 1200°C

Series A

Figure 4.12 shows the results for high frequency permittivity testing of samples from series A, which have been sintered for one hour at 1100°C followed by a further hour at 1200°C.

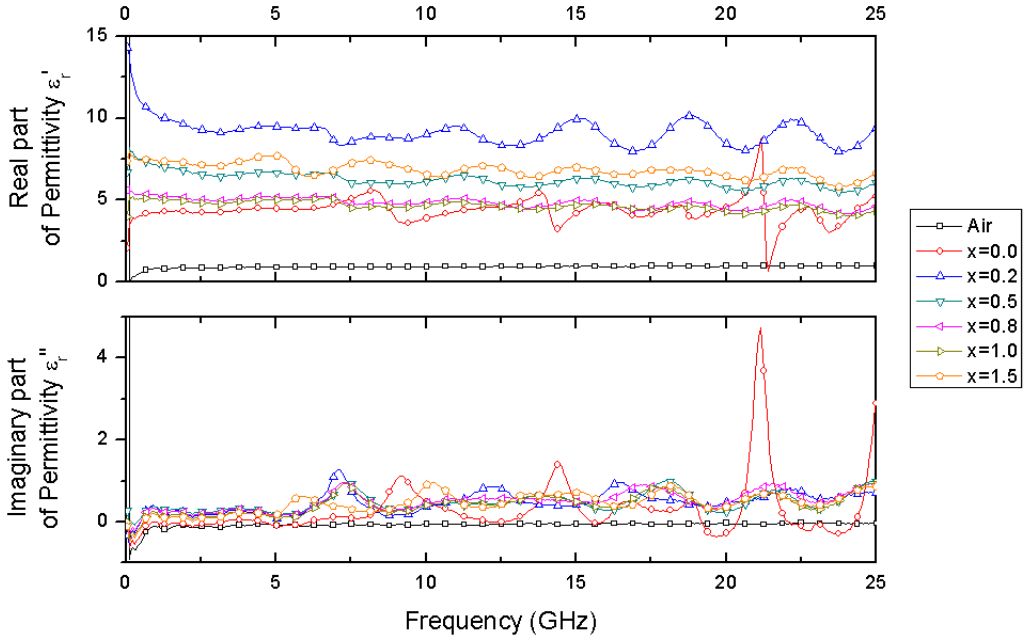

Figure 4.12: Real and imaginary part of permittivity for series A $BaBi_xFe_{12-x}O_{19}$ after sintering for one hour at 1100°C followed by a further hour at 1200°C. Oscillations for sample $x = 0.0$ is caused by back reflections.

The undoped barium hexaferrite ($x = 0.0$) sample has the lowest permittivity ($\varepsilon_r =$

$4.26 - 0.048j$ at 2.45GHz) and sample $x = 0.2$ has the largest permittivity ($\varepsilon_r = 9.31 - 1.30j$ at 2.45GHz). The undoped sample shows the largest variations in permittivity at frequencies higher than 5GHz, caused by reflections from the back of the sample. The highest permittivity ($x = 0.2$) sample has the largest variations of the doped materials. The reasons for the magnitude of the reflections being larger for these two samples are different. The pure barium hexaferrite sample has large reflections because it has the lowest loss; thus the strength of the reflections are significant in the results. The $x = 0.2$ highest permittivity sample displays large magnitude reflections for a different reason; the larger relative permittivity of the sample means that reflections within the sample when displayed as permittivity results are proportionally larger and so are more visible in Figure 4.12. It is also observed that the pattern of the variation in the graph at high frequencies is comparable across all the bismuth composition samples.

Series PS

Pellets from series PS were used to provide another set of results for comparison since these have been sintered for one hour at 1100°C followed by a further hour at 1200°C. However only samples with composition $x = 0.5$, 0.8 and 1.5 were of acceptable quality for characterisation. The results are shown in Figure 4.13.

The graph shows that both the real and imaginary parts of permittivity are similar for each composition. The largest at 2.45GHz is the $x = 0.5$ composition where $\varepsilon_r = 11.38 - 2.702j$, followed by the $x = 0.8$ composition where $\varepsilon_r = 10.74 - 2.117j$ and finally the $x = 1.5$ pellet where $\varepsilon_r = 10.07 - 1.342j$. The trends of the graphs are similar to those of other series, however the traces show variation at a lower frequency of around 3GHz. The data for the air trace is flat and is as expected.

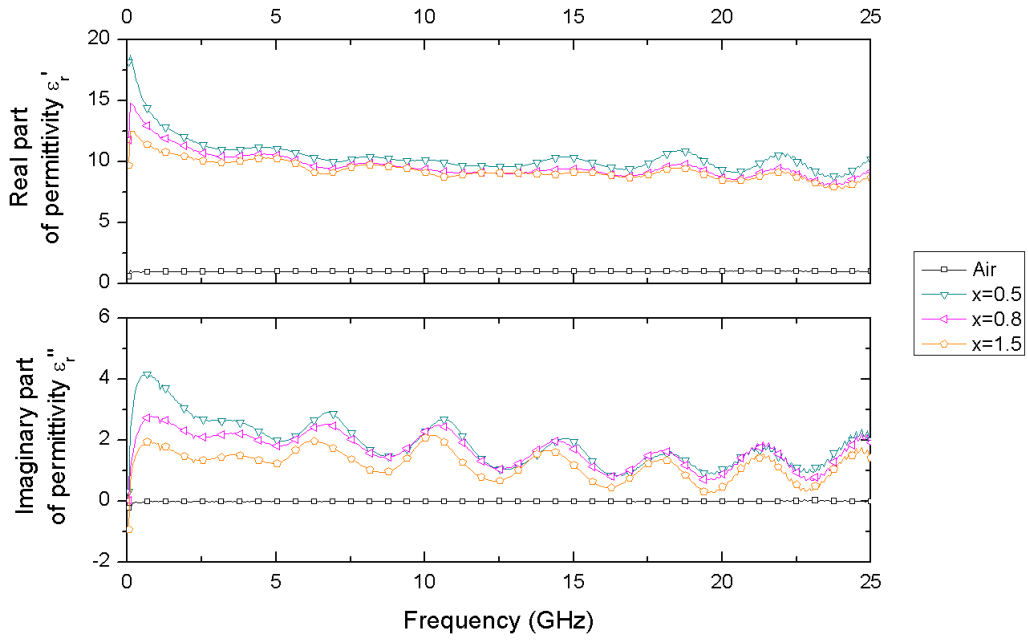

Figure 4.13: Real and imaginary part of permittivity for series PS $BaBi_xFe_{12-x}O_{19}$ after sintering for one hour at 1100°C followed by a further hour at 1200°C.

Series E

Series E is composed of samples which have been sintered for three hours at 1200°C. Figure 4.14 shows the measured permittivity for these samples over the frequency range 45MHz – 25GHz.

An increase in the undoped barium hexaferrite permittivity is observed, compared to the shorter sintering time, to a value of $\varepsilon_r = 8.46 - 1.02j$ at 2.45GHz. However, larger magnitude reflection are also visible for this sample compared with other sintering regimes for the material. The highest permittivity sample is $x = 0.8$ by a considerable margin where $\varepsilon_r = 11.81-$ at 2.45GHz.

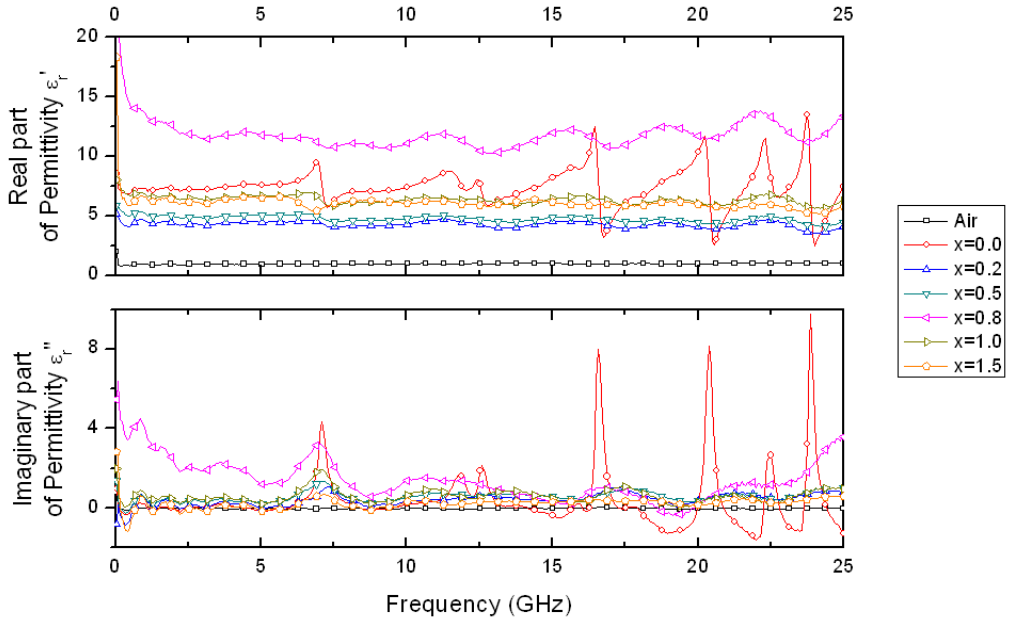

Figure 4.14: Real and imaginary part of permittivity for series E $BaBi_xFe_{12-x}O_{19}$ after sintering for three hours at 1200°C. Oscillations for sample $x = 0.0$ is caused by back reflections.

4.3.5 Permittivity results at 1200°C as a function of substitution level

This section presents the real and imaginary parts of permittivity and loss tangents for series A and PS which have been sintered for one hour at 1100°C followed by a further hour at 1200°C and series E which has been sintered for three hours at 1200°C at a constant frequency of 2.45GHz. This allows the permittivities of different compositions and sintering regimes to be directly compared, however only three pellets from series PS were of acceptable physical quality for characterisation.

The both parts of permittivity and the loss tangents follow the same trend for each series. Pellets from series A show that by adding bismuth the permittivity of the material increases. The maximum permittivity value here is acheived with the $x = 0.2$ sample where $\varepsilon_r = 9.31 - 1.303j$. From this point the permittivity decreases steadily before again increasing slightly for the final $x = 1.5$ sample.

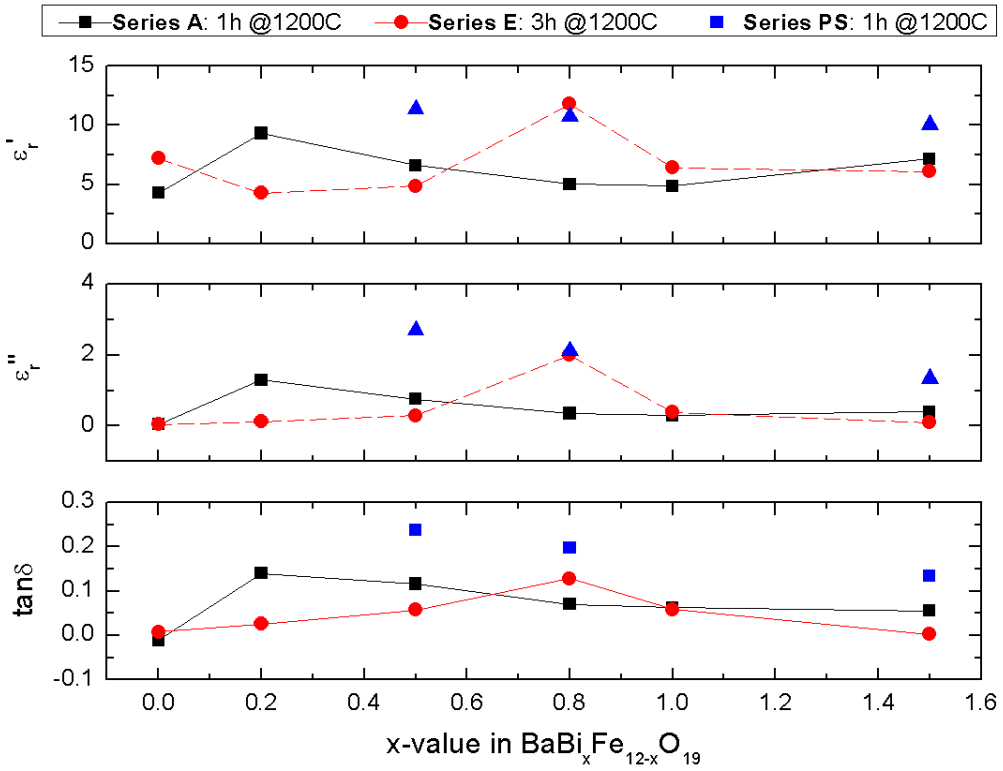

Figure 4.15: Real and imaginary part of permittivity (ε_r', ε_r'') and loss tangent (tanδ) for Series A, PS and E $BaBi_xFe_{12-x}O_{19}$ which have a maximum sintering temperature of 1200°C

For the series E samples there is a noticeable increase in the permittivity of the undoped barium hexaferrite sample to $\varepsilon_r = 7.18 - 0.039j$ most likely due to a greater level of formation of the compound with the longer sintering duration. With added bismuth the permittivity of the material initially drops to a minimum of $\varepsilon_r = 4.27 - 0.126j$ for $x = 0.2$. Permittivity then increases slightly for the $x = 0.5$ sample before a large increase to the recorded maximum of $\varepsilon_r = 11.81 - 1.995j$ for the $x = 0.8$ sample. This is followed by a steep drop in permittivity for the $x = 1.0$ point and then a more gradual decrease for the final $x = 1.5$ sample.

Surviving samples from series PS fall within the range of the other samples. The $x = 0.5$ sample has the highest permittivity of these where $\varepsilon_r = 11.38 - 2.702j$, the $x = 0.8$ sample falls between the series A and E values while the $x = 1.5$ sample again has a large permittivity.

The series A pellets do share some similarities with the low permittivity results detailed in Chapter 3 Section 3.4.5. The undoped sample displays low permittivity steeply climbing to a maximum for the $x = 0.2$ sample and then decreasing again. For series E the higher permittivity for the unsubstituted barium hexaferrite was also observed at low frequency, however this value was still lower than the bismuth containing material. At 2.45GHz the undoped sample has a higher real part of permittivity than all samples with the exception of the $x = 0.5$ composition.

The measured value of the losses of the materials are in-line with results for those at the lower sintering temperature of 1100°C; being relatively low with respect to the high real part of permittivity. This confirms the suitability of the material for high frequency applications.

The range of permittivity values are smaller for high frequency measurements than for the low frequency measurements. This could in part be due to to relaxation frequency of the undoped material being higher than the bismuth containing material. However this is difficult to investigate because there is a gap in the frequency response data from 3MHz up to 45MHz (the top limit of the LCR meter and the bottom of the VNA). This would be an interesting area for further study.

4.4 Sample thickness considerations

The coaxial probe characterisation method used requires a sample to have a smooth surface and also to appear infinitely deep to the probe. The minimum thickness required is dependent upon the frequency of operation. Fan et al. [22] found that ideally the sample thickness should be larger than the diameter of the outer conductor of the probe, however at lower frequencies errors were not large for samples with a thickness approximately the same as the probe outer diameter. The probe used in these measurements has an outer conductor diameter of 2.5mm with a flange of diameter 15.5mm. The implication of this is since sample thickness varies over the range 3 – 6mm measurements can be taken with a reasonable anticipated level of accuracy.

The permittivity of the sample also affects the minimum thickness for a sample. This is because the measurement system measures the reflection from the sample back into the line. Lower permittivity materials display a greater change in reflection coefficient with small changes in permittivity; consequently the measurement is more sensitive to variations in permittivity [23]. Because different permittivities have an effect on the reflection coefficient, this should be considered when the minimum sample depth is

calculated.

4.4.1 Experimental investigation of sample thickness

A simple method to discover if a sample is sufficiently thick to achieve reliable measurements is to place a shorting block behind the pellet and see if this alters the measured permittivity [23]. Figure 4.16 shows the result of this measurement using two different sample compositions. The top graph shows a low permittivity $x = 0.0$ sample both with and without the metallic shorting block in place, while the bottom graph shows the same measurement for a higher permittivity $x = 0.5$ sample.

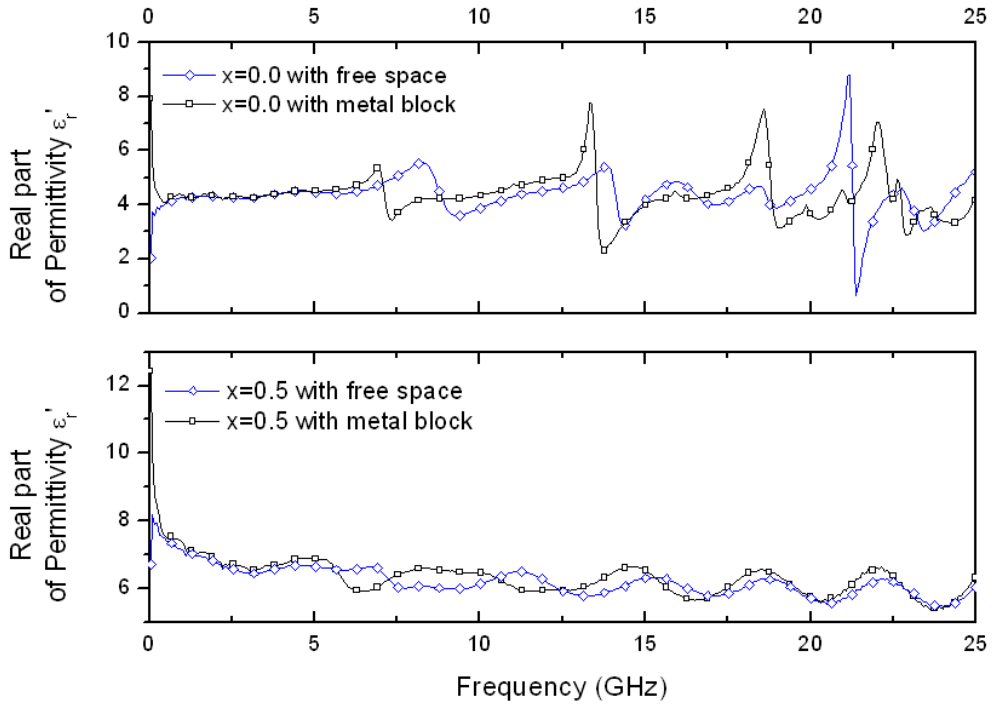

Figure 4.16: Graph showing the different effect on the measured permittivity (real part) for two samples when backed by air or a metal block ($x = 0.0$ sample thickness 3.4mm, $x = 0.5$ sample thickness 4.1mm)

Figure 4.16 shows that the measured permittivity of the sample is constant until 6GHz and then begins to show less desirable trends where there is a great deal of variation in

the permittivity graphs. The undoped barium hexaferrite pellet (top panel of Figure 4.16, $x = 0.0$) is 3.4mm thick and the bismuth substituted pellet (bottom panel of Figure 4.16, $x = 0.5$) is 4.1mm thick.

If the sample appears infinite to the probe then there should be no difference to the graph when the sample is backed by air or backed by a metal block. From the experimental results it can be concluded that the samples are sufficiently thick at low frequencies up to approximately 6GHz. This is consistent with the results from the formulaic approach. At frequencies higher than 6GHz the trace shows variations in permittivity which are shifted to lower frequencies when the sample is backed with a metal block, indicating that there is interference from a reflected signal via the far surface of the pellet. The high frequency data is still of interest however, because any large differences in permittivity would still be noticeable.

For all the different sintering regimes, it remains apparent that the undoped barium hexaferrite exhibits more extreme behaviour when examining permittivity trends. This can be explained as follows;

- A material which has lower loss is required to have a greater thickness because a signal will propagate with less attenuation through it, meaning that a stronger reflection from the back surface of the pellet is measured.

The permittivities of the bismuth substituted compounds are not significantly different from the undoped barium hexaferrite at the these frequencies, so if the main reflection mechanism was dominated by the real part of permittivity the other samples would show a similar magnitude change. It was also found in Chapter 3 Section 3.4 (where low frequency permittivity results were presented) and Section 4.3 from this chapter, that

the loss of the undoped barium hexaferrite is much lower than that of the bismuth substituted materials. From this the conclusion is drawn that the low loss is significant in the reflections observed in the permittivity graphs.

4.5 Modelling in Comsol Multiphysics to investigate sample properties upon high frequency measurements

This section provides simulation results for the magnetic and electric fields and S-parameter data for a variety of sample permittivities, permeabilities and thicknesses. This investigation was conducted to discover the limits of the measurement frequency for different types of samples due to the change of more than one sample property across a series. The coaxial probe and associated software used in the experimental system assume that the material under test has no magnetic properties which is not the case for barium hexaferrite and bismuth substituted barium hexaferrite. Simulation work was undertaken to understand the effect that this would have upon the high frequency characterisation.

Using the RF Module in Comsol Multiphysics (In-Plane waves, Hybrid mode) the interaction between the coaxial probe and the sample was modelled. This mode allows frequency to be set as a dependent variable within the system and the S-parameters to be plotted against frequency after the simulation is complete.

The axial symmetry of the system was exploited to allow more accurate simulation results without the processing overheads associated with a full three-dimensional model. The sample chosen to model was the $x = 0.5b$, series C pellet, which had been sintered for

one hour at 1100°C and has a diameter of 20mm and a thickness of 5.737mm. The low frequency (20Hz) permittivity of this sample was characterised as $\varepsilon_r = 75 - 1.20j$ (Chapter 3 Section 3.4). At high frequency the measured permittivity is lower; $\varepsilon_r = 7.8 - 0.96j$ at 2.45GHz. Both these values are used within the simulation to investigate the effect of sample permittivity of the maximum measurable frequency of the system.

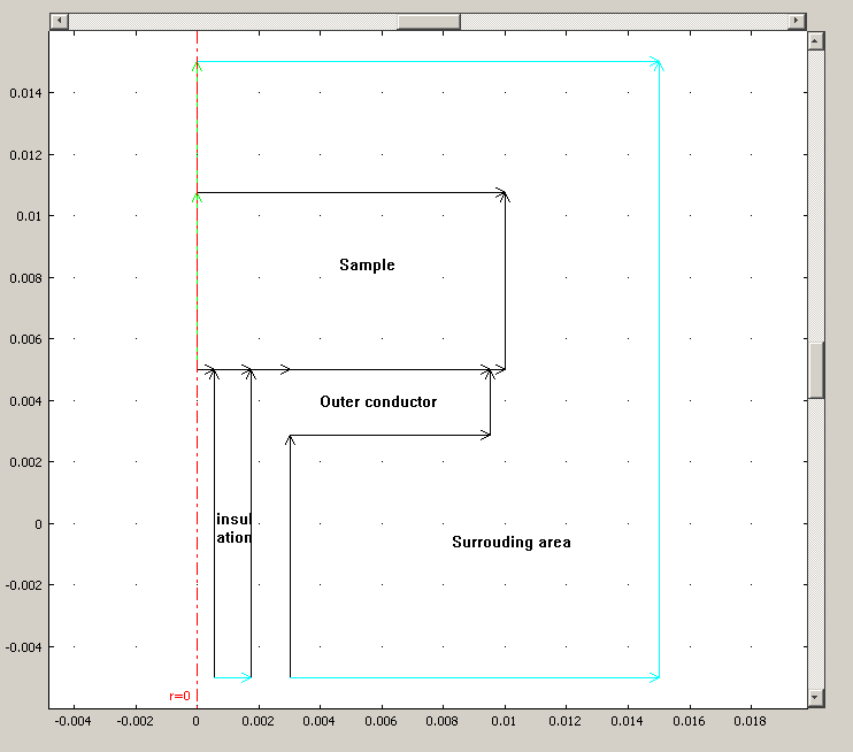

Figure 4.17: Model geometry and boundary conditions for coaxial probe simulation with model parts labelled.

The model geometry was established to simulate the experimental system as closely as possible by passing through the axial symmetry point of the probe and the sample as show in the insert of Figure 4.5. Figure 4.17 shows the geometry and boundary conditions. The red dashed line on the left of the figure indicates the axial symmetry plane of the model which passes through the centre of the sample and the inner conductor of the coaxial line of the probe. The PTFE insulation in the centre of the line and the outer conductor are labelled along with the sample at the termination of the probe. The area around

the probe and sample is included to investigate the electric field in the immediate area surrounding the probe and sample. The coaxial line is composed of an inner conductor (radius 0.5385mm), insulation (radius 1.2115mm) and outer conductor (radius 1.25mm). In addition to this the outer conductor terminates the line via a grounding flange, which brings the total outer conductor radius at the end of the line to 7.75mm. The end of the probe has a flange diameter of 15.5mm; slightly smaller than the diameter of the sample as observed in the model image.

Boundary conditions were established such that the cross section across the insulator was set as an input port with coaxial wave excitation (light blue line at the end of the PTFE insulation in Figure 4.17). The edges of the inner and outer conductors were set as perfect electric conductors (black lines), the edges of the surrounding area of the model were set as scattering boundary conditions and the edges of the sample in the model were established as continuity conditions and thus were handled automatically by Comsol.

The subdomain settings contained three areas; the sample, the insulation in the coaxial line and the surrounding area. The sample subdomain was varied dependent on the sample parameter under investigation; initially the sample was established to have a permittivity of $\varepsilon_r = 7.8 - 0j$ and a permeability of $\mu_r = 1 - 0j$. The insulator within the coaxial line was set with a permittivity of $\varepsilon_r' = 2.2 - 0j$ [24] and the surrounding area, representing free space around the experimental set-up was set as $\varepsilon_r = 1 - 0j$.

4.5.1 Effect of varying sample permittivity

The initial model of the system used the sample thickness of 5.737mm and the permittivity of the sample was altered. Figures 4.18 and 4.19 show the electric field distribution and strength at 25GHz for a sample with a permittivity of $\varepsilon_r = 7.8 - 0j$ and $\varepsilon_r = 75 - 0j$ respectively. These images show that the electric field strength is highest within the coaxial line and in the area where the line terminates into the sample as expected.

The most noticeable feature observed in Figures 4.18 and 4.19 is the distribution of the electric field over the simulation area. For the higher permittivity sample, the greatest concentration of contour lines (representing electric field strength) is contained within the sample under test at the termination of the coaxial probe and in the area which backs the sample. This is consistent with the dielectric properties of the material; a higher real part of permittivity indicates that a material is more able to store electrical energy, hence the greater concentration of the electric field within the sample.

The situation observed for the lower permittivity material shown in Figure 4.18 shows a significant number of electric field contour lines propagating into the surrounding area around the sample and the probe. The strength of the electric field is still greatest within the coaxial line and the area of the sample at its termination, however because the material has a lower permittivity ($\varepsilon_r = 7.8 - 0j$) it does not contain the electrical energy from the probe as effectively. The lower permittivity results in a much lower impedance mismatch for a signal passing through the sample material and on to the surrounding area, presenting the field patterns shown. A final point to note is that the electric field strength outside of the sample is weak, the contour lines are indicative of small magnitude variations in the field. When this data was presented as a filled plot,

the variation of the electric field was difficult to discern.

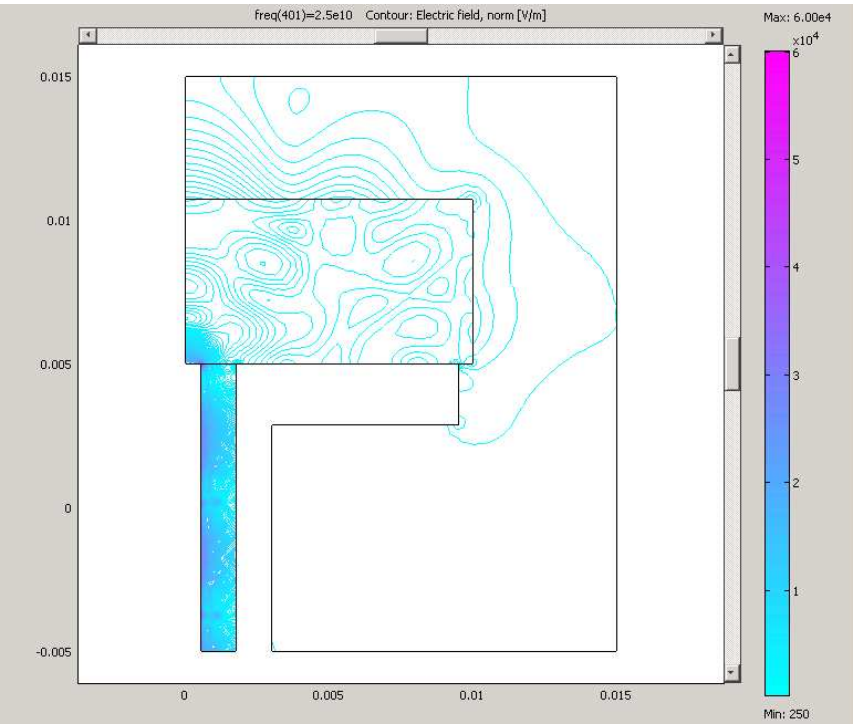

Figure 4.18: Sample permittivity $\varepsilon_r = 7.8 - 0j$. Contour plot shows electric field strength at 25GHz.

The S-parameters for the system can be displayed as either the scalar value S11, or in log form as decibels (dB). The S11(dB) data and the corresponding frequency point for each simulation were exported as a text file, which was then imported into OriginLab 7.0 for analysis. Figure 4.20 shows the S11 parameters from the samples with differing permittivity detailed above.

The S11 responses for the two altered permittivity samples show a markedly different response across the frequency range. For the lower permittivity sample (bottom graph) there are large areas of the response where there is no resonance (compared to the higher permittivity situation) and the S11 graph is flat. Not only does resonance occur more often for the higher permittivity sample, but the first resonance occurs at a lower frequency. This can be explained by considering that resonance occurs at frequencies

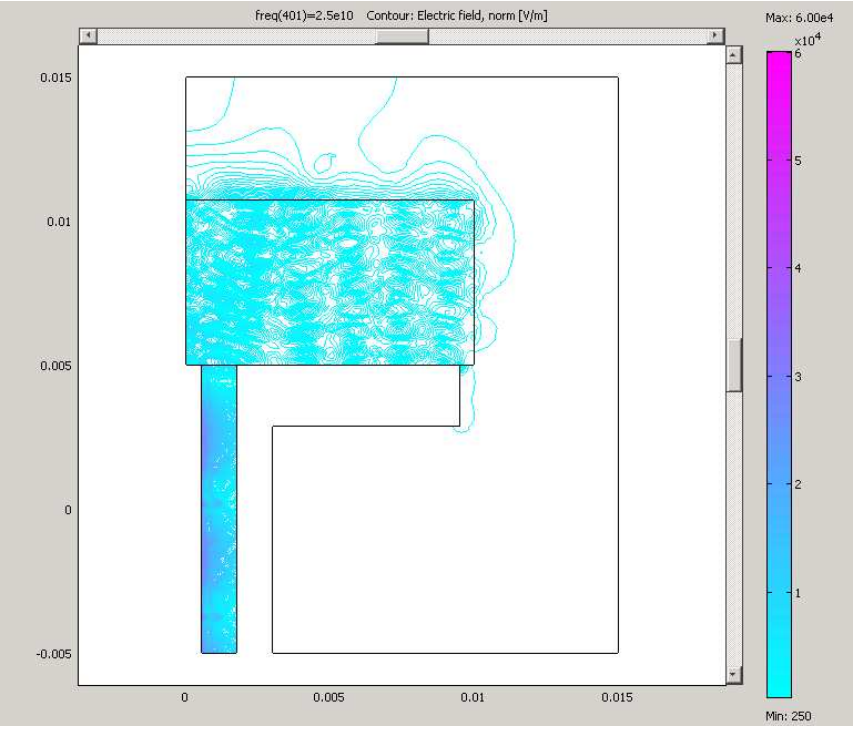

Figure 4.19: Sample permittivity $\varepsilon_r = 75 - 0j$. Contour plot shows electric field strength at 25GHz.

which are multiples of half wavelengths and the varying permittivity of the material between the two simulations. In the situation where there are two materials; one with a higher real part of permittivity (denoted ε'_{r1}) and the second with a lower value (denoted ε'_{r2}), both which are greater than the permittivity of a vacuum. The wave velocity of an electromagnetic wave as it passes through the material will be reduced to a greater extent for the material with higher permittivity, ε'_{r1} than for the lower permittivity material ε'_{r2}. This results in a smaller relative wavelength inside the sample material than would be the case if that wave was propagating in free space (indeed the greater the permittivity of the material, the shorter this relative wavelength becomes) this allows more resonances, which satisfy the multiple of $\lambda/2$ rule, to be set up within the material which is otherwise identical.

At higher frequencies, in the resonance region of the simulation data, the maximum mag-

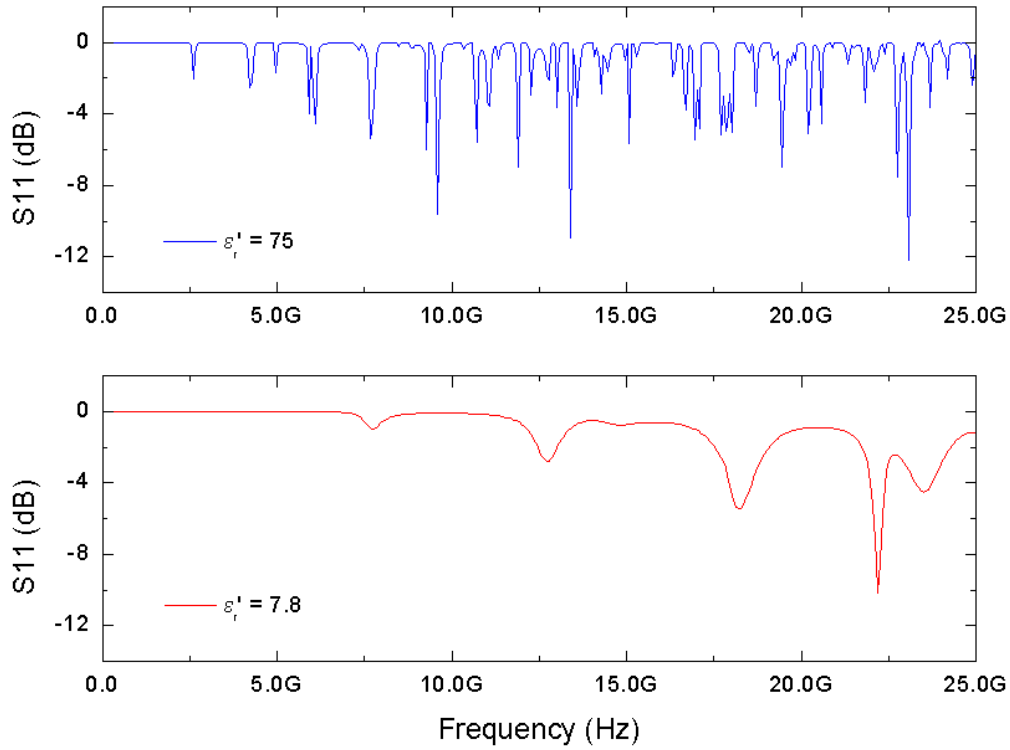

Figure 4.20: S11 response verses frequency (45MHz – 25GHz) for sample permittivity $\varepsilon_r = 7.8 - 0j$ (top graph) and $\varepsilon_r = 75 - 0j$ (bottom graph).

nitude of the reflections are similar for both samples; implying this is dominated by the physical depth of the sample, rather than dielectric properties. The effect where a higher permittivity sample causes more and lower frequency resonances in the S11 parameters was not observed in experimental permittivity results. This is somewhat misleading as the methods do not provide directly comparable variables; S11 and formatted permittivity are not linked by a simple linear relationship. Additionally the Comsol modelling package has no facility for taking account of the imaginary part of permittivity or permeability of a sample; thus the materials are all assumed to be perfect with no losses. In reality the imaginary components of these properties do have an impact upon the responses of the material. The experimental results (Section 4.3) show that undoped barium hexaferrite has larger magnitude reflections; this is due to the material having the lowest loss of all

the samples. As a result this material is best represented by the simulations conducted and a greater variation in permittivity which corresponds to a lower loss and a greater number of resonances was observed.

4.5.2 Effect of varying sample permeability

Barium hexaferrite is a material which has some magnetic properties in combination with the dielectric ones as a result of its iron content. In previous simulation work, the assumption has been made that sample permeability (μ_r) was equal to unity. This simplified the simulation conditions and also reflected that the software used in conjunction with the high frequency coaxial probe assumes that the material under test has no magnetic properties.

The subdomain settings of the model were altered such that the sample permeability is now not equal to unity, but two ($\mu_r = 2 - 0j$). The two varying sample permittivities $\varepsilon_r = 7.8 - 0j$ and $75 - 0j$ used above were utilised again. Figure 4.21 shows the low permittivity sample and Figure 4.22 shows the higher permittivity sample, both with the new permeability of $\mu_r = 2 - 0j$.

The low permittivity sample (Figure 4.21) shows a distinct change in the electric field distribution within the sample; the electric field patterns are more concentrated within the material under test. The surrounding area around the probe and the sample shows a very similar electric field distribution only with more concentrated contour lines around the local maxima and minima. The magnetic field associated with the system is a lot more noticeable and stronger; in previous simulations where $\mu_r' = 1$ it was negligible and concentrated within the coaxial line. Both the electric and magnetic field distributions

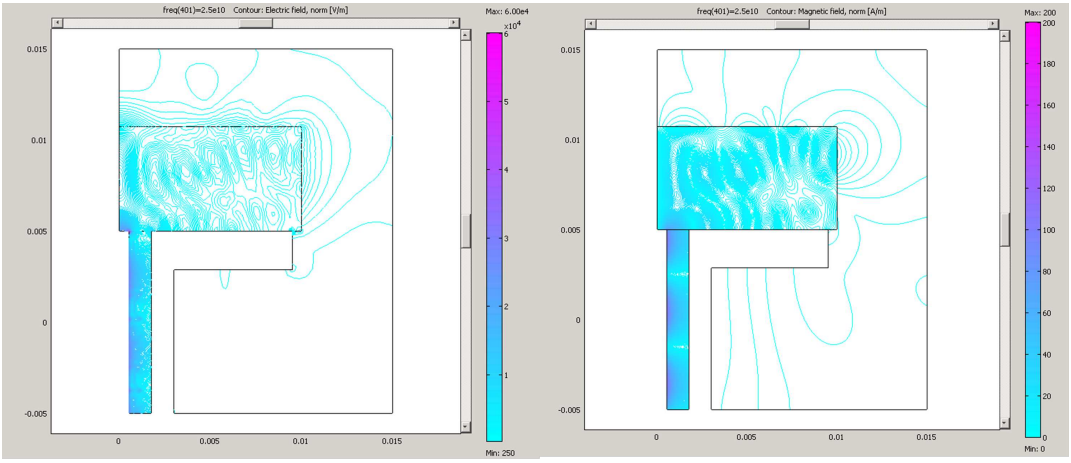

Figure 4.21: Sample permittivity $\varepsilon_r = 7.8 - 0j$, sample permeability $\mu_r = 2 - 0j$. Contour plot on left shows electric field strength and plot on right shows the magnetic field strength at 25GHz.

are reminiscent of the field patterns observed in common magnets.

The greater concentration of electric and magnetic field lines within the sample body for a higher permeability material is reminiscent of the effects observed for higher permittivity materials. This result is as expected when the speed of light within a material is considered; the velocity of an electromagnetic wave in a medium is given by [25]:

$$v = \frac{c}{\sqrt{\varepsilon_r \mu_r}} \tag{4.1}$$

where v is the speed of light in a medium (ms^{-1}), c is the speed of light in a vacuum ($2.99792458 \times 10^8 \text{ms}^{-1}$ [26]), ε_r is the permittivity of the medium and μ_r is the permeability of the medium.

Thus for a material with a higher permittivity or permeability the speed of the wave within the sample will be slowed by a greater amount. This is observed by the greater concentration of electrical and magnetic field lines within the sample presented in simulation

results.

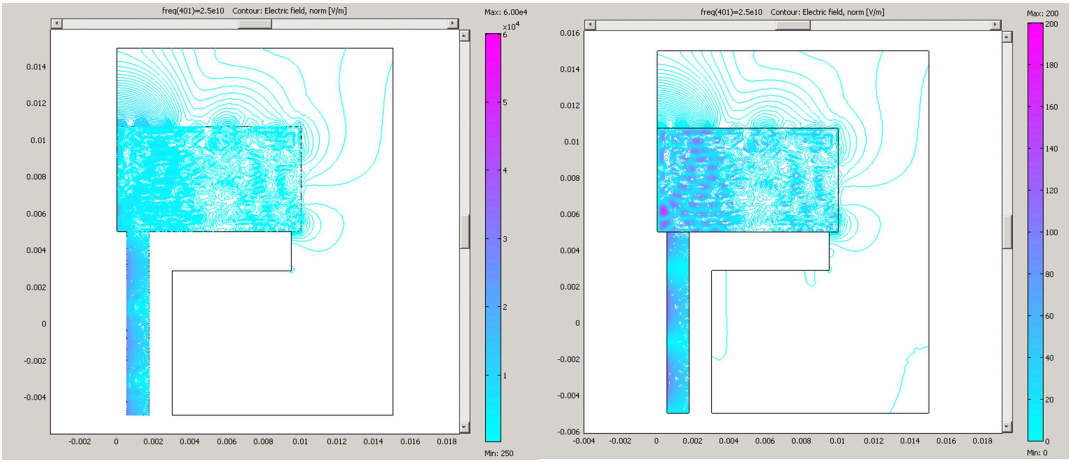

Figure 4.22: Sample permittivity $\varepsilon_r = 75 - 0j$, sample permeability $\mu_r = 2 - 0j$. Contour plot on left shows electric field strength and plot on right shows the magnetic field strength at 25GHz.

Figure 4.22 where the higher permittivity material is combined with a permeability of $\mu_r' = 2$ shows a similar result to the non-magnetic simulation with the majority of the electric field variation contained within the material under test and the coaxial line. There is a larger variation in electric field within the surrounding area, but this is still small compared with the field strength within the line and the sample.

To provide an insight into the effect of adding a magnetic element to the material under test; S11 parameters for the low permittivity sample ($\varepsilon_r = 7.8 - 0j$) are shown for when permeability is set to either $\mu_r' = 1$ or 2, as seen in Figure 4.23.

The overall trends observed remain constant for the two materials; at low frequencies the response is flat before entering the resonance region at higher frequencies, which increase in magnitude with frequency. The higher permeability material (top graph) displays a greater degree of resonance than the lower permeability material (bottom graph). The mechanism for this can be considered in a similar way to the effect on the S11 parameters when the permittivity of a sample is altered; when an electromagnetic wave propagates

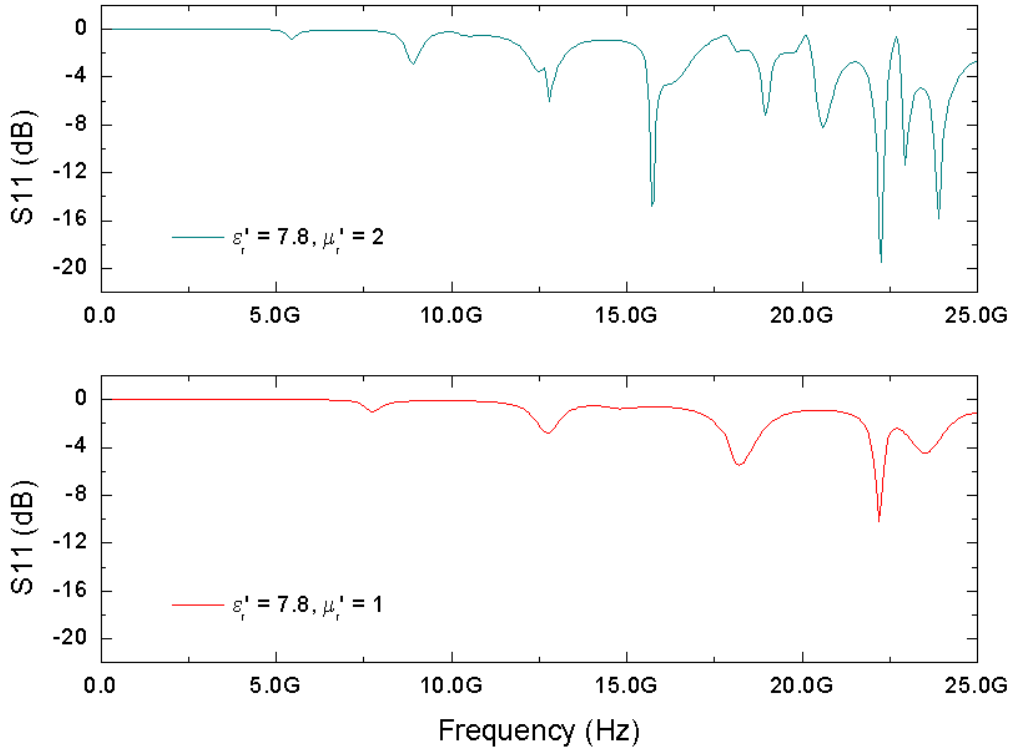

Figure 4.23: S11 response verses frequency (45MHz – 25GHz) for sample permeability $\mu_r = 1 - 0j$ (top graph) and permeability $\mu_r = 2 - 0j$ (bottom graph). Sample permittivity is held constant at $\varepsilon_r = 7.8 - 0j$.

inside a material with a permeability greater than that of a vacuum the wave velocity of that wave will be lower than if it travelled through a vacuum. This lower wave velocity results in a shorter wavelength for the wave compared to that of free space. This smaller value of wavelength allows more resonances which satisfy the $\lambda/2$ criteria and this effect is more pronounced as the material permeability increases.

4.5.3 Effect of varying sample thickness

The thickness of the sample under test is a critical parameter for the high frequency coaxial probe measuring scheme. The material under test at the termination of the line must be sufficiently thick to appear infinitely deep to the probe (see Section 4.4 for a more detailed discussion). To investigate the effect of sample thickness upon the resulting S-parameters of the material, the representation of the sample within the model was changed from a depth of 5.737mm to 10mm and the simulation repeated.

The larger sample size simulation results for the electric and magnetic fields (Figure 4.24) shows clear nodes and anti-nodes formed by both the electric and magnetic field components. These are more concentrated near to the axial symmetry plane and near the termination of the coaxial line. The field patterns outside of the sample and coaxial line are of a similar pattern and intensity to those observed in Figure 4.18 for the smaller sample.

Figure 4.25 shows the S11 simulation data for a sample where the subdomain settings were identical; sample permittivity, $\varepsilon_r = 7.8 - 0j$; sample permeability, $\mu_r = 1 - 0j$; sample thickness was the only parameter altered. An interesting feature is that the resonance pattern shows the same pattern but the resonances begin at a lower frequency

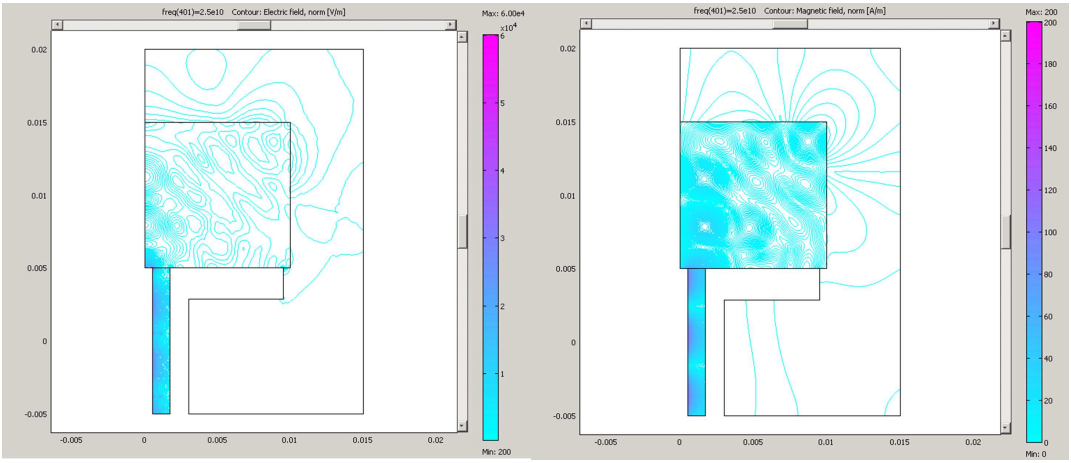

Figure 4.24: Sample permittivity $\varepsilon_r = 7.8 - 0j$, sample permeability $\mu_r = 1 - 0j$. Contour plot on left shows electric field strength and plot on right shows the magnetic field strength at 25GHz.

for the thinner sample. The 5.737mm sample (bottom graph) displays five resonance frequencies which are shared with the 10mm sample (top graph) only compressed to within a lower frequency range of up to 18GHz with an additional final resonance at 22GHz. Both simulation conditions show the result that at higher resonant frequencies the magnitude of the S11 response increases and although the shape of the resonance peaks is shifted in frequency for different depth samples, the magnitude of the resonance is not directly translated. A resonance peak which is shifted down in frequency for a larger sample will now have a smaller magnitude than in a thinner sample; for example the fourth resonance peak at 22GHz on the 5.737mm sample has a magnitude of the order -10dB, when this is frequency shifted in the 10mm thickness sample results to 17.5GHz the magnitude reduces to the order of -8dB.

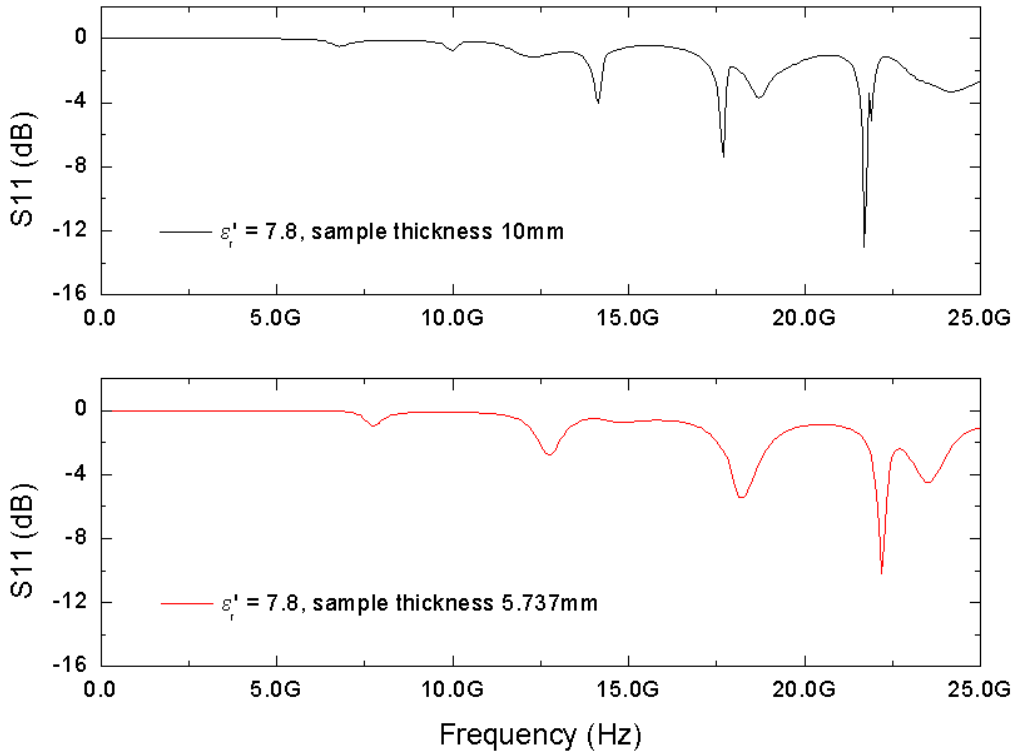

Figure 4.25: S11 response verses frequency (45MHz – 25GHz) for sample permittivity $\varepsilon_r = 7.8 - 0j$, permeability $\mu_r = 1 - 0j$. Sample thickness = 5.737mm (top graph) and sample thickness = 10mm (bottom graph).

4.5.4 Simulation results for 'ideal' dielectric resonator antenna material

Within Chapter 6 Section 6.1.4, it is discussed that research by Kitra et al. [27] found the ideal material for use within a dielectric resonator antenna would have a permittivity of $\varepsilon_r' = 6$ and a permeability of $\mu_r' = 6$. The simulation was repeated with the subdomain properties altered so that the sample properties represented this ideal material.

Figure 4.26 shows the electric and magnetic field distributions for this sample. As expected from previous simulations, the fields are strongest and most concentrated within the coaxial line and the area of the sample which terminates the line. This is expected as the speed of light is reduced even more by the high permittivity and permeability (Equation 4.1). The magnetic field strength is greater in this material due to the larger sample permeability.

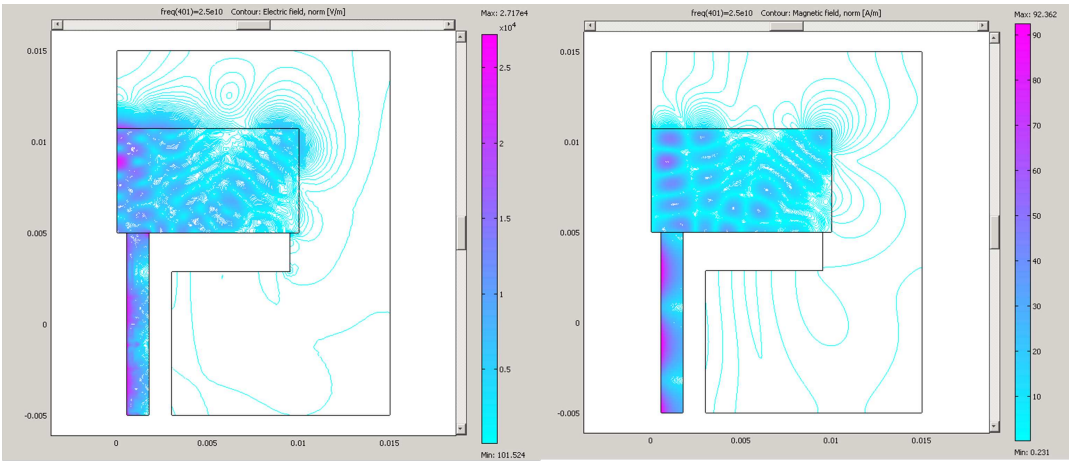

Figure 4.26: Sample permittivity $\varepsilon_r = 6 - 0j$, sample permeability $\mu_r = 6 - 0j$. Contour plot on left shows electric field strength and plot on right shows the magnetic field strength at 25GHz.

The larger than unity permittivity and permeability values have the effect of concentrating relatively strong electric and magnetic fields within the sample material and the area directly behind it. However the results seen are not drastically different to the response

seen for the $\varepsilon_r' = 7$, $\mu_r' = 2$ material which is based upon the actual barium hexaferrite samples indicating that the materials developed are potentially suitable for antenna design.

4.6 Chapter conclusions and future work

4.6.1 Conclusions

The coaxial probe method for high frequency permittivity characterisation was introduced. It is a broadband non-destructive measurement regime. Several different approaches to modelling the interaction between the probe and sample at the termination of the line.

The experimental set-up at The University of Nottingham was described. It is based around a 3.5mm coaxial probe connected to an HP8510 VNA which is in turn connected to a PC which calculates the real and imaginary parts of permittivity from the reflected S11 parameters of the system.

The permittivity of four standard liquids were measured to validate the accuracy of the system. These agreed with results published in the literature.

Results are presented for the permittivity of barium hexaferrite and bismuth substituted barium hexaferrite with a range of doping levels and subjected to a variety of sintering regimes. All showed similar trends where both real and imaginary parts of permittivity were stable until approximately 6GHz. After this value variations in the permittivity graphs are observed with the largest of these consistently observed for the unsubstituted barium hexaferrite materials. It was concluded the reason for these variations is due to

samples not being thick enough to appear infinite to the probe. Therefore reflections via the furthest surface of the sample are detected, altering the permittivity values. It was theorised that the $x = 0.0$ samples are most effected by this because the material has a lower loss compared to bismuth containing samples.

Permittivity results were presented as a function of bismuth substitution level at a constant frequency of 2.45GHz (selected because this is the operational frequency of Bluetooth and Wi-fi) to allow comparisons across sintering regimes.

The highest permittivity material at this frequency for samples sintered at 1100°C is the $x = 1.5$ pellet which has been sintered for three hours. It has a permittivity of $\varepsilon_r = 14.69 - 1.664j$. Of the samples sintered at 1200°C the highest permittivity sample with $\varepsilon_r = 11.81 - 1.995j$ is the $x = 0.5$ material which has been sintered for three hours.

Simulation work was conducted using Comsol Multiphysics 3.3a which investigated the S-parameters and electromagnetic fields of samples with different permittivity, permeability and thickness over the test frequency range. The S11 data shows that the material resonates at lower frequencies for samples with higher permittivities, permeabilities and for thicker samples. The electric and magnetic field patterns for the sample and surrounding area indicates that the fields are stronger and contained more within the sample and the area directly behind it for higher permittivity and permeability materials.

4.6.2 Future work

The test range for high frequency measurements could be improved by fabricating samples which are physically larger and so would appear infinitely thick to the probe. This would

allow characterisation of permittivity to take place over a wider frequency range up to the calibration limit of 25GHz.

A system which takes into account the permeability of the material which is not equal to unity would also improve the accuracy of the measurements. This could be accomplished by implementing the Frequency-Varying method with the existing coaxial system [28] or by using a system incorporating a transmission line [24].

4.7 References

[1] Agilent Technologies. Split Post Dielectric Resonantors for Dielectric Measurements of Substrates. Online: http://cp.literature.agilent.com/litweb/pdf/5989-5384EN.pdf, Accessed: August 2011.

[2] N R Greenacre. *Measurement of the high temperature dielectric properties of ceramics at microwave frequencies*. PhD thesis, Department of Electrical and Electronic Engineering, The University of Nottingham, 1996.

[3] T. W. Athey, M. A. Stuchly, and S. S. Stuchly. Measurement of radio-frequency permittivity of biological tissues with an open-ended coaxial line - Part 1. *IEEE Transactions on Microwave Theory and Techniques*, 30(1):82–86, 1982.

[4] M Arai, J G P Binner, and T E Cross. Estimating errors due to sample surface roughness in microwave complex permittivity measurements obtained using a coaxial probe. *IEE Electronics Letters*, 31(2):115–117, 1995.

[5] M. A. Stuchly, T. W. Athey, C. M. Samaras, and G. E. Taylor. Measurment of radio frequency permittivity of biological tissues with an open-ended coaxial line: Part 2

- Experimental results. *IEEE Transactions on Microwave Theory and Techniques*, 30(1):87–91, 1982.

[6] M. M. Brady, S. A. Symons, and S. S. Stuchly. Dielectric behaviour of selected animal tissues in vitro at frequencies from 2 to 4 GHz. *IEEE Transactions on Biomedical Engineering*, 28(3):305–307, 1981.

[7] F. M. Ghannouchi and R. G. Bosisio. Measurement of microwave permittivity using six-port reflector with an open-ended coaxial line. *IEEE Transactions on Instrumentation and Measurement*, 38(2):505–508, 1989.

[8] S. S. Stuchly, C. L. Sibbald, and J. M. Anderson. A new sdmittance model for open-ended waveguides. *IEEE Transactions on Instrumentation and Measurement*, 29(3):176–183, 1994.

[9] C. L. Pournaropoulous and D. K. Misra. A study on the coaxial aperture electromagnetic sensor and its application in material characterization. *IEEE Transactions on Instrumentation and Measurement*, 43(2):111–115, 1994.

[10] Gaetano Panariello, Luigi Verolino, and Gaetano Vitolo. Efficient and accurate full-wave analysis of the open-ended coaxial cable. *IEEE Transactions on Microwave Theory and Techniques*, 49(7):1304–1309, 2001.

[11] D. Berube, F. M. Ghannouchi, and P. Savard. A comparative study of four open-ended coaxial probe models for permittivity measurements of lossy dielectric/biological materials at microwave frequencies. *IEEE Transactions on Microwave Theory and Techniques*, 40(10):1928–1934, 1996.

[12] Pascal De Langhe, Luc Martens, and Daniel De Zutter. Design rules for an experimental setup using an open-ended coaxial probe based on theoretical modelling. *IEEE Transactions on Instrumentation and Measurement*, 43(6):810–817, 1994.

[13] J. P. Grant, R. N. Clarke, G. T. Symm, and N. M. Spyrou. A critical study of the openended coaxial line sensor technique for RF and microwave complex permittivity measurements. *Journal of Physics E: Scientific Instruments*, 22:757–770, 1989.

[14] N. Marcuvitz. *Waveguide Handbook*, volume 21 of *IEE Electromagnetic Waves Series*. Peter Peregrinus Ltd., London, 1993 edition, 1993.

[15] M. Okoniewski, J. Anderson, E. Okoniewska, K. Caputa, and S. S. Stuchly. Further analysis of open-ended dielectric sensors. *IEEE Transactions on Microwave Theory and Techniques*, 43(8):1986–1989, 1995.

[16] L. F. Chen, C. K. Ong, C. P. Neo, V. V. Varadan, and V. K. Varadan. Microwave Electronics: Measurement and Materials Characterization. John Wiley and Sons Ltd., 2004.

[17] L. S. Anderson, G. B. Gajda, and S. S. Stuchly. Dielectric measurements using a rational functional model. *IEEE Transactions on Microwave Theory and Techniques*, 42:199–204, 1994.

[18] M Arai. *Open-ended coaxial probes for high temperature dielectric measurements*. PhD thesis, Department of Electrical and Electronic Engineering, The University of Nottingham, 1995.

[19] J R Mosig, J E Besson, M Gex Fabry, and F E Gardiol. Reflection of an open-ended coaxial line and application to nondestructive measurement of materials. *IEEE Transactions on Instrumentation and Measurement*, 30(1):46–51, 1981.

[20] J Barthel, K Bachhuber, R Buchner, and H Hetzenauer. Dielectric spectra of some common solvents in the microwave region. Water and lower alcohols. *Chemical Physics Letters*, 165(4):369–373, 1990.

[21] A. Petosa, A. Ittipiboon, Y.M.M. Antar, D. Roscoe, and M. Cuhaci. Recent advances in dielectric-resonator antenna technology. *IEEE Antennas and Propagation Magazine*, 40(3):35–48, 1998.

[22] S. Fan, K. Staebell, and D. Misra. Static analysis of an open-ended coaxial line terminated by layered media. *IEEE Transactions on Instrumentation and Measurement*, 39(2):435–437, 1990.

[23] Agilent Technologies. Basics of measuring the dielectric properties of materials. http://cp.literature.agilent.com/litweb/pdf/5989-2589EN.pdf, 2005.

[24] J. Baker Jarvis, E.J. Vanzura, and W.A. Kissick. Improved technique for determining complex permititvity with the transmission / reflection method. *IEEE Transactions on Microwave Theory and Techniques*, 38(8):1096–1103, 1990.

[25] M.H. Weik, editor. *Computer Science and Communications Dictionary*. Kluwer Academic, 2 edition, 2000.

[26] J. Daintith, J. Clark, H.M. Clarke, D. Cooper, J. Cullerne, D.E. Edwards, R. Rennie, and D.E. Ward. *Dictionary of Physics*. Oxford University Press, 6th edition, 2009.

[27] M.I. Kitra, P. McEvoy, J.C. Vardaxoglou, and J.R. James. Material loaded antennas and their contribution towards low-SAR. In *IEE Technical Seminar on Antenna Measurements and SAR*, 2004.

[28] S. Wang, M. Niu, and Deming Xu. A frequency-varying method for simultaneous measurement of complex permititvity and permeability with an open-ended coaxial probe. *IEEE Transactions on Microwave Theory and Techniques*, 46(12):2145–2147, 1998.

Chapter 5

High frequency near-field permittivity

Scanning near-field microwave microscopy is motivated by the need to investigate localized properties of materials which are not satisfied by traditional far-field techniques, which are limited in nature to measure the properties of a material over a large area (millimetre to centimetre range dependant on measurement technique) so cannot resolve details finer than this scale [1].

Abbes criterion [2] applies to microscope technologies operating in the far-field, such as standard optical microscopes and those also operating in the microwave frequency range. The criterion states that the resolution of any microscope operating in the far-field is limited by the wavelength used to probe the material. Hence a microscope operating at microwave frequency with a wavelength of millimetres is undesirable because its resolution will be restricted to the order of $\lambda/2$ (where λ is wavelength in metres) [2] [3]. Microscopes operating in the near-field region are not restricted by this and so

greater resolution can be achieved at higher frequencies.

Near-field optical microscopy pre-dates the technology relating to devices operating at microwave frequency although there are many similarities between the two, most significantly the need to characterise the tip–sample interaction of the set-up. The drive to develop a near-field microscope with a microwave operating frequency was to characterise the electrical properties of a sample, rather than the optical properties. The concepts and knowledge obtained from developments in the optical range were used to develop and improve microwave frequency microscopes [4].

Near-field probes fall into two broad categories:

- Broadband probes;
- Resonant probes.

Broadband probes allow characterisation of a material over a wide frequency range by utilising waveguide properties. Resonant probes use a resonant cavity to study a small area of a sample; providing high sensitivity but over a narrower frequency range [5].

The principles of broadband probes were discussed at the start of Chapter4 High frequency dielectrics and permittivity. Some of these methods can be translated to smaller sizes and used as near-field probes, however the following discussion will focus on resonant methods.

5.1 Coaxial resonator probes

Coaxial resonator probes are commonly used in near-field microwave microscopy and are based upon resonant-perturbation theory. They are fabricated by making a hole in the end

wall of the coaxial resonant cavity and extending the central conductor to pass beyond the cavity wall. The basic design has a blunt tip which provides a spatial resolution equal to the area of the inner conductor [1]. To gain higher accuracy the resonant cavity design is improved by mounting a sharpened metal tip on the centre conductor of a high quality microwave frequency coaxial resonator [6]. Resonators which terminate with a sharp point give greater spatial resolution dependant upon the bluntness of the tip; a sharper tip provides higher resolution [7]. When the sample under test is brought into close proximity (less than 1mm [8]) of the probe tip, the cavity is perturbed and becomes a probe of the dielectric properties of the area of the sample directly below the probe tip [9].

Quantitative measurements of the dielectric properties of a sample are collected on the assumption that the probe tip radius and effective field range are much smaller than the operational wavelength [5]. A quasi-static model can then be used for calculations (where the wave nature can be ignored). The probe tip is considered a charged conducting sphere with different considerations for the situation when the probe is in contact with the sample and for the situation when it is still within the near-field but is not in contact [4].

The value of the permittivity of the sample is usually derived from one of two measurement methods. In the first, the resonant frequency and the quality factor of the resonator are measured. Next the sample is introduced to the probe and the shift in resonant frequency and the change in the quality factor of the resonator are recorded. In the alternate method the resonant frequency and subsequent shift when a sample is introduced is captured along with the reflected power from the sample [10] [9].

5.1.1 Modelling tip–sample interaction as an equivalent circuit

For analysis and further understanding of the microscope operation, the interaction between the sample and the probe can be presented as an equivalent circuit. This technique was first used in resonant probes within a planar circuit application [11]. The approach is adaptable for use with a coaxial resonator probe approach as shown in Figure 5.1.

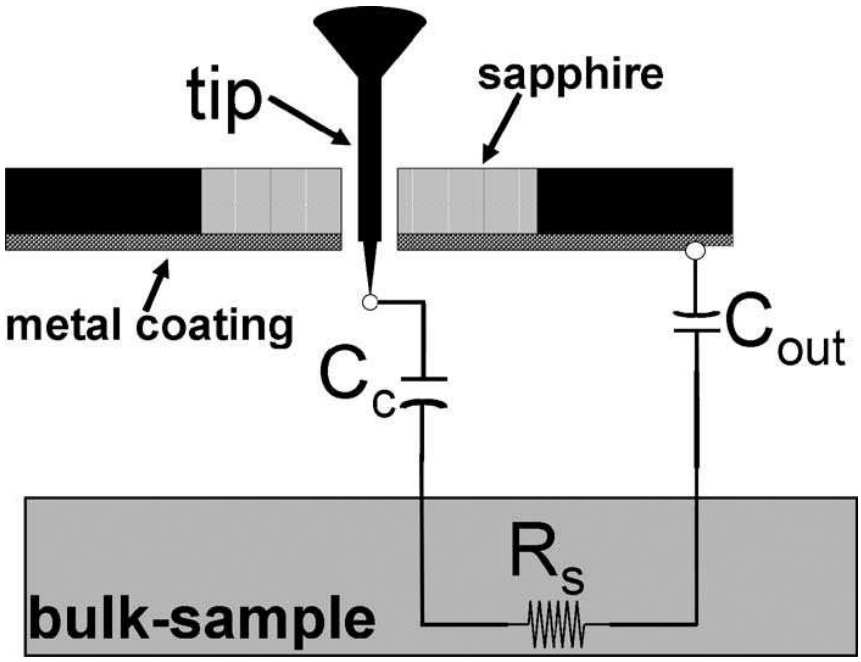

Figure 5.1: Equivalent circuit showing probe-sample interaction. The tip is in effect an antenna brought near the sample. The coupling capacitance C_c is in series with the material resistance R_s [12]

In this approach adopted by Imtiaz et al. [12], the sample is electrically in parallel with the capacitance of the resonator. The tip–sample coupling capacitance C_c is the sum of the tip–sample geometrical capacitance (C_x) and the material capacitance (C_s). The capacitance between the outer conductor of the probe and the sample can be discounted because $C_{out} \gg C_c$. The tip–sample geometrical capacitance C_x, is modelled using the quasi-static approach [4]. The impedance of the sample is presented as a series combination of the material capacitance and resistance (C_s and R_s respectively). When the experimental data is analysed it is observed that the frequency shift is more dependant

on the capacitances C_x and C_s, while the quality factor of the resonator, Q, is sensitive mainly to the sample resistance R_s.

The methodology above applies only to a bulk sample; modelling for a heterogeneous sample complicates the system because the sample capacitance and resistance (C_s and R_s) do not remain constant. The resolution will also be dependant on the dimensions of the probe which will effect the tip–sample geometrical capacitance C_x.

5.1.2 Modelling tip–sample interaction as a point charge

A different approach to the lumped circuit method detailed above is to use a point charge interaction model as introduced by Gao et al. [4]. This provides a model for a tip modelled as a sphere or a point charge either in contact with, or slightly elevated from a sample.

5.1.3 Sample preparation and x-y stage

The properties of the sample under test dictate to a certain extent, the experimental set-up which can be utilised. If a sample is homogeneous, only one measurement is required to characterise the permittivity. If the sample is heterogeneous it can be placed on a moveable x-y stage and the sample characterised at several different points on the surface to build up an effective 'image' or 'map' of permittivity.

Sample permittivity is calculated from the magnitude and phase of a signal reflected back from the sample, thus any separation between the probe and the sample is an important factor to consider and sample topography must be taken into account. If a sample is smooth measurement and calculations are less complex than for those of rough sample.

The dependence on sample topography can also be exploited to image a topographical map of a sample with a uniform permittivity. To this end, different measurement set-ups are employed depending on the sample topography and whether a contact or non-contact measurement is required.

5.1.4 Non-contact method

In this measurement scheme a blunt open coaxial probe is positioned a short distance ($<$ 1mm) above the sample under test and is most commonly used to measure sheet resistance [13], however it can also used to measure the permittivity of materials [8].

The frequency shift of the resonator is recorded as the probe passes over the sample. This value is related to the dielectric constant of the material beneath the probe by use of a calibration curve where a sample with known dielectric properties is used as a control. The sensitivity of the microscope can be increased by reducing the probe–sample distance, however the instrument then becomes more affected by sample topography [8].

5.1.5 Contact method

The basis of most contact methods is to place a sharp probe tip, protruding from the central conductor of a coaxial resonant cavity into soft contact with the material under investigation. Soft contact is the term used when the probe and sample are in contact but the probe does not scratch the surface of the sample [9]. This is a contact force of approximately 50μN applied by the sample, which is held in contact with the probe tip by a "spring-loaded cantilever support" [14]. Both bulk materials and thin films can have dielectric properties quantified using this method by altering the calibration method for

the microscope [8].

5.1.6 Maintaining a constant distance between the sample and probe tip

There are two widely used operating systems for controlling the distance between the probe and the sample for near-field coaxial resonator microscopes;

- Frequency following;
- Distance following.

In a frequency following (FF) set-up the coaxial cavity structure is held at resonance by adjusting the frequency of a microwave source which is controlled via a feedback loop. A change in the sample dielectric properties causes the resonant frequency of the cavity to change, which is measured from the power response near the resonant frequency [15]. The feedback signal is proportional to the resonant frequency shift of the system, which is related to the dielectric properties of the material under test [13][16].

A distance following (DF) method takes account of the topography of a sample by maintaining a constant distance between the probe tip and test material. This can be in the form of contact with the surface of the sample or by height modulation distance following [9].

5.1.7 Summary

In summary; to achieve good spatial resolution the following issues must be solved or a compromise reached:

- The probe tip must pass over the sample at a distance less than the resolution sought;
- Sample topography will affect the results of any experiment and must be taken into account to avoid producing misleading data;
- If a distance following method is employed then the distance between the sample and the probe tip must remain constant and be monitored and controlled to achieve this.

5.2 Design of near-field probe

A simple probe was constructed by the modification of an SMA connector. This connector was chosen due to the wide range of types available and relative inexpense and can be used reliably at frequencies up to 18GHz [17]. A cable plug connector was soldered to a tungsten needle, forming the centre conductor then wrapped in PTFE tape to provide insulation and to reduce impedance mismatch between the VNA cable connection and the probe. The tungsten probe tips were selected from a range manufactured by GGB Industries. The solid tungsten needles were 38mm long with a 0.51mm diameter shaft, tapering to a tip of between 0.5 – 10μm diameter, dependant on the specification selected. A needle was cut to a total length of 9mm so that the tip protruded approximately 3mm beyond the outer conductor. A diagram showing the design of the probe is shown in Figure 5.2.

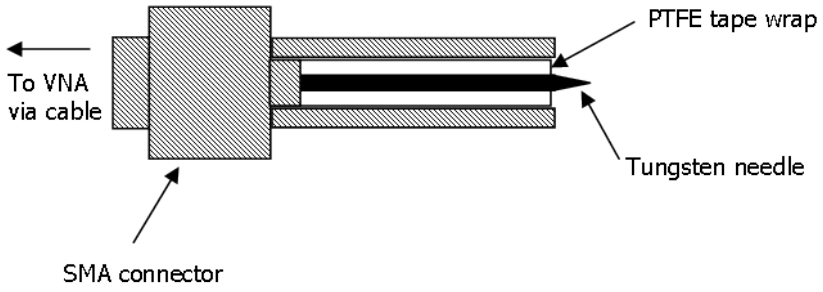

Figure 5.2: Cross sectional diagram showing the design of the near-field probe prototype. The metal SMA connector components are shaded grey, the PTFE is white and the tungsten needle which is soldered into the central conductor is coloured black.

5.2.1 Characteristic impedance

For a coaxial line, the characteristic impedance of the system can be calculated by [18]:

$$Z_0 = \frac{138}{\sqrt{\varepsilon'_r}} \times log_{10}\frac{d_1}{d_2} \tag{5.1}$$

Where Z_0 is the characteristic impedance of the line; ε'_r is the real part of permittivity of the insulation of the coaxial line; d_1 is the inner diameter of the outer conductor; and d_2 is the outer diameter of the inner conductor.

With no PTFE tape wrapped around the inner conductor the characteristic impedance of the probe was calculated as 82Ω. As shown in Equation 5.2.

$$\begin{aligned} Z_0 &= \frac{138}{\sqrt{\varepsilon'_r}} \times log_{10}\frac{d_1}{d_2} \\ &= \frac{138}{\sqrt{1}} \times log_{10}\frac{2 \times 10^{-3}}{0.51 \times 10^{-3}} \\ &= 81.9\Omega \end{aligned} \tag{5.2}$$

The possibility of operating the VNA in 75Ω mode was considered, however the cables connecting the probe to the VNA would also need to be replaced. The inclusion of the PTFE tape for insulation reduced the characteristic impedance of the probe to 55.2Ω, as calculated in Equation 5.3. This value was not idea because a small impedance mismatch was still present, however it was acceptable for the prototyping phase of development.

$$\begin{aligned} Z_0 &= \frac{138}{\sqrt{\varepsilon_r'}} \times log_{10}\frac{d_1}{d_2} \\ &= \frac{138}{\sqrt{2.2}} \times log_{10}\frac{2\times10^{-3}}{0.51\times10^{-3}} \\ &= 55.2\Omega \end{aligned} \tag{5.3}$$

5.3 System in used at The University of Nottingham

High frequency measurements of the S-parameters of the probe in contact with various materials were taken using an Anritsu ME7808B Broadband Network Analyser. The system was calibrated using an auto-cal module 36582KKF (40MHz – 40GHz range) in conjunction with the module software installed on a connected PC. The cable from port 1 of the VNA was connected to the right hand port of the auto-cal module through a connector. The software was set-up to ignore the presence of the connector which was used to connect the cable plug probe to the end of the coaxial line. This allowed the experimental set-up to be calibrated up to the start of the probe itself; the probe was past the measurement plane so S-parameters recorded are due to the probe and the material the probe was in contact with.

5.3.1 Characterisation up to 20GHz

After calibration the probe was held in contact with the samples under test; air, epoxy resin, PTFE, a barium titante and epoxy resin mixture and a control test where the probe was removed from the end of the line. Each measurement was repeated twice in the range 40MHz – 20GHz and an average plotted to reduce random errors. The frequency range was selected taking into account the SMA connector used to construct the probe has a maximum recommended operating frequency of 18GHz. The results were saved and imported into Origin for processing.

The graph in Figure 5.3 shows the average data for the 9mm needle probe from 40MHz – 20GHz. There is a clear resonance peak at around 13GHz, with a frequency shift which is dependant on the material under test. The other observation made was when the probe is in air and not in contact with a sample it was more susceptible to noise.

The graph shows that there is a S11 minimum of -2.14dB at 13.18GHz for the probe in air; for PTFE the minimum is -2.37dB at 12.98GHz; a minimum of -2.47dB at 13.05GHz for the epoxy resin sample; and the largest difference is for the barium titanate and epoxy mixture which displayed a minimum of -3.10dB at 12.88GHz. These results show that there is a shift in the resonance frequency when the probe is in contact with different materials, even those which has a similar permittivity; the permittivity of air is 1 by definition and the permittivity of epoxy resin is approximately 5 although this is frequency dependant [19][20]. The permittivity of PTFE of $\varepsilon_r' = 2.1$ [21] shows a response similar to that of the epoxy resin. The most significant shift in S11 magnitude and frequency is observed for the barium titanate and epoxy resin mixture which has a permittivity of $\varepsilon_r' = 7.8$ at 2.5GHz [22].

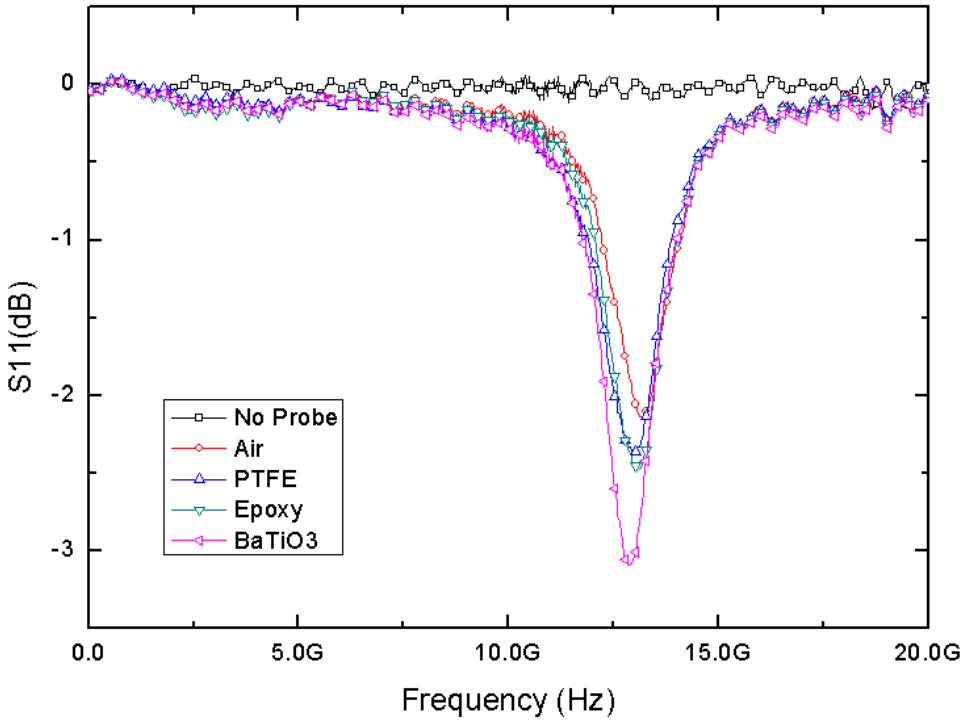

Figure 5.3: 9mm length inner conductor cable probe in contact with different materials over a frequency range 40MHz – 20GHz

5.3.2 Characterisation up to 40GHz

Using the same samples as above the experimental set-up was tested over the range 40MHz – 40GHz. Although the probe was constructed from components which have a guaranteed performance of up to 18GHz it was decided that it would be an interesting exercise to observe the probe response at higher frequencies. The system was calibrated using the auto-cal unit three times with 16 point switch averaging. Each material was measured twice and an average of the two was taken which was then smoothed using the five point adjacent average method and then plotted, as shown in Figure 5.4.

The response shows three resonant frequencies; the first at 13GHz, the second at approximately 30GHz and a final resonance at 38GHz. From the analysis of the data the following conclusions were drawn;

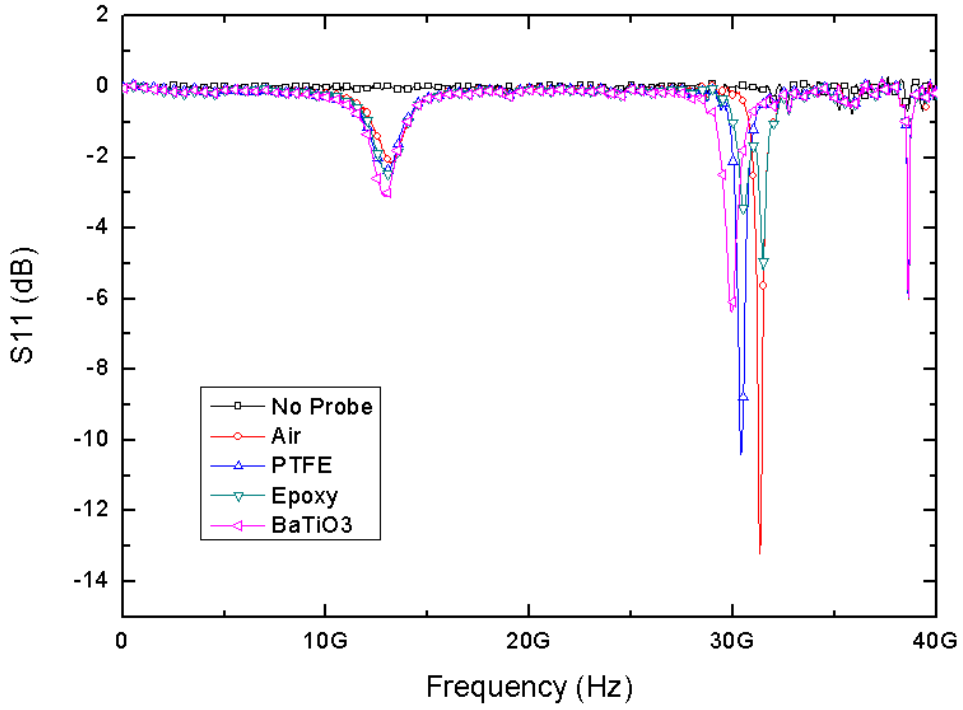

Figure 5.4: 9mm length inner conductor cable probe in contact with different materials over a frequency range 40MHz – 40GHz

- The epoxy resin measurement data displayed a double peak at the second resonance frequency;
- At the first resonance frequency a greater frequency shift was observed for materials with a lower permittivity. The value of this minimum is also lower for higher permittivity materials;
- The second resonance peak again shows a greater frequency shift for lower permittivity materials but in contrast to the first peak, it is the lower permittivity materials which display the lowest S11 values;
- The final resonance frequency shows no relative frequency shift for any of the materials measured. The S11 minimum values are all within one decimal place of each other, which is too close to draw any meaningful conclusions;

- The "No Probe" trace is also a measure of how accurate the calibration is because this is the start of the measurement plane. It shows no resonance across the test frequency range and remains approximately zero.

5.4 Characterisation of barium hexaferrite samples using near-field probe

The resonant coaxial probe was used in conjunction with the HP 8510 VNA to investigate the resonant frequency shift when the probe was in contact with barium hexaferrite and bismuth doped barium hexaferrite samples. The line was calibrated up to the probe itself using the standard short/open/load configuration. S11 data was recorded for different positions on the samples, stored to disk and then imported into Origin for post-processing.

The probe was designed to detect changes in permittivity across a small area around the probe tip. As a result of this the positioning of the probe on the sample surface must be considered when studying the resulting S11 parameters. Two different sampling approaches were employed; cross sampling and diagonal sampling. Cross sampling was where five points in a cross shape from near the centre of the pellet were taken. Diagonal sampling was where five sampling positions were taken in a straight line passing through the centre of the sample and out towards both edges. A schematic to illustrate both sampling regimes is given in Figure 5.5.

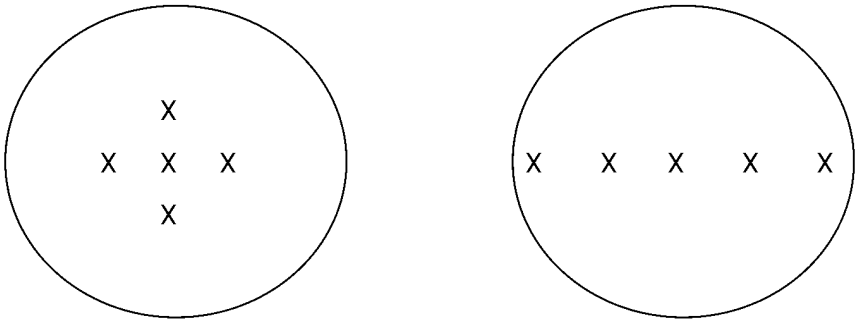

Figure 5.5: Comparison of sample positions for cross and diagonal sampling regime on the surface of a sample pellet

5.4.1 Undoped samples

Figure 5.6 shows the S11 data for both cross and diagonal sampling points on the same pellet (series E: sintered for three hours at 1200°C, sample $x = 0.0a$). The two resonance frequencies centred around 7.5GHz and 14.5GHz are clearly visible in both the top and bottom graphs. The top graph shows the results from the cross sampling regime and the bottom graph shows the diagonal pattern sampling. The S11 data for the cross sampling regime shows closer agreement than that for the diagonal sampling method. This variation is due to differing sample properties in the vicinity of the probe tip; the cross sampling pattern contains points all located around the centre of the pellet whereas the diagonal sampling contains two data points near to the edges of the sample. The greater S11 variation for the diagonal sampling indicates that the permittivity of the material changes nearer to the edges, most likely due to physical properties (as EDX data in Chapter 2 Section 2.8.4 showed homogeneous composition for undoped samples) such as greater compression of the material at the edges when it was pressed into pellet form. Figure 5.7 shows the S11 variation in the sampling points for the diagonal sampling more clearly. Points one and five are furthest from the centre of the sample and show the most variation, indicating the probe is effective in detecting changes in permittivity

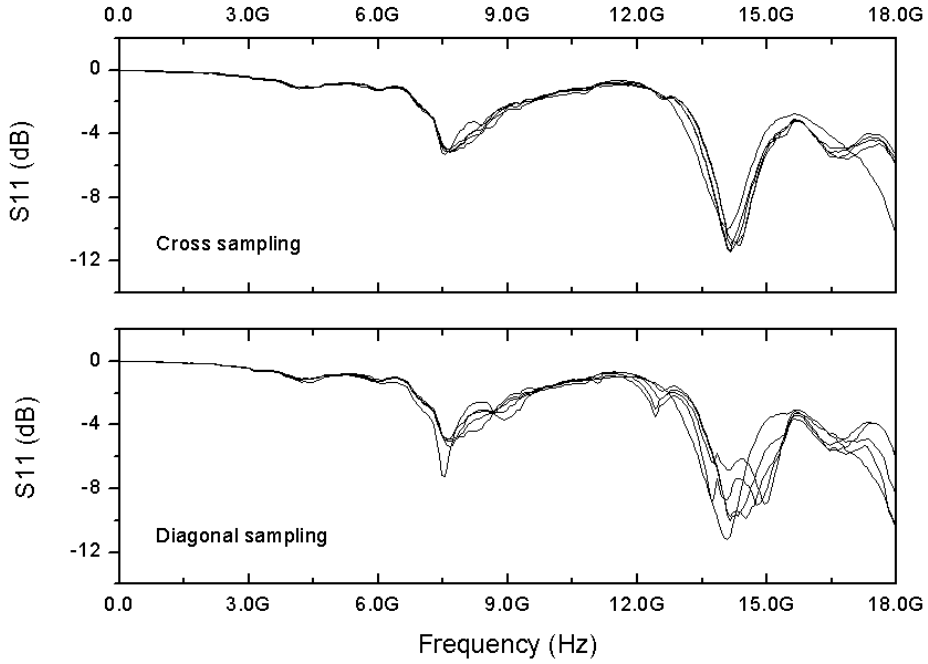

Figure 5.6: S11 data for the same sample; comparison of cross and diagonal sampling regime. Each trace on the graph represents a different sample position, indicated by a cross in Figure 5.5

across a sample.

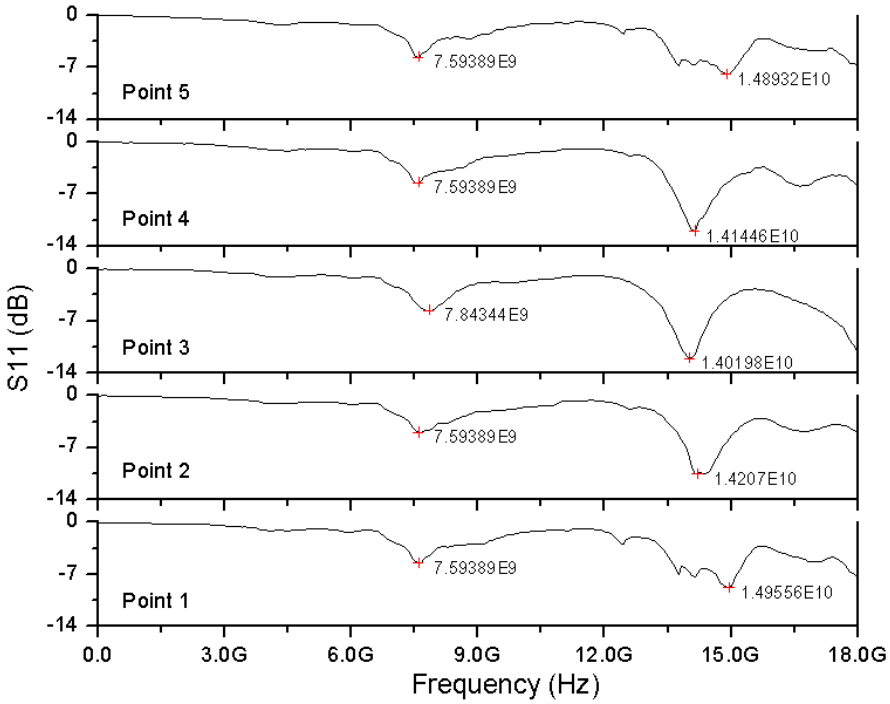

Figure 5.7: S11 data for the same sample; diagonal sampling variation of different positions

5.4.2 Bismuth substituted samples

It has been established that the probe design is suitable for detecting small changes in permittivity across a sample. Next the probe was used to investigate the differing S11 responses of different barium hexaferrite and bismuth substituted barium hexaferrite samples. Cross sampling was used as this had been shown as the most repeatable. The interest here is in potential differences in permittivity, so sample points will remain near the centre to reduce the influence of edge effects on the measurements. Figure 5.8 shows the average of the cross pattern sampling for a variety of pellets which have been sintered at 1100°C for three hours.

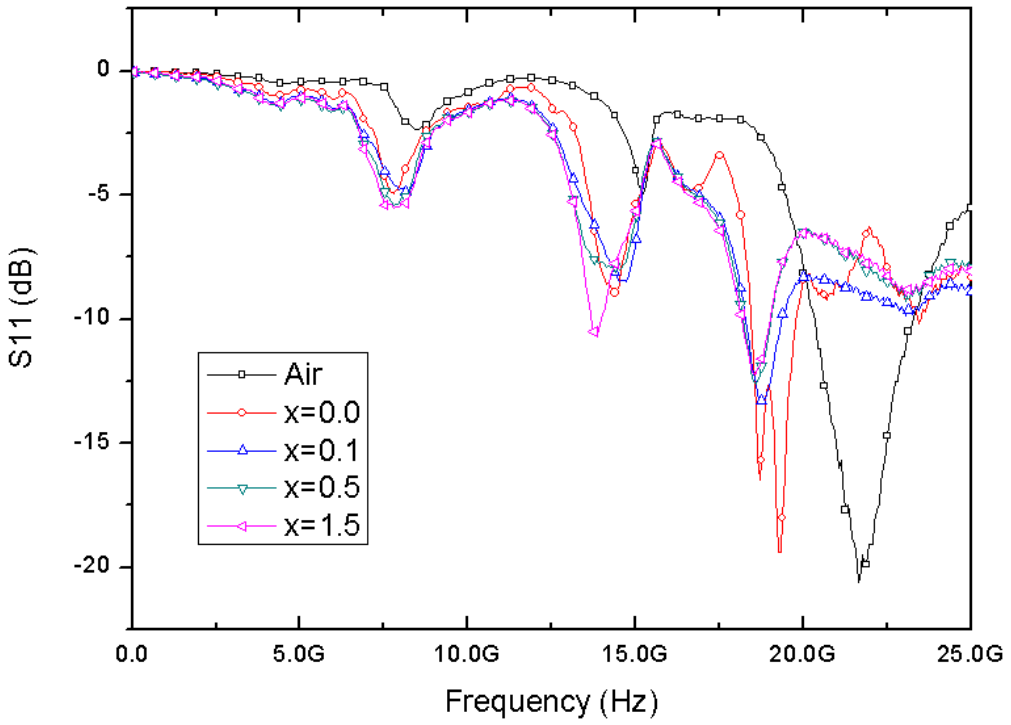

Figure 5.8: S11 data for different sample pellets from series D which have been sintered for three hours at 1100°C

There is a clear difference in the measured response for the probe in contact with air, undoped barium hexaferrite and the bismuth containing samples. The variations between

the S11 parameters for the bismuth substituted barium hexaferrite are more difficult to discern between. The degradation of the response quality after 18GHz is witnessed by the noise in the trace at these higher frequencies.

An interesting feature of the probe used in conjunction with the HP8510 VNA as opposed to the Anritsu ME7808B VNA is the shift in resonant frequencies:

- HP8510 has resonant frequencies at 7.5, 14 and 22GHz.
- Anritsu ME7808B has resonant frequencies at 13, 30 and 38GHz.

Due to the unpredictable behaviour of the SMA connector the probe is fashioned from above 18GHz these frequencies will be removed from consideration. The resonances at 13 and 14GHz are considered to be equivalent, however the lower resonance at 7.5GHz observed when the HP8510 VNA is used is not present on the data gained from the Anritsu machine. The reason for this is unclear although it could be a calibration issue as the Antritsu VNA is checked against the manufacturers standards every year while this procedure has not been performed on the HP VNA for a longer period of time.

5.5 Chapter conclusions and future work

5.5.1 Conclusions

The background theory of the operation and design of near-field microwave microscopy has been presented, with a focus on how dielectric properties are extracted. Different schemes for maintaining reliable results despite changing sample topography was discussed.

The design of a simple prototype resonant coaxial probe was explored and tested with control materials with a uniform permittivity and also on more complex barium hexaferrite and bismuth substituted barium hexaferrite samples. Bismuth containing samples have a heterogeneous permittivity on a microscopic level which was detected by small variations in the S11 data collected via the probe.

The resonant coaxial probe constructed from the cable plug connector and tungsten needle functions effectively as a near-field permittivity sensor. The resonant frequency and depth of resonance (and therefore Q-factor) alter when the probe is in contact with a material with a different permittivity compared to that of air. This can be used to either determine the dielectric properties of several different uniform dielectric materials in relation to each other. Alternatively it can be used to investigate the localised permittivity of an area of a sample which is in contact with the probe on the surface of a material which has heterogeneous dielectric properties. The results taken from the probe were easier to interpret when the permittivities of the the sample points (be it on different samples, or different sample points on the same material) have a greater range of differences than with points which have small variations in the dielectric properties, because the changes in the resonant frequency and magnitude of that resonance are clearer.

A clear change in the S11 data was shown for the barium hexaferrite material compared to the bismuth containing samples. The bismuth doped samples do show variation in S11 but this is not as defined between samples as the resolution of the prototype probe was limited.

5.6 Future work

The prototype of the near-field probe manufactured within this work confirmed the operation of the measurement scheme. This design could be improved upon to yield more accurate results.

By reducing the characteristic impedance of the probe to 50Ω the impedance mismatch between the line and the probe and would also be reduced and therefore increase the accuracy of the probe. This can be achieved by designing a probe where the inner diameter of the outer conductor satisfies Equation 5.3 where the outer diameter of the inner conductor is 0.51mm diameter (the dimension of the tungsten needle used as an inner conductor).

A survey of the literature indicates that by further reducing the diameter of the probe tip which comes in contact with the sample, the changes in the S-parameters will be caused by a smaller area on the sample surface, thus increasing the sensitivity of the probe.

A sample stage could be developed to automate the sampling process to make it less time intensive to characterise samples and also more repeatable. In addition the resonant frequencies for different sampling positions could be used to build up a visual map of sample permittivity to improve interpretation and understanding of the results.

5.7 References

[1] S. M. Anlage, D. E. Steinhauer, B. J. Feenstra, C. P. Vlahacos, and F. C. Wellstood. Near-field microwave microscopy of materials properties. *Microwave Superconduc-*

tivity, pages 239–269, 2001.

[2] E. Abbe. Beitrge zur theorie des mikroskops und der mikroskopischen, Wahrnehmung. *Arch. Mikrosc. Anat. Entwicklungsmech.*, 9:413 468, 1873.

[3] E. Abbe. Note for the proper definition of the amplifying power of a lens or a lens-system. *J. R. Microsc. Soc*, 4:348–351, 1884.

[4] C. Gao and X. D. Xiang. Quantitative microwave near-field microscopy of dielectric properties. *Review of Scientific Instruments*, 69(11), 1998.

[5] B. T. Rosner and D. W. van der Weide. High-frequency near-field microscopy. *Review of Scientific Instruments*, 73(7), 2002.

[6] Chen Gao, Fred Duewer, and X. D. Xiang. Quantitative microwave evanescent microscopy. *Applied Physics Letters*, 75(19):3005–3007, 1999.

[7] Q. Zhang and P. J. McGinn. Imaging of oxide dielectrics by near-field microwave microscopy. *Journal of the European Ceramics Society*, 25:407–416, 2005.

[8] J. F. Zurcher. Material imaging with the use of a microwave cavity perturbation technique. *Microwave and Optical Technology Letters*, 33(2), 2002.

[9] L. F. Chen, C. K. Ong, C. P. Neo, V. V. Varadan, and V. K. Varadan. Microwave Electronics: Measurement and Materials Characterization. John Wiley and Sons Ltd., 2004.

[10] T. W. Athey, M. A. Stuchly, and S. S. Stuchly. Measurement of radio-frequency permittivity of biological tissues with an open-ended coaxial line - Part 1. *IEEE Transactions on Microwave Theory and Techniques*, 30(1):82–86, 1982.

[11] M. Tabib Azar, D.-P. Su, A. Pohar, S. R. LeClair, and G. Ponchak. 0.4 mm spatial resolution with 1 GHz (wavelength = 30cm) evanescent microwave probe. *Review of Scientific Instruments*, 70(3):1725–1729, 1999.

[12] Atif Imtiaz, Thomas Baldwin, Hans T. Nembach, Thomas M. Wallis, and Pavel Kabos. Near-field microwave microscope measurements to characterize bulk material properties. *Applied Physics Letters*, 90, 2007.

[13] D. E. Steinhauer, C. P. Vlahacos, S. K. Dutta, B. J. Feenstra, F. C. Wellstood F. C, and S. M. Anlage. Quantitative imaging of sheet resistance with a scanning near-field microwave microscope. *Applied Physics Letters*, 72(7), 1998.

[14] D. E. Steinhauer, C. P. Vlahacos, F. C. Wellstood, S. M. Anlage, C. Canedy, R. Ramesh, A. Stanishevsky, and J. Melngailis. Imaging of microwave permittivity, tenability, and damage recovery in (Ba, Sr)TiO_3 thin films. *Applied Physics Letters*, 75(20), 1999.

[15] T. Wei, X. D. Xiang, W. G. Wallace Freedman, and P. G. Schultz. Scanning tip microwave near-field microscope. *Applied Physics Letters*, 68(24), 1996.

[16] A. Tselev, S. M. Anlage, H. M. Christen, R. L. Moreland, V. V. Talanov, and A. R. Schwartz. Near-field microwave microscope with improved sensitivity and spatial resolution. *Review of Scientific Instruments*, 74(6), 2003.

[17] Amphenol RF. SMA Connector Series. http://www.amphenol.co.uk/onlinecatalogue.htm, Accessed: November 2008.

[18] T.R. Kuphaldt. *Lessons in Electric Circuits*. 2003.

[19] Liisi Jylh, Johanna Honkamo, Heli Jantunen, and Ari Sihvola. Microstructure-based numerical modelling method for effective permittivity of ceramic/polymer composites. *Journal of Applied Physics*, 97, 2005.

[20] Youhua Gao, Erzhi Wang, Yanbin Li, and Hui Li. Analysis of transient electric field for epoxy spacer under lightning impulse voltage. *IEEE Transactions on Magnetics*, 42(4):595–598, 2006.

[21] J. Baker Jarvis, E.J. Vanzura, and W.A. Kissick. Improved technique for determining complex permititvity with the transmission / reflection method. *IEEE Transactions on Microwave Theory and Techniques*, 38(8):1096–1103, 1990.

[22] L M Ridgway. Measurement of high permititvity materials using microwaves. Master's thesis, Department of Electrical and Electronic Engineering, The University of Nottingham, 2006.

Chapter 6

Antenna applications

Microwave frequency covers the range of the electromagnetic spectrum with wavelengths from 1mm to 33cm [1], effectively a frequency in free space of 300GHz – 900MHz. This falls between the wavelengths of radio and optical waves and hence technologies operating at microwave frequency draw on methods also used by these neighbouring bands [2]. Antennas used at microwave frequency include horn antennas, reflector antennas and parabolic antennas. Higher frequency methods adapted for microwave techniques include the use of lenses to focus or direct a signal.

Over the last century communications advances have meant that the electromagnetic spectrum within the radio range has become increasingly crowded leading governments to assign spectrum space to users. Within the United Kingdom bandwidth is allocated by the communications regulator Ofcom [3]. By moving to higher frequencies within the microwave range more bandwidth is available which can be used to transmit either higher quality, or a larger quantity of standard quality signals. The modulation of a signal required for transmission is a much smaller percentage of the frequency spectrum

at microwave frequency than in the lower range, thus reducing the competition for space within the usable spectrum. For example; a simple amplitude modulated signal operating at 1000kHz with a modulation of 5kHz (ie 10kHz bandwidth in total) will use 1% of the spectrum space at that frequency. In comparison, 1% of the spectrum at 4GHz is 40MHz; a bandwidth large enough to transmit a high quality signal, or several lower quality ones [4].

The move to higher frequencies is not however, a trivial matter. When operating wavelengths become comparable to the physical dimensions of components and connections they exhibit greater losses caused by the skin effect and the effects of the capacitances and inductances can no longer be neglected. These design challenges are not only relevant to antenna design, but for any device which operates at microwave frequencies. Materials which components are constructed from may behave differently within the microwave range and therefore it is important to characterise materials at these frequencies. Mechanisms for this behaviour are detailed in Chapter 3.

The main frequencies of interest for this work are 2.40 – 2.485GHz which is that of Bluetooth [5]; 2.4, 3.7 and 5GHz which covers the various operating frequencies of wireless Local Area Networks (W-LAN) covered by the IEEE standards within IEEE 802.11 [6]; and for mobile telecommunications the 0.9GHz and 1.8GHz bands for Global system for Mobile Communications (GSM) technology [7] and 2.2GHz which is used for Universal Mobile Telecommunication System (UMTS) implementations [8].

The efficiency of any antenna is an important value for consideration. In its simplest form it can be expressed a figure of merit relating the energy supplied to the antenna to the energy radiated out from the antenna, such that:

$$Efficiency = \frac{Energy_{radiated}}{Energy_{input}} \tag{6.1}$$

The total efficiency of the antenna system is also effected by any impedance mismatch between the antenna and the feed such that the total efficiency will be equal to the antenna efficiency multiplied by the impedance mismatch loss of the antenna. The value for the efficiency will be between 0 and 1 and so is often quoted as a percentage figure. Dish and horn antennas which radiate into free space can have efficiencies approaching 100% whereas antennas used in mobile phone other small electronic devices may have an efficiency of between 20 – 70%. The act of placing an antenna within a device reduces the efficiency because energy is lost into neighbouring components [9] [10].

This chapter is concerned with reviewing the potential application of barium hexaferrite and bismuth substituted barium hexaferrite as a material for use in antenna design, therefore only antenna schemes in which a dielectric material is a component are considered.

6.1 Dielectric materials and antennas

Materials with a large dielectric constant have been used in an attempt to reduce the physical size of antennas [11][12], however this is not without problems. The electric field is concentrated around the region of high permittivity material (the near-field); resulting in an antenna with low efficiency which can only operate over a narrow frequency range [13]. The concentration of the electric field within the near-field, while not helpful in antenna design, does have applications in detecting the dielectric properties of materials

within a small area near the probe, which are considered in Chapter 5.

Another problem arises from the concept of characteristic impedance; a material which has a large dielectric constant, but a permeability of unity will have a low intrinsic impedance as set out in Equation 6.2.

$$\eta = \sqrt{\frac{\mu_0 \mu_r}{\varepsilon_0 \varepsilon_r}} \tag{6.2}$$

Where η is the intrinsic impedance in Ohms (Ω), μ_0 and μ_r are the permeabilities of free space and of the material respectively, and ε_0 and ε_r are the permittivities of free space and of the material respectively. Thus a material with a high relative permittivity and small relative permeability will have a low characteristic impedance. This is significant to the design of antennas when we consider the case of the intrinsic impedance of free space, where relative permittivity and permeability are both equal to unity, then Equation 6.2 is simplified to:

$$\begin{aligned} \eta &= \sqrt{\frac{\mu_0}{\varepsilon_0}} \\ &= \sqrt{\frac{4\pi \times 10^{-7}}{8.854 \times 10^{-12}}} \\ &= 376.73\Omega \end{aligned} \tag{6.3}$$

Any impedance mismatch between the intrinsic impedance of an antenna and that of the propagating medium (normally free space) will cause reflections at the boundary of the dielectric and that of air which increases the field inside the dielectric hence introducing losses. If a material was developed which had a permittivity and permeability with similar

(ideally identical) values, then the characteristic impedance of the device will match the intrinsic impedance of the air surrounding it. If achieved this would produce desirable efficiency gains.

6.1.1 Patch antennas

A patch (also referred to as a microstrip) antenna is, in its simplest form, a ground and a conducting plane separated by a dielectric substrate with a coaxial connection between the two. Because of the nature of their structure, they can be contained within thin packages and are lightweight so can mounted onto buildings unobtrusively and with relative ease. They are commonly used as local area network (LAN) and Bluetooth antennas [14] with high end devices used in applications such as spacecraft communications [15].

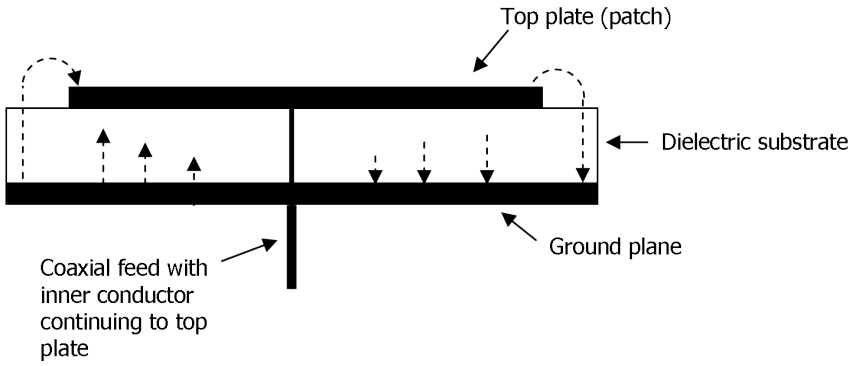

Figure 6.1: Diagram illustrating patch antenna structure and connections. The electric field is shown by dashed arrows.

Coaxial fed patch antennas are most commonly circular or rectangular (however a variety of other shapes are viable). Although dependant upon the thickness and dielectric properties of the substrate, a rectangular patch antennas is approximately half a wavelength wide and a circular patch antenna around 0.55 – 0.6λ in diameter ($\lambda = 0.125$m at 2.45GHz; thus antennas are in the region of 5cm large). The simple structure makes

them inexpensive to fabricate although restricted by a limited bandwidth, however this attribute can be improved by increasing the thickness of the substrate material. [4]

The option to fabricate patch antennas directly by etching onto a printed circuit board enables the construction of antenna arrays. Phased arrays are composed of several antennas mounted together to improve the gain and directivity compared to a single element. Individual antennas within the array can be powered on or off resulting in the ability to control the directivity of the array without physically moving it [4]. Thus the patch antenna becomes more useful than it first appeared.

6.1.2 Dielectric loaded patch antennas

A dielectric loaded patch antenna is a modification of a standard patch antenna. Here an additional dielectric resonator material is incorporated into the design with the result of increases in antenna bandwidth without alterations to the radiation patterns and gain of the original device. Permutations which have been investigated include using different shapes of patch antenna, different shapes of resonator material, different permittivities for resonant materials and altering the position of the resonant material on the patch [16] [17].

6.1.3 Dielectric lens antennas

Electromagnetic radiation signals can be reflected and refracted, as observed with visible light. Within the high range of the microwave frequency band (30GHz and upwards) dielectric lenses can be used to increase the directivity of a signal [4] [18]. By relating the dielectric properties of the material to the refractive index, a lens can be designed

which focuses the signal or converts the signal from a spherical wave form on one side of the lens, to a plane wave form on the other as seen in Figure 6.2. Dielectric antennas have applications in wireless broadband transmissions such as computing [19], uncompressed high definition television signals and radar collision avoidance [20]. Materials used to form dielectric lenses include Rexolite ($\varepsilon_r' = 2.53$), quartz ($\varepsilon_r' = 3.80$) [21], silicon ($\varepsilon_r' = 11.70$) [22] and Plexiglass ($\varepsilon_r' = 2.53$) [19]. These cover a large range of permittivities at high frequencies and unsubstituted barium hexaferrite is within this range, making it and bismuth doped barium hexaferrite a potential material for this application.

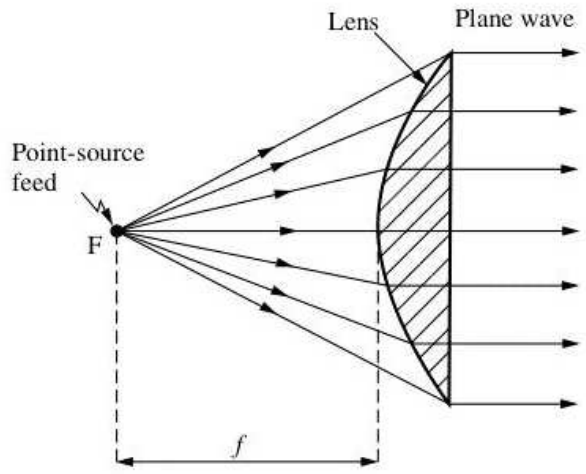

Figure 6.2: Diagram illustrating dielectric lens antenna configuration [23].

6.1.4 Dielectric resonator antennas

A dielectric resonator antenna (DRA) is formed by an antenna encased within or near to a dielectric material, which is designed to resonate at a specific frequency of interest [2]. The antenna can be a monopole [24] [25] or dipole [26]. Modifications to these basic designs can be used to introduce additional resonance frequencies to the antenna which

are chosen according to the specific application of the device [27]. Common shapes for the dielectric material used include circular [28], rectangular [29] or hemispherical [30] configurations. When a higher permittivity material is used the operational frequency decreases, however this is accompanied by a trade-off which sees a decrease in bandwidth [12]. The resonant frequency of the antenna is dependant upon the dimensions of the material used for the antenna and its dielectric properties. The antenna is most efficient at its resonant frequency, however modifications such as including two dielectric materials in the design can broaden the resonance peak enabling use over a wider frequency range [26].

Circular DRAs have two resonant modes which can be taken advantage of dependant on the positioning of the feed to the material. Figure 6.3 shows the $HE_{11\delta}$ and $TM_{01\delta}$ modes within the dielectric material.

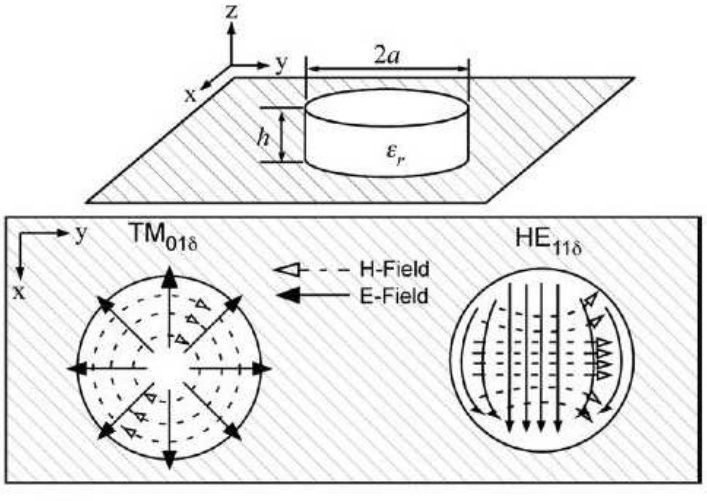

Figure 6.3: Modes available in a circular dielectric resonator antenna [31].

A circular DRA is operated to drive the $TM_{01\delta}$ mode by locating the coaxial probe feed within the centre of the dielectric material. The requirement to drill a hole for the a

coaxial feed in the dielectric material makes this configuration more difficult to construct, so attention was focussed on the $HE_{11\delta}$ design.

To excite the $HE_{11\delta}$ mode, the feed for the antenna is located outside of the dielectric material but still in contact with it, illustrated in Figure 6.4.

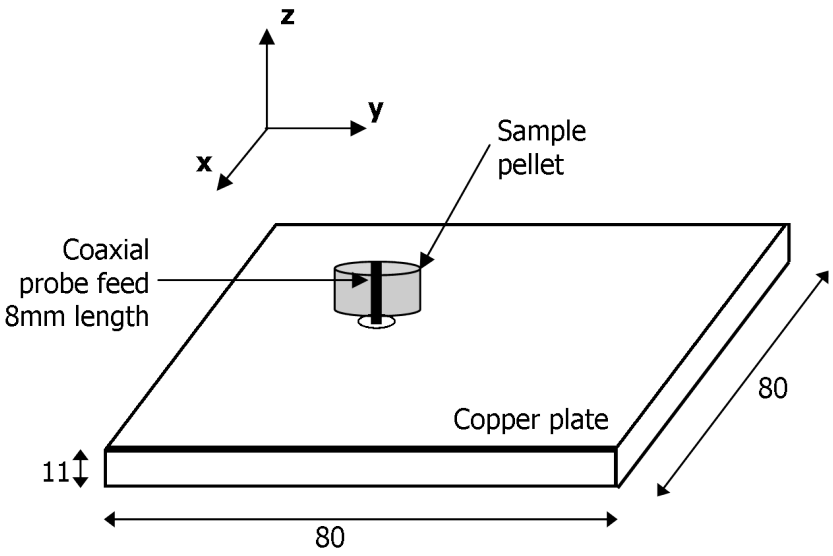

Figure 6.4: Diagram illustrating circular dielectric resonator antenna.

The dominant frequency in this mode can be calculated using the conventional dielectric wave-guide mode (CDWM), given as [32] [12]:

$$f_0 = \frac{3 \times 10^8}{2\pi\sqrt{\varepsilon_r'}} \sqrt{\left(\frac{1.841}{a}\right)^2 + \left(\frac{\pi}{2h}\right)^2} \tag{6.4}$$

Where f_0 is the resonant frequency, ε_r' is the real part of permittivity, a is the radius and h is the hight of the dielectric cylinder material. The resonant frequency of these antennas usually fall within the range 1 – 5GHz.

De-constructing Equation 6.4 it was observed that by altering the physical dimensions and permittivity of a sampled used within a DRA the resonant frequency can be modified

to operate in the desired range such that:

- Increasing sample permittivity will result in a lower resonant frequency;
- Increasing the thickness of the sample will result in a lower resonant frequency;
- Increasing the diameter of the sample will result in a lower resonant frequency.

Some of these parameters are more easily modified than others, however this does allow for a greater degree of flexibility in antenna design.

This type of antenna has applications within the telecommunications industry. In this field research focuses on reducing the physical size of antennas while maintaining acceptable bandwidth and efficiency values [33]. In addition, radiation limits are placed on mobile phone handsets by law. This is termed the Specific Energy Absorption Rate (SAR) this is "the rate at which energy is absorbed in body tissues, in watts per kilogram (Wkg^{-1})" [34].

A SAR limit of $2.0Wkg^{-1}$ in 10g of tissue was set within the International Commission on Non-Ionizing Radiation Protection (ICNIRP) Guidelines 1998 for devices operating from 0-300GHz [34]. This applied to all member states of the European Union from late 1999 [35].

Research into this topic identifies barium hexaferrite or a related compound could be used to fabricate a material loaded antenna which satisfies the SAR limit and provides desirable efficiency and bandwidth values [25].

6.2 Barium hexaferrite and bismuth substituted barium hexaferrite used as a material within a dielectric resonator antenna

This section considers the suitability of the barium hexaferrite and bismuth substituted barium hexaferrite compounds as the dielectric component of a dielectric resonator antenna.

Due to the samples formed being cylindrical in nature, the case of a cylindrical dielectric resonator antenna was considered.

The resonant frequency of an example pellet was calculated using Equation 6.4. The sample chosen was the $x = 0.5b$, series C pellet, which had been sintered for one hour at 1100°C. It has a diameter of 20mm, a thickness of 5.737mm and a permittivity of $\varepsilon_r = 7.8 - 0.96j$ at 2.45GHz (it was seen in Chapter 4 that the measured permittivity was approximately constant from 1 – 6GHz, so the permittivity at 2.45GHz is acceptable to use). These values were substituted into the formula as shown in Equation 6.5.

$$\begin{aligned} f_0 &= \frac{3 \times 10^8}{2\pi\sqrt{7.8}} \sqrt{\left(\frac{1.841}{10 \times 10^{-3}}\right)^2 + \left(\frac{\pi}{2 \times 5.737 \times 10^{-3}}\right)^2} \\ &= 5.641 \text{ GHz} \end{aligned} \tag{6.5}$$

This frequency is higher than that used in mobile telephony and Bluetooth applications. However this value can potentially be altered by modifying some properties of the material which is used to form the DRA (discussed in Section 6.1.4), to reiterate, the following

properties can be altered to shift the resonant frequency of the antenna:

- Increasing sample permittivity will result in a lower resonant frequency;
- Increasing the thickness of the sample will result in a lower resonant frequency;
- Increasing the diameter of the sample will result in a lower resonant frequency.

The permittivity of the sample will be dependant on both of the composition of the pellet and the smoothness of the exterior faces. This cannot be modified once pellets have been formed, but the permittivity can be taken into account by referring back to the high frequency permittivity measurements taken using the coaxial probe.

The physical properties of the sample; the thickness and the diameter can both be used to alter the frequency of the DRA set-up. Of these the sample thickness is easiest to change during the fabrication process by adding more green mixture to the die for pressing to form a thicker pellet and vice-versa.

The diameter of the sample is more difficult to change due to the fixed 20mm diameter of the die used in the fabrication process although this could be changed by using another die of a different diameter to form the sample pellets.

It should be noted that Equation 6.4 does not provide an input for the permeability of a resonator material. The magnetic properties of a sample used as the resonator in the DRA are likely to have an effect upon the resonant frequency of the device. This will be discussed further in Section –ref

The values of sample properties of pellet $x = 0.5b$ from series C used in Equation 6.4 were used as a control figure and then varied to investigate the impact on the resulting resonant frequency. First the effect of altering permittivity was calculated. The value was

doubled from $\varepsilon_r' = 7.8$ to $\varepsilon_r' = 15.6$ and other values were kept constant, as presented in Equation 6.6:

$$\begin{aligned} f_0 &= \frac{3 \times 10^8}{2\pi\sqrt{15.6}} \sqrt{\left(\frac{1.841}{10 \times 10^{-3}}\right)^2 + \left(\frac{\pi}{2 \times 5.737 \times 10^{-3}}\right)^2} \\ &= 3.989\ \text{GHz} \end{aligned} \tag{6.6}$$

By doubling the permittivity of the resonator material the resonant frequency has shifted from 5.641GHz to 3.989GHz.

The next parameter to be changed was the sample thickness. The original value of 5.737mm was increased by 1mm to 6.737mm, as in Equation 6.7:

$$\begin{aligned} f_0 &= \frac{3 \times 10^8}{2\pi\sqrt{7.8}} \sqrt{\left(\frac{1.841}{10 \times 10^{-3}}\right)^2 + \left(\frac{\pi}{2 \times 6.737 \times 10^{-3}}\right)^2} \\ &= 5.079\ \text{GHz} \end{aligned} \tag{6.7}$$

Increasing the thickness of the material by 1mm has the effect of reducing the resonant frequency from 5.641GHz to 5.079GHz.

The final sample property to be changed was the diameter, from a 20mm diameter to a larger 22mm diameter as shown below in Equation 6.8:

$$\begin{aligned} f_0 &= \frac{3 \times 10^8}{2\pi\sqrt{7.8}} \sqrt{\left(\frac{1.841}{11 \times 10^{-3}}\right)^2 + \left(\frac{\pi}{2 \times 5.737 \times 10^{-3}}\right)^2} \\ &= 5.486\ \text{GHz} \end{aligned} \tag{6.8}$$

Increasing the diameter of the sample by 2mm (and thus the radius by 1mm) reduced the resonant frequency from 5.641GHz to 5.486mm.

From these values it can be concluded that of the physical properties, modifying the thickness of the sample is the most effective way to change the resonant frequency of the material. This is also convenient from a fabrication viewpoint because this is the easiest of the physical properties to control. The thickness of the samples vary between each pellet which will have to be taken into account when the resonant frequencies are characterised for the different samples. There is no consideration of the length of the probe feed to excite the resonant material within this equation, so the Comsol simulation package was utilised to investigate the effect of changing this element.

6.3 Modelling a dielectric resonator antenna in Comsol Multiphysics

The RF module: Electromagnetic Waves within Comsol Multiphysics 3.3a was used to model various configurations of DRA. Three-dimensional modelling was used to create the two different dielectric resonator antenna types; where the coaxial feed is within the material, and where the feed is outside of the probe. The model was based upon using the series C $x = 0.5b$ sample which has been used in previous simulations. It has a diameter of 20mm and a thickness of 5.737mm with a high frequency permittivity of $\varepsilon r = 7.8 - 0.96j$ at 2.45GHz. The frequency range 40MHz – 20GHz was used to investigate the resonant frequency of the system by adding a scalar variable representing the operational frequency to the simulation parameters.

6.3.1 Inside material probe feed

With the coaxial probe feed located inside the dielectric material the $TM_{01\delta}$ mode is excited. In its basic form the coaxial feed is located in the centre of the pellet and the depth the probe penetrates into the material is varied. Figure 6.5 shows the model geometry for a 4mm probe depth located in the centre of the sample.

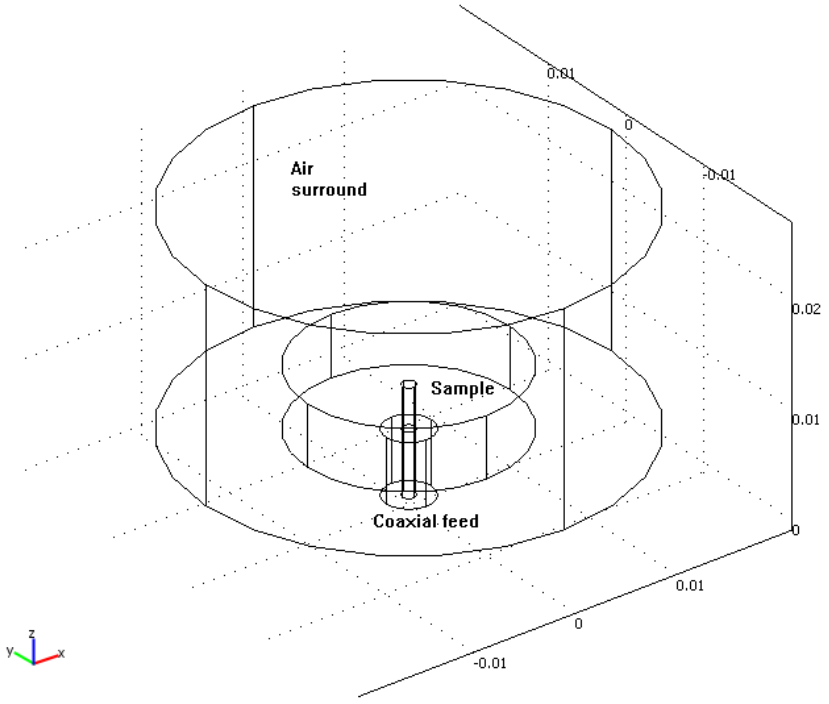

Figure 6.5: Model geometry for DRA with coaxial feed inside the sample with model parts labelled.

The boundary conditions were established so that the end of the coaxial line was set as a coaxial input port; the edges of the inner and outer conductors of this line as perfect electric conductors; the plane including and extending beyond the bottom edge of the sample also as a perfect electric conductor to represent a ground plane; the edges of the large air surrounding area were set as scattering boundary conditions for a spherical wave condition.

Figure 6.6 displays the S11 simulation results for the DRA operating in $TM_{01\delta}$ mode

plotted to the same scale. All of the simulation results show a first resonant frequency at 7.7GHz which varies in magnitude with the differing probe depths; the greatest magnitude is -32.5dB for the 4mm probe and the smallest of -0.99dB when the probe does not penetrate the sample. There are further resonances at higher frequencies which vary dependant upon the probe depth. The simulation results can be used to decide upon the suitability of a set-up for an antenna; if the device was operating at 7.7GHz and the broadband behaviour of the device was not critical, a 4mm depth probe provides a strong resonance frequency which would produce a good performance antenna at this specific frequency. If a higher operational frequency was needed or the DRA was required to operate over a wider frequency range, one of the other probe depths such as the 5mm set-up may be more appropriate. This is because the 5mm length provides a more broadband antenna, which can be seen by observing the response below -10dB; this covers a wider range of frequencies for the 5mm probe and a smaller range for other designs.

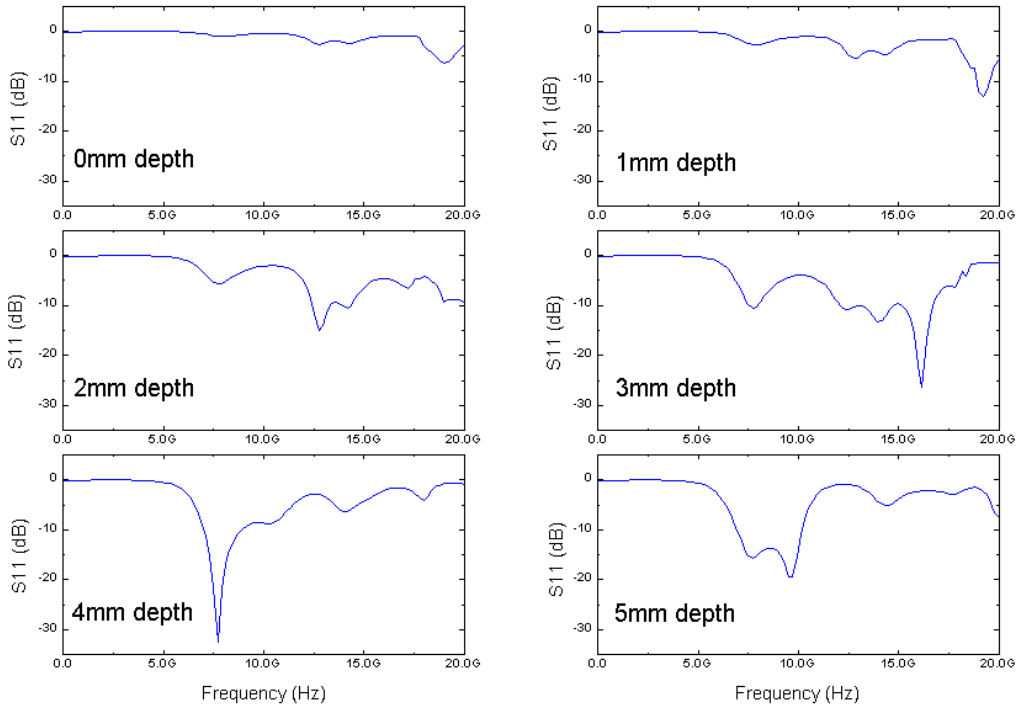

Figure 6.6: S11 simulation results for DRA with coaxial feed in centre of the material and varying probe depths

6.3.2 Outside material probe feed

The variation the of DRA where the coaxial probe feed is located outside the sample but in contact with it is used to excite the $HE_{11\delta}$ mode. This configuration also has the benefit of not requiring the sample to be drilled to accept a probe feed, which is desirable with barium hexaferrite due to brittleness of the material and the safety requirements due to the process releasing small particles of barium hexaferrite into the atmosphere during the machining procedure.

The model geometry is shown in Figure 6.7 with the barium hexaferrite sample highlighted. The sample used in the simulation was the series C $x = 0.5b$ sample, with properties given above. Boundary conditions were also the same as those defined above and the simulation was run over the frequency range 40MHz – 20GHz.

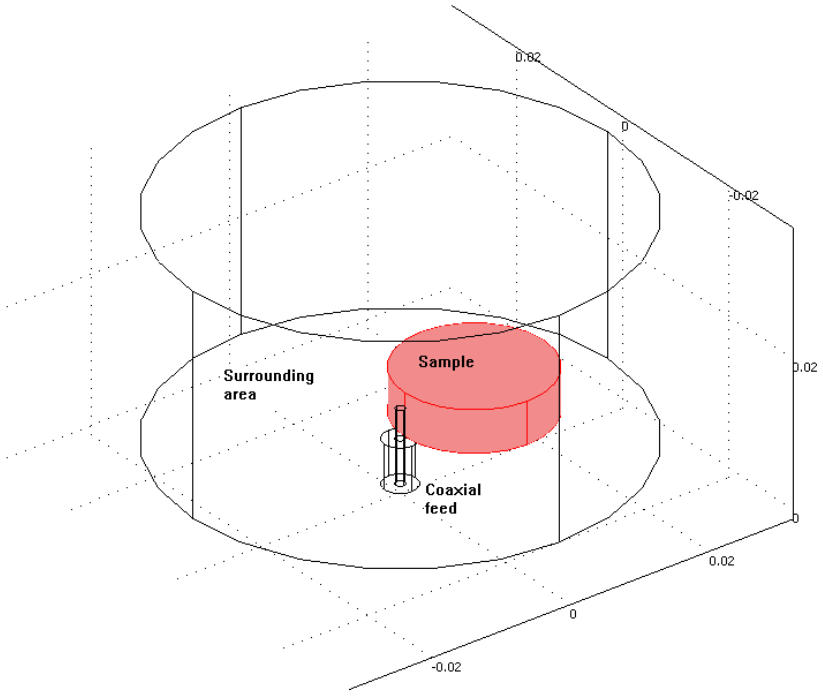

Figure 6.7: Model geometry for DRA with coaxial feed outside the sample with model parts labelled and sample region highlighted.

Simulation results for a range of different coaxial probe feed lengths from 1 – 8mm (including a 5.737mm probe feed, which is equal to the height of the sample pellet) are shown in Figure 6.8 all plotted to the same scale. Although difficult to see in the smaller length probes, all simulations show the first resonance frequency of the system at 5.85GHz which varies in magnitude dependant upon the probe length. The largest magnitude resonances are seen for the longer probe feeds; ranging from -0.124dB for the 1mm probe feed; -4.744dB for the 5.737mm probe; to a maximum of -7.518dB for the 8mm probe. The differing probe lengths all also show a second resonant peak at 7.71GHz before patterns become more difficult to discern. An interesting feature of this second resonance frequency is the magnitude is greatest when the probe feed length is equal to the thickness of the sample pellet (-0.780dB for 1mm probe; -14.597dB for 5.737mm probe; and -13.1dB for 8mm probe). The bandwidth of this antenna configuration is similar for most probe lengths; the response dips both above and below the -10dB point while the frequencies at which this occurs is more dependent upon the probe length with longer probes producing resonances beginning at lower frequencies.

The first resonant frequency at 5.85GHz is slightly higher than that calculated in Equation 6.5, however the simulation takes a surrounding area of air into account which is neglected in the equation form, which will limit the accuracy of this simple equation. From a device design standpoint, for use within telecommunications, the resonances within the lower frequency ranges are most suitable for exploitation by setting the probe length dependant upon the resonant frequency where the antenna will be operating. Beyond the first two resonant frequencies mentioned here there are additional resonances at higher frequencies which have the potential to be used by devices operating in this range.

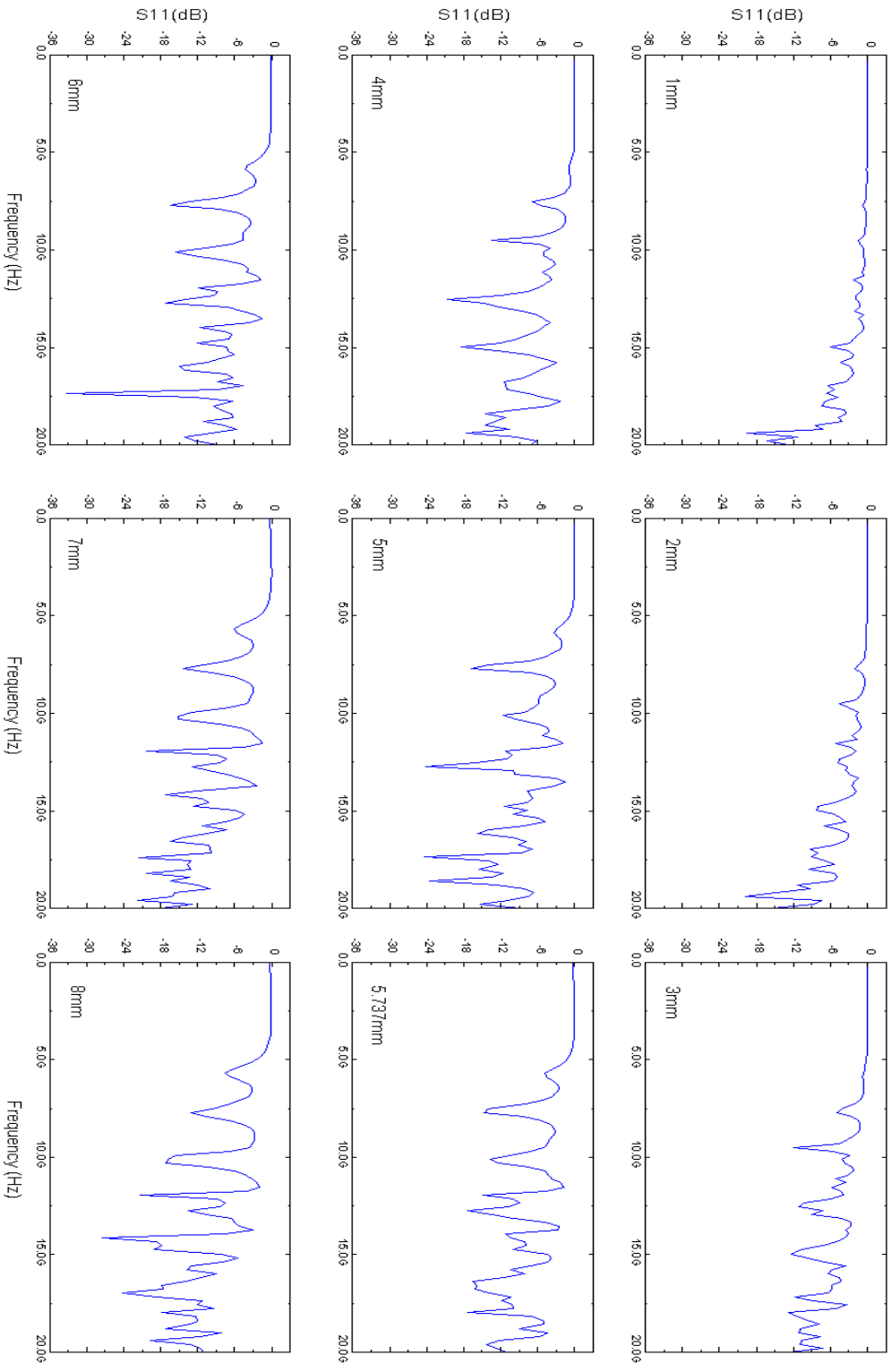

Figure 6.8: S11 simulation results for DRA with coaxial feed in contact with outside edge of the material and varying probe lengths

6.4 Fabrication of barium hexaferrite DRA

The outside material feed which excites the $HE_{11\delta}$ mode was the selected configuration for the construction of a DRA using the barium hexaferrite sample pellets. The design consisted of a copper plate which acted as a ground plane with a small hole drilled near the centre to accommodate the inner conductor and insulation of an SMA connector which provided the excitation to the barium hexaferrite pellet. Barium hexaferrite sample pellets were in turn placed on the copper plate in contact with the probe feed before the antenna system was characterised over the 45MHz – 20GHz range. Figure 6.9 shows the design of the DRA with a barium hexaferrite sample pellet in place.

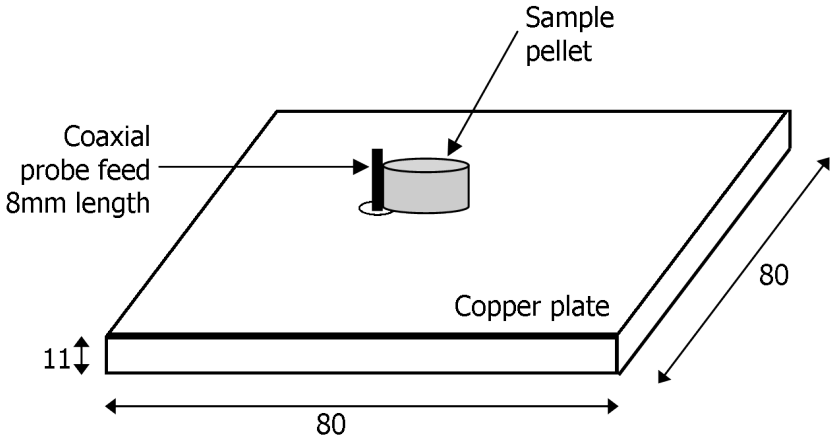

Figure 6.9: Image showing the design of the simple DRA with a sample pellet in place. Main body of coaxial connector underneath copper plate is not shown (all dimensions in mm)

6.5 S11 results for DRA

6.5.1 S11 results DRA using samples which have been sintered at 1100°C

Series F

Series F contains six sample pellets which have the same low level of bismuth content ($BaBi_{0.1}Fe_{11.9}O_{19}$) sintered for three hours at 1100°C. The similarities of this pellet series allowed further investigation to validate the experimental method and so these results are presented first.

Sensitivity of measurement to sample pellet orientation

Conclusions on method accuracy were drawn from the similarities between the resonant frequencies of the whole series, between different sides of the same pellet and when the sample was rotated on the conducting plate. Figure 6.10 shows the results of this investigation where one pellet is taken and the S-parameters charactered. The figure shows the results for the series F pellet $x = 0.1f$ which was placed into position and S11 recorded (top left), then rotated by 180° maintaining the same surface in contact with the conducting plate (top right). The bottom left graph shows the S11 data when the sample was then flipped over so that the other face of the pellet was in contact with the conducting plate. The final section of the graph (bottom right) shows the resulting S11 data when the material is rotated 180°C.

The first observation is that the S11 results for side 2 of the pellet are virtually identical; the resonant peaks are centred in the same position for both measurements and the magnitude of the resonances are similar (the most significant resonance at 9.55GHz has

a magnitude of -27.93dB for point 1 and -27.55dB for point 2). For side 1, the overall shape of the S11 response and positions of the resonant frequencies are similar, however not as close as the agreement shown for side 2 (the dominant resonant peak is -36.76dB at 8.95GHz for point 1 and -44.89dB at 9.00GHz for point 2). The strong resemblances in S11 results between point 1 and 2 for each separate side of the sample pellet allows the conclusion to be drawn that the positioning of the pellet in relation to the probe feed is not significant to resonant frequency positions and depth. Indeed this is supported when considering the theory of resonant modes; these are established throughout the body of the sample, not locally near to the probe feed, so it is expected that rotating the pellet should not have an adverse effect on the antenna response. The slight variations in the S11 pattern observed for side 1 are likely to be due to small material defects which are not accounted for when considering a theoretical perfect homogeneous sample with ideally smooth surfaces.

By comparing the S11 data of side 1 and side 2 it can be seen that the shape of the response is broadly similar with three clear resonant peaks, the second of which has the greatest magnitude. The centre position of the resonance shifts between side 1 and 2, from 6.51GHz to 6.32GHz respectively for the first peak; 8.95 – 9.00GHz to 9.55GHz for the second peak; and 13.0 – 13.1GHz to 13.4GHz for the final peak. The first resonant peak is at a higher frequency for side 1 and the next two peaks are at lower frequencies compared to side 2. Thus the conclusion was drawn that although there are differences in the S11 measurements depending on which face of the pellet is in contact with the copper ground plane, the similarities are more significant. The most likely reason for these changes are small deviations from a perfect cylinder shape in the barium hexaferrite sample pellets. These variations will be exaggerated by the design of

the prototype antenna due to the pellets simply being placed onto the copper plate rather than attached with conducting epoxy resin which would minimize the air gaps between the material and the ground plane due to surface roughness.

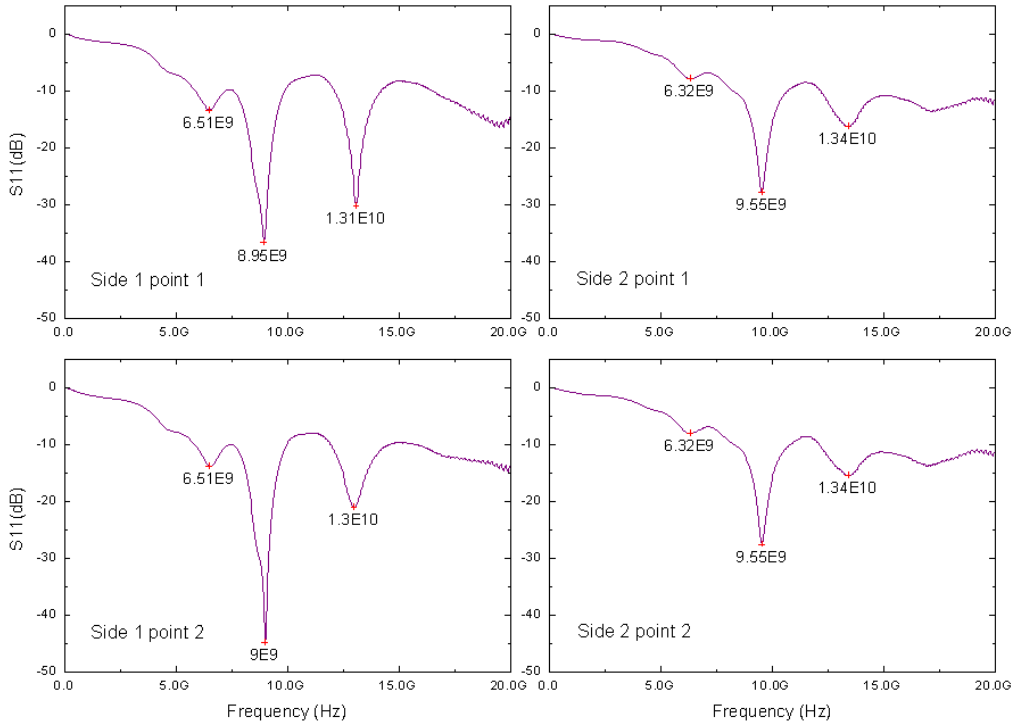

Figure 6.10: DRA S11 results for series F, pellet $x = 0.1f$ composition $BaBi_{0.1}Fe_{11.9}O_{19}$. Graphs to the left of the figure show results for side 1 when the material is rotated 180° for each measurement. Graphs on the right show the same process for the reverse side of the pellet

Series F - All samples

Figure 6.11 shows S11 results for a DRA antenna assembled from the six different pellets from series F. Data was collected for the situation when each face of the pellet was in contact with the ground plane. Results presented here were those where the first resonant frequency was the higher of the two for consistency.

The S11 patterns are notably similar in terms of resonance frequency peak positions and magnitudes. All graphs present the same pattern of a first resonant peak from 6.32

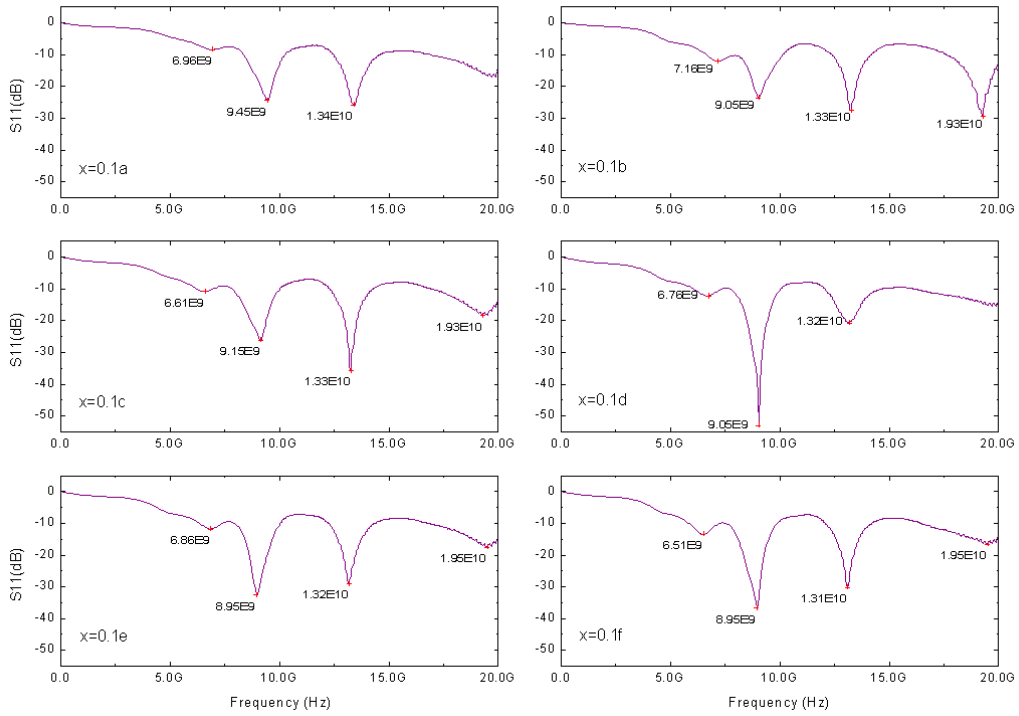

Figure 6.11: DRA S11 results for sample pellets from series F, composition all $BaBi_{0.1}Fe_{11.9}O_{19}$ over the frequency range 45MHz – 20GHz

– 7.16GHz which has the smallest magnitude; a second larger resonant peak centred around 8.95 – 9.8GHz; and a third peak from 13.1 – 13.5GHz depending on the pellet under scrutiny. The $x = 0.1b, c, e$ and f display a forth resonant peak above 18GHz however due to the performance of the SMA connector which forms the feed for the antenna only being guaranteed up to 18GHz this was not taken into consideration as a potential operational mode.

Conclusions

The first resonant frequency shows a variation of 0.84GHz between the lowest and highest frequency centres from all pellets and all sides; the second frequency peak has a variation of 0.85GHz; and the third resonance a 0.4GHz difference. Some differences in the

resonant frequency position were expected due to both physical defects (as investigated earlier) and because although the pellets all have the same composition there will be some variation in the material properties across the series. Taking these factors into account, the conclusion was drawn that the experimental method produces reliable results and that resonant frequencies are repeatable for pellets of the same composition treated by the same sintering regime.

Series A

Series A consists of samples containing varying levels of bismuth doping which have been sintered for one hour at 1100°C followed by a further hour at 1200°C. These pellets were placed onto the DRA antenna base and the resulting S11 parameters were recorded as shown in Figure 6.12.

The first observation is that the $x = 0.0$ undoped sample has a very different S11 response to the other pellets which contain varying levels of bismuth. The first resonant frequency for the undoped pellet is centred at 4.13GHz but it has a very small magnitude (-0.694dB) compared to higher frequency resonances. The higher frequency resonances from 8.5GHz have a much greater magnitude and occur more often at higher frequencies. The other samples which contain bismuth display a more similar response with five clear resonance peaks for the majority of compositions; the exceptions being the materials with the lowest and highest concentrations of bismuth. Both $x = 0.2$ and $x = 1.5$ display a double dip peak at the second resonant frequency around 7.3 – 7.4GHz. The $x = 0.2$ sample also has an additional resonance at 8.86GHz, which is visible only as a small dip on the graphs for other compositions. The first resonant frequency is centred between 3.48 – 3.73GHz over the whole selection of pellets and sides, lower than that of the

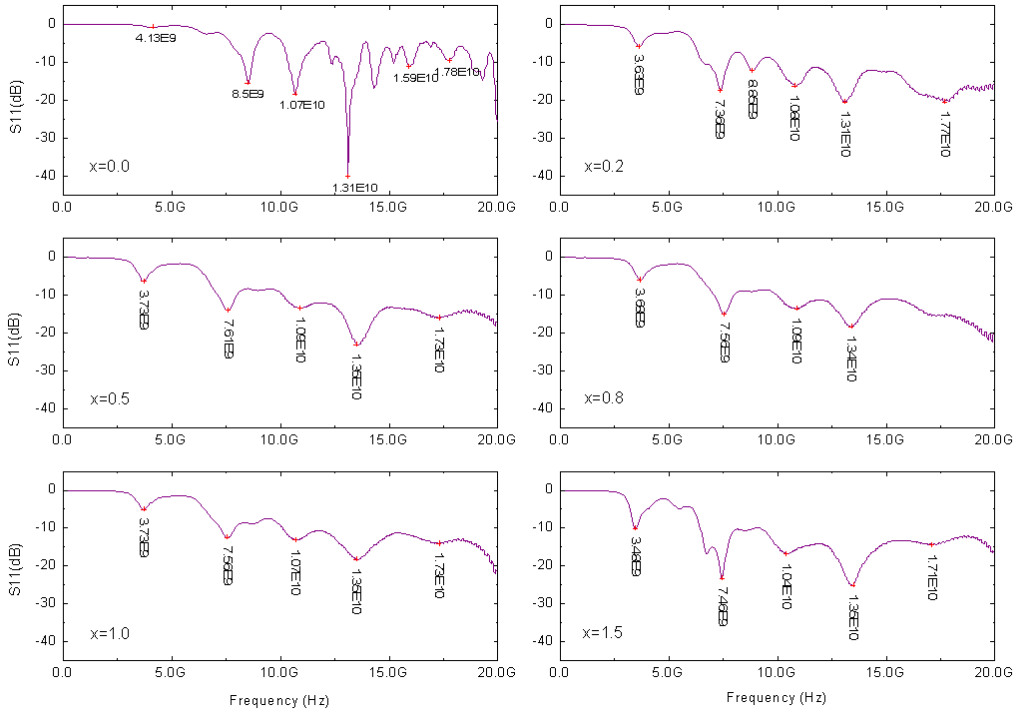

Figure 6.12: DRA S11 results for sample pellets from series A, composition $BaBi_xFe_{12-x}O_{19}$ over the frequency range 45MHz – 20GHz

parent barium hexaferrite sample. This result is expected when the higher permittivity of the bismuth containing samples is considered which will lower the resonant frequency of the antenna configuration.

Series B

Series B is composed of a variety of pellets containing differing levels of bismuth which have been sintered for one hour at 1100°C. Figure 6.13 shows the S11 data when these pellets are used within the DRA set-up.

This series contains two compositions which have repeat pellets; the lowest and highest concentration of bismuth, samples $x = 0.2$ and $x = 1.5$. The S11 data shows good agreement for the same composition $x = 0.2a$ and b and the $x = 1.5a$ and b

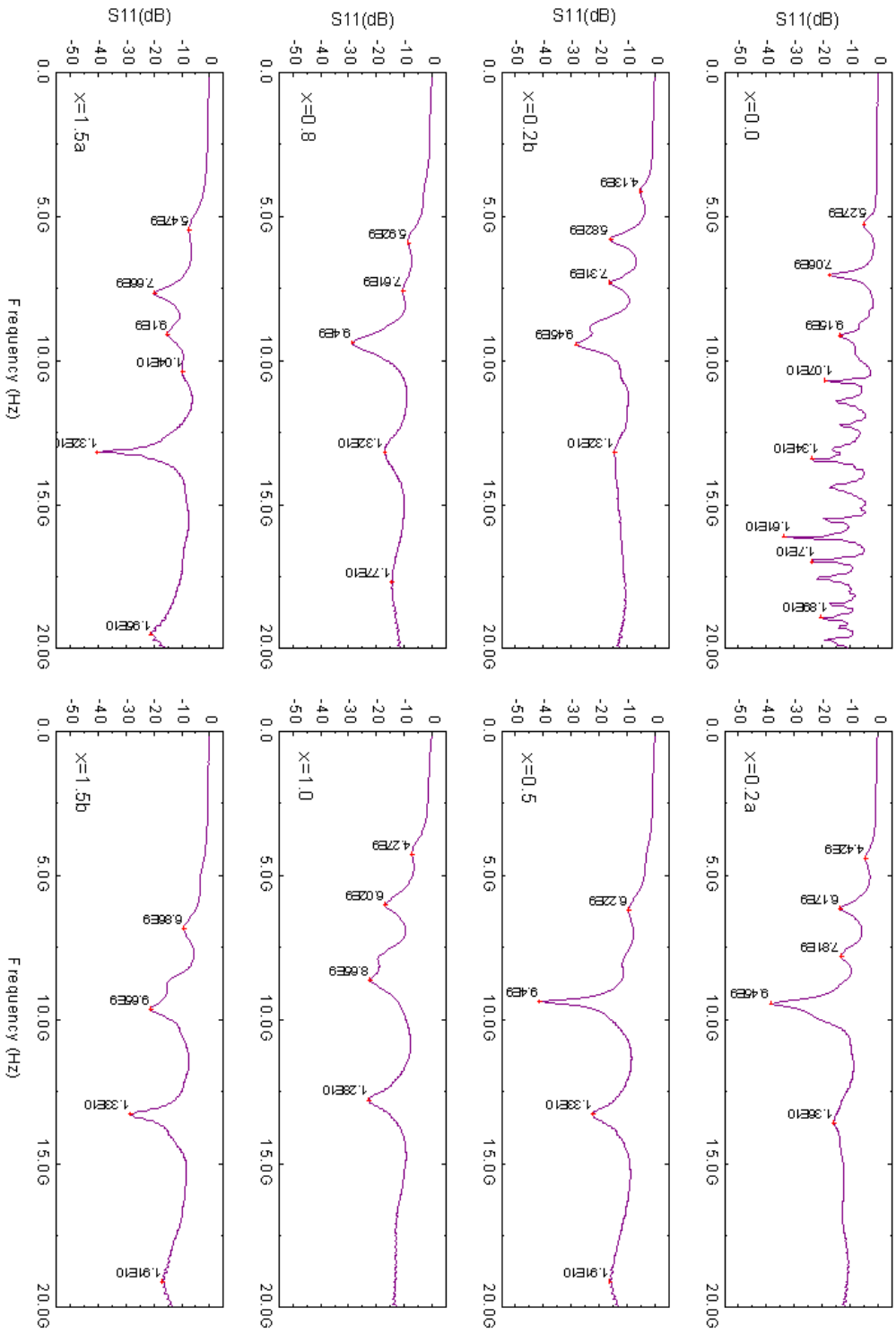

Figure 6.13: DRA S11 results for sample pellets from series B, composition $BaBi_xFe_{12-x}O_{19}$ over the frequency range 45MHz – 20GHz

samples.

Series C

Graphs for series C pellets are presented in a slightly different format because there are repeat pellets for each composition. Figures 6.14, 6.15, 6.16, 6.18, 6.19 and 6.20 show the S11 data for DRA antennas assembled with these samples. The 'Side 1' and 'Side 2' referred to in the following data is simply a marker to distinguish between the two possible orientations of each pellet on the DRA rig.

Sample composition x = 0.0

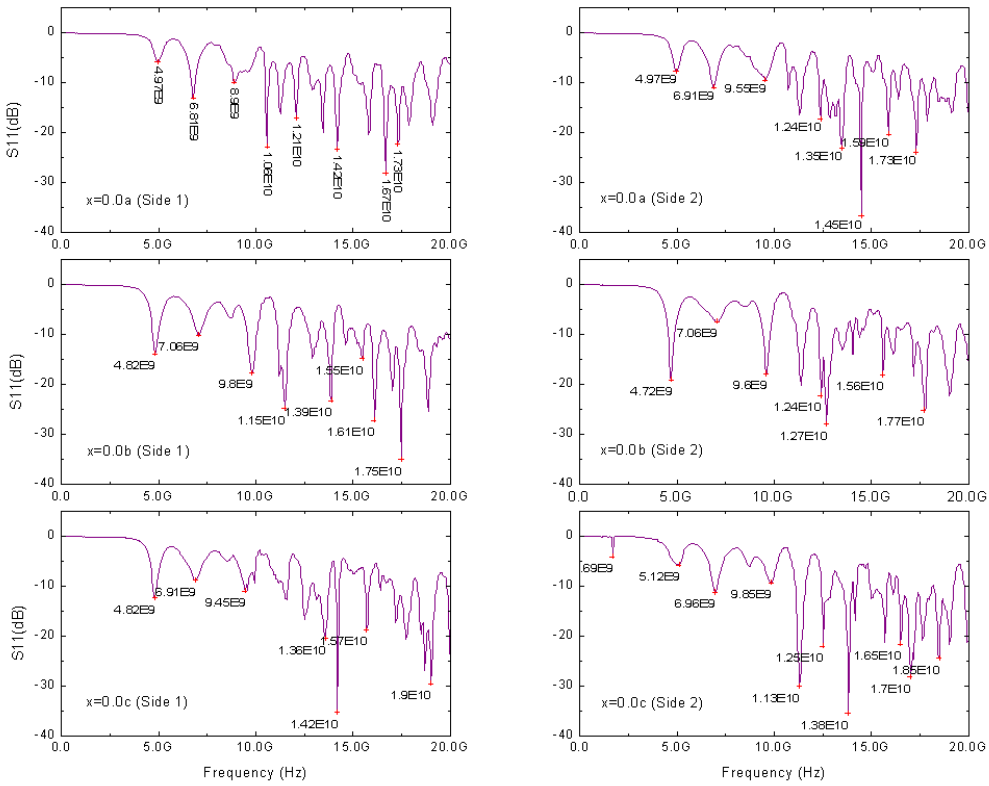

Figure 6.14: DRA S11 results for sample pellets from series C, composition $BaFe_{12}O_{19}$ over the frequency range 45MHz – 20GHz

Figure 6.14 presents the S11 parameters of the DRA set-up when an undoped barium hexaferrite sample is the resonant material. These three different samples have the same composition having been formed at the sample time from the same green mixture and sintered at the same time, thus subjected to the exact same sintering regime. The graphs display the response for both sides of the three pellets. With the exception of $x = 0.0c$ side 2, the first resonant peak occurs across the small range 4.72 – 4.97GHz with a magnitude of -5.865 – -19.09dB. The cause of the unexpected S11 response of sample $x = 0.0c$ side 2 is most likely to be due to surface imperfections on side 2 which is the surface in contact with the grounding plate rather than an issue with the pellet as a bulk, because the results for side 1 are in line with the other sample results. Due to the low loss nature of the material, many resonant peaks occur in the higher frequency ranges which makes it more difficult to draw firm conclusions about high frequency performance of this potential antenna. However the consistency of the position of the first resonant frequency peak verifies the set-up but leads to the conclusion that this frequency is too high for Wi-fi and Bluetooth applications, but this device could be used for other higher frequency applications.

Sample composition x = 0.2

The S11 response of the DRA when the lowest concentration of bismuth is added to the barium hexaferrite pellet mixture is shown in Figure 6.15. The first observation is that the shapes of these responses are similar both between the different faces of the same pellet and when the two individual pellets are compared. The first resonant frequency is small and the shape is not a distinct peak with the exception of sample $x = 0.2c$ side 1 (bottom left graph), occurring over the range 4.37 – 4.72GHz with a magnitude of -4.540 – -

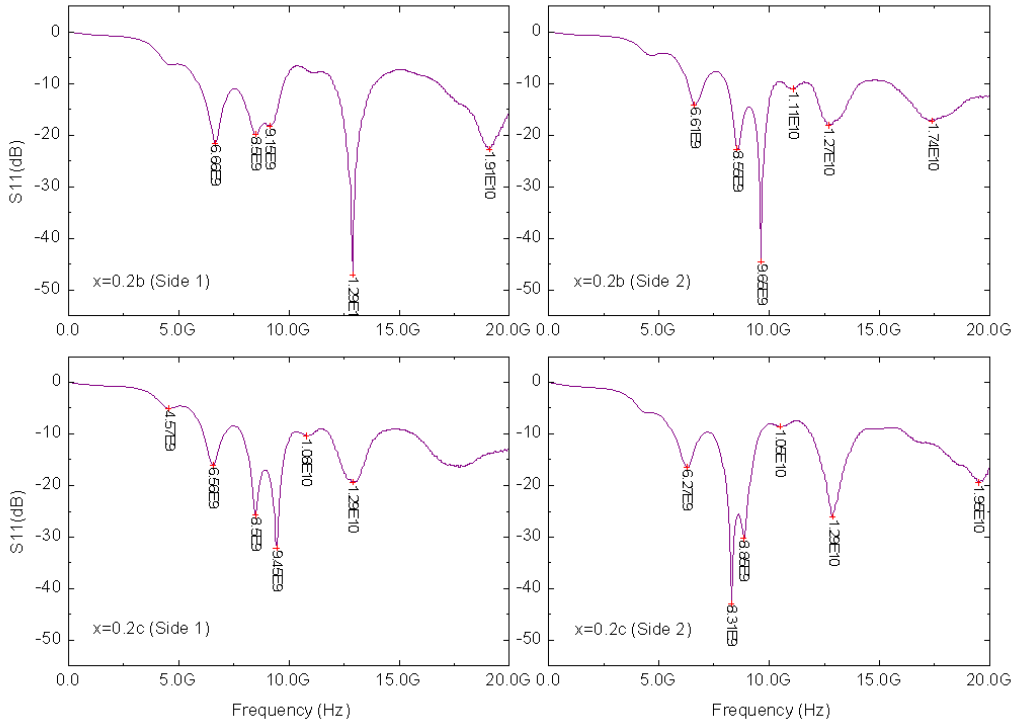

Figure 6.15: DRA S11 results for sample pellets from series C, composition $BaBi_{0.2}Fe_{11.8}O_{19}$ over the frequency range 45MHz – 20GHz

6.362dB for all graphs. This value is consistently lower than that of the undoped material of this series; confirming that the addition of bismuth to increase the permittivity of the material has reduced the frequency and increased the magnitude of the resonance of the antenna, making the material more suitable for telecommunications purposes. The higher frequency resonant positions of the DRA are also notably similar between the graphs. A second resonant frequency occurs between 6.27 – 6.66GHz followed by a double peak with a first part between 8.31 – 8.56GHz and a second part between 8.88 – 9.65GHz. A forth small indistinct resonance frequency is located around 10.6 – 11.1GHz and a fifth across the 12.7-12.9GHz. Although the position of each of these resonances is constant for each sample and side, the magnitudes of these peaks vary considerably.

Sample composition x = 0.5

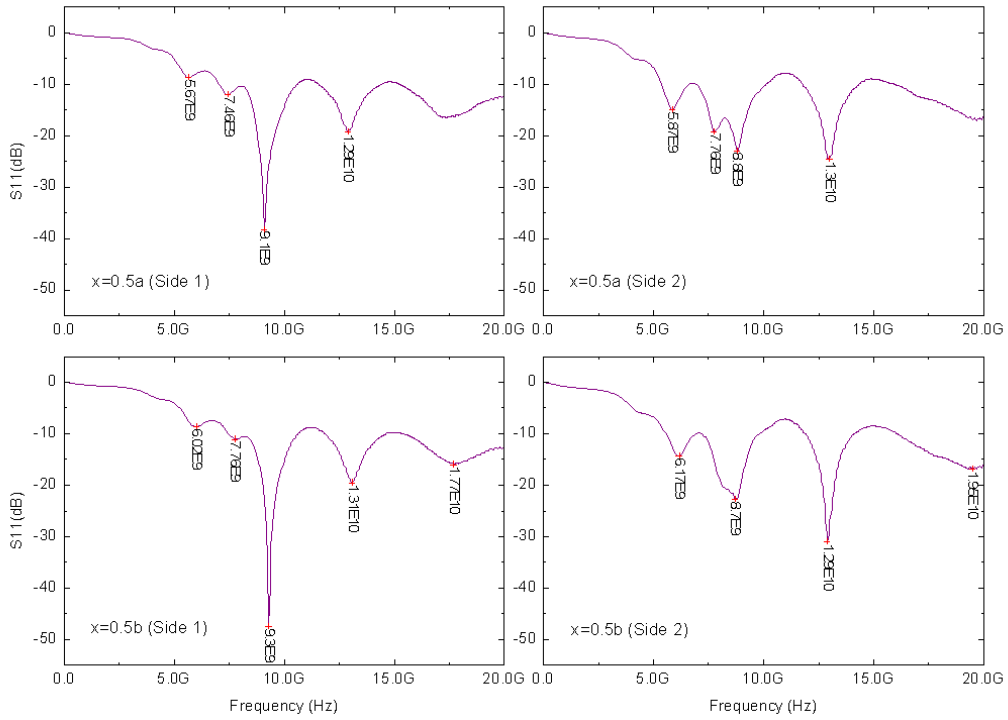

Figure 6.16: DRA S11 results for sample pellets from series C, composition $BaBi_{0.5}Fe_{11.5}O_{19}$ over the frequency range 45MHz – 20GHz

Figure 6.16 shows the S11 parameters for the DRA rig when pellets of composition $BaBi_{0.5}Fe_{11.5}O_{19}$ are used at the resonant material. An interesting feature of these results is the frequency responses are more similar between different sample pellets than for different sides of the same pellet; $x = 0.5a$ side 1 is more similar to $x = 0.5b$ side 1 (top and bottom left graphs) than their respective side 2 graphs, and in turn the S11 data for $x = 0.5a$ side 2 is also very similar to $x = 0.5b$ side 2 (top and bottom right graphs). The results for side 1 also bear a strong similarity to the $x = 0.5$ pellet from series B which has been subjected to the same sintering conditions, thus confirming repeatability for pellets of the same composition and sintering regime synthesised at different times.

The details of the S11 response for the series C $x = 0.5$ pellets show resonant peaks in similar positions over the frequency range, but with varying magnitudes and resolutions. For the side 1 traces there is one peak at 9.1 or 9.3GHz which is narrow and displays a much greater magnitude than the others (maximum of -47.46dB compared to -19.24dB for the next largest). Overall trends observed in all samples are an initial resonance ranging from 5.67 – 6.17GHz with magnitude -8.868 – -14.984dB. A second peak around 7.5GHz which is separate on the side 1 graphs but forms the first part of a double peak on the side 2 traces along with a second part at 8.8GHz. The comparable peak on the side 1 graphs is the high Q-factor peak described before. A final forth peak is separate and distinct for all samples over the 12.9 – 13.1GHz range.

Comparison of theoretical and test results

The $x = 0.5b$ pellet from series C was of special interest due to the initial DRA calculations and simulations being used as sample values. The theoretical value of resonant frequency given by Equation 6.4 for this pellet was calculated as 5.641GHz. The simulated value for this pellet from Comsol was 5.85GHz. The experimental data shows a first resonant frequency of 6.02GHz for side 1 and 6.17GHz for side 2, both higher than the theoretical values. A graph presenting these results is shown in Figure 6.17.

The equation used to calculate the resonant frequency does not allow for the inclusion of a permeability term (μ_r) however it is likely that the magnetic properties of the material will have an effect upon the resonant frequency of the system. To investigate this, Equation 6.4 was rearranged such that the experimentally found resonant frequency and sample dimension could be input to produce the apparent permittivity (ε_r) of the material. It was found that when the resonant frequency of 6.02GHz was used the

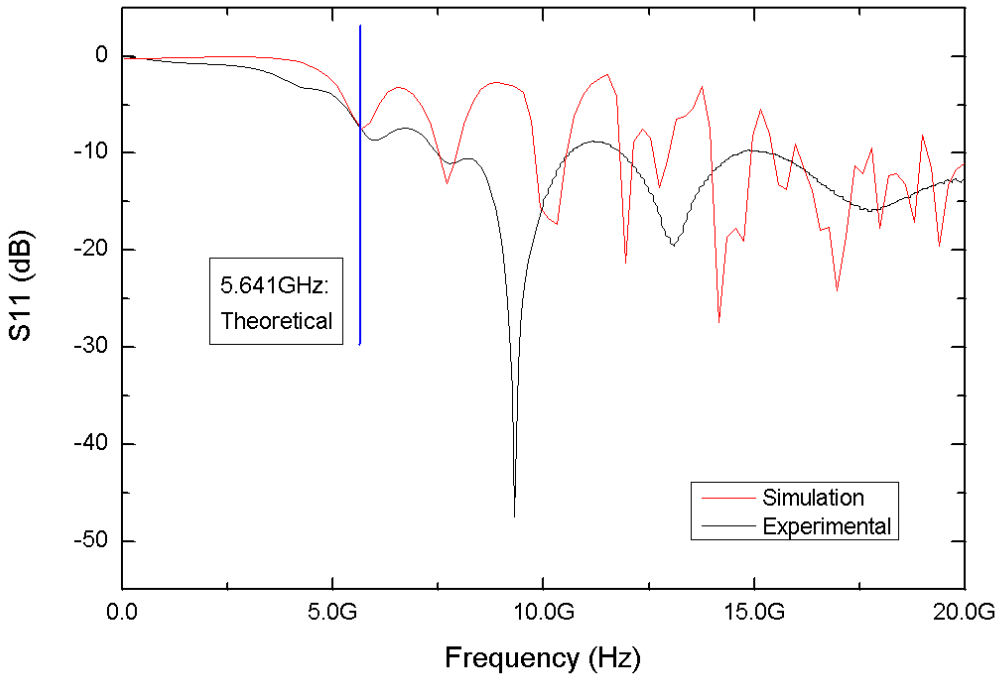

Figure 6.17: DRA S11 results for sample pellets from series C sample x=0.5b, theoretical, simulation and experimental results over the frequency range 45MHz – 20GHz

apparent permittivity of the material was calculated as $\varepsilon_r' = 6.848$ (there is no provision for calculating the imaginary part of permittivity). This value is lower than the measured high frequency permittivity of the material found in Chapter 4 of $\varepsilon_r = 7.8 - 0.96j$. The unknown effect of the permeability in the theoretical resonant frequency calculation is likely to contribute towards this discrepancy in the resonant frequency found theoretically and that found experimentally.

Sample composition x = 0.8

S11 parameters for the DRA when samples with the composition $BaBi_{0.8}Fe_{11.2}O_{19}$ are shown in Figure 6.18. This set of samples display a series of four resonant peaks with good agreement in results between samples. Interestingly there is a stronger correlation between the different pellets than there is between different faces of the same pellet;

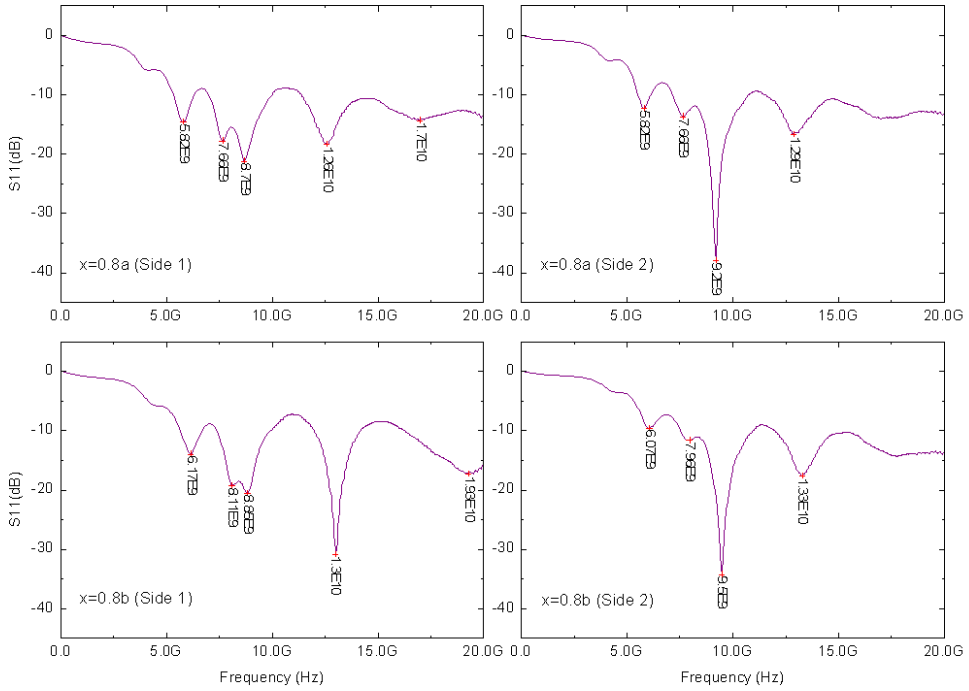

Figure 6.18: DRA S11 results for sample pellets from series C, composition $BaBi_{0.8}Fe_{11.2}O_{19}$ over the frequency range 45MHz – 20GHz

$x = 0.8a$ side 1 and $x = 0.8b$ side 1 are similar, so too are $x = 0.8a$ side 2 and $x = 0.8b$ side 2, this was also observed for the $x = 0.5$ samples within this series. The data for all scenarios show a potential earlier resonance frequency at around 4GHz, magnitude from -3.363 – -5.601dB, which was not sharp enough to be located by the peak finding tool in the Origin software used to produce the graphs.

The $x = 0.8a$ side 2 and $x = 0.8b$ side 2 graphs show very similar resonant frequency positions to those displayed by the series B sample of the same composition.

Sample composition x = 1.0

The $x = 1.0$ pellets from series C DRA results are shown in Figure 6.19. Three of the graphs $x = 1.0a$ side 2 and both $x = 1.0b$ samples appear to be very similar in terms

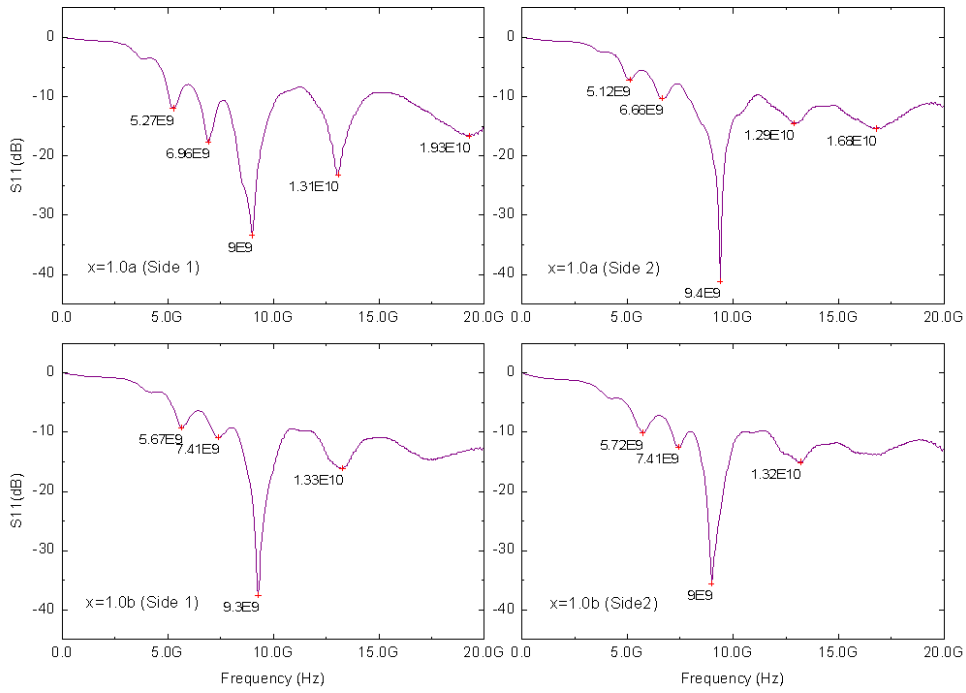

Figure 6.19: DRA S11 results for sample pellets from series C, composition $BaBiFe_{11}O_{19}$ over the frequency range 45MHz – 20GHz

of both the positions of the resonant peaks and the magnitude of these. Upon closer examination even the $x = 1.0a$ side 1 graph which at first glance did not appear as similar as the others in this set does have the same overall shape with four distinct resonant peaks up to 18GHz in similar positions to the other data sets. The key difference is that the magnitudes of these peaks are more equal; rather than the one much larger peak at the 9.0 – 9.4GHz position shown in the other traces. This sample composition of $BaBiFe_{11}O_{19}$ shows a first resonant frequency at around 3.8 – 4.0GHz which does not form a distinct peak and so was not highlighted by the peak finding tool used for the other peaks, this effect was also observed for the $x = 0.8$ samples. The similarity between samples in this set was interesting because they are not similar to the comparable pellet in series B, where although there are still four clear resonances below 18GHz these are at slightly lower frequencies and there is also a double type resonant peak in place of the

large magnitude peak observed for series C.

Sample composition x = 1.5

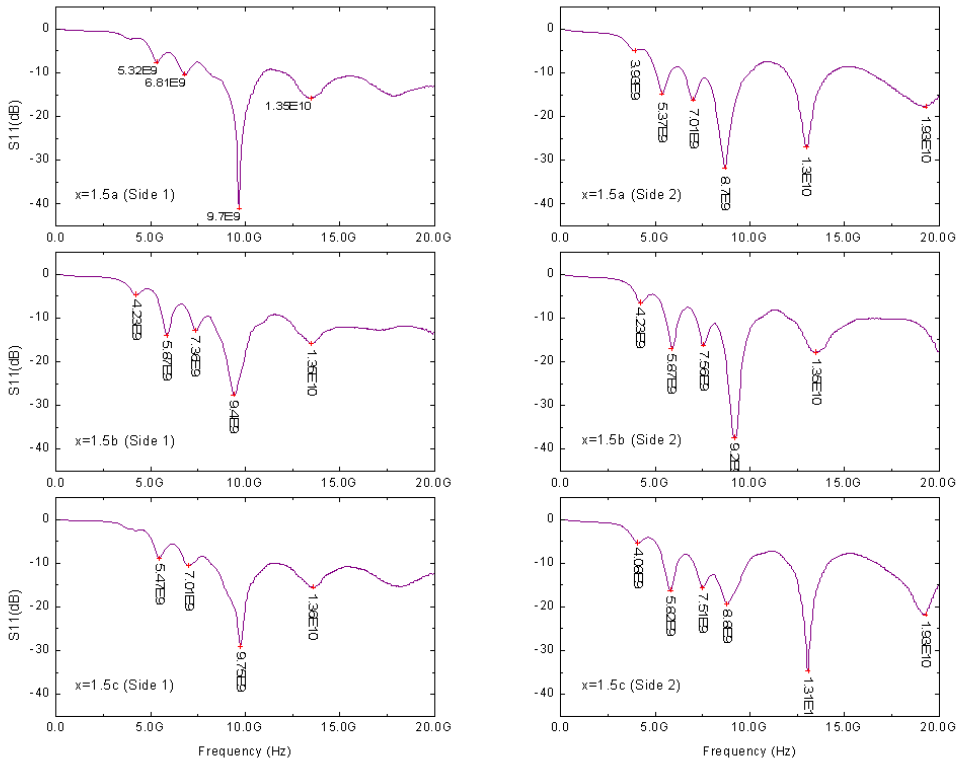

Figure 6.20: DRA S11 results for sample pellets from series C, composition $BaBi_{1.5}Fe_{10.5}O_{19}$ over the frequency range 45MHz – 20GHz

There are three separate pellets of composition $BaBi_{1.5}Fe_{10.5}O_{19}$ in series C. The S11 data when these samples are used within the DRA set-up are shown in Figure 6.20. All samples and sides have the same basic S11 results with five resonant frequencies below 18GHz which vary in magnitude between samples. Plots for $x = 1.5a$ side 1 and $x = 1.5c$ side 1 do not show clearly the first resonant frequency as there are no distinct peaks, but these are still visible on the graphs. As with the $x = 1.0$ set of samples, the $x = 1.5$ samples for series C do not display very similar S11 parameters to the same composition pellets in series B.

Conclusions

Of the bismuth containing samples the extreme range samples containing the least ($x = 0.2$) and the most bismuth ($x = 1.5$) have the greatest numbers of resonant frequencies.

Series D

Series D contains barium hexaferrite pellets with varying levels of bismuth, which have been sintered for three hours at 1100°C.

Sample composition x = 0.0

The S11 parameters for a DRA assembled with the undoped barium hexaferrite sample $x = 0.0b$ within this series are shown in Figure 6.21. The first resonant frequency varies between 5.57 – 5.67GHz and a magnitude of -5.924 – -6.460dB between side 1 and 2 of the material. The pattern is similar to that of other barium hexaferrite S11 DRA graphs where there are many resonances at higher frequencies.

Sample composition x = 0.2

Figure 6.22 shows the S11 parameters for the antenna assembled using pellet $x = 0.2b$ for both orientations of the sample on the ground plane. Both traces show three resonant frequencies in similar positions however the magnitude of the resonant peaks are greater for side 2 (both graphs are plotted to the same scale for ease of comparison). The first resonant frequency falls between 6.81 – 6.96GHz with a magnitude of -8.941 – -13.140dB. The second resonant frequency takes the form of a double peak for both graphs but is

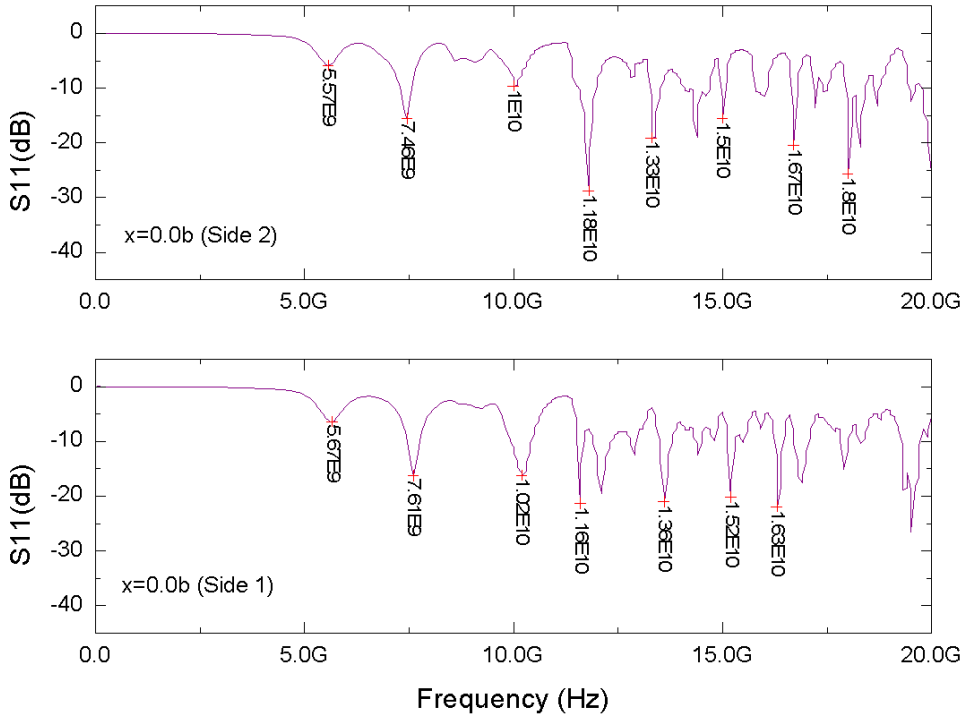

Figure 6.21: DRA S11 results for sample pellets from series D, composition $BaFe_{12}O_{19}$ over the frequency range 45MHz – 20GHz

more pronounced for side 2 due to the larger magnitude of all peaks. The first part of this peak occurs between 8.75 – 8.9GHz, magnitude -13.891 – -27.004dB followed by a larger magnitude peak of -19.154dB for side 1 and -60.08dB for side 2 between 9.4 – 9.7GHz. The final resonance peak below 18GHz falls at 13.1GHz for both configurations with a magnitude of -17.546dB and -42.666dB for side 1 and 2 respectively.

Sample composition x = 0.5

Series D pellet composition $BaBi_{0.5}Fe_{11.5}O_{19}$ is the first of this series to have two samples available for comparison. The S11 sweep for when these pellets are placed into the DRA rig are shown in Figure 6.23. Again these graphs show three main resonant peaks below 18GHz; a first resonant frequency at around 6 – 7GHz, a second double peak at

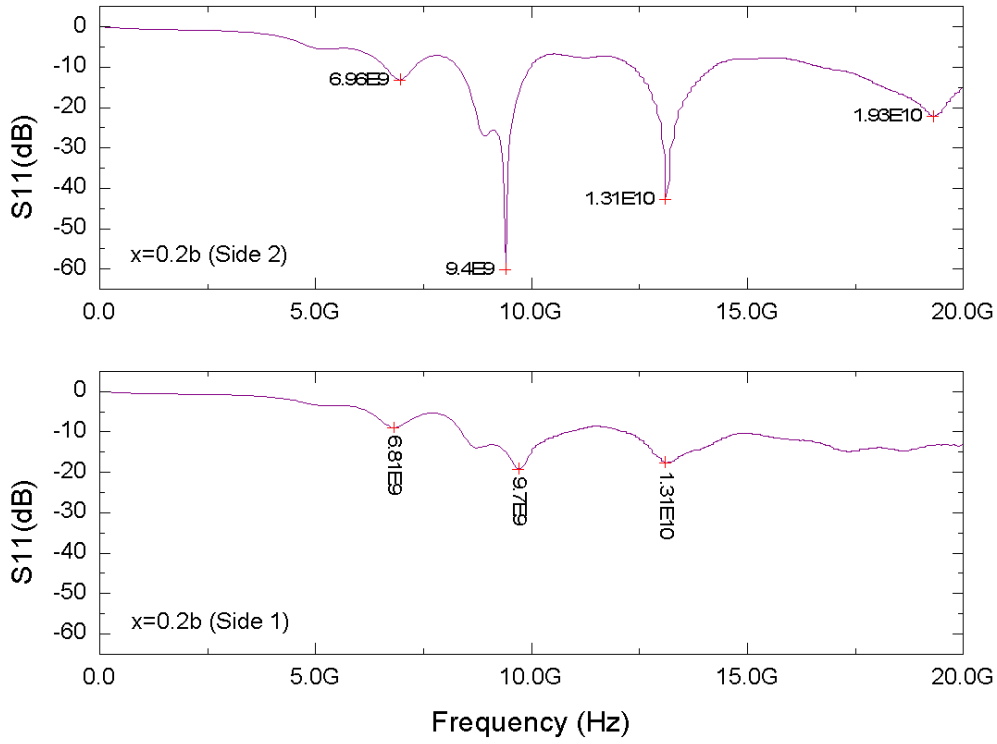

Figure 6.22: DRA S11 results for sample pellets from series D, composition $BaBi_{0.2}Fe_{11.8}O_{19}$ over the frequency range 45MHz – 20GHz

around 9-10GHz and then a final resonance located at around 13-14GHz. There is good agreement for the S11 results between $x = 0.5a$ side 1 and $x = 0.5b$ side 1 and also between $x = 0.5a$ side 2 and $x = 0.5b$ side 2 in addition to the same overall correlation in the response from the different pellets. The first resonant frequency occurs between 6.17 – 6.81GHz with a magnitude of -5.971 – -12.109dB. The second double peak resonance has its first part between 8.01 – 8.6GHz with magnitude -8.271 – -16.452dB followed by a larger second part to this resonance between 9.05 – 9.95GHz with magnitude -16.393 – -31.08dB. The double peak effect is more noticeable on the side 2 graphs where the magnitude of these peaks is not as large so the first part of the resonance is easier to see. The final resonant peak occurs between 13.0 – 13.9GHz with a magnitude of -16.631 – -25.163dB this is the largest magnitude resonant peak for the side 2 graphs.

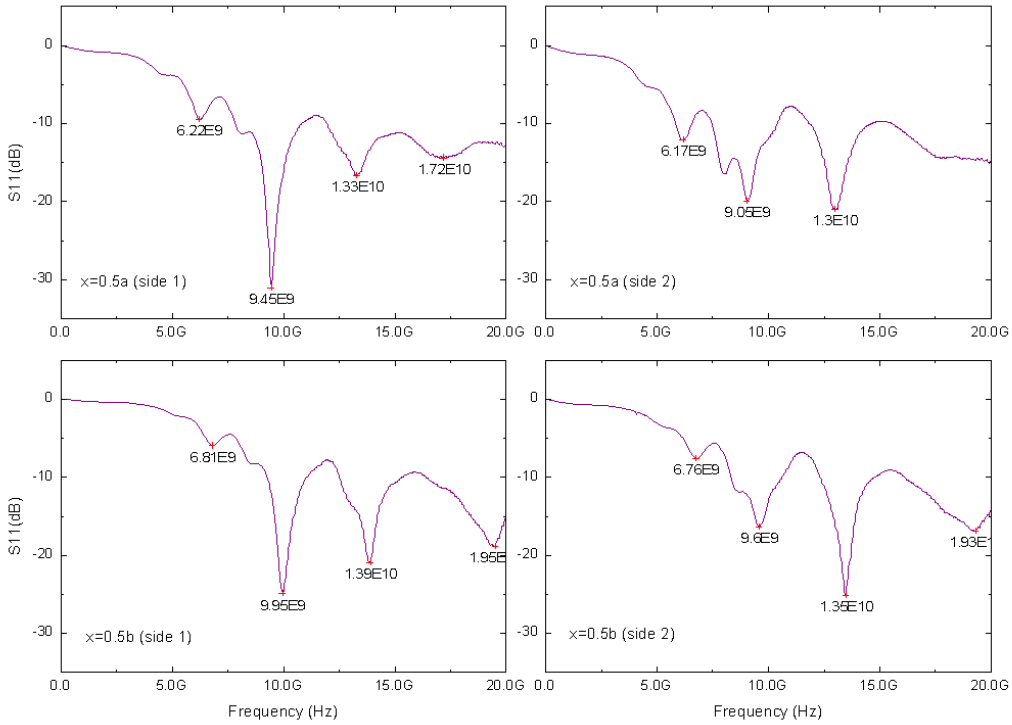

Figure 6.23: DRA S11 results for sample pellets from series D, composition $BaBi_{0.5}Fe_{11.5}O_{19}$ over the frequency range 45MHz – 20GHz

Sample composition x = 0.8

The S11 parameters for the $x = 0.8b$ pellet are shown in Figure 6.24. The graphs for both side 1 and side 2 show the same overall pattern with three main resonant frequencies below 18GHz but with different magnitude resonant peaks. The first resonant frequency falls between 6.22GHz (magnitude -8.033dB) and 6.17GHz (magnitude -11.206dB) for side 1 and 2 respectively. The second resonant frequency is a double peak shape as seen for other pellets in this series. This is clearer for the side 2 graph where the magnitude of the second part of the peak is not as large so does not dominate the response in the same way. For side 1 the first part of the resonance occurs at 8.11GHz with a magnitude of -9.975dB and the second part at 9.6GHz with a magnitude of -44.158dB. This resonance again occurs at 8.11GHz for the first part (magnitude -15.437dB) and a second peak

at 9.05GHz with a magnitude of -17.747dB. The final resonance under 18GHz occurs between 13.1 – 13.4GHz (-18.043 – -28.731dB magnitude). The second resonance is the largest magnitude response for side 1 whereas the third resonance is the greatest response for side 2.

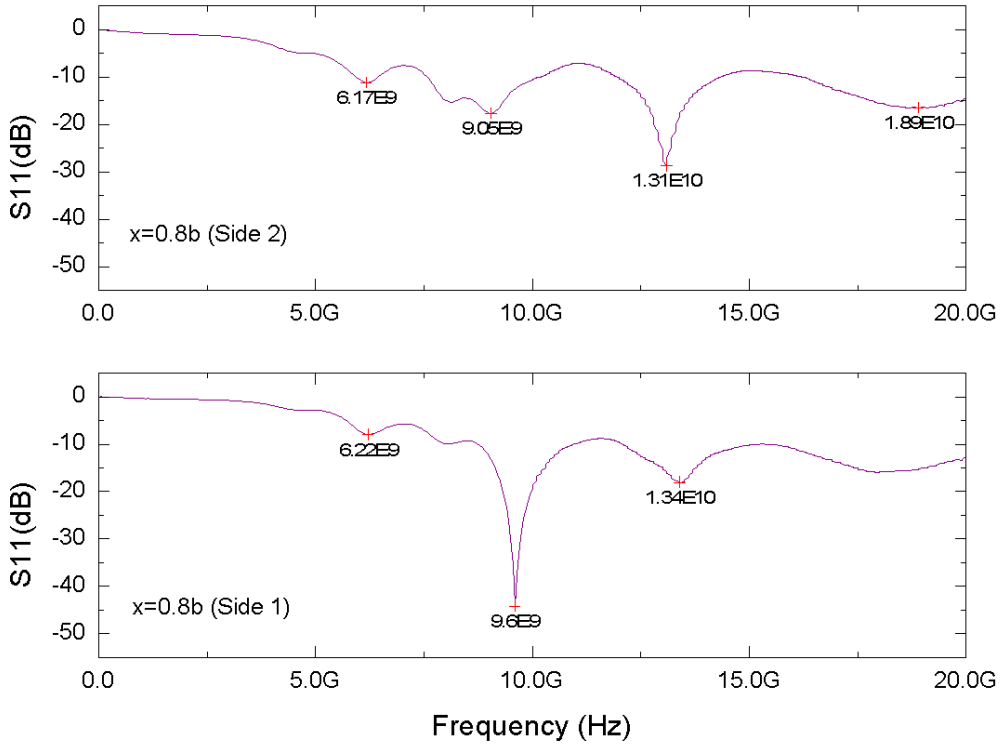

Figure 6.24: DRA S11 results for sample pellets from series D, composition $BaBi_{0.8}Fe_{11.2}O_{19}$ over the frequency range 45MHz – 20GHz

Sample composition x = 1.0

Pellets with composition $BaBiFe_{11}O_{19}$ were placed within the DRA experimental set-up and the resultant S11 parameters recorded as shown in Figure 6.25. The two pellets within this series show good agreement in resonant frequency positions both between the different orientations of the same pellet and between the separate pellets, with some variations in the magnitude of the response. Also displayed is the now familiar pattern of

three main resonant peaks which has a double peak shape to a greater or lesser extent as the second resonant position. The first resonant frequency falls between 5.97 – 6.91GHz with a magnitude of -5.133 – -8.600dB across the range of samples and orientations. The second resonant frequency is the largest magnitude peak for three out of the four traces (the $x = 1.0b$ side 2 graph being the exception, which is also the condition where the double peak is most distinct), falling in the range 7.56 – 8.70GHz and -6.801 – -10.724dB for the first part of this double peak and 9.30 – 10.0GHz and -15.382 – -36.072dB for the second part. The aforementioned $x = 1.0b$ side 2 sample shows the most distinct occurrence of the double peak which appears to effect the full scale magnitude achieved by the resonance; the other graphs have a smaller magnitude first peak and proportionally much larger second part to the resonance. The final resonance frequency of the range occurs between 13.5 – 13.6GHz with the side 1 traces having a smaller magnitude of between -16.211 – -16.777dB and side 2 traces displaying a greater magnitude between -20.532 – -21.743dB.

Sample composition x = 1.5

The final pellets characterised in the DRA rig were the $x = 1.5$ set which contain the greatest bismuth levels with chemical formula $BaBi_{1.5}Fe_{10.5}O_{19}$. The S11 parameters for these antenna configurations are shown in Figure 6.26. The first distinct resonant frequency occurs between 5.72 – 6.86GHz with magnitude -8.293 – -15.576dB. There is a lower frequency resonance at around 4.3 – 5.0GHz visible in the traces, however it has a very small magnitude (-2.756 – -5.738dB) so was not identified by the software used for post processing. The second resonance frequency, which appeared as a double peak for other sample compositions has a more distinct shape with two more separated peaks

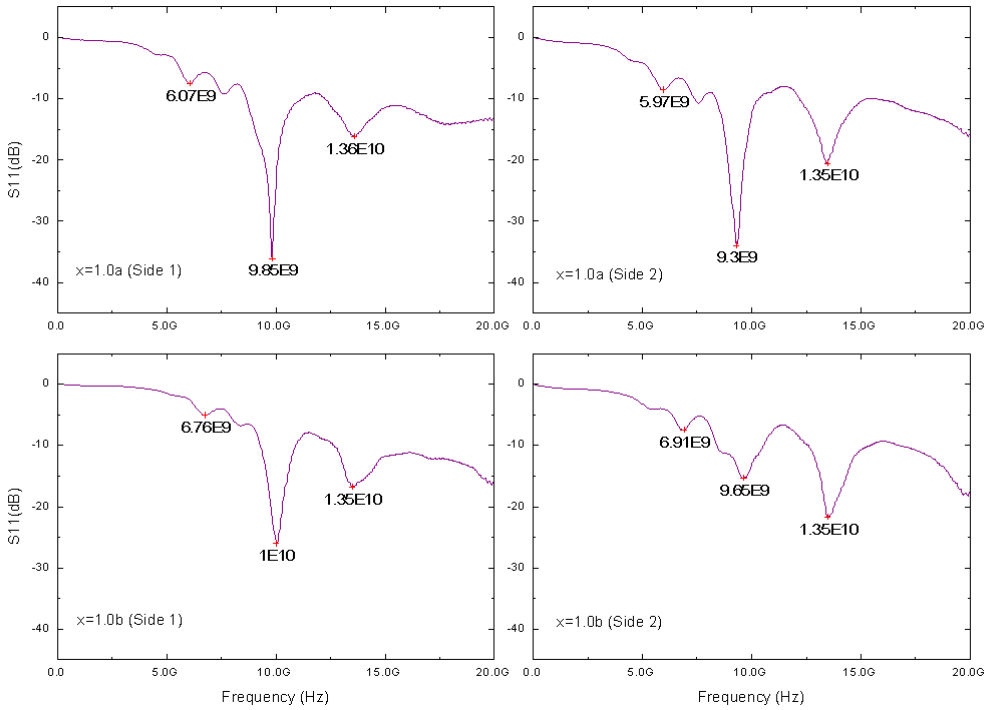

Figure 6.25: DRA S11 results for sample pellets from series D, composition $BaBiFe_{11}O_{19}$ over the frequency range 45MHz – 20GHz

with the exception of graph $x = 1.5b$ side 1 which shows the more familiar double peak shape. The first of these peaks occurs between 7.31 – 8.50GHz with -9.859 – -14.558dB magnitude. The second part of the response in this frequency zone occurs between 9.05 – 9.85GHz with -21.396 – -43.791dB magnitude. This peak is the largest magnitude response for all graphs except the $x = 1.5b$ side 1 condition which is the double peak trace; this corresponds to the result found for the $x = 1.0b$ side 2 trace. There is a final resonance from 13.5 – 14.2GHz with magnitude -16.250 – -23.493dB which is the greatest magnitude resonance for the $x = 1.5b$ side 1 sample.

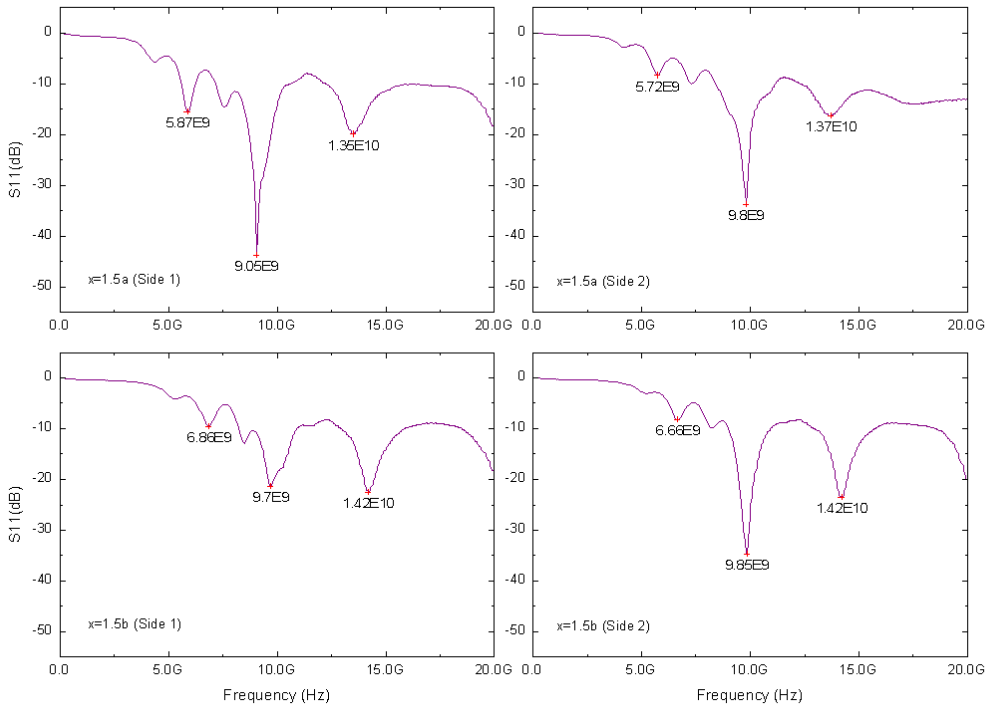

Figure 6.26: DRA S11 results for sample pellets from series D, composition $BaBi_{1.5}Fe_{10.5}O_{19}$ over the frequency range 45MHz – 20GHz

Conclusions

All pellets in series D which contain bismuth display three main resonant peaks; the first around 5 – 6GHz, the second around 9GHz which in some cases forms part of a double peak effect and a final resonance around 13 – 14GHz. Some samples have a further higher frequency resonance above 18GHz, however this has been ignored because the SMA connector used within the DRA set-up is only reliable up to 18GHz. The first resonant frequency is always the smallest peak in terms of magnitude, the largest being one of the higher frequency peaks.

Series E

Series E contains pellets with a range of bismuth content which have been sintered for three hours at 1200°C. Figure 6.27 displays the S11 responses for the DRA antenna assembled from these samples.

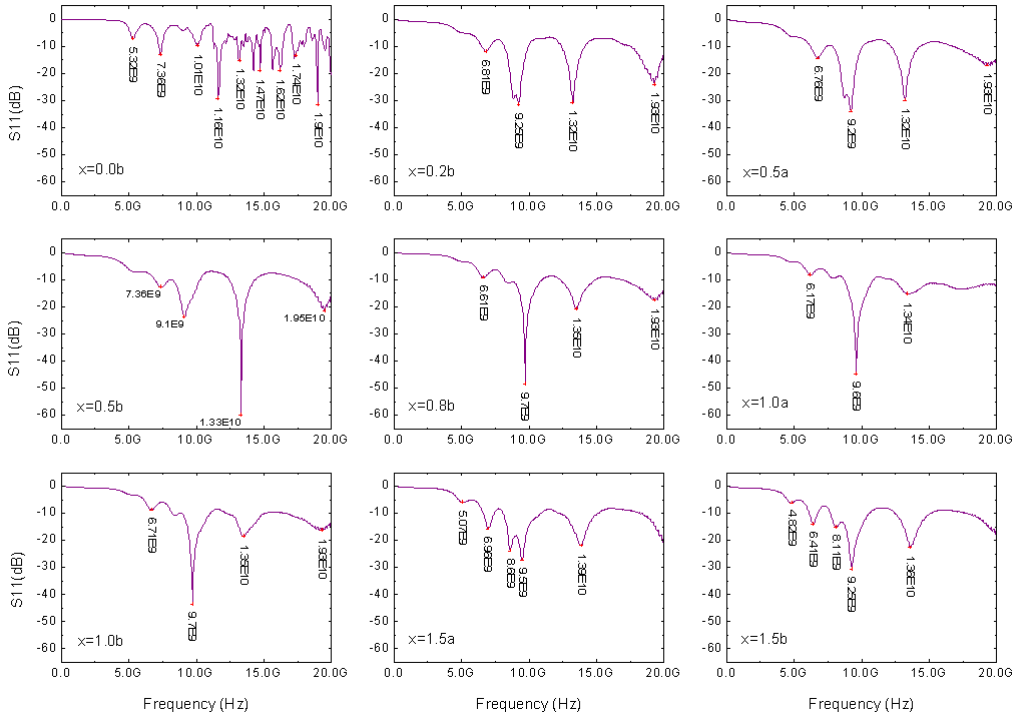

Figure 6.27: DRA S11 results for sample pellets from series E, composition $BaBi_xFe_{12-x}O_{19}$ over the frequency range 45MHz – 20GHz

Sample composition x = 0.0

The first set of S11 data presented for series E is the parent barium hexaferrite sample which displays a similar pattern to the other undoped samples across all sintering regimes with a large number of resonant frequencies. The first resonant peak occurs at 5.32GHz with a magnitude of -7.180dB.

Sample composition x = 0.2

The lowest concentration of added bismuth sample is shown with the $x = 0.2b$ graph. The pattern visible in other bismuth containing pellets is shown here by the three main resonant frequencies below 18GHz, with the second resonant frequency present as a double peak. The first resonant frequency occurs at 6.81GHz with magnitude -11.866GHz. The second resonant area is split into two peaks; the first part of the resonance located at 8.85GHz, magnitude -29.018dB and the second peak of the resonance is 9.25GHz, magnitude -31.589dB. The final peak occurs at 13.2GHz with a magnitude of -30.690dB.

Sample composition x = 0.5

Next is the $x = 0.5a$ and $x = 0.5b$ same composition pellets ($BaBi_{0.5}Fe_{11.5}O_{19}$). These traces appear to be rather different however they do both show the same pattern of three resonant frequencies below 18GHz; the $x = 0.5a$ graph shows a double peak at the second resonance frequency while the $x = 0.5b$ displays three separate peaks. The $x = 0.5a$ data has a first resonant peak at 6.76GHz with magnitude -14.321dB compared to 7.36GHz and -12.636dB for $x = 0.5b$. The double peak resonance for the $x = 0.5a$ graph is a similar shape to the comparable peak on the $x = 0.2b$ graph. The first part of the resonance occurs at 8.75GHz with a magnitude of -28.771dB, the second part of the peak is located at 9.20GHz, magnitude -33.848dB. The second resonant frequency for $x = 0.5b$ is a single peak centred at 9.10GHz with magnitude -23.734dB, occurring in the middle of the double peak of the $x = 0.5a$ trace. The position of the final resonance peak is located at 13.2GHz for $x = 0.5a$ and at 13.3GHz for $x = 0.5b$ with magnitudes of -29.809dB and -59.773dB respectively.

Sample composition x = 0.8

S11 parameters for the $x = 0.8b$ sample again show three main resonant peaks. The first resonance occurs at 6.61GHz, magnitude -9.112dB, then there is a small peak at 8.45GHz (magnitude -11.217dB) followed by the largest magnitude resonance of all of -48.508dB at 9.70GHz. The final resonance occurs at 13.5GHz with a magnitude of -20.771dB.

Sample composition x = 1.0

The graphs for $x = 1.0a$ and $x = 1.0b$ show good agreement in the shape of the traces with a small first resonant frequency followed by an even smaller second resonance, then the largest magnitude response and finally another resonant peak below 18GHz. The position of the first resonant frequency is 6.17GHz (magnitude -8.225dB) for $x = 1.0a$ and 6.71GHz (magnitude -8.688dB) for $x = 1.0b$. The second very small peak is located at 7.91GHz for $x = 1.0a$ and 8.41GHz for $x = 1.0b$, with magnitudes ranging from -9.384 – -10.756dB. The largest magnitude resonance is centred at 9.60GHz depth -44.656dB for $x = 1.0a$ and at 9.70GHz depth -43.490dB for $x = 1.0b$. The final resonant peak is located at 13.4GHz with magnitude -15.274dB and at 13.5GHz with magnitude -18.479dB for $x = 1.0a$ and $x = 1.0b$ respectively.

Sample composition x = 1.5

The final two graphs in Figure 6.27 show the S11 data for the DRA set-up with the highest concentration bismuth substituted barium hexaferrite sample. These graphs show good agreement between the two samples in terms of the shape of the S11 response and both

display a greater number of peaks than other different composition samples in the series. The first resonant frequency is centred at 5.07GHz with magnitude -5.957dB for $x = 1.5a$ and at 4.82GHz with magnitude -6.069dB for $x = 1.5b$. Interestingly unlike the other bismuth containing samples, the S11 response before this first resonant frequency is very flat, whereas in other samples there is a slope down to the first resonance peak which is detected by the Origin peak finding tool. It is possible that the greater concentration of bismuth is contributing to the much clearer initial resonance at a lower frequency than the other composition pellets. The next resonance peak is located at 6.96GHz (-15.629dB) and at 6.41GHz (-13.927dB) for $x = 1.5a$ and $x = 1.5b$ respectively. This peak is located in a position more in-line with the first resonance observed for the other bismuth containing samples, lending gravity to the conclusion that the first resonant peak of this composition is a better defined resonance which presents as a slope for the other DRA material set-ups. The third and forth resonant peaks form a double peak resonance with the magnitudes of the two peaks being more equal in the $x = 1.5a$ graph. For this first sample the first part of this resonance is located at 8.60GHz and the second part at 9.50GHz with magnitudes of -23.836dB and -27.153dB respectively. The double peak pattern is shifted to a slightly lower frequency for the $x = 1.5b$ material with the first peak centred at 8.11GHz and the second at 9.25GHz with respective magnitudes of -14.992dB and -30.517dB. The final resonant peak corresponds to the approximate values seen for other bismuth concentration pellets, being 13.9GHz with a magnitude of -21.908dB for $x = 1.5a$ and 13.6GHz with a magnitude of -22.638dB for $x = 1.5b$.

Conclusions

When series E is viewed as a whole it is seen that the undoped barium hexaferrite pellet has an S11 response which is very different from the other pellets in the series, but does have strong similarities with the same composition pellets in other series despite the different sintering conditions. The bismuth containing samples with the exception of the highly doped $x = 1.5a$ and $x = 1.5b$ pellets show the same overall response with three main resonant frequencies below 18GHz (which is the maximum reliable frequency of the SMA connector used within the DRA rig), the second resonance sometimes appearing as a double peak shape. The final sample compositions of $x = 1.5a$ and $x = 1.5b$ show a resonant peak at a lower frequency than the other samples which has been discussed above. The addition of bismuth to barium hexaferrite has reduced the number of resonant frequencies which a DRA can operate within, however the magnitude of these resonances has increased, particularly for the higher frequency resonances.

6.5.2 Conclusions across all series

For all series the undoped barium hexaferrite sample displayed a greater number of resonant frequencies across the range, but these are sharper and begin to occur at higher frequencies than pellets which contain bismuth. Of the samples which do have bismuth in their composition there are usually three main resonance zones in addition to a small preak at lower frequency within the 45MHz – 18GHz region; the first resonance frequency occurs between 4 – 7GHz depending on the individual sample. At some positions instead of one peak, resonances which are located close together form a double peak shape where the two resonances merge into a larger region. This effect could be due to potential

anisotropy of the material causing usually dormant modes to become excited. This peak splitting is not a undesirable effect; in some cases it actually increases the bandwidth of the system as indicated by the S11 response remaining below -10dB for a wider frequency range. The DRA rig was shown to be a feasible set-up for further study.

6.6 Relationship between measured higher side of permittivity with coaxial probe and resonant frequency of DRA antenna

In Chapter 4 Section 4.3 it was noted that there was a difference in recorded permittivity dependant on which side of the pellet was in contact with the coaxial probe, with one side giving a higher value of permittivity than the other. The most likely reason for these variations were small changes in surface roughness of a pellet, which could result in differing permittivity because the contact between the sample and the coaxial probe would not be ideal. This surface roughness could have an impact on the resulting S11 parameters when the pellets are used to from a DRA. Prior investigation earlier in this section of the differences in the S11 data when the pellet is rotated to have different sides in contact with the grounding plane concluded that there was not a large difference however there was some. The purpose of this series of experiments was to investigate if there was any correlation between the higher permittivity side of a pellet and the S11 response of the DRA dependant on the orientation of the pellet in the rig.

6.6.1 Experimental method and results

The first part of work undertaken was to characterise the high frequency permittivity of the pellets using the coaxial probe method detailed above. Each pellet was characterised when side 1 and then side 2 was in contact with the probe. This orientation was recorded and pellets were stored so that the side 1 and side 2 terminology could be transferred to the DRA characterisation. Figure 6.28 shows the permittivity results for the highest permittivity side for each pellet.

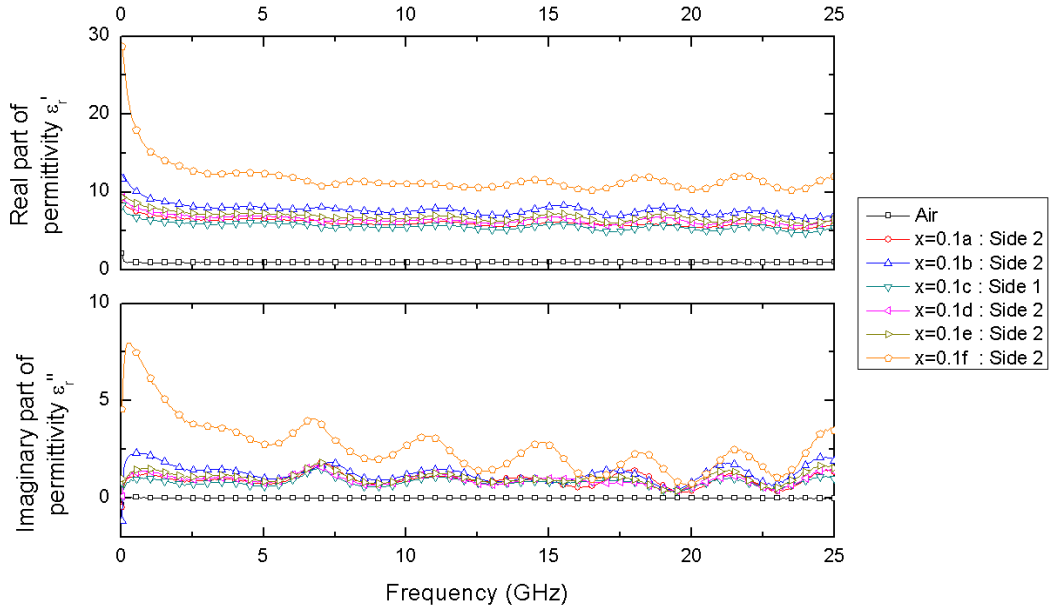

Figure 6.28: Real and imaginary part of permittivity for Series F $BaBi_xFe_{12-x}O_{19}$ after sintering for three hours at 1100°C

The first observation is that the permittivity results show good agreement with the previously recorded results; where five of the six samples have similar permittivities and the final $x = 0.1f$ pellet has a markedly higher real and imaginary part of permittivity.

The second part of the experiment was to record the S11 response of the DRA antenna for each orientation of the pellet such that side 1 in contact with the probe corresponded to side 1 being in contact with the grounding plane of the DRA configuration. The data

in Figure 6.29 shows the results which correspond to the lowest resonance frequency out of the two pellet orientations.

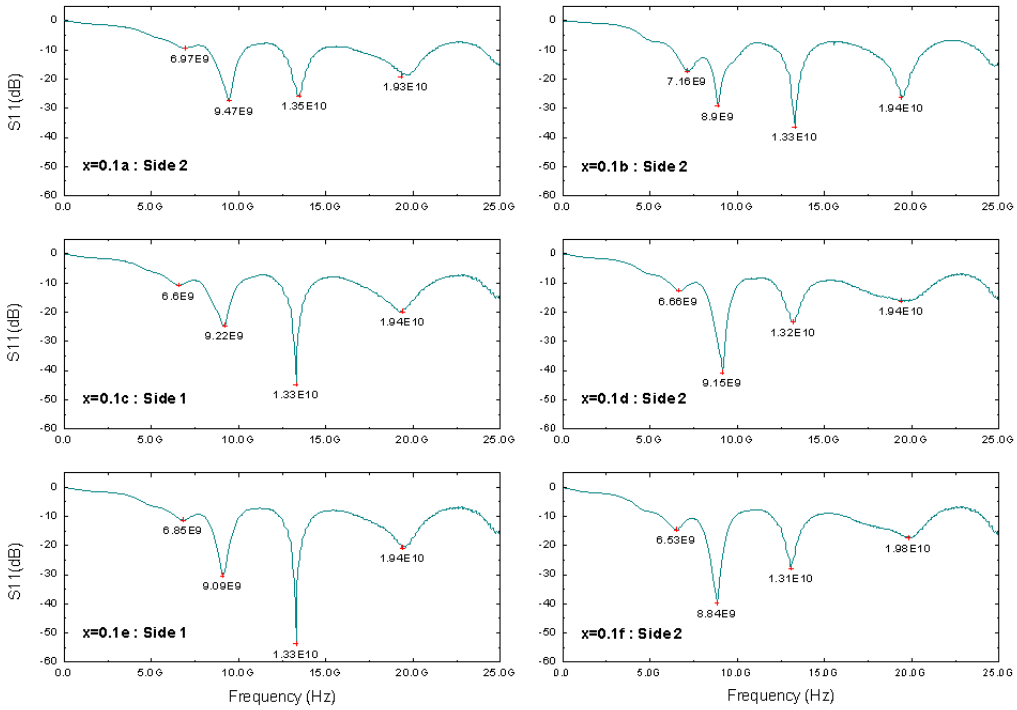

Figure 6.29: DRA S11 results for sample pellets from series F, composition $BaBi_{0.1}Fe_{11.9}O_{19}$ over the frequency range 45MHz – 25GHz

In five out of six cases the face of the pellet which gave a higher permittivity result corresponded to a lower value of resonant frequency when that face was in contact with the grounding plane of the DRA set-up. This supports the conclusion that surface roughness variations are present and alter the results; the DRA results change only slightly between the different faces of the pellets because resonant modes are set up throughout the body of the pellet; the coaxial probe is more affected by the change of sample orientation and is more sensitive to a non-smooth sample surface because the measurement relies on surface reflections between the probe and the material under test. The pellet face which gives both the higher permittivity from the coaxial probe

characterisation scheme and the lower resonant frequency in the DRA set-up is most likely to be the smoother side of the pellet. This conclusion was drawn from the logic that a rougher pellet surface introduces more air gaps between either the sample and the probe face or the sample and the DRA grounding plate, resulting in a lower bulk permittivity value. This is observed directly in the coaxial probe measurement by a lower recorded permittivity for that face and indirectly in the S11 parameters for the DRA where a lower sample permittivity results in a higher resonant frequency, as laid out in Equation 6.4. The experimental results also concur with this equation when the sample $x = 0.1f$ is considered; this pellet has a markedly higher permittivity than the other samples in this set ($\varepsilon_r = 12.806 - 3.8296j$ while the others fall into the range $\varepsilon_r = 5.948 - 0.7032j$ to $\varepsilon_r = 8.182 - 1.444j$), this corresponds to a small but significant shift in the resonant frequency of the DRA it forms. The first resonant frequency of the $x = 0.1f$ pellet is 6.53GHz, the next nearest is 6.60GHz ($x = 0.1c$ pellet) and the rest span the range up to 7.16GHz. Confirming the result that a higher permittivity sample provides a lower resonant frequency when used within a DRA.

6.7 Prototype DRA

A more advanced prototype DRA was constructed using the copper base described above in Section 6.4. Work was carried out at The University of Nottingham Malaysia Campus by Belle Ooi Pei Cheng. A pellet from series E which has been sintered for three hours at 1200°C degrees and has sample composition $x = 0.2$, $BaBi_{0.2}Fe_{11.8}O_{10}$ was used as the resonator component for the antenna. This sample (labelled $x = 0.2a$) was characterised as having a sample permittivity of $\varepsilon_r = 3.978 - 0.0986j$ at 2.45GHz, it is

4.731mm thick and has a diameter of 20mm. The pellet was attached to the antenna base using conductive epoxy resin and left to cure for 48 hours.

6.7.1 Theoretical value for resonant frequency of DRA

The expression presented initially in Equation 6.4 was used to calculate the theoretical resonant frequency of the antenna. Results are presented below:

$$f_0 = \frac{3 \times 10^8}{2\pi\sqrt{\varepsilon_r'}} \sqrt{\left(\frac{1.841}{a}\right)^2 + \left(\frac{\pi}{2h}\right)^2} \tag{6.9}$$

$$\begin{aligned} f_0 &= \frac{3 \times 10^8}{2\pi\sqrt{3.978}} \sqrt{\left(\frac{1.841}{10 \times 10^{-3}}\right)^2 + \left(\frac{\pi}{2 \times 4.731 \times 10^{-3}}\right)^2} \\ &= 9.088 \text{ GHz} \end{aligned} \tag{6.10}$$

The first resonant frequency of 9.088GHz is larger notably greater than the calculated values for the prototype with the series C $x = 0.5b$ sample as the resonator of 5.641GHz. This is due to a combination of factors; the lower permittivity of the material and the smaller pellet height.

6.7.2 Experimental value for resonant frequency of DRA

The DRA rig with the series E $x = 0.2a$ pellet attached was characterised over the range 50MHz – 20GHz to collect the S11 parameters to determine the resonant frequencies of the system. Results are presented in Figure 6.30.

There are three clear resonant frequencies for this antenna; 6.6GHz, 9.55GHz and

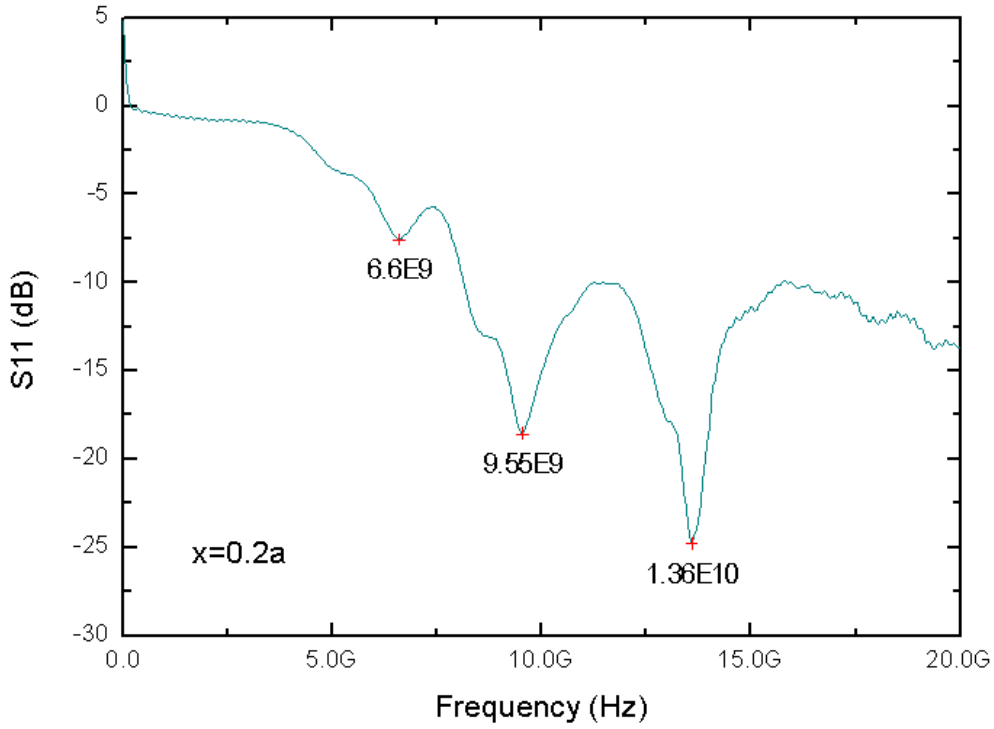

Figure 6.30: DRA S11 results using pellet from series E $x = 0.2a$, composition $BaBi_{0.2}Fe_{11.8}O_{19}$ over the frequency range 50MHz – 20GHz

13.6GHz. The second frequency of 9.55GHz is close to the theoretical value calculated in Equation 6.10 of 9.088GHz, however there is a distinct resonance at the lower frequency of 6.6GHz which is potentially of more interest for current Wi-fi applications than the larger magnitude, higher frequency resonances.

6.7.3 Radiation patterns for bismuth substituted barium hexaferrite DRA

The radiation patterns for the DRA were captured at two frequencies of 6.615GHz and 13.615GHz using an Agilent 8757D Scalar Network Analyzer in conjunction with an Agilent E8257D PSG Analog Signal Generator. These frequencies were selected for their experimental importance; 6.615GHz because this is the closest to the first clear resonance shown in the S11 data in Figure 6.30; and 13.615 because this is the closest frequency

to the largest magnitude resonance found from the S11 values.

The radiation patterns for each frequency were recorded for three different orientations of the system; the *x-y*, *x-z*, and *y-z* planes. The geometry of the system including the planes is shown in Figure 6.31.

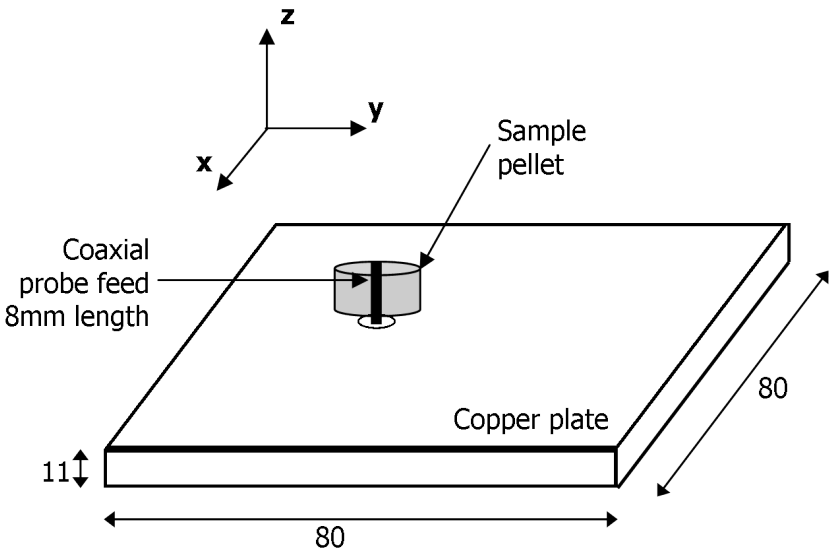

Figure 6.31: Diagram illustrating circular dielectric resonator antenna.

Data used to plot radiation patterns for the antenna is in its unprocessed form, given as $B/R-M$ where B is the received signal from port B which is the detector in the system. R is the total signal sent from the signal generator to the transmitting test antenna. M is the normalised value when a through calibration has been performed. Therefore the $B/R - M$ value which is used to plot graphs represents the signal received from the test antenna ignoring all losses within cables and other components. This information is then processed by a normalisation routine to present values on a clearer scale for plotting.

The normalisation procedure does not impact the shape of the radiation patterns presented. The procedure followed is for each orientation, to find the maximum recorded

value across all three test frequencies and use this as a constant which is added to each of the output values to provide a clearer scale.

Results at 6.615GHz

At the first resonance frequency of 6.615GHz the radiation patterns of the antenna are shown. The *x-y* plane (Figure 6.32) displays a large main lobe around 180° which extends and absorbs side lobes, so in effect extends from 90° through to 285°. There is a back lobe of similar magnitude also present.

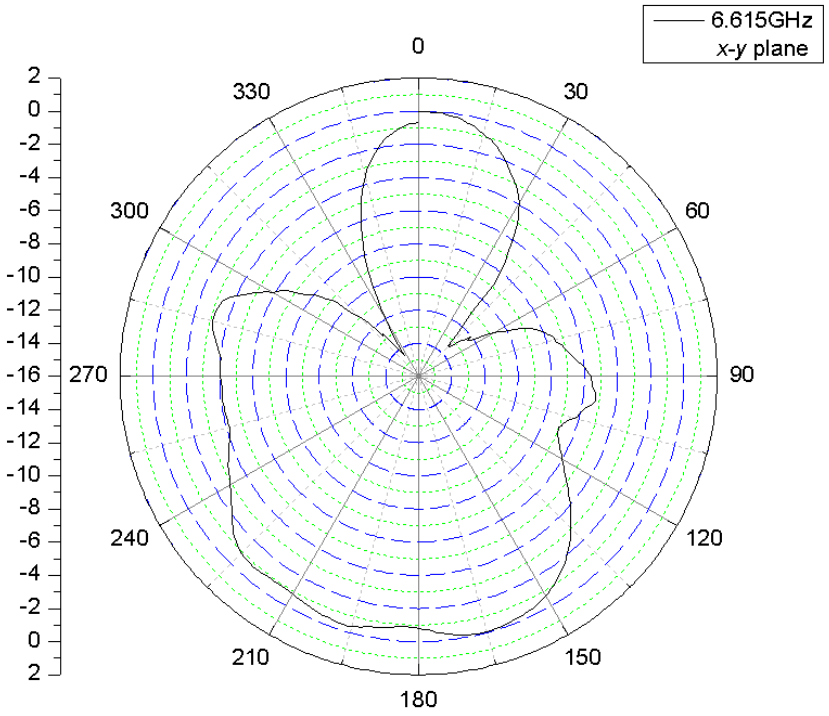

Figure 6.32: Radiation pattern for the *x-y* plane for DRA operating at 6.615GHz.

The radiation pattern for the *x-z* plane (Figure 6.33) appears as a butterfly shape; two wide main lobes of approximately equal sizes centred around 60° and 315°. There are two smaller lobes present at 135° and 240°.

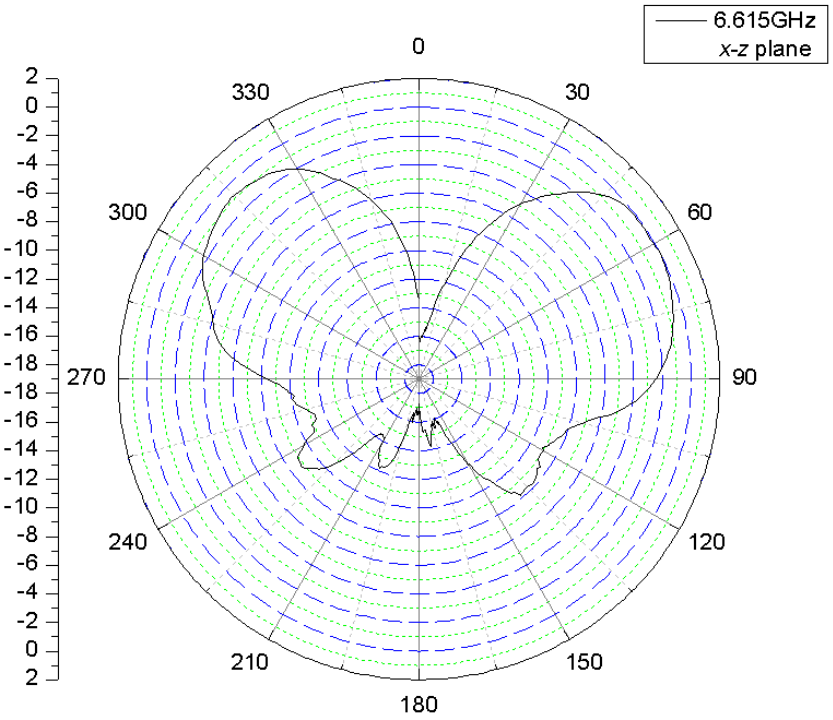

Figure 6.33: Radiation pattern for the *x-z* plane for DRA operating at 6.615GHz.

The *y-z* pattern (Figure 6.34) displays a somewhat mismatched main lobe centred around 0° which is of larger magnitude on the 355° side of the threshold. A clear additional side lobe is present at 255° and there is also a back lobe of significant magnitude at 180°.

These radiation patterns show a good resemblance to simulation results produced for a similar configuration DRA published by Peng et al. [12]. There are differences due to the experimental set-up and inaccuracies due to the practical implementation of the system, however the similarities remain.

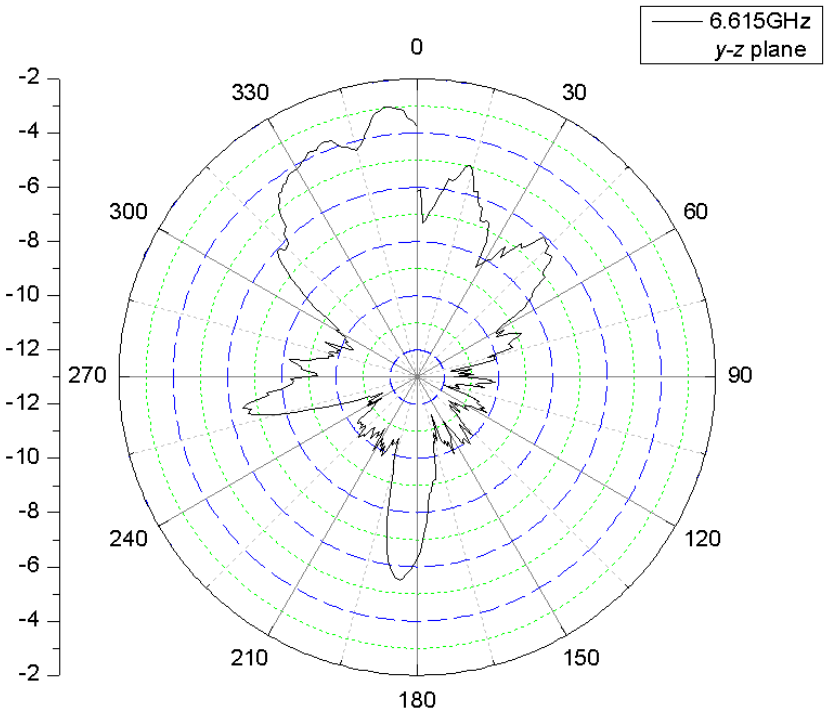

Figure 6.34: Radiation pattern for the *y-z* plane for DRA operating at 6.615GHz.

6.7.4 Results at 13.615GHz

The radiation patterns at the highest frequency resonance of 13.615GHz are presented in Figures 6.35, 6.36 and 6.37.

The *x-y* plane (Figure 6.35) displays a strong response over the range 90° through to 270° with additional smaller magnitude lobes at 0°, 45° and 315°. The main lobe is a similar pattern to that seen at the lower 6.615GHz frequency for the same plane.

Data for the *x-z* plane radiation patterns presented in Figure 6.36 also shows a similar response to that of the same plane at 6.615GHz with the familiar butterfly shape. The two main lobes are located at 75° and 315° with two smaller but still discernible lobes at 120° and 255°.

The final measurements which detail the radiation pattern of the *y-z* plane are presented

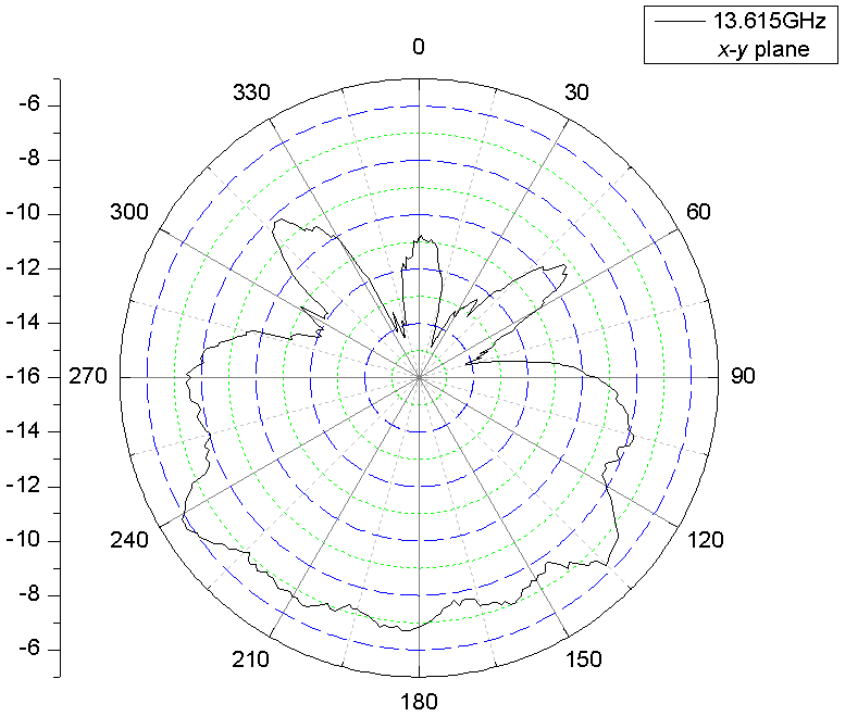

Figure 6.35: Radiation pattern for the *x-y* plane for DRA operating at 13.615GHz.

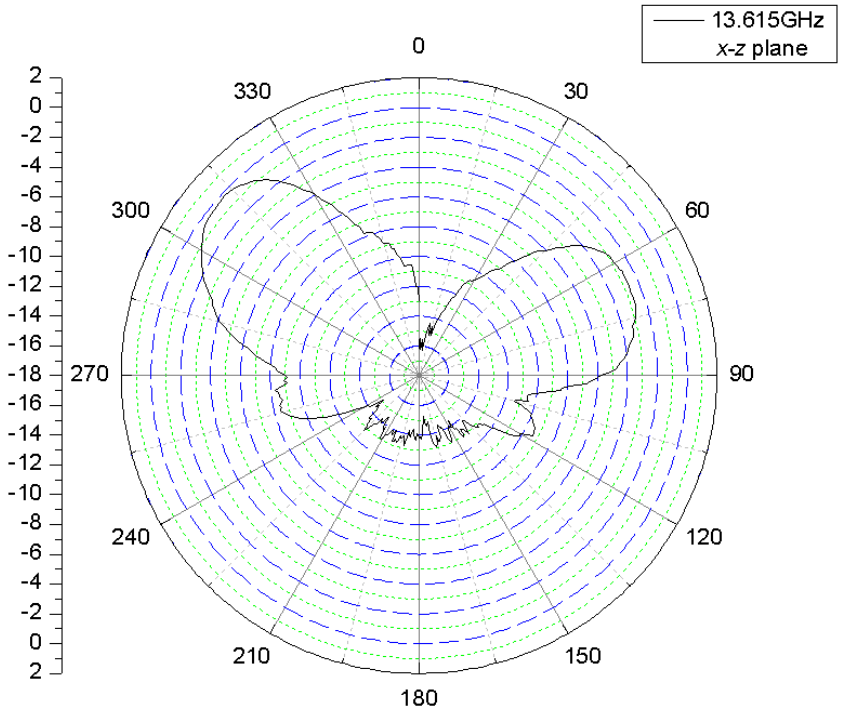

Figure 6.36: Radiation pattern for the *x-z* plane for DRA operating at 13.615GHz.

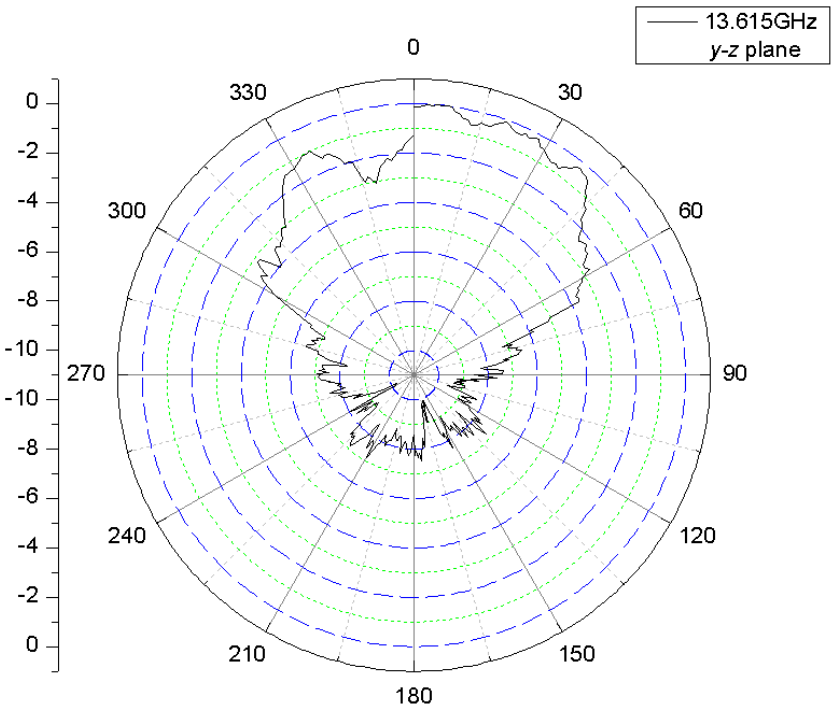

Figure 6.37: Radiation pattern for the *y-z* plane for DRA operating at 13.615GHz.

in Figure 6.37). There is a main lobe centred around 0° however (as was also observed for the 6.615GHz pattern in the same plane) there is a discontinuity over the 359° to 0° threshold. This main lobe spans from 0° to 60° in the positive direction and from 0° to 300° in the opposite direction. There are smaller side lobes present in the 90° to 270° region also.

The results for the radiation patterns at this frequency also show a correlation with the simulated DRA results by Peng et al. [12], giving confidence in both the antenna system and the measurements.

6.7.5 Conclusions

The resonant frequency radiation patterns resemble simulation results published by others. From this the conclusion was drawn that the antenna system behaved as expected. Other materials used within dielectric loaded antennas fall between the range of real part of 2.5 – 3.8 with loss tangents between 0.0001 – 0.01 [36]. Bismuth substituted barium hexaferrite presents a higher real part of permittivity and a loss of around the same order of magnitude, confirming the suitability of use in dielectric loaded antennas. Simulation work has been performed by others who show that an even higher permittivity material would be more desirable [17]; work presented here provides a step towards that goal.

The device shows promise as an antenna for LAN and possibly mobile telephony applications, however the design requires modification to operate at the desired frequency and to satisfy SAR requirements for mobile phone handsets. Further work to investigate the efficiency of the antenna would also be of use.

6.8 Chapter Conclusions and future work

6.8.1 Conclusions

The motivations behind moving communications technology upwards into the microwave range for more efficient encoding of signals was introduced and three different antenna designs which make use of a dielectric material were presented. Of these the dielectric resonator antenna (DRA) was studied in more detail.

For a DRA operating in the $HE_{\delta 11}$ mode the coaxial feed to the antenna is located

outside but in contact with the dielectric material pellet. This set-up was chosen for ease of fabrication over the DRA $TM_{01\delta}$ operational mode which would require the sample to be drilled to accommodate the coaxial feed.

The $x = 0.5b$ sample from series C which has been sintered at 1100°C for one hour was used as an example for theoretical calculations by using the pellets physical dimensions and high frequency permittivity. The dominant frequency calculated from the equations given in the literature [32] [12] was 5.64GHz.

The same sample specifications were used to create models within Comsol Multiphysics 3.3a for the antenna operating in first the $TM_{01\delta}$ mode, followed by the $HE_{\delta 11}$ mode when the length of the coaxial feed was altered. All probe depths give the same first resonant frequency of 7.7GHz in $TM_{01\delta}$ mode, however the magnitude of this resonance is variable achieving a maximum of -32.5dB for a 4mm probe depth. Simulations of the probe set up to excite the $HE_{\delta 11}$ mode where the feed was outside the sample showed that all probe lengths gave a first resonant frequency of 5.85GHz with varying magnitudes. This magnitude was greatest when the probe feed was equal to the height of the sample pellet.

A DRA base was manufactured and the barium hexaferrite and bismuth substituted barium hexaferrite samples placed on the rig before S11 data of the system was collected over the frequency range 45MHz – 20GHz. Pellets from series F which have the same composition and sintering regime were used to investigate the reliability of the system. It was found that the orientation of the sample had very little effect on the resultant S-parameters of the system.

For all series the undoped barium hexaferrite sample displayed a greater number of

resonant frequencies across the range, but these are sharper and begin to occur at higher frequencies than pellets which contain bismuth. Of the samples which do have bismuth in their composition there are usually three main resonance zones in addition to a small preak at lower frequency within the 45MHz – 18GHz region. At some positions instead of one peak, resonances which are located close together form a double peak shape where the two resonances merge into a larger region. This effect could be due to potential anisotropy of the material causing usually dormant modes to become excited. This peak splitting is not a undesirable effect; in some cases it actually increases the bandwidth of the system as indicated by the S11 response remaining below -10dB for a wider frequency range.

The first resonance frequency occurs between 4 – 7GHz depending on the individual sample. The $x = 0.5b$ series C pellet has a first resonance at 6.02GHz compared to a theoretical value of 5.64GHz and a simulated value of 5.85GHz; there is a good level of agreement between the values. The resonant frequency is higher than the operational frequency for Bluetooth and Wi-fi of 2.45GHz, however it is suitable for higher frequency antenna applications such as 5GHz Wi-fi.

A link between the side dependency of high frequency permittivity and the side dependence of the resonant frequency of the DRA was established. When the face of the pellet which gives a higher value of permittivity from the coaxial probe is in contact with the ground plate of the DRA assembly, the resonant frequency of the antenna reduces slightly. It was reasoned that this is most likely the smoother side of the pellet, which in turn provides a better contact with the plate.

A dielectric resonator antenna was successfully constructed using a bismuth substituted

barium hexaferrite sample as the resonator device. The antenna was tested experimentally and found to have resonance frequencies at 6.6GHz, 9.55GHz and 13.6GHz, in comparison to a calculated value of 9.088GHz. The performance of the antenna was characterised at 6.615GHz (the closest value to the first experimentally located resonant frequency) and at 13.615GHz (the largest magnitude resonance found experimentally) and radiation patterns presented. At these two resonant frequencies the radiation patterns resembled simulated results published by other authors [12] which showed a greater degree of directivity which must be taken into account for this system to be developed into a feasible product.

6.8.2 Future work

The dielectric resonator antenna is a basic structure which incorporates a wide variety of variations to both the antenna feed and the dielectric material. The feed could be altered from the simple coaxial feed to a coplanar loop or a microstrip line. Resonator materials for the antenna can take a wide variety of shapes such as rectangular, elliptical or even stacked composites of different permittivity materials. It would be interesting to investigate these variations on the basic DRA form in the future.

Barium hexaferrite and bismuth substituted barium hexaferrite is of additional interest when used in a DRA; by magnetising the resonator material (which then maintains it's polarisation) the frequency response of the antenna can be altered to provide a wider resonance, allowing the device to be operated efficiently over a wider range [31]. Future work would investigate this effect and its potential for use in mobile telephony applications.

6.9 References

[1] J. Daintith, J. Clark, H.M. Clarke, D. Cooper, J. Cullerne, D.E. Edwards, R. Rennie, and D.E. Ward. *Dictionary of Physics*. Oxford University Press, 6th edition, 2009.

[2] J.J. Carr. *Practical Antenna Handbook*. McGraw-Hill, 4th edition, 2001.

[3] Ofcom. Ofcom spectrum management. http://spectruminfo.ofcom.org.uk/spectrumInfo/ukpfa, Accessed: January 2010.

[4] L. E. Frenzel. *Principles of Electronic Communication Systems*. McGraw-Hill, 3rd edition, 2008.

[5] Bluetooth SIG. Specification of the Bluetooth systems version 4.0, December 2009.

[6] IEEE. IEEE 802.11 Wireless Local Area Networks.

[7] UK Radiocommunications Agency. UK Radio Interface Requirement [IR2014], 2000.

[8] UK Radiocommunications Agency. UK Radio Interface Requirement [IR2019], 2000.

[9] J.D. Kraus and R.J. Marhefka. *Antennas For All Applications*. McGraw - Hill, 3rd edition, 2003.

[10] P.J. Bevelacqua. Antenna Efficiency and Antenna Gain. Online: http://www.antenna-theory.com/basics/gain.php, Accessed: August 2011.

[11] J.S. Colburn and Y. Rahmat Samii. Patch antennas on externally perforated high dielectric constant substrates. *IEEE Transactions on Antennas and Propagation*, 47(12):1785–1794, 1999.

[12] Z. Peng, H. Wang, and X. Yao. Dielectric resonator antennas using high permittivity ceramics. *Ceramics International*, 30:1211–1214, 2004.

[13] H. Mosallaei and K. Sarabandi. Magneto-dielectrics in electromagnetics: Concept and applications. *IEEE Transactions on Antennas and Propagation*, 52(6):1558–1567, 2004.

[14] B. Ambedkar. Broadband stacked patch antenna for Bluetooth applications. http://www.techrepublic.com/whitepapers/broadband-stacked-patch-antenna-for-bluetooth-applications/951573, Accessed: Febuary 2009.

[15] Antenna Development Corporation. UHF antennas for space. http://www.antdevco.com/ADC-08060511280sheet.pdf, Accessed: May 2008.

[16] J. George, C.K. Aanandan, P. Mohanan, K.G. Nair, H. Sreemoolanathan, and M.T. Sebastian. Dielectric Resonator Loaded Microstrip Antenna For Enhanced Impedance Bandwidth And Efficiency. *Microwave and Optical Technology Letters*, 17(3):205–207, 1998.

[17] P. V. Bijumon, S. K. Menon, M. T. Sebastian, and P. Mohanan. Enhanced Bandwidth Microstrip Patch Antennas Loaded With High Permittivity Dielectric Resonators. *Microwave and Optical Technology Letters*, 35(4):327–330, 2002.

[18] T. Komljenovic. Lens antennas Analysis and synthesis at mm-waves. *Internal publication, FER Department of Telecommunications, University of Zagreb*, 2008.

[19] C. Fernandes, V. Brankovic, S. Zimmermann, M. Filipe, and L. Anunciada. Dielectric lens antennas for wireless broadband communications. *Wireless Personal Communications*, 10:19–32, 1998.

[20] T. Shimizu and T. Yoneyama. A NRD guide fed dielectric lens antenna with high gain and low sidelobe characteristics. *IEICE Transactions on Electronics*, 88(7):1385–1386, 2005.

[21] A.V. Boriskin, G. Godi, R. Sauleau, and A.I. Nosich. Small hemielliptic dielectric lens antenna analysis in 2-D: boundary integral equations versus geometrical and physical optics. *IEEE Transactions on Antennas and Propagation*, 56(2):485–492, 2008.

[22] M.J.M. van der Vorst, P.J.I. de Maagt, A. Neto, A.L. Reynolds, R.M. Heeres, W. Luinge, and M.H.A. Herben. Effect of internal reflections on the radiation properties and input impedance of integrated lens antennas - Comparison between theory and measurements. *IEEE Transactions on Microwave Theory and Techniques*, 49(6):1118–1125, 2001.

[23] J. Musil and F. Zacek. *Microwave Measurements of Complex Permititvity by Free Space Methods and their Applications*. Elsevier, 1986.

[24] M.N. Suma, P.V. Bijumon, M.T. Sebastian, and P. Mohanan. A compact hybrid CPW fed planar monopole/dielectric resonator antenna. *Journal of the European Ceramic Society*, 27:3001–3004, 2007.

[25] M.I. Kitra, C.J. Panagamuwa, P. McEvoy, J.C. Vardaxoglou, and J.R. James. Low SAR ferrite handset antenna design. *IEEE Transactions on Antennas and Propagation*, 55(4):1155–1164, 2007.

[26] A.A. Kishk, A.W. Glisson, and G.P. Junker. Bandwidth enhancement for split cyclindrical dielectric resonator antennas. *Progress in Electromagnetics Research*, 33:97–118, 2001.

[27] C.J. Panagamuwa, M.I. Kitra, P. McEvoy, J.C. Vardaxoglou, and J.R. James. Multiband material loaded low-SAR antenna for mobile handsets. In *Wideband and Multiband Antennas and Arrays*, 2005.

[28] K.W. Leung and K.M. Luk. Circular dielectric resonator antenna of high dielectric constant for low-profile applications. In *Ninth International Conference on Antennas and Propagation*, 1995.

[29] R.K. Mongia and A. Ittipiboon. Theoretical and experimental investigations on rectangular dielectric resonator antennas. *IEEE Transactions on Antennas and Propagation*, 45(9):1348–1356, 1997.

[30] C. Fumeaux, D. Baumann, and R. Vahldieck. Advanced FVTD simulation of dielectric resonator antennas and feed structures. *Applied Computational Electromagnetics Society Journal*, 19(3):155–164, 2004.

[31] A Petosa. *Dielectric Resonantor Antenna Handbook*. Artech House, Incorporated, 2007.

[32] S.A. Long, M.W. McAllister, and L.C. Shen. The resonant cyclindrical dielectric cavity antenna. *IEEE Transactions on Antennas and Propagation*, 31(3):406–412, 1983.

[33] M.I. Kitra, P. McEvoy, J.C. Vardaxoglou, and J.R. James. Material loaded antennas and their contribution towards low-SAR. In *IEE Technical Seminar on Antenna Measurements and SAR*, 2004.

[34] International Commission on Non-Ionizing Radiation Protection. *Guidelines for lim-*

iting exposure to time-varying electric, magnetic, and electromagnetic fields (up to 300GHz), 1997.

[35] Council recommendation of 12 July 1999 on the limitation of exposure of the general public to electromagnetic fields (0 Hz to 300 GHz). Official Journal of the European Communities, July 1999.

[36] G. Johnson. Lossy Capactiors. Online: http://www.eece.ksu.edu/ gjohnson/tcchap3.pdf, Accessed: August 2011.

Chapter 7

Low frequency inductance and magnetic properties

While many materials do have dielectric properties, a considerably smaller number have magnetic properties. Materials which do have are magnetic have a permeability greater than unity. The permeability of a material is "a measure of the ability of that material to support the formation of a magnetic field within itself" [1]. Those substances which have both a permittivity and a permeability greater than unity are referred to as magneto-dielectric materials. It is important to characterize both the permittivity and permeability of a material over the frequency range of the application to fully understand the behaviour of a potential device.

7.1 Permeability

Permeability is a measure of the interaction of a material with an applied magnetic field. The relative permeability of a material is the permeability of that material divided by the permittivity of free space ($\mu_0 = 4\pi \times 10^{-7}$ [H m^{-1}], Equation 7.1). For all the following discussion, permeability assumes relative permeability unless stated otherwise. It is a complex value where the real part of permeability (μ_r') represents the magnetic energy stored within the material and the imaginary part (μ_r'') represents the energy lost. The loss tangent (*tan*δ) provides a measure of the magnetic inefficiency of the material; the ratio of the imaginary to the real part of permeability as shown in Equation 7.3.

$$\mu_r = \frac{\mu}{\mu_0} \tag{7.1}$$

$$\mu_r = \mu_r' - j\mu_r'' \tag{7.2}$$

$$tan\delta = \frac{\mu_r''}{\mu_r'} \tag{7.3}$$

7.2 High frequency magnetic properties of barium hexaferrite

At the time of writing no published work exists on the high frequency magnetic properties of bismuth substituted barium hexaferrite.

Barium hexaferrite displays different values of permeability dependant upon the formation process. Samples which have been sintered for a longer duration at higher temperatures tend to have higher permeabilities, but can be affected by ferromagnetic resonance which can reduce this value at some frequencies [2]. Work has also been undertaken which increased the permeability by doping barium hexaferrite with magnesium, cobalt and copper [3]. Most work on the magnetic properties of barium hexaferrite and related compounds focuses on the static magnetic properties and does not investigate the properties with respect to frequency.

7.3 Permeability measurement methods

At low frequencies impedance analysis using LCR meters can be used to find the permeability of a material. The basis of this method is the formation of an inductor by coiling a wire around the material under test. For best results the sample should be a toroidal shape. The change in inductance caused by the presence of the material compared to the inductance of the unloaded experimental set-up is then used to calculate the permeability [2].

At higher frequencies, impedance analysis cannot be utilised for permeability measurement. Instead network analysis is employed. Network analysis operates by placing the material under test either at the termination of a transmission line or within a section of the line. Set-ups where the material forms the termination will only yield one set of measurements; the reflection coefficient of the system, which can be translated to S-parameters in the form of S11 data. This can only be used to determine the permittivity of a sample (a reflection method was used to characterise the high frequency sample

permittivity in Chapter 4). To determine both the dielectric and magnetic properties of a material the reflection and transmission properties of a sample must be recorded. The complete set of parameters of S11, S12, S21 and S22 are collected and processed to determine the permittivity and permeability [4] [5].

7.4 Low frequency permeability: Inductance measurement method

A simple inductor was constructed to measure the relative inductance of the coil when barium hexaferrite and bismuth substituted barium hexaferrite samples were inserted compared to the air filled coil. This does not give a definitive value of complex permeability, however the relative measurements produced show trends across and between pellet series.

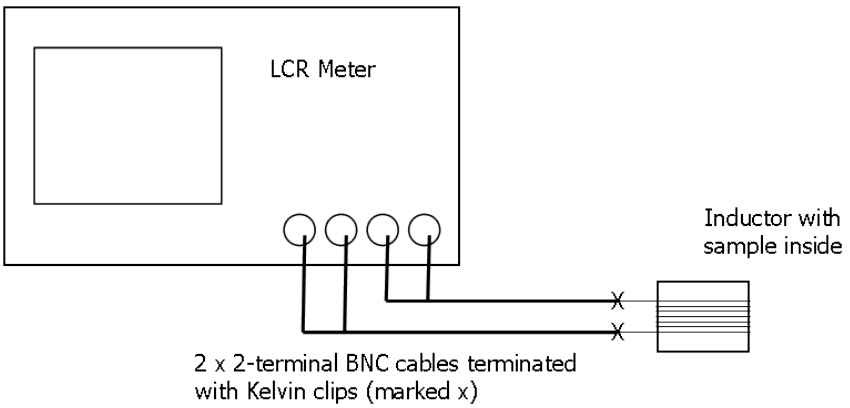

Figure 7.1: Diagram showing the experimental setup with the LCR meter connected via two 2-terminal BNC cables terminated by kelvin clips to the inductor. Sample is placed inside the inductor so that the coil is over the material.

The coil was constructed from enamelled wire wrapped around a 20mm diameter rod (which was then removed) and has ten complete turns. The ends of the wire forming the coil were attached to the Wayne Kerr 6440B LCR meter using the four terminal

kelvin clip connections (shown in Figure 7.1). The sample pellet under investigation was placed inside the coil and the inductance of the system recorded over the 20Hz – 3MHz frequency range. From these values a measure of the relative inductance is gained by dividing this value by the measured value of inductance of the coil in air as shown in Equation 7.4.

$$L_{rel} = \frac{L_{sample}}{L_{air}} \tag{7.4}$$

Four separate coils were constructed; inductors one and four consist of ten turns which are placed against each other without overlapping; inductor two is also made of ten turns but these do overlap; inductor three has fifty turns which overlap.

7.5 Low frequency relative inductance results

7.5.1 Relative inductance results after sintering at 1100°C

Series F

Series F consists of six pellets with the same composition ($x = 0.1$, $BaBi_{0.1}Fe_{11.9}O_{19}$) which have been subjected to the same sintering conditions (three hours at 1100°C). Due to the similarity of these samples, results for series F are presented first to enable a discussion concerning the accuracy of the measurement regime. Figure 7.2 shows the relative inductance given by L_{sample}/ L_{air} for each pellet in series F when characterised using inductor four.

The first observation from the inductances of the series F pellets is that the values

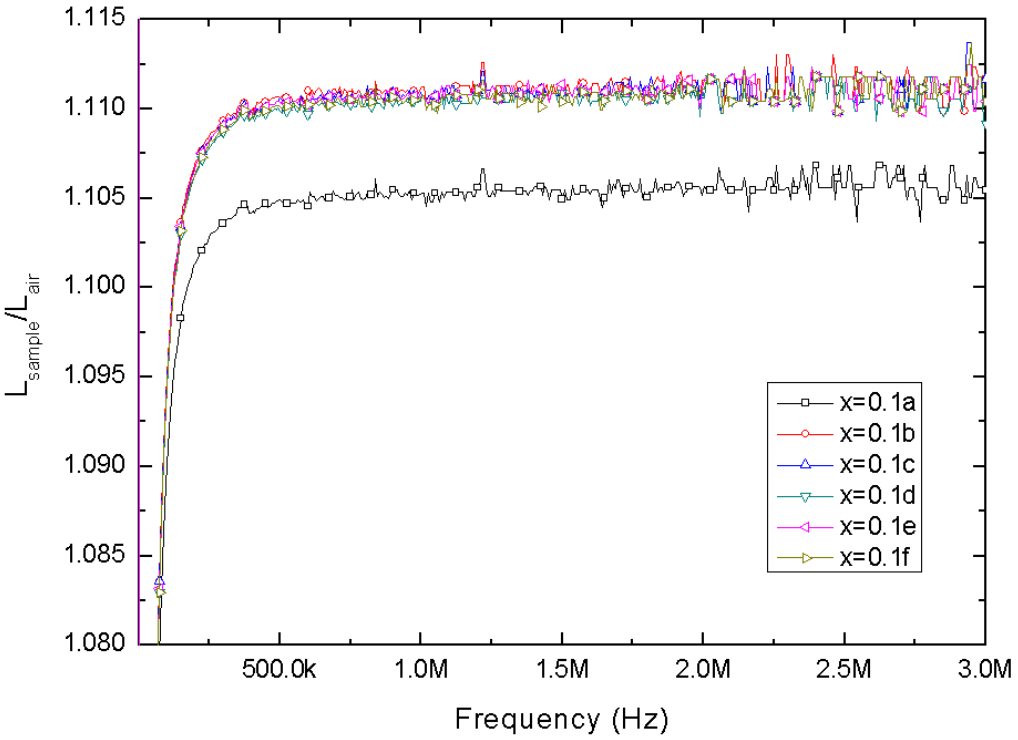

Figure 7.2: $L_{sample}/\ L_{air}$ for series F pellets which have been sintered for three hours at 1100°C across the frequency range 20Hz – 3MHz

are similar for five of the six samples with the $x = 0.1a$ sample being markedly lower than the other materials. At 1MHz sample $x = 0.1a$ has $L_{sample}/\ L_{air} = 1.10529$, the other five samples $x = 0.1, b, c, d$ and e range from $1.11073 - 1.11122$ at the same frequency. The reason for the lower magnetic value of the $x = 0.1a$ pellet is unclear; samples were fabricated and sintered concurrently and there are no clear physical defects on the pellet. Thus it is concluded that the lower magnetic value is potentially due to microscopic variations within the sample. At low frequencies (below approximately 300kHz) the inductances recorded are not constant and decrease with the test frequency, this effect was noted for all subsequent data sets irrespective of the sample under test. The values remain constant from 300kHz upwards to 3MHz, however there is slightly more noise at the very high frequencies above 2MHz. The larger variation in the traces

above 2MHz is in part due to the measurement resolution of the LCR meter used to record the inductance data; which is 2nH below 2MHz and 5nH above this threshold. These inductance values are used to calculate the relative magnetic properties of the samples according to Equation 7.4 and transferred to the graph shown in Figure 7.2. A further point is that the range of inductance values are smaller for the series F than for the other series which contain different composition pellets. The main feature of the series F results show that the samples have similar properties as expected and thus the experimental method is valid.

Series B

Series B samples contain barium hexaferrite pellets with a variety of bismuth substitution levels. The samples in this series have been sintered for one hour at 1100°C. Pellets were characterised using inductors one, two and four; the results are shown in Figures 7.3 and 7.4.

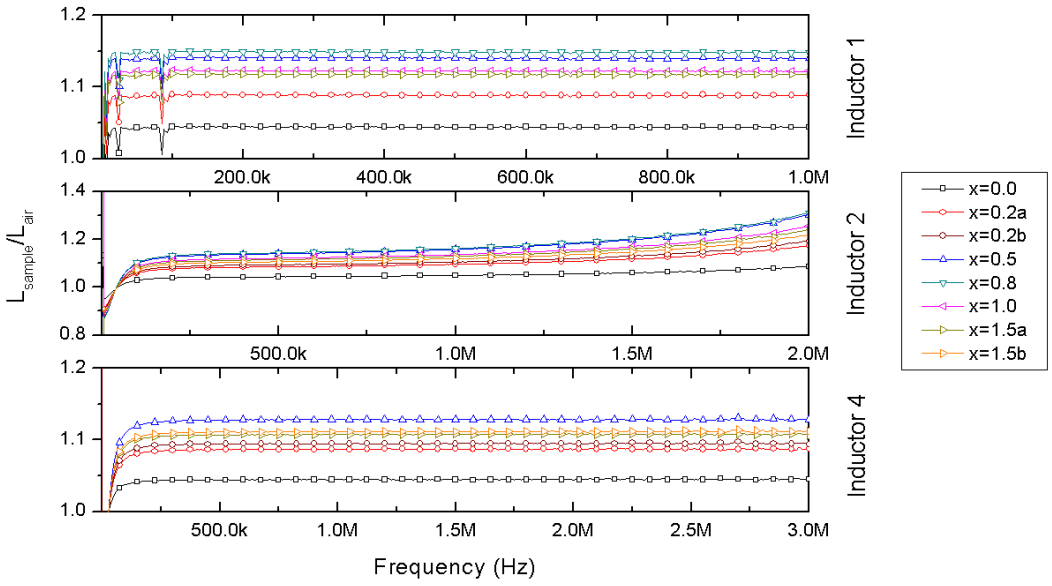

Figure 7.3: L_{sample}/ L_{air} for series B pellets which have been sintered for one hour at 1100°C from 20Hz – 1MHz for inductor one, from 20Hz – 2MHz for inductor two and from 20Hz – 3MHz for inductor four

Inductor one (top graph) shows that samples have low L_{sample}/ L_{air} values when the test frequency is low, which increases rapidly. Then there is a sharp dip at 25kHz before the trace recovers to the previous high value and is constant until 85kHz where there is another dip. The traces are then constant until the maximum frequency of 1MHz. These trends are seen for all samples. The dips in the traces were unexpected but could not be retested because inductor one broke during a subsequent measurement. It is hypothesised that these irregularities in the graphs were due to a possible calibration error at the frequencies where the dips occur because they are not present in the same pellets characterised using inductor four which has the same number of turns arranged in the same non-overlapped way. Additional supporting evidence is found in the series C pellets which have the same compositions and sintering conditions characterised with the same inductor which also do not show dips in the L_{sample}/ L_{air} values. The sample with the lowest inductance is the undoped $x = 0.0$ sample which has $L_{rel} = 1.04437$ at 1MHz compared to the maximum of 1.14879 at the same frequency for the $x = 0.8$ pellet.

The data for inductor two (middle graph) shows a very similar response to that of data collected with inductor one. The undoped barium hexaferrite material has the lowest relative inductance and the $x = 0.5$ and $x = 0.8$ have the largest, with other samples falling within these ranges.

The L_{sample}/ L_{air} values for inductor four are shown in the bottom graph of Figure 7.3, which has the same structure as inductor one. Not all samples were tested because the inductor coil has a slightly smaller diameter than inductor one, so some samples would have fitted into the coil but could not have been removed. Thus these samples were omitted from characterisation. The overall measurement trends are as seen for other

pellet series characterised using inductor four; low L_{sample}/ L_{air} values are seen at low frequencies, which then increase rapidly until the values stabilise at 300kHz, remaining constant to the maximum test frequency of 3MHz. Those samples which were tested show L_{sample}/ L_{air} values inline with the measurements taken with the other inductors; the sample with the smallest relative inductance is the $x = 0.0$ sample with $L_{sample}/ L_{air} = 1.04451$ at 1MHz. The bismuth containing samples all show greater inductance values than the parent barium hexaferrite compound. The $x = 0.8$ sample which had shown the greatest L_{sample}/ L_{air} value when tested in the other inductors would not fit into inductor four so was not tested. The next highest pellet tested in inductor one was the $x = 0.5$ sample which is indeed the highest of the inductor four samples with relative inductance 1.12809 at 1MHz.

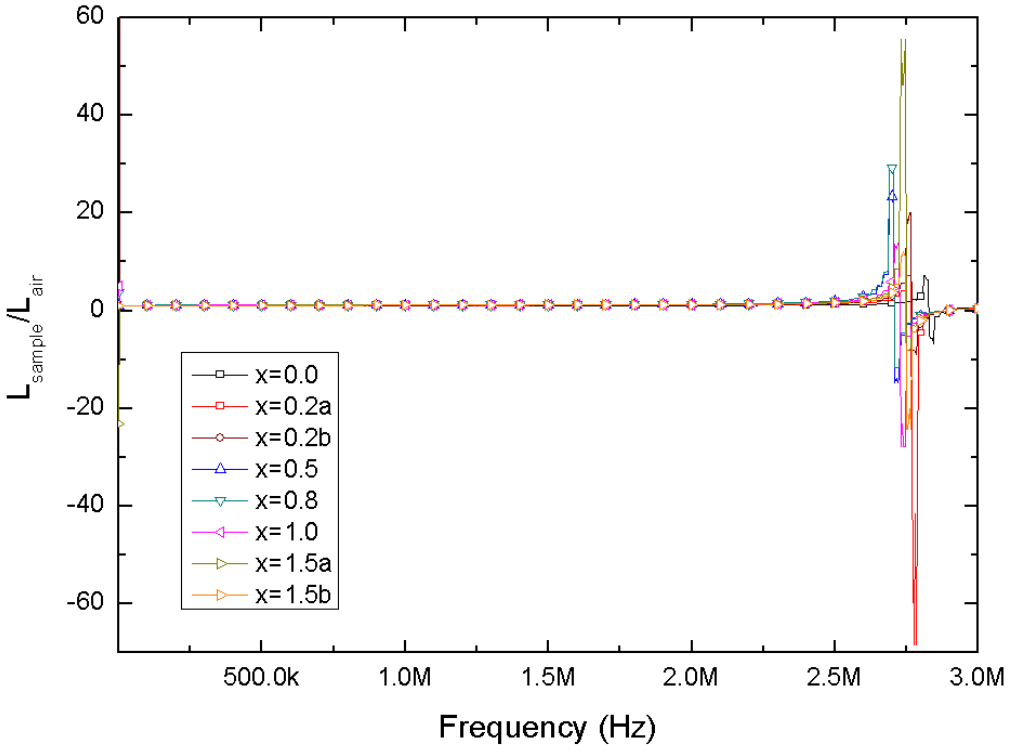

Figure 7.4: L_{sample}/ L_{air} for series B pellets which have been sintered for one hour at 1100°C from 20Hz – 3MHz for inductor two

Figure 7.4 shows results for inductor two across the whole frequency range of the LCR meter (20Hz – 3MHz). This displays a markedly different response in comparison to the other two inductors in Figure 7.3. The low frequency L_{sample}/ L_{air} values are similar to those given by inductor one, increasing from a low value to an approximately constant value from 100kHz to 1.5MHz before rapidly increasing and then decreasing as the experimental set-up resonates due to the overlap of the turns on this inductor. During the stable phase of the measurement up to 1.5MHz the L_{sample}/ L_{air} values show the same pattern as the inductor one measurements; the $x = 0.0$ sample has the lowest value and the $x = 0.8$ sample the largest (1.04902 and 1.16217 respectively at 1MHz). This resonance is due to the overlap of the coils on this inductor inflicting a self-resonance on the system. The nature of this resonance is similar to that seen in parallel L C circuits where the resonant frequency is proportional to $1/$ inductance; this is observed in Figure 7.4 where the undoped barium hexaferrite material which has a lower relative inductance causes resonance at a slightly higher frequency than the bismuth containing samples. This resonance is seen for all subsequent sample sets and so inductor two was not used beyond 2MHz (the limit of the stable region).

The relative inductance results for the series B pellets confirm the validity of the experimental method; the samples show the same hierarchy of L_{sample}/ L_{air} values within the stable phase of the response when tested in different inductors.

Series C

Pellets in series C contain a variety of samples with different levels of bismuth substitution in the barium hexaferrite compound which have been sintered for one hour at 1100°C.

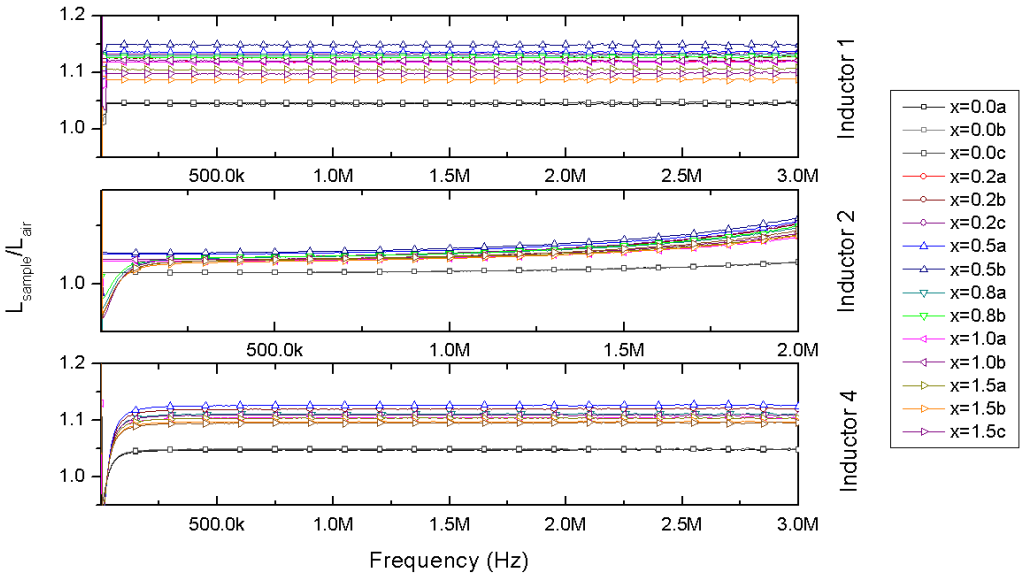

Figure 7.5: $\mathrm{L_{sample}/\ L_{air}}$ for series C pellets which have been sintered for one hour at 1100°C from 20Hz – 3MHz (20Hz – 2MHz for inductor two)

Figure 7.5 shows the same overall trends as seen for the series B pellets tested in the same set of inductors; with inductors one and four displaying low $\mathrm{L_{sample}/\ L_{air}}$ values at low frequencies however the majority of the response is flat. Inductor two has a flat response up until 1.5MHz at which point the experimental set-up resonates, making measurements above this frequency unreliable. For all inductors the $x = 0.0$ sample has the smallest $\mathrm{L_{sample}/\ L_{air}}$ value which is repeated for the $x = 0.0a, b$ and c pellets. For this series the $x = 0.5$ pellet has the highest recorded inductance (1.12716 at 1MHz using inductor four), however the range of the bismuth containing samples are all close and notably larger than the undoped pellets.

Series D

Series D is composed of a variety of samples with different bismuth concentrations, chemical formula $\mathrm{BaBi}_x\mathrm{Fe}_{12-x}\mathrm{O}_{19}$ for $x = 0.0, 0.2, 0.5, 0.8, 1.0$ and 1.5 which have been

sintered for three hours at 1100°C. The relative inductance measurements are shown in Figure 7.6.

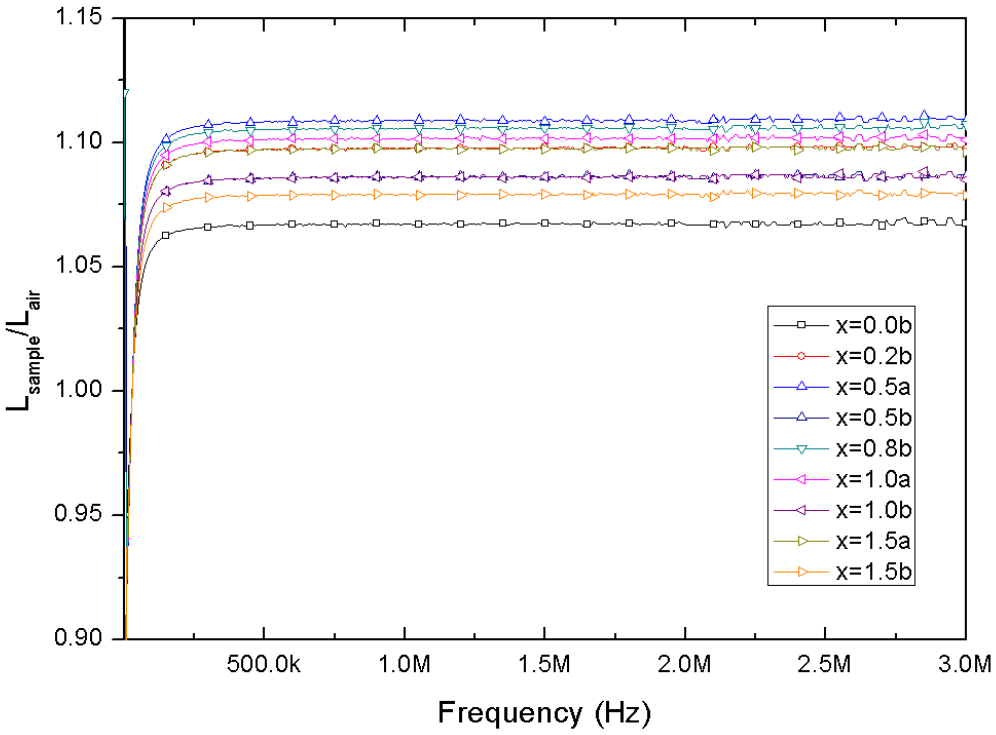

Figure 7.6: L_{sample}/ L_{air} for series D pellets which have been sintered for three hours at 1100°C from 20Hz – 3MHz

As seen for previous series, the low frequency relative inductance values are very small, increasing rapidly up to 150kHz where the rate of increase slows until the L_{sample}/ L_{air} values become approximately constant at frequencies above 300kHz and again, slightly more variation in the graph is seen above 2MHz where the resolution of the LCR meter decreases. The $x = 0.0$ sample has the lowest relative inductance of 1.06726 at 1MHz. The highest L_{sample}/ L_{air} sample is the $x = 0.5a$ pellet (1.1088 at 1MHz). There is a larger range of inductances for this series than was previously seen, however the addition of bismuth is found to consistently increase the magnetic properties of the material.

7.5.2 Relative inductance results at 1100°C as a function of substitution level

Comparison of series B and series C

Series B and C have been subjected to the same sintering regime of one hour at 1100°C allowing comparisons on the repeatability of magnetic properties of the materials and also to clearly present the effect of bismuth concentration on the magnetic properties.

Figure 7.7 shows the L_{sample}/ L_{air} values for pellets from series B and C for inductors one and two at 1MHz with increasing bismuth content. The graphs show good agreement between both samples and the trends seen between inductors, indicating that results are reliable. For all circumstances the undoped $x = 0.0$ samples are the lowest, the relative inductance then increases when bismuth is added. The highest values of L_{sample}/ L_{air} are the $x = 0.5$ and $x = 0.8$ before inductance drops for the $x = 1.0$ sample before then recovering slightly at the $x = 1.5$ level.

Relative inductance at 1100°C

Figure 7.8 shows the L_{sample}/ L_{air} values for pellets from series B, C and D placed in inductor four. These have all been sintered at 1100°C; series B and C for one hour and series D for three at this temperature .

The first observation is that the overall trends are the same for all pellet series; the undoped barium hexaferrite samples have the lowest relative permeabilities. When bismuth is added the inductance increases upto a maximum value for all series at the $x = 0.5$ value and then tails off at higher bismuth levels but still remains higher than the undoped

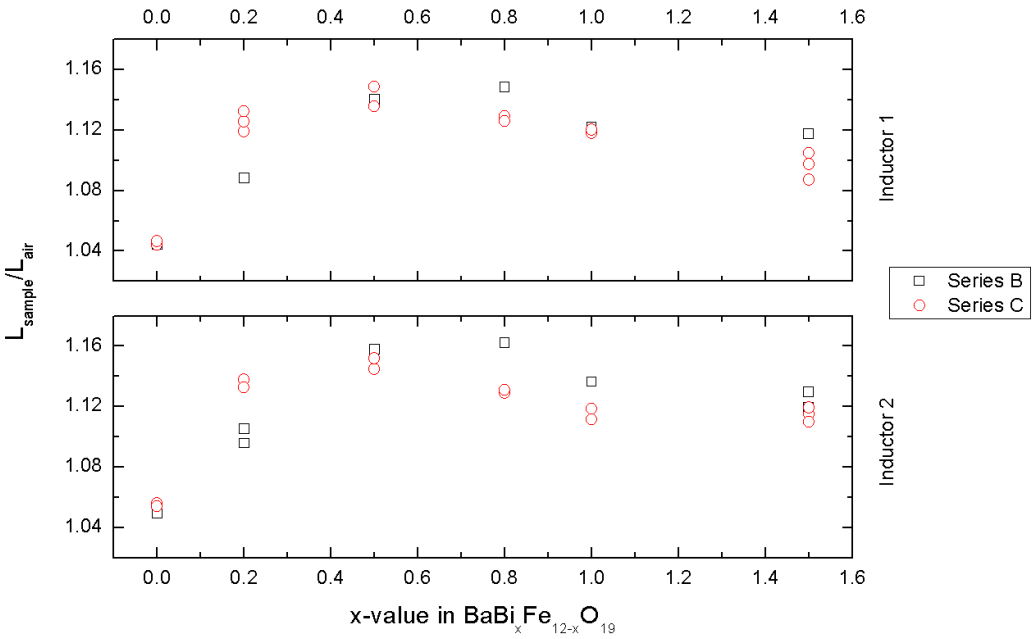

Figure 7.7: L_{sample}/ L_{air} for series B and C pellets when placed in inductor 1 and 2 at 1MHz

material. The absolute values of L_{sample}/ L_{air} do show some variation and the series D pellets have a consistently lower relative inductance than series B and C pellets with the exception of the undoped $x = 0.0$ sample.

Density measurements from Section 2.6 show that there is no noticeable difference in densities between the pellets, indicating that this is not contributing to the lower inductance. However, it is hypothesised that for the undoped barium hexaferrite sample, being sintered for a longer period of time would allow for more of the starting material to have reacted compared to a single hour at this temperature. This could potentially explain the higher inductance observed for the series D undoped material compared to series B and C. The lower inductance for the bismuth containing samples in series D is potentially due to the low melting point of bismuth oxide at 817°C and boiling point of 1890°C [6]; at the sintering temperature of 1200°C for longer durations some of the bismuth could be lost to the atmosphere as it begins to evaporate.

The tends seen in Figure 7.7 which shows the samples from series B and C tested with inductors one and two are repeated here for inductor four. The lowest L_{sample}/ L_{air} values are for the undoped barium hexaferrite samples (1.04451 for series B and a midpoint of 1.04932 for the three series C pellets), which is most likely due to the incomplete formation of the material. The addition of bismuth increases the L_{sample}/ L_{air} values before a maximum is achieved at $x = 0.5$ (1.12809 for series B and 1.12716 for series C). The large range of values for the $x = 0.2$ samples for these series is considered to be for similar reasons that the low frequency permittivity values (Chapter 3, Section 3.4.3); a low sintering temperature and short duration combined with a low level of bismuth present results in a wide variation in the proportion of the reagent materials which have been converted into the final product. This is because bismuth substitutes first into the $4f_2$ sites (suggested by Winotai et al. [7]) but has not reached the saturation value of $x = 0.32$ as proposed by Ram et al. [8]. The maximum inductance achieved at the $x = 0.5$ level is also akin to that seen for the permittivity trends at the same frequency. Here it is considered that the maximum level of bismuth substitution into the $4f_2$ sites is reached and after this point bismuth continues to substitute into the next preferred 2b sites (discussed in more detail within Chapter 2, Section 2.2) which still enhances the magnetic properties of the material. Inductance then slowly decreases up to the maximum bismuth concentration of samples $x = 1.5$, which is still greater than the undoped sample values. The series B $x = 0.8$ and $x = 1.0$ samples are missing from this graph due to their diameters being too great for them to be removed from the inductor.

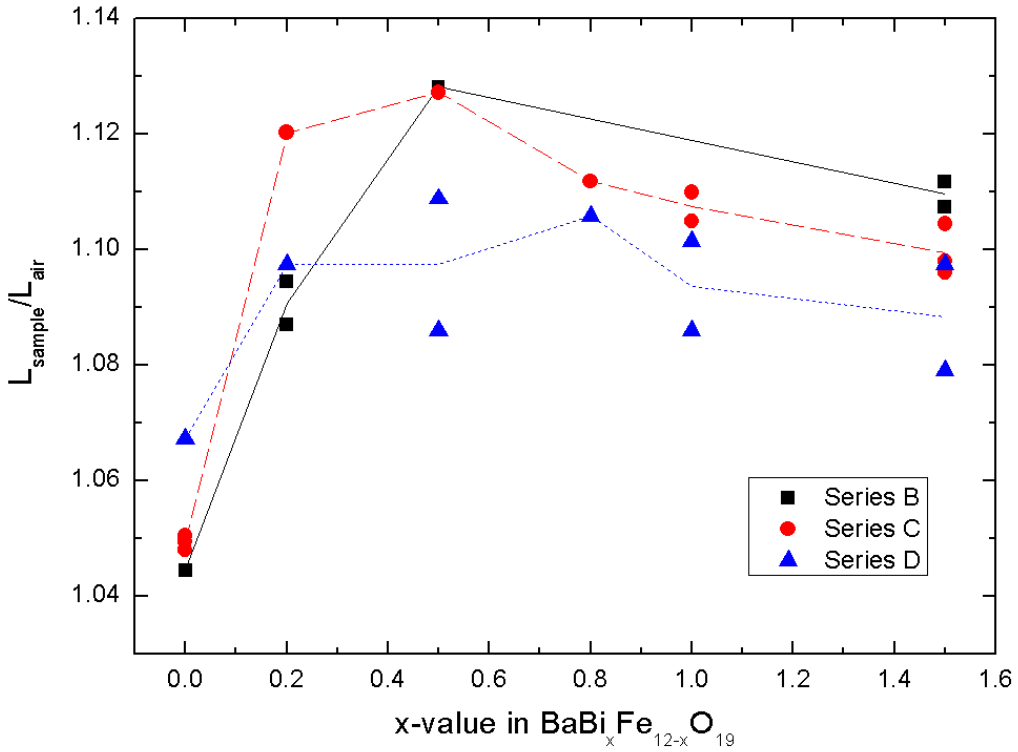

Figure 7.8: L_{sample}/ L_{air} for series B, C and D pellets at 1MHz. Series B and C have been sintered for one hour at 1100°C, series D pellets have been sintered for three hours at 1100°C.

7.5.3 Comparison to permittivity results at 1100°C

The trends seen in the relative inductance values with respect to bismuth content at 1MHz are the same as those observed for the permittivity at the same frequency; increasing from a low value for the $x = 0.0$ sample to a maximum at $x = 0.5$ and then slowing reducing as bismuth increases up to the maximum of $x = 1.5$. The underlying processes in the material formation is most likely responsible for both the trends in the permittivity and permeability (see Chapter 3 Section 3.4.3)

7.5.4 Relative inductance results after sintering at 1200°C

Series A

Series A is made up from six different bismuth composition barium hexaferrite samples, composition $BaBi_xFe_{12-x}O_{19}$ with x-values $0.0, 0.2, 0.5, 0.8, 1.0$ and 1.5 sintered first for one hour at 1100°C followed by a further hour at 1200°C. The L_{sample}/ L_{air} results using inductor four are shown in Figure 7.9.

The first observation from the inductance graph is that all samples show the same overall pattern, similar to that seen with the series F pellets where the L_{sample}/ L_{air} value is small at low frequencies, rapidly increasing up to 300kHz where the inductance then remains constant up to the maximum frequency of 3MHz. There is a slightly greater degree of variation in the trace above 2MHz where the resolution of the LCR meter reduces from 5nH to 2nH as observed for the series F results, however it is less apparent because the scale of the graph is larger to fit the wider range of L_{sample}/ L_{air} values due to the wider range of sample compositions. The parent compound barium hexaferrite

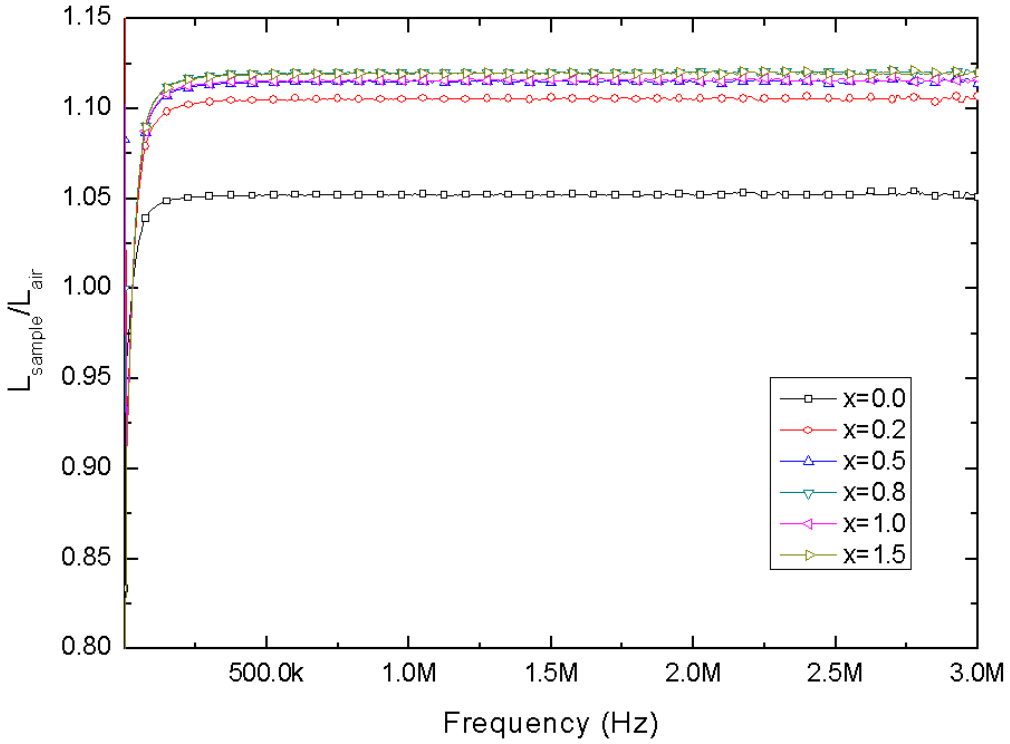

Figure 7.9: L_{sample}/ L_{air} for series A pellets which have been sintered for one hour at 1100°C followed by a further hour at 1200°C from 20Hz – 3MHz

material shows a markedly lower inductance than the other samples; 1.05242 at 1MHz, compared to a maximum of 1.11968 for the $x = 0.8$ sample. The smallest inductance of the bismuth containing samples is the $x = 0.2$ sample ($L_{sample}/ L_{air} = 1.10534$), the remaining samples are all more similar with $Ł_{rel}$ ranging from $1.11523 - 1.11919$.

Series PS

Series PS samples were subjected to the same sintering regime as series A (one hour at 1100°C followed by a further hour at 1200°C) however these pellets are only 16mm in diameter compared to other series which are 20mm. This results in a smaller recorded inductance due to the air gap between the sample and the inductor coils. However the results still provide a useful comparison for reference.

Figure 7.10 shows the inductance data when series PS pellets were placed within inductor four. The inductance is small for low frequencies, increasing rapidly until the response stabilises and levels out above 300kHz. There is greater variation in the traces above 2MHz where the resolution of the LCR meter increases, although the value still remains approximately constant. Again, the undoped sample has a lower L_{sample}/ L_{air} value than the bismuth containing samples; $L_{rel} = 1.04055$ for sample $x = 0.0$ compared with a range from $L_{sample}/ L_{air} = 1.05094 - 1.05984$ for the bismuth containing samples at 1MHz. The absolute values of inductance recorded are lower for the series PS pellets; in the region of 4.2μH compared to 4.5μH for series A pellets at 1MHz, thus contributing to the greater variation in the L_{sample}/ L_{air} above 2MHz because the 5nH resolution is more significant and a lower overall scale on the graph in Figure 7.10.

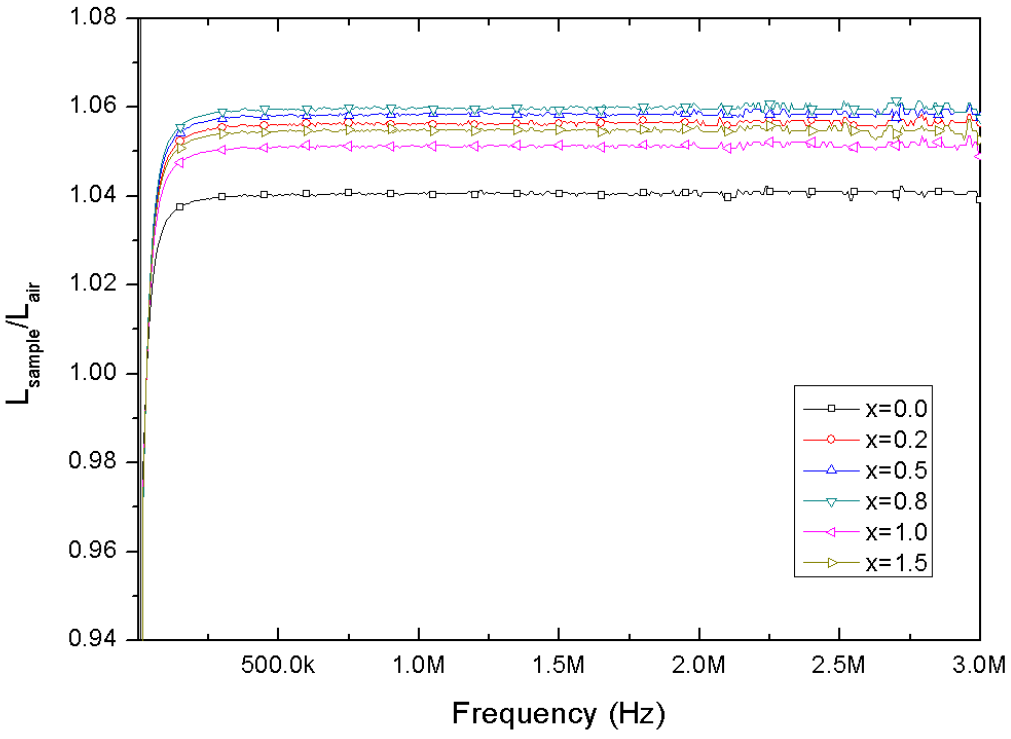

Figure 7.10: L_{sample}/ L_{air} for series PS pellets which have been sintered for one hour at 1100°C followed by a further hour at 1200°C from 20Hz – 3MHz

Series E

Series E samples have been sintered for three hours at 1200°C and contain a variety of bismuth concentration pellets. The L_{sample}/ L_{air} results are shown in Figure 7.11. The now familiar pattern of low inductance values at low frequencies increasing rapidly before levelling off after 300kHz and with some increased variation above 2MHz caused by lower LCR meter resolution.

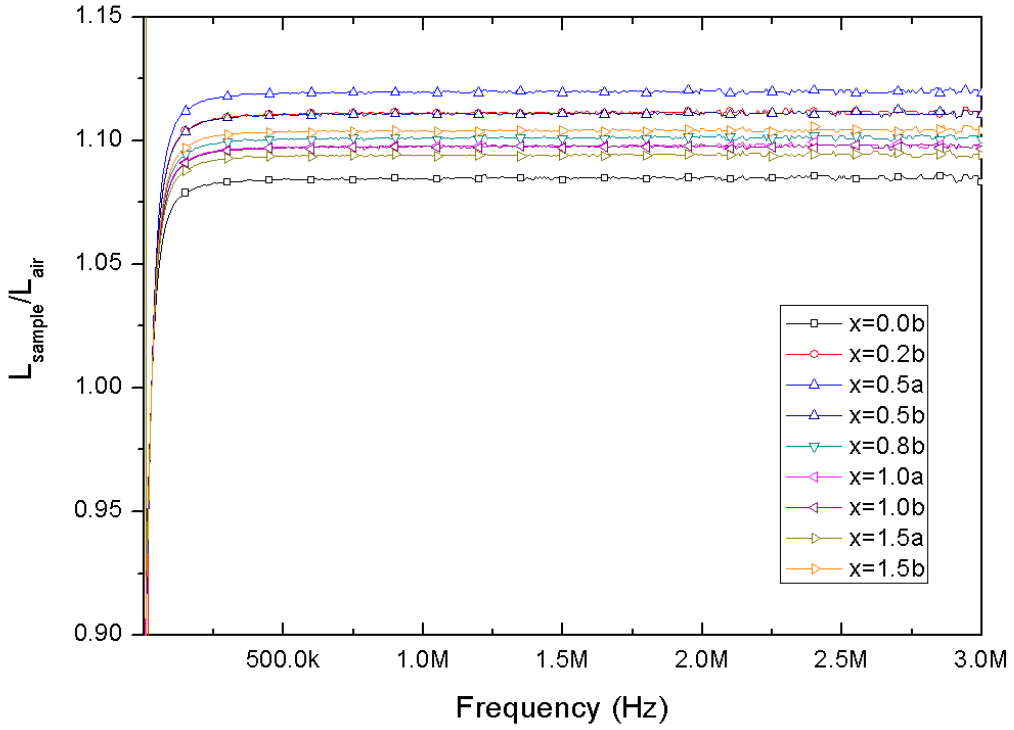

Figure 7.11: L_{sample}/ L_{air} for series E pellets which have been sintered for three hours at 1200°C from 20Hz – 3MHz

The lowest L_{sample}/ L_{air} is the $x = 0.0$ barium hexaferrite sample which is 1.0848 at 1MHz. The highest value is the $x = 0.5a$ sample which is 1.1199 at 1MHz. This highest value is more inline with the lower 1100°C samples than with the other 1200°C pellets of series A and PS. The bismuth containing pellets are all covered within the range $1.09419 - 1.1199$.

7.5.5 Relative inductance results at 1200°C as a function of substitution level

In this section the relative inductances of samples from series A, PS and E are compared at the fixed frequency of 1MHz. Pellets from series A and PS have been sintered at 1100°C for one hour, then cooled to room temperature before being sintered again at a maximum temperature of 1200°C for a further hour. Series E samples have been sintered for three hours at 1200°C. Relative inductance results for each of these series display an approximately constant response at frequencies higher than 300kHz, hence taking data at 1MHz is representative of the series above the 300kHz threshold. Data is presented as bismuth substitution level (in terms of the x-value of the material) against the relative inductance.

The same trends can be seen for the series A and PS pellets in Figure 7.12. The unsubsituted material has the lowest relative inductance which increases with the addition of bismuth to a maximum value when $x = 0.8$ before dropping slightly at $x = 1.0$ and then increasing again at $x = 1.5$ to a similar value to that of the maximum at $x = 0.8$. The values of the PS samples are lower than those of series A due to the smaller 16mm diameter pellets.

The trend presented by the series E samples is more similar to that of the 1100°C samples where L_{sample}/ L_{air} increases from a low value at $x = 0.0$, increasing to a maximum at $x = 0.5$ before falling, although similarly to both series A and PS the inductance of the $x = 1.5$ samples does increase again instead of continuing to fall.

An interesting feature of the relative inductance results at 1200°C is that they do not bear a similarity to the permittivity trends of the same samples at the same frequency

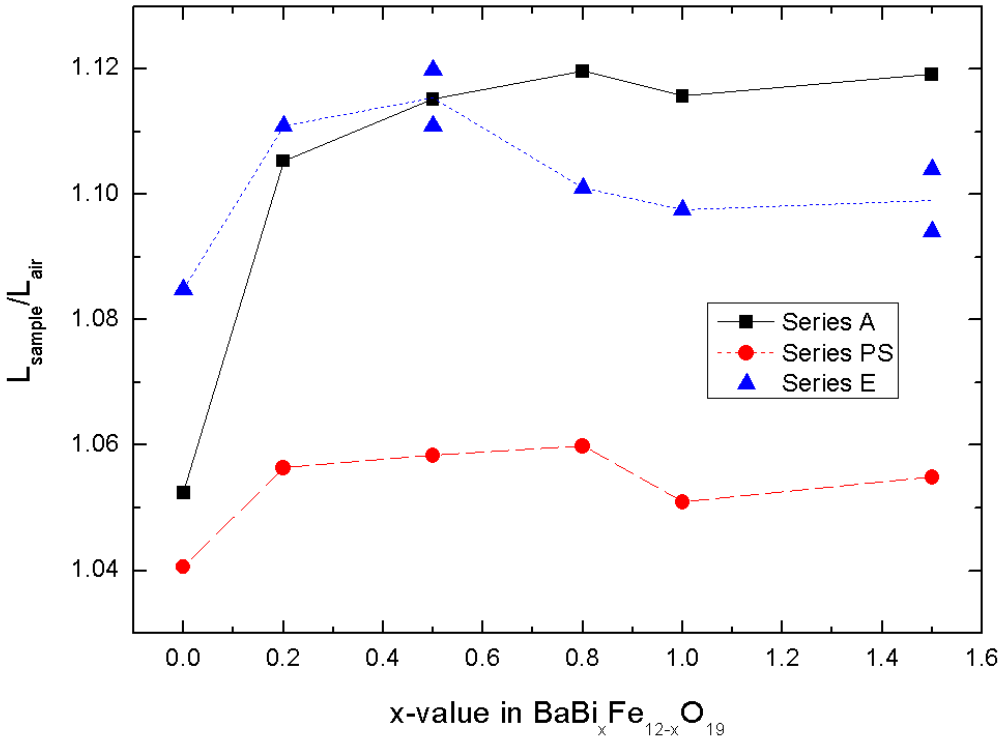

Figure 7.12: L_{sample}/ L_{air} for series A, PS and E pellets at 1MHz. Series A and PS have been sintered for one hour at 1100°C followed by a further hour at 1200°C, series E pellets have been sintered for three hours at 1200°C.

(Chapter 3, Section 3.4.5) which was observed for the samples sintered at 1100°C.

The undoped barium hexaferrite sample in series E has the highest relative inductance of all the $x = 0.0$ samples across the series; this would likely be due to it possessing the highest degree of formation of all the samples having undergone the longest sintering duration at the hottest temperature, allowing more of the material to reach the barium hexaferrite formation threshold of 1050°C.

When comparing the series A and series E samples, it is noted that the $x = 0.2$ samples are separated by a much smaller range than the same composition pellets after sintering at 1200°C. This adds weight to the previous assertion that the $x = 0.2$ substitution value is critical for bismuth substituted barium hexaferrite; the higher sintering temperature provides conditions which allow a greater level of substitution of the bismuth ions into the $4f_2$ sites thus a greater level of formation is achieved for series A samples with a shorter sintering duration, bringing the results closer to the series E data.

The addition of bismuth to the compound consistently increases the magnetic properties of the sample, indicated by the increase in the relative inductance values. Even at high bismuth substitution levels the inductance remains higher than that of the undoped samples indicating that bismuth has substituted into the iron sites in the lattice.

7.5.6 Conclusions

The L_{sample}/ L_{air} values of all samples when tested with inductors one or four which are composed of ten non-overlapping turns display a low inductance at low frequencies, which increases rapidly before stabilising at a constant value from 300kHz through until the limit of the test frequency at 3MHz. Samples characterised with inductor two show

resonance effects at frequencies than 2MHz.

Samples from series B and C were characterised using inductors one and two and the inductance values compared. A good level of agreement was seen between inductors and in trends for relative inductance with respect to sample composition.

For samples sintered at 1100°C the trends when L_{sample}/ L_{air} is plotted against bismuth doping levels, trends are similar to those seen for permittivity results at the same frequency. This is accredited to the presence of bismuth increasing the inductance of the material as it first substitutes into the $4f_2$ sites, reaching a maximum at the $x = 0.5$ level before slowly decreasing as bismuth then substitutes into the 2a sites. At sintering temperautres of 1100°C the highest relative inductance is for the $x = 0.5$ sample from series B with $L_{sample}/ L_{air} = 1.128$ which has been sintered for one hour. The same composition pellet from series C which has been subjected to the same sintering regime possesses a L_{sample}/ L_{air} value very close to the maximum of series B with $L_{rel} = 1.127$.

With the exception of the unsubsituted barium hexaferrite material, samples from series D which have been sintered for three hours at 1100°C have lower L_{rel} values. It is speculated that this was in part due to the evaporation of bimuth oxide into the atmosphere within the furnace.

After sintering at a maximum of 1200°C the highest L_{sample}/ L_{air} value is the $x = 0.5$ pellet from series E where $L_{rel} = 1.199$. The trends observed for series E are more similar to those seen for sample series sintered at the lower 1100°C temperature. Series A and PS samples show a sharp increase with initial bismuth addition and then continue to increase at a lower rate until a maximum at $x = 0.8$ ($L_{sample}/ L_{air} = 1.119$ for series A). It is possible that the higher maximum for series E is reached at a lower doping level

because the longer sintering duration facilitates a more complete reaction that in one hour.

The relative inductance of the undoped barium hexaferrite is increased by sintering for longer durations and at higher temperatures. However the presence of bismuth consistently increases the L_{sample}/ L_{air} values, enhancing the magnetic properties of the material.

7.6 Magnetic properties

Barium hexaferrite and bismuth substituted barium hexaferrite are both magnetic materials; their structure contains a large number of magnetic domains. In their unbiased state, that is without having been exposed to an external magnetic field, these domains are randomly aligned with the result that the material does not have a net magnetic moment in any one direction. [9]

A magnetic material can be characterised by its hysteresis loop. This is the graphically representation between an externally applied field and the magnetisation of the material. An example hysteresis loop is shown in Figure 7.13.

The hysteresis loop begins at the intercept of both axes where the applied field (H) and material magnetisation (M) are both zero. As the applied field strength is increased the magnetisation of the sample also increases until the material reaches magnetic saturation (M_s); the magnetisation of the samples does not increase further even with an increase in the applied field strength. After this point the applied field is reduced. When the magnetic field reaches zero the sample still has a remnant magnetism (M_r). Next as the applied field is increased in the opposite direction the magnetism of the sample continues

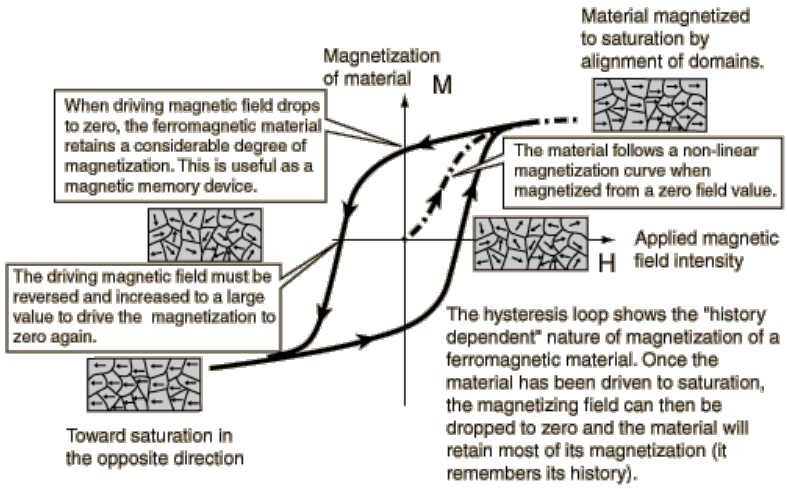

Figure 7.13: Sample hysteresis loop showing the relationship between an applied field and the resulting magnetisation of a magnetic material adapted from [10].

to reduce until it reaches zero. This point on the graph indicates the coercive force (H_c), which is the value of magnetic field strength required to neutralise the magnetism of the material. With the increasing applied field the sample becomes magnetised in the opposite direction until another saturation point is reached. After this the applied field is reduced and then changes polarity before increasing again, completing the hysteresis loop in the other direction. [11] [12]

7.6.1 Magnetic properties of bismuth substituted barium hexaferrite

Very little has been published on the topic of magnetic properties of bismuth substituted barium hexaferrite. One paper by Ram et al. [13] and another by Pal et al. [14] investigated the magnetic properties of the material. Ram presented no hysteresis loops but data in tabular form for M_s, H_c and M_r / M_s for one composition of $BaBi_xFe_{12-x}O_{19}$ where $x < 0.32$ albeit with a variety of sintering regimes. The authors found that the coercivity of the material decreased with the addition of bismuth and also with the sintering of samples for long periods of time at higher temperatures, however there was

little change in the magnetic saturation values.

Pal [14] investigated a wider range of sample compositions ($x = 0.0, 0.2, 0.3, 0.4$ and 0.8) however these materials were produced using a method of calcining and firing rather than the straightforward solid state method followed within this work, which is likely to have an effect on the final magnetic properties. One hysteresis loop was presented for sample composition $x = 0.4$ and tabular data for M_s and H_c for the other compositions. The authors found that the saturation magnetisation initially increased with the addition of bismuth until a maximum at sample composition $x = 0.3$ whilst the coercive force was at a minimum. After this point the coercive force again increases while the magnetisation saturation drops.

This work will present hysteresis loop data and cover a wider range of sample compositions and to confirm or dispute the findings of these two previous papers. The formation process is likely to be important as for the unsubstituted barium hexaferrite it has been reported that denser samples with finer grains produce materials with greater coercivity [15].

7.6.2 Experimental procedure

The equipment used to characterise the hysteresis loop of a material is a vibrating sample magnetometer (VSM). The main component of the set-up is a large solenoid which is used to produce a magnetic field, this is the applied field for the hysteresis loop data. The sample magnetisation is detected by using a Hall effect probe located near to the sample under test.

System in use at The University of Nottingham

The VSM at The University of Nottingham is located within the School of Physics and Astronomy. The system was constructed in-house and the controlling software was developed as a student project, consequently the operation of the system will be detailed within this section. A schematic diagram of the equipment used is shown in Figure 7.14.

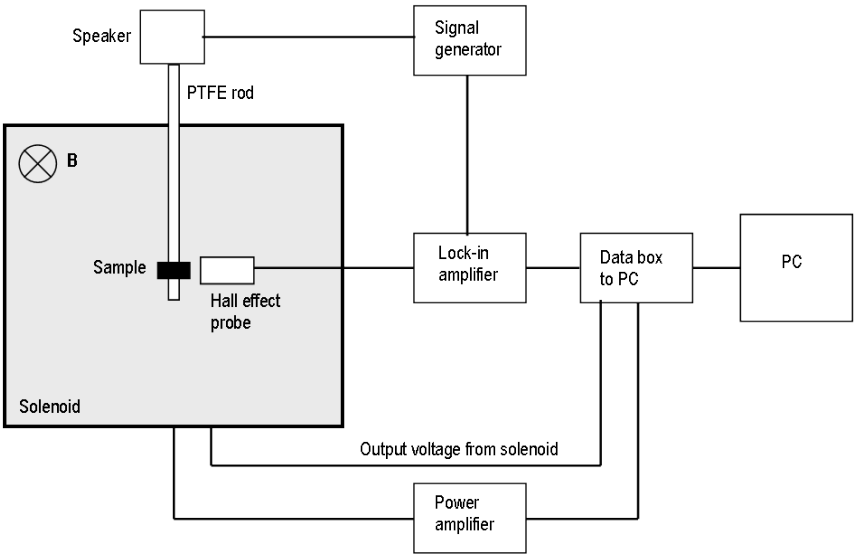

Figure 7.14: Diagram showing VSM system set-up adapted from [16].

The main components of the system; the solenoid and the Hall effect probe are located on the right hand side of the diagram in Figure 7.14. There are several other parts to the set-up required to produce a meaningful output.

The voltage supplied to the solenoid is controlled via a Matlab program on a connected PC. This value is confirmed by a separate output reading which also reduces any effect of a time delay before the solenoid and the generated magnetic field responds to a new input voltage. This voltage is input back to the PC and represents the strength of the magnetic field generated by the solenoid and therefore is one of the values used to generate hysteresis loop data.

The Hall effect probe is a device which (as the name implies) is based upon the exploitation of the properties of the Hall effect to measure the strength of a magnetic field by a resultant voltage. The Hall effect is defined as "the production of an electromotive force within a conductor ... through which a current is flowing when there is a strong transverse magnetic field. The potential difference develops at right angles to both the current and the field [and] is caused by the deflection of charge carriers by the field" [1]. In the VSM system the voltage generated by the Hall probe is recorded and used to quantify the strength of the magnetic field to which the probe is subjected using the relationship given in Equation 7.5 [17]:

$$V_H = \frac{B\,I}{n\,e\,d} \tag{7.5}$$

Where V_H is the potential difference across the Hall probe in volts, B is the strength of the magnetic field in tesla, I is the current passing through the probe in amps, n is the density of the charge carriers in m^{-3}, e is the charge of an electron in coulombs, and d is the depth of the conductor used within the Hall probe in m. By using the same Hall probe and keeping the supplied power the the device constant, all terms in the equation other than the magnetic field term B also remain constant thus the Hall voltage is directly proportional to the magnetic field strength the device is subjected to. From this reasoning the Hall probe was used to measure the magnetic field generated by the barium hexaferrite sample placed within the coils as it becomes magnetised. The probe was aligned such that only fields originating from the sample would be detected and the applied field generated by the solenoid would be neglected.

The sample itself was attached to a PTFE rod suspended in the centre of the solenoid.

The rod was in turn connected to a loudspeaker, thus the sample could be vibrated with a known signal. This signal was compared to the output from the Hall probe using the lock-in amplifier; all components of the signal with frequencies which did not correspond to the driving reference signal frequency were removed. The remaining data presents a larger voltage when the probe is in the presence of a stronger magnetic field.

Program operation, data collection and storage was controlled via a Matlab program operating on the connected PC. Data presented here has not been formatted into the standard applied magnetic field intensity (in Oe) and material magnetisation (in Am^{-1}). To convert the data into this form a scaling factor is required, however since the VSM set-up was developed in-house finding this term is not a trivial task. Unfortunately due to time constraints this work has yet to be completed, however results presented here are still valid in showing the resultant magnetisation of the material in the presence of an applied magnetic field.

Samples from series A which contain a variety of bismuth substitution values which have been sintered for one hour at 1100°C followed by a further one hour at 1200°C were in turn placed within the VSM rig and characterised.

7.6.3 Results

The program controlling the VSM allows the user to specify the sampling time for two complete cycles of the hysteresis loop. A longer sampling time produces results with finer resolution but is also time intensive. The data presented in Figure 7.15 shows the results collected for the same sample (composition $x = 1.0$) for a program run time of five and ten minutes.

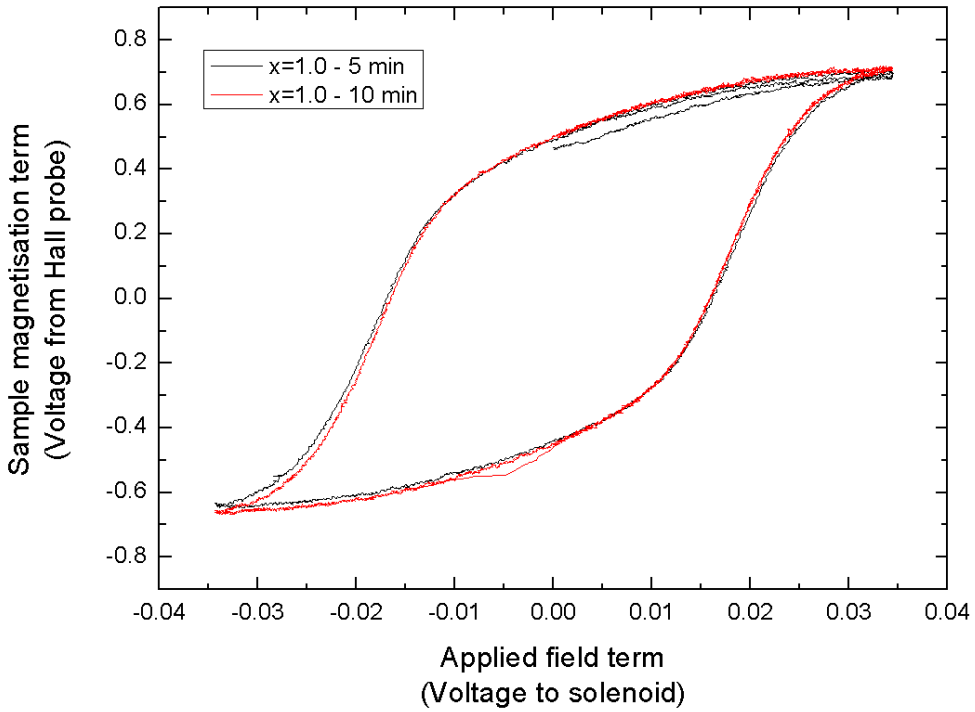

Figure 7.15: Hysteresis loop for sample $x = 1.0$ from series A showing the differences for a run time of five (black trace) and ten (red trace) minutes for two loops.

Both hysteresis loops show good agreement for both the five and ten minute data collection times. The five minute (black trace) data has less overlap between the two sweeps in the top segment of the loop; indicating that the ten minute data collection regime is slightly more accurate (more overlap is seen here resulting in the traces appearing as one loop). Thus the decision was made to use a ten minute sampling time for the series A pellets within the VSM.

Figure 7.16 shows the hysteresis loops for barium hexaferrite and bismuth substituted barium hexaferrite samples from series A using a ten minute collection regime. Results are presented for pellets with compositions $x = 0.0, 0.5, 1.0$ and 1.5. The $x = 0.8$ sample was found to have broken during the process upon removal and so results were not valid. The $x = 0.2$ material did not remain adhered to the PTFE rod during characterisation

and so results could not be obtained, after several attempts this was abandoned.

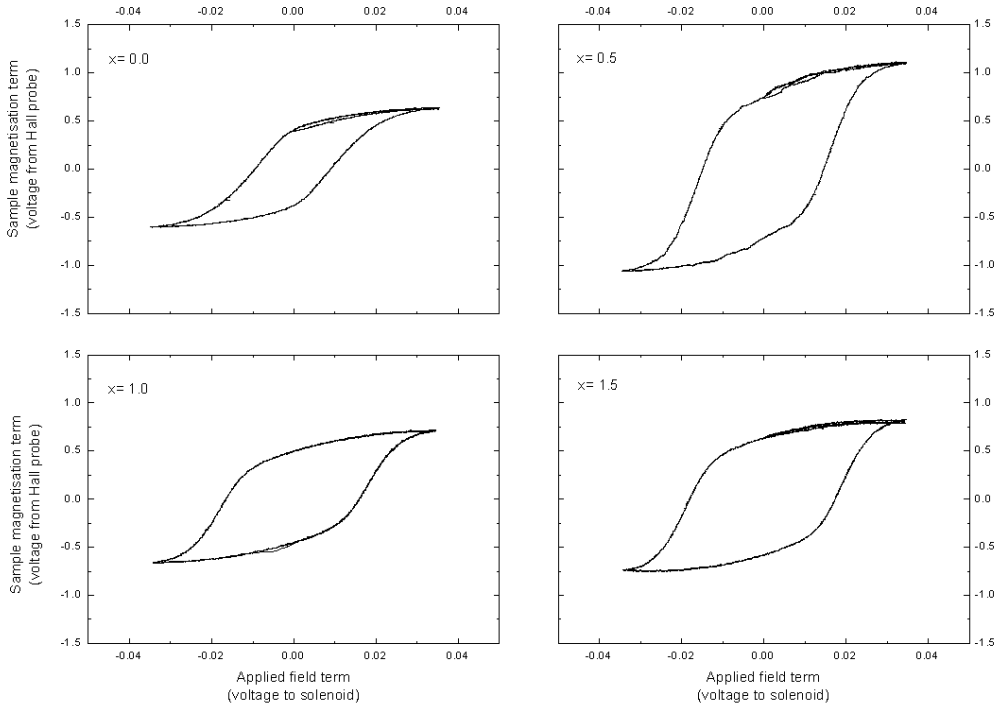

Figure 7.16: Hysteresis loop for samples from series A sample composition $BaBi_xFe_{12-x}O_{19}$ when the data collection time is set for 10 minutes

The clear first impression for the results presented in Figure 7.16 is that the unsubstituted barium hexaferrite sample has a hysteresis loop which is less similar than the bismuth containing materials; it has a lower magnetic saturation (M_s), lower remnant magnetism (M_r) and a smaller coercive force (H_c). With the addition of bismuth all of these values increase as detailed in Table 7.1.

Sample composition	Magnetic saturation (M_s)	Remnant magnetism (M_r)	Coercive force (H_c)
$x = 0.0$	0.643	0.416	0.00948
$x = 0.5$	1.010	0.748	0.01480
$x = 1.0$	0.715	0.504	0.01656
$x = 1.5$	0.792	0.639	0.01821

Table 7.1: Magnetic properties for samples with composition $BaBi_xFe_{12-x}O_{19}$ from series A

The addition of bismuth alters the magnetic properties of the barium hexaferrite, most

notably the coercive force required to demagnetise the material is increased. There are also increases in the values for magnetic saturation and the remnant magnetism. There are variations between the doped $x = 0.5, 1.0$ and 1.5 pellets indicating that the quantity of bismuth present also impacts upon the magnetic properties. By adding bismuth barium hexaferrite becomes more magnetically 'hard' and thus stronger as a permanent magnet.

Results presented here show that for the samples with added bismuth the magnetic saturation and remnant magnetisation values are higher which the coercive force is lower for the lowest concentration of bismuth. This finding supports those reported by Pal et al. [14], however due to covering a wider range of sample compositions which have not been studied before, it also appears that after a slight drop for sample composition $x = 1.0$ the magnetic saturation and remnant magnetism values do increase again for the $x = 1.5$ pellet.

7.6.4 Conclusions

The hysteresis loops obtained by using the VSM set-up showed that the addition of bismuth to barium hexaferrite altered the magnetic properties of the sample. The hysteresis loop became more square for higher bismuth concentrations while the magnetic saturation and remnant magnetism values were greater for the lowest bismuth substitution level studied (composition $x = 0.5$). Further study is required to investigate the magnetic properties of bismuth substituted barium hexaferrite more fully, however since the procedure results in permanently magnetised samples this is not a trivial matter, hence why only one series was tested within this work. Figure 7.17 demonstrates the

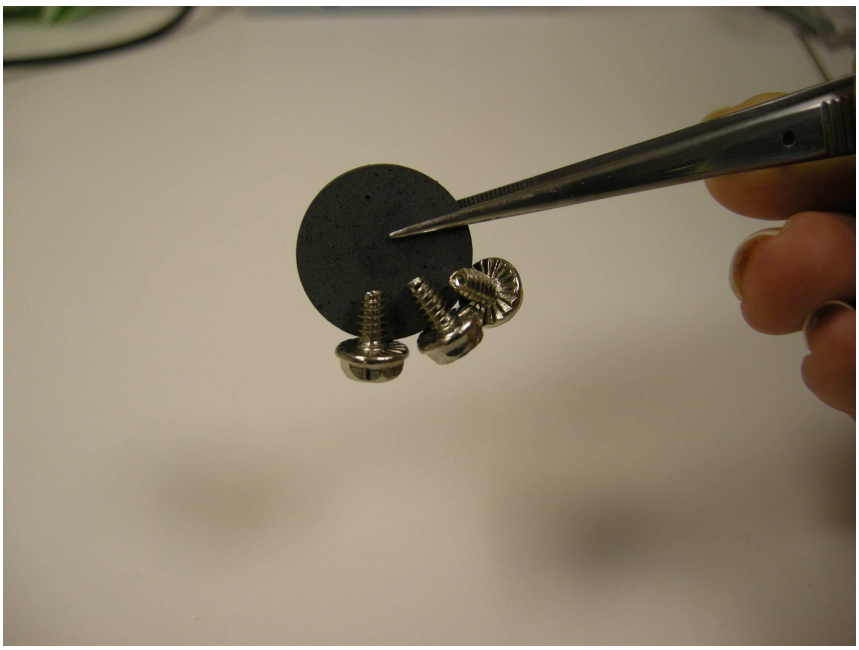

Figure 7.17: Image of pellet composition $x = 0.5$ after VSM characterisation. The sample remains magnetised and can be used to hold several screws in the air

permanent magnetic nature of the samples after VSM characterisation.

7.7 Chapter conclusions and future work

7.7.1 Conclusions

The concept of permeability as a measure of the magnetic storage potential of a material was introduced. A brief discussion of possible measurement regimes was given before the selected inductance measurement scheme and experimental equipment was presented.

Inductors were fabricated to place the barium hexaferrite and bismuth substituted barium hexaferrite samples inside. An inductor was connected to a Wayne Kerr 6440B LCR meter and the inductance of the system over the frequency range 20Hz – 3MHz was recorded. This value was divided by the inductance measured when the coil was empty during

post-processing and it was these L_{sample}/ L_{air} results which were presented.

The L_{sample}/ L_{air} values display a low inductance at low frequencies which rapidly increase before stabilising to a constant value at frequencies above 300kHz.

The trends seen in the relative inductance values with respect to bismuth content at 1MHz are the same as those observed for the permittivity at the same frequency; increasing from a low value for the $x = 0.0$ sample to a maximum at $x = 0.5$ and then slowing reducing as bismuth increases up to the maximum of $x = 1.5$. It was concluded that this was most likely due to bismuth first substituting into the $4f_2$ sites and then after the maximum at $x = 0.5$ continuing to substitute into the 2a positions in the lattice. Thus the magnetic properties of the sample reach a peak at the $x = 0.5$ level before additional bismuth ions distort the lattice structure, impeding the magnetic properties.

The samples sintered at 1200°C display a more mixed set of results. The trends for series E pellets which have been sintered for three hours are similar to those seen for 1100°C sintered materials. Series A and PS show the same trends which vary from the other series. There is a sharp initial increase when bismuth is introduced into the compound, then a more gradual increase up to composition $x = 0.8$ then a slight drop before the values recover at the $x = 1.5$ sample composition.

It was consistently found that the relative inductance of barium hexaferrite was increased by sintering for longer periods of time and/or higher temperatures. It was concluded that this is likely due to a greater level of formation for the undoped compound. The addition of bismuth increases the relative inductance far beyond those achieved from the undoped material.

The magnetisation of a sample in the presence of an applied magnetic field was considered. An example hysteresis loop was shown and key parts illustrated. The system used to collect data to plot hysteresis curve data was described which utilises a vibrating sample magnetometer. Results showed that the magnetic properties of the sample were altered with the introduction of bismuth. The lowest concentration bismuth sample ($x = 0.5$ in this case) had greater magnetic saturation and remnant magnetism values than other samples. However the higher bismuth concentration materials display more square hysteresis loops.

Although the purpose of this work was to primarily investigate barium hexaferrite and bismuth substituted barium hexaferrite for potential use in telecommunications devices, the magnetic properties are still of interest and it was important to quantity these and to take them into account in the design of any future device.

7.7.2 Future work

The permeability of the samples could be looked at in more detail; they could be machined into toroidal shapes and tested with a specifically designed test fixture. This work was not undertaken due to the destructive nature of this method.

The VSM became available close to the end of the PhD and thus time was limited. If this had been available sooner further work would have been carried out in this area. This testing regime is also a destructive one in that the samples remain as permanent magnets once they are removed from the applied field.

7.8 References

[1] J. Daintith, J. Clark, H.M. Clarke, D. Cooper, J. Cullerne, D.E. Edwards, R. Rennie, and D.E. Ward. *Dictionary of Physics*. Oxford University Press, 6th edition, 2009.

[2] P Shepherd, K. Mallick, and R. Green. Magnetic and structural properties of M-type barium hexaferrite prepared by co-precipitation. *Journal of Magnetism and Magnetic Materials*, 311(2):683–692, 2007.

[3] L. B. Kong, Z. W. Li, G. Q. Lin, and Y. B. Gan. Magneto-Dielectric Properties of MgCuCo Ferrite Ceramics: Electrical, Dielectric, and Magnetic Properties. *Journal of the American Ceramic Society*, 90(7):21042112, 2007.

[4] Agilent Technologies. Agilent 85071D materials measurement software. 2001.

[5] Agilent Technologies. De-embedding and embedding S-parameter networks using a vector network analyzer. 2004.

[6] P. Patnaik. *Handbook of Inorganic Chemical Compounds*. McGraw-Hill, 2003.

[7] P. Winotai, S. Thongmee, and I.M. Tang. Cation distribution in bismuth-doped M-type barium hexaferrite. *Materials Research Bulletin*, 35:1747–1753, 2000.

[8] S. Ram. Observation of enhanced dielectric permittivity in Bi^{3+} doped $BaFe_{12}O_{19}$ ferrite. *Journal of Magnetism and Magnetic Materials*, 80:241–245, 1989.

[9] L. Solymar and D. Walsh. *Lectures on the Electrical Properties of Materials*. Oxford University Press, 4th edition, 1988.

[10] H. Young. *University Physics*. Addison-Wesley, 8th edition, 1992.

[11] J.C. Anderson, K.D. Leaver, P. Leevers, and R.D. Rawlings. *Materials Science for Engineers*. Nelson Thornes Ltd., fifth edition, 2003.

[12] W. H. Hayt. *Engineering Electromagnetics*. McGraw-Hill, 4th edition, 1981.

[13] S. Ram, H. Krishnan, K.N. Rai, and K.A. Narayan. Magnetic and electrical properties of Bi_2O_3 modified $BaFe_{12}O_{19}$ hexagonal ferrite. *Japanese Journal of Applied Physics*, 28(4):604–608, 1989.

[14] M. Pal, P. Brahma, D. Chakravorty, and D.C. Agrawal. Magnetic properties of Ba hexaferrites doped with bismuth oxide. *Journal of Magnetism and Magnetic Materials*, 147:208–212, 1995.

[15] T. Ogasawara and M.A.S. Oliveira. Microstructure and hysteresis curves of the barium hexaferrite from co-precipitation by organic agent. *Journal of Magnetism and Magnetic Materials*, 217:147–154, 2000.

[16] R. Powell. Vibrating Sample Magnetometer Project, 2008.

[17] A. Marikani. *Engineering Physics*. PHI Learning, 2nd edition, 2009.

Chapter 8

Conclusions

The following chapter presents a summary of the main conclusions from the previous chapters.

8.1 Barium hexaferrite

Bismuth substituted barium hexaferrite of composition $BaBi_xFe_{12-x}O_{19}$ was formed via the solid state synthesis method. Formation was confirmed by XRD analysis and images produced from SEM showed a structure similar to that observed for the parent compound barium hexaferrite formed by the same method. It was found that the added bismuth acts as a sintering aid; with bismuth containing compounds formed whilst undoped equivalents were only partially formed after the same sintering regime. Work presented within this chapter resulted in a number of bismuth substituted barium hexaferrite samples from a range of sintering regimes for further analysis in subsequent chapters.

8.1.1 Future work

The investigation of a wider range of sample compositions and sintering regimes would be beneficial. The characterisation of the physical properties of the material could be improved upon by more detailed profiling of surface roughness and a more accurate method for measuring the pellet density (such as the Archimedes method). The technique of microwave sintering could also be refined to produce bismuth substituted barium hexaferrite within a much reduced time period over conventional heating methods.

8.2 Low frequency dielectrics and permittivity

A parallel plate capacitor method was used to calculate the permittivity of samples over the frequency range 20Hz – 3MHz. It was found that bismuth containing samples had a consistently higher permittivity than their undoped counterparts.

After sintering at 1100°C the highest permittivity was recorded as $\varepsilon_r = 75.04 - 6.517j$ at 1MHz for sample composition $BaBi_{0.5}Fe_{11.5}O_{19}$ after sintering for three hours. This was explained by considering that this is consistent with previously published data suggesting this point is the saturation point for bismuth substituting into the $4f_2$ sites in the lattice. Interestingly the drop in permittivity at the $x = 0.8$ level was found to correlate to the splitting of peaks at the 23° position in the XRD data.

The samples sintered at 1200°C contain the highest permittivity sample where $\varepsilon_r = 86.18 - 9.910j$ at 1MHz for sample composition $BaBi_{0.2}Fe_{11.8}O_{19}$ which had been sintered for one hour at 1200°C followed by a further hour at 1200°C. The comparison of doping levels versus permittivity at a constant frequency of 1MHz showed that after the highest

permittivity values at $x = 0.2$ values then decrease with increasing bismuth content. It was hypothesised that the reason for the highest permittivity being found at this composition was due to the higher sintering temperature facilitating a more rapid and complete reaction, so saturation into the $4f_2$ sites was achieved sooner.

It was found that a high permittivity material could be produced after sintering for relatively short periods of time due to the addition of bismuth to barium hexaferrite.

8.2.1 Future work

The main improvement which could be made to improve the accuracy of the parallel plate characterisation scheme used within this work would be to coat both sides of the pellet with a conductive coating to eliminate the effect of air gaps on the measurements.

8.3 High frequency dielectrics and permittivity

A coaxial probe system was used to collect permittivity data at high frequencies (range 45MHz – 20GHz). It was found that results were reliable up to the 6GHz threshold, at which point reflections from the back surface of the sample caused oscillations in the permittivity data.

Data for the permittivity of samples against substitution level were presented at a constant frequency of 2.45GHz for the different sintering temperatures. At 1100°C the highest permittivity sample was the $x = 1.5$ ($BaBi_{1.5}Fe_{10.5}O_{19}$) material which had been sintered for three hours, with $\varepsilon_r = 14.69 - 1.664j$. These results are different to those observed at low frequencies, however trends for the lower doping levels of $x = 0.0, 0.2$

and 0.5 do agree with the trends at lower frequencies. After the $x = 0.5$ level the trends diverge.

At 1200°C the highest permittivity sample where $\varepsilon_r = 11.81 - 1.995j$, is the $x = 0.5$ material which has been sintered for three hours at this temperature. The data for pellets from series A show the same trends as the low frequency results. The three hour sintered pellets also show similar trends to low frequency data with the exception of the $x = 0.2$ sample which has a lower permittivity relative to the other compositions.

The reasons for these differences are most probably due to a combination of materials properties and physical effects. It was noted that the surface of the material where the probe is placed in contact with the pellet will be important because the nature of the measurement means that the permittivity values are calculated from the reflection of this surface.

8.3.1 Future work

The modification of the physical shape of the samples to make them larger so that they appear infinite to the probe would allow the reliable test frequency range to be increased to incorporate higher frequencies (a maximum of 25GHz is possible with the existing test fixtures). The implementation of a frequency varying characterisation method would also allow the measurement of high frequency permeability which would be of added value.

8.4 High frequency near-field permittivity

A prototype near-field permittivity sensor was developed and proven effective by characterising the resonant frequencies of different permittivity materials. A different permittivity material in the vicinity of the probe tip alters the resonant frequencies recorded. This probe was used to investigate the surface of a bismuth substituted barium hexaferrite pellet. This found slight changes in resonant frequency positions at different points on the material but these are not significant compared to the differences observed for different permittivity materials. This shows that although there are small variations in the permittivity across the face of the samples, this is unlikely to effect the overall measured bulk permittivity of the bismuth substituted barium hexaferrite materials.

8.4.1 Future work

The work completed within this chapter could be developed further by the manufacture of a more sensitive probe (i.e. one with a smaller diameter tip) to increase the accuracy of the measurements. The system would also be improved by the use of an automated sample stage to allow measurements to be taken over a shorter time duration.

8.5 Antenna applications

Simulation work using Comsol Multiphysics was conducted to develop a design for a dielectric resonator antenna (DRA). This was then fabricated and initial tests carried out using a wide variety of bismuth substituted barium hexaferrite samples. The theoretical first resonant frequency of an example rig was calculated at 5.64GHz, simulations of

the same set-up produced a first resonant frequency at 5.85GHz and experimental data produced an initial resonance at 6.02GHz. The differences between these values were concluded to be most likely due to non-perfect conditions in the difference between then theoretical and simulation, and real-world considerations such as the quality of the contact between the resonant material and the ground plate in the experimental system.

For samples which contained bismuth the first resonant frequency of the system occurs between 4 and 7GHz depending on the specific material.

Radiation pattern data was collected for a DRA set-up at two resonant frequencies of 6.6GHz and 13.6GHz. At resonance the radiation patterns showed good agreement with published simulation results. This system has the potential to be further developed into a feasible system.

8.5.1 Future work

The work into DRAs could be expanded to include a wider variety of resonator shapes other than cylindrical. The option to magnetise samples to potentially enhance the bandwidth of the antenna is also of interest for future work.

8.6 Low frequency permeability and magnetic properties

Low frequency magnetic properties of the samples were characterised using an inductor set-up in conjunction with an LCR meter. The relative inductance of a sample was found by dividing the inductance of the system with the sample in place by the inductance of the empty rig. The relative inductance is small at low frequencies and rapidly increases

until after 300kHz where values are approximately constant.

The trends in relative inductance at 1MHz for the samples sintered at 1100°C shows the same patterns as those for the permittivity at this frequency. This was attributed to the additional bismuth first substituting into the $4f_2$ sites in the lattice until saturation and then substituting into the 2a positions. For samples sintered at 1200°C the series E pellets which have been subjected to this temperature for three hours show trends more similar to those sintered at 1100°C while series A and PS show agreement with each other. It was repeatedly found that addition of bismuth increased the relative inductance of the material far beyond that of the undoped parent compound.

Hysteresis loops were presented for series A samples and again showed that the addition of bismuth alters the magnetic properties of the material. At the $x = 0.5$ composition the greatest magnetic saturation and remnant magnetism values were observed; however samples with higher bismuth concentrations displayed more square hysteresis loops. It is likely that the highest degree of magnetic saturation and remnant magnetism occurs when the material has the highest number of bismuth ions substituted into the $4f_2$ sites which will occur at the $x = 0.5$ level. The samples became permanently magnetised after characterisation with the VSM.

8.6.1 Future work

The characterisation of the absolute values of the permeability of samples would be an interesting and useful topic of work to undertake. If more samples were available then further study of the hysteresis loops of a wider range of samples would be undertaken.

8.7 Summary

This thesis set out to further scientific knowledge by characterising the dielectric and magnetic properties of bismuth substituted barium hexaferrite over a wide frequency range. This has been achieved.

Work presented has shown the dielectric and magnetic properties of a wider range of bismuth substitution levels than previously existed over a wider frequency range. Data was presented for all compositions, not a single 'best case' result. Analysis to link permittivity and inductance results to doping levels was undertaken. A prototype near-field permittivity sensor was used to investigate the homogeneity of bismuth substituted barium hexaferrite. A dielectric resonator antenna was constructed using a bismuth containing sample as the resonant material. Work in this area has not previously been conducted.

In conclusion, this work has achieved the aims set out in the introduction. Future work on each topic has been suggested at the end of each relevant chapter.

Appendix A

Low frequency dielectrics and permittivity

A.1 An alternative parallel plate capacitor characterisation scheme - non-contacting electrode method

The low frequency results obtained for sample permittivity in Chapter 3 were obtained using the simple contacting electrode method (detailed in Section 3.2). This method is popular due to its simplicity and relative speed (useful when characterising large sample sets). A variation of the parallel plate capacitor method where the effect of an air gap between the electrode and the MUT is taken into account is the 'non-contacting electrode method' [1].

This regime requires two separate capacitance (C) and dissipation factor (D) measure-

[1] Agilent Technologies. Solutions for measuring permittivity and permeability with LCR meters and impedance analysers, 2008.

ments; one where the MUT is present with a small air gap between the sample and the top electrode, and a second measurement where the sample holder is empty but the separation between the plates is equal to that of the first measurement (Figure A.1).

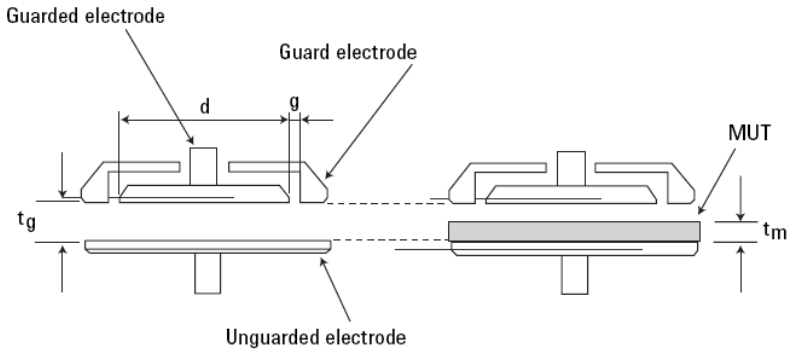

Figure A.1: Non-contacting electrode method of characterising sample dielectric properties; diagram of plate separation for the two measurements required. t_g is the the plate separation distance between electrodes for the empty cell, t_m is the thickness of the material under test, d is the diameter of the guard ring and g is the thickness of the guard ring[1].

For this method to deliver greater accuracy than the standard contacting electrode system, the assumption is made that the air gap for the measurement with the MUT is very small compared to the thickness of the sample pellet. The real part of permittivity of the material is calculated in Equation A.1 [1]

$$\varepsilon_r' = \frac{1}{1 - \left(1 - \frac{C_g}{C_m}\right) \times \frac{t_g}{t_m}} \tag{A.1}$$

where ε_r' is the real part of permittivity; C_g (in Farads) is the measured capacitance of the air gap between the electrodes with no sample in-between; C_m (in Farads) is the measured capacitance of the gap between the electrodes with the sample in place when there is a small gap between the sample and top electrode (same separation as the empty cell set-up); t_g (in metres) is the plate separation distance between electrodes; and t_m (in metres) is the thickness of the MUT.

The imaginary part of permittivity is calculated using Equations A.2 [1] and A.3

$$tan\delta = D_m + \varepsilon'_r \times (D_m - D_g) \times \left(\frac{t_g}{t_m} - 1\right) \tag{A.2}$$

$$tan\delta = \frac{\varepsilon''_r}{\varepsilon'_r} \tag{A.3}$$

where symbols are those defined above and additionally, $tan\delta$ is the loss of the material; D_m is the measured dissipation factor of the system with the sample in place; D_g is the dissipation factor of the empty cell; and ε''_r is the imaginary part of permittivity.

Pellets from series F (three hours sintering at 1100°C) were characterised using the non-contact electrode method for low frequency characterisation from 20Hz – 3MHz. Graphs for the real and imaginary parts of permittivity are presented in Figure A.2.

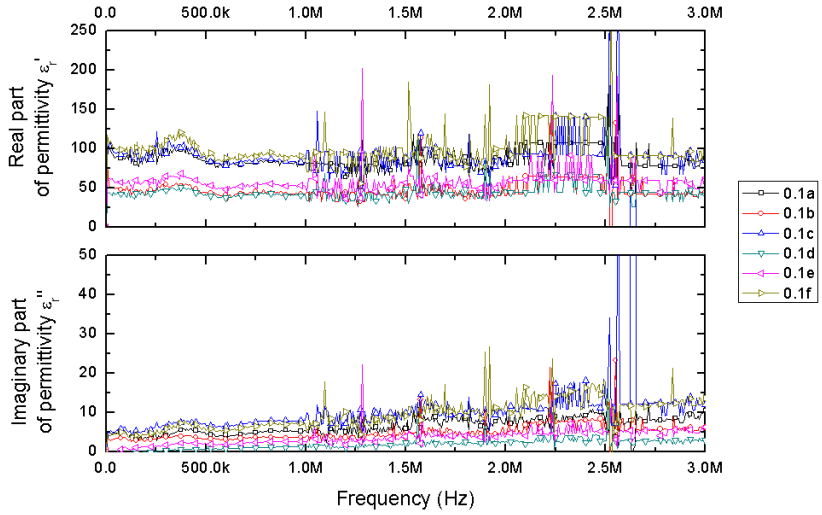

Figure A.2: Real and imaginary parts of permittivity for series F pellets sintered at 1100°C for three hours, calculated using the non-contact electrode method for the parallel plate capacitor set-up

The most noticeable feature of the graphs is the large variation in permittivity for both real and imaginary parts at frequencies above 1MHz. This was noted for the imaginary

part of permittivity from the standard contacting electrode method for parallel plate characterisation, however not to the extent observed here. Upon investigation it was concluded that the change of resolution for capacitance measurements above 1MHz (Section 3.4.2 Table 3.4) is significant for calculation of permittivity from the non-contacting electrode method. Equation A.1 used to calculate the real part of permittivity uses the recorded capacitance of the gap between the electrodes with both the MUT in place and when the cell is empty. The capacitance of the empty cell for the plate separation of a typical measurement falls in the 0.1pF range. This means that below 1MHz it will be measured to two decimal places and at 1MHz and above to one decimal place (when the MUT is in place capacitance is around 10pF so is not the limiting factor) with measurements coerced to the nearest value. The imaginary part of permittivity is effected in the same way due to the real part of permittivity being used in that calculation (Equation A.3). An example of how the dielectric properties change with variation in measured capacitance is given in Table A.1 for two adjacent frequency points.

C_g (pF)	ε_r'	ε_r''
0.14	97.9	12.1
0.15	91.2	12.3

Table A.1: Example of how variation in air gap capacitance results in a large change in calculated permittivity. (Taken from data for series F $x = 0.1f$ pellet, side 2 at 2.01MHz and adjacent point)

Below 1MHz variation in both the real and imaginary parts of permittivity is still present to a lesser degree. The range is larger than observed for permittivities calculated using the standard contacting electrode method. The contacting electrode method is less affected by the change of resolution because capacitances measured all contain the MUT and thus have a larger capacitance, resulting in these being recorded more accurately. Therefore it was concluded that the contacting electrode method was more appropriate for characterising dielectric properties using the equipment available.

A.2 Three-dimensional modelling in Comsol Multiphysics

A three-dimensional representation of an existing bismuth substituted barium hexaferrite pellet between two capacitor plates was generated using Comsol Multiphysics. This was sample $x = 0.5b$ from series C (one hour sintering at 1100°C), which was 5.737mm thick, 20mm in diameter and had a maximum experimentally measured permittivity of $\varepsilon_r = 75 - 1.20j$ at 20Hz. The geometry established for the model is shown in Figure A.3.

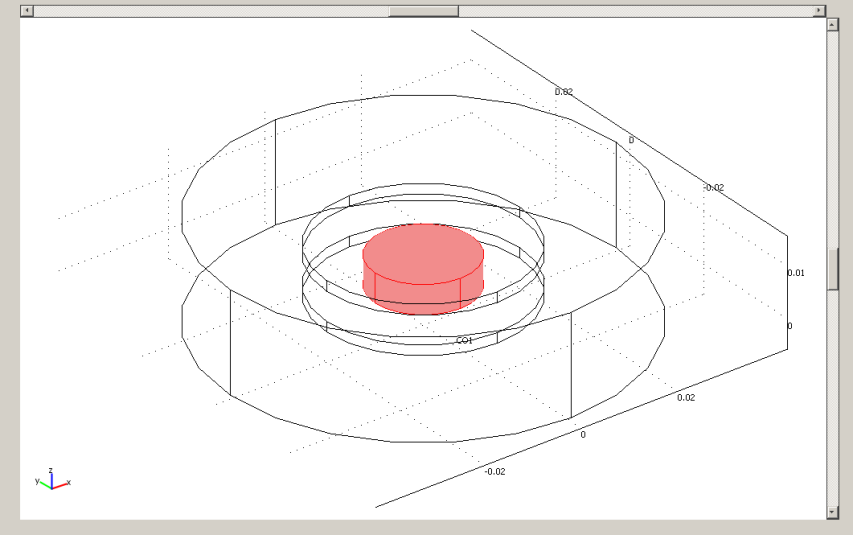

Figure A.3: Modelled geometry of series C $x = 0.5b$ sample. The pellet can be seen as the shaded disk between two capacitor plates. The surrounding area is the limit of the air surrounding the model for simulation purposes.

The solver parameters were established to calculate the capacitance of the system over the same frequency range that the LCR meter can measure experimentally (20Hz – 3MHz). This was accomplished by setting the geometry which represents the top plate of the sample holder as a port. This port is then set as an input and the input property is set to the 'energy method'. The bottom plate was set as a ground plane and the other selectable boundaries (representing the limits of the surrounding space) were set to zero charge/symmetry. The remaining boundaries are internal to the structure and so

are automatically set as continuity conditions by Comsol.

Once the problem was solved, various parameters are available for display in the output mode. The capacitance of the system was shown to be constant across the frequency range 20Hz – 3MHz at 13.8pF. This value is larger than the experimentally recorded value of 9.2pF at 20Hz, however Comsol has no facility to model the losses within the material, so this higher value is not unexpected. The actual sample also contains physical imperfections not modelled by the simulation which will again reduce the measured capacitance. Experimental results show that the capacitance is frequency dependant; decreasing by around 1pF over 20Hz – 3MHz due to increasing losses in the material with increasing frequency. The model does not model loss, so the capacitance remains constant. To save on simulation time, further models were evaluated only at a constant frequency of 20Hz.

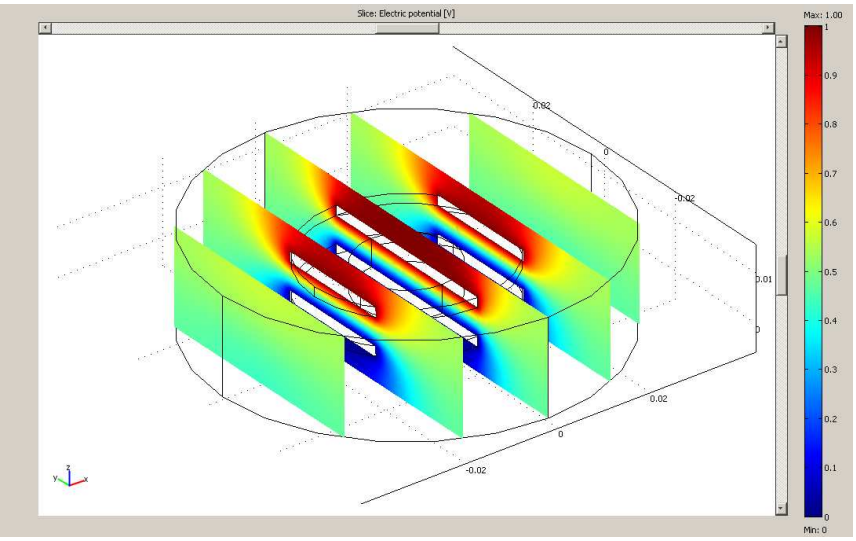

Figure A.4: Slice plot showing electric potential by colour gradient. Sample permittivity $\varepsilon_r = 75 - 0j$

A slice plot representing electric potential across the sample and the surrounding area is shown in Figure A.4. As expected, the value is the maximum of 1V at the top plate where the energy is supplied to the system, falling to 0V at the bottom plate (which is

grounded), shown by the colour gradient shifting from red to blue.

Attempts were made to model the effect of a small air gap and a rough sample surface in 3D, however this made the mesh for the problem too fine and as a consequence the solver ran out of memory. Further models were simulated in two-dimensions, which is not as representative of the physical system, but still provides a useful tool for making comparisons between different experimental situations.